Université de Paris
En cotutelle avec Universitè de Cagliari

Ecole doctorale STEP'UP 560

Laboratoire Astroparticule et Cosmologie

Dark matter search and neutrino physics in Liquid Argon

Par Michela Lai

Thèse de doctorat de Physique de l'Univers

Dirigée par Davide Franco
Et par Walter Marcello Bonivento

Présentée et soutenue publiquement le 05/02/2021

Devant un jury composé de :

Davide Franco, Directeur de recherche, Universitè de Paris, Directeur de thèse
Walter Marcello Bonivento, Chargè de recherche, Universitè de Cagliari, Co-directeur de thèse
Juan José Gómez Cadenas, Professeur des Universités, Donostia International Physics Center (University of Basque Country), rapporteur
Leszek Roszkowski, Professeur des Universités, National Centre for Nuclear Research, 02-093 Warsaw, rapporteur
Nicola Serra, Professeur des Universités , University of Zurich, examinateur
Alessandra Tonazzo, Professeur des Universités, Universitè de Paris, examinatrice
Gianluca Usai, Professeur des Universités, Universitè de Cagliari, examinateur

Except where otherwise noted, this work is licensed under
https://creativecommons.org/licenses/by-nd/3.0/fr/

Titre : Recherche de matière noire et physique des neutrinos dans l'argon liquide

Résumé : Plusieurs observations astrophysiques, tant galactique que cosmologique, montrant qu'il y a une "masse manquante" dans l'Univers observable, peuvent être expliquées en supposant une matière non lumineuse, donc appelée "matière noire". L'un des candidats les plus prometteurs est le Weak Interacting Massive Particle (WIMP), une particule massive non relativiste, capable d'une interaction gravitationnelle et d'une interaction faible avec la matière baryonique.
Le présent travail est axé sur le potentiel physique en plus de la recherche des WIMPs des détecteurs de matière noire remplis d'argon liquide, comme DarkSide et DEAP-3600. L'argon liquide est une cible optimale grâce à ses rendements élevés de scintillation et d'ionisation.
DEAP-3600 est un détecteur monophasique qui exploite uniquement le canal de scintillation, tandis que DarkSide-20k et Argo, les futures expériences à l'échelle des tonnes du programme DarkSide, sont des chambres de projection temporelle (TPCs) biphasiques qui examinent les signaux de scintillation et d'ionisation. La grande masse (3.3 tonnes) de la cible de DEAP-3600 a permis d'effectuer une analyse pour rechercher des Multi Interacting Massive Particles (MIMPs), une possible alternative aux WIMPs, à des masses supérieures à 10^{16} GeV et avec une section efficace indépendante du spin matière noire-argon d'environ 10^{-22} cm^{2} . Ce travail est la phase préparatoire à l'ouverture de 3 années de collection de données.
Du présent aux futurs détecteurs de matière noire, DarkSide-20k et Argo seront caractérisés par une sensibilité extraordinaire aux faibles reculs d'énergie. Ceci est principalement la conséquence de la haute résolution énergétique des photodétecteurs choisis, les photomultiplicateurs de silicium (SiPMs). Les SiPMs personnalisées ont été fabriques pour la recherche de la matière noire dans DarkSide-20k; par conséquence, les SiPMs ont été ici caractérisées, avec un accent sur leurs bruits corrélés : les afterpulses et les optical crosstalks. La même sensibilité à basse énergie apporte également un fort potentiel de détection des neutrinos de supernova par coherent elastic neutrino-nucleus scattering (CEvNS) dans l'argon en exploitant le signal d'ionisation. L'étude de sensibilité correspondante est ici réalisée et il montre que l'émission de neutrinos sera détectée pour toute supernova galactique, avec une bonne précision dans la reconstruction des principaux paramètres de l'éclatement, c'est-à-dire l'énergie totale des neutrinos et leur énergie moyenne.

Mots clefs : physique des particules; matière noire; physique des neutrinos; neutrinos de supernova; photomultiplicateur au silicium; argon liquide; DarkSide ; DEAP-3600 ; analyse des données; simulations.

Title : Dark matter search and neutrino physics in Liquid Argon

Abstract :
Several astrophysical observations, both on a galactic and cosmological scales, showing that there's a "missing mass" in the observable Universe, can be explained assuming a non-luminous kind of matter, hence called "dark matter". One of the most promising candidates is the Weakly Interacting Massive Particle (WIMP), a non-relativistic massive particle, gravitationally and weakly interacting with baryonic matter. The present work is specifically focused on the physics potential besides WIMP search of dark matter detectors filled with Liquid argon, like DarkSide and DEAP-3600. Liquid argon is an optimal target thanks to its high scintillation and ionization yields. DEAP-3600 is a single-phase detector, exploiting the scintillation channel only, while DarkSide-20k and Argo, future tonne scale experiments from the DarkSide program, are dual-phase Time Projection Chambers (TPCs), looking at both scintillation and ionization signals. The large mass (3.3 tons) of the DEAP-3600 target has allowed me to perform an analysis to search for Multi Interacting Massive Particles (MIMPs), a dark matter candidate alternative to WIMPs, at masses above 10^{16} GeV and with argon-dark matter spin-independent cross-section of about 10^{-22} cm^{2} , fully setting up the upcoming unblinding of three years of data taking. Going from the present to the future dark matter detectors, DarkSide-20k and Argo will be characterized by an extraordinary sensitivity at low energy recoils. This is mainly consequence of the high energy resolution of the chosen photodetectors, Silicon Photomultipliers (SiPMs). Custom SiPMs have been designed for the dark matter search in DarkSide-20k; hence, SiPMs have been here characterized, with a focus on their correlated noises, namely afterpulses and optical crosstalks. The same sensitivity at low energy brings also to a strong potential in detecting supernova neutrinos via coherent elastic neutrino-nucleus scattering (CEvNS) in argon by exploiting the ionization signal. The related sensitivity study is here performed showing that the neutrino emission will be detected for any galactic supernova, with a good accuracy in reconstructing the main parameters of the burst, namely the total energy of neutrinos and
their average energy.

Keywords : particle physics; dark matter; neutrino physics; supernova neutrinos; silicon photomultiplier; liquid argon; data analysis ; simulations.

Resume de these – Michela Lai

Mes recherches au doctorat étaient axées sur le potentiel physique d'un détecteur rempli d'argon liquide, à la fois pour la recherche de la matière noire et la physique des neutrinos. Plus précisément, ces détecteurs sont conçus pour détecter l'un des candidats les plus prometteurs de la matière noire : les particules massives faiblement interagissantes (PSIF).
La première année a été principalement passée à l'Université de Cagliari, en Italie. Les quatre premiers mois ont été consacrés à la compréhension du détecteur DarkSide-50 et des futurs détecteurs DarkSide-20k et Argo. J'ai dû étudier la scintillation en argon liquide, les observables disponibles, les arrière-plans dans une recherche WIMP habituelle.

Après quelques mois la conception de DarkSide-20k et Argo a été modifiée, de sorte qu'un certain temps a été consacré à étudier en détail à partir du rapport technique de la collaboration la nouvelle conception du détecteur.
En décembre 2018, j'ai passé trois semaines à Paris, sous la direction de Davide Franco. L'objectif principal de ces semaines a été d'apprendre à coder dans ROOT et à effectuer des simulations Monte Carlo. À mon retour, j'ai pu commencer à travailler sur l'étude de sensibilité de DarkSide-20k et d'Argo aux neutrinos émis par une éventuelle supernova d'effondrement du noyau, qui est maintenant le chapitre 6 de ma thèse de doctorat.

Le premier résultat a été de reproduire le taux différentiel des événements compte tenu du flux de neutrinos à la Terre et de la section transversale dominante pour les reculs à l'énergie ~ 10 MeV dans l'argon liquide, qui est le noyau de neutrinos élastique cohérent diffusion un. À titre de contre-vérification, le résultat a été comparé à un papier lié à la même sensibilité dans un détecteur de matière noire rempli de xénon. Une fois que cela a été fait, je pouvais travailler sur le jouet Monte Carlo simulation elle-même, basé sur une statistique Poissonian.

La première sortie a été la découverte des détecteurs de supernova à des distances croissantes. Il a été découvert que nos futurs détecteurs vont certainement détecter les neutrinos d'une supernova d'effondrement de noyau non seulement si cela explose dans notre galaxie, mais aussi dans le Grand et le Petit Nuage de Magellan. Cette étude a été présentée par moi comme exposé dans deux réunions générales de la Collaboration. Également au cours de la première année, selon ce qui est exigé de l'Université de Cagliari, j'ai effectué deux activités de tutorat, en particulier dans « General Physics 1 » (traduit de l'italien) et « Physics Laboratory 2 ». J'ai également assisté à une conférence sur la physique au-delà du modèle standard, tenue par mon superviseur local Walter Bonivento.

Au cours de la première année, l'accord entre les deux universités a été finalisé, de sorte que la deuxième année a été principalement passée à l'Université Paris Diderot, à APC, sous la supervision de Davide Franco.

Grâce à son aide au cours de la deuxième année, mon activité de recherche a été stimulée. Alors que le travail sur les supernova a été revu par la collaboration DarkSide, nous avons commencé à travailler du côté matériel. Plus précisément, nous avons travaillé sur PyReD, le nouveau code de reconstruction qui était au stade de développement à l'époque basé sur le codage Python et testé pour la première fois sur les données ReD, un petit détecteur rempli d'argon liquide à Naples.

Le premier objectif de ReD est de tester la sensibilité d'un TPC d'argon liquide à la modulation quotidienne du taux de WIMP ; si ce résultat est atteint, il garantira la sensibilité des futurs détecteurs DarkSide, DarkSide-20k et Argo, aux WIMPs également sous le « plancher de neutrinos », où l'arrière-plan provenant des neutrinos atteignant le détecteur ne sera pas négligeable.
Pour chaque événement déclenché dans le détecteur, les photocapteurs installés dans le récipient d'argon liquide stockent une forme d'onde, dont l'intégration donne le nombre de photoélectrons reconstruits, dans le code de reconstruction habituel.

Contrairement aux expériences déjà en cours comme DarkSide-50 ou DEAP-3600, les prochains détecteurs de matière noire dans l'argon liquide ne seront pas équipés de tubes de photomultiplicateurs (PMT) mais de photomultiplicateurs de silicium (PMM).
Les SiPMs ont de nombreux avantages par rapport aux PMTs : ils sont beaucoup plus radiophoniques, ils ont un bruit sombre plus faible, ils sont insensibles à un champ magnétique et surtout ils ont une résolution d'énergie plus élevée au niveau d'un photoélectron.
Les principaux inconvénients sont le temps de recharge des diodes d'avalanche et la contribution des bruits corrélés, à savoir les afterpulses et les crosstalks optiques. Avec PyReD, après un étalonnage personnalisé de la réponse Single photoElectron à travers des analyses laser, la somme des hauteurs des pics peut également renvoyer le nombre de photoélectrons dans le SiPM.

Plus précisément, la variable d'intérêt était la « proéminence » des pics, c'est-à-dire combien ils dépassent par rapport aux pics avoisinants les plus proches, après soustraction de la référence.
D'une part, nous avons commencé à examiner la façon dont les reculs en raison d'éventuelles PGRF peuvent être discriminés par ceux en raison d'un événement de fond en examinant la charge rapide évaluée à partir des hauteurs des pics; en d'autres termes, une « discrimination de forme de pouls ». basé sur la proéminence, au lieu de l'intégration de la forme d'onde, comme habituellement fait par la collaboration DarkSide et aussi par la collaboration ReD.

En effet, la discrimination de forme d'impulsion basée sur l'intégration de la forme d'onde peut en principe être affectée par le temps de recharge long du SiPM.

D’autre part, nous avons travaillé sur la caractérisation des bruits corrélés dans les SiPMs développés sur mesure pour la recherche de matière noire dans DarkSide-20k, de la Fondazione Bruno Kessler. Le travail sur la discrimination des formes de pouls s’est poursuivi pendant quelques mois, mais je n’ai pas été en mesure d’arriver à une conclusion exceptionnelle à l’époque, alors nous avons décidé de nous concentrer sur la caractérisation des bruits corrélés.

Plus précisément, la caractérisation a été effectuée sur un ensemble de parcours laser dans ReD, pris de décembre 2018 et janvier 2019. J’ai déterminé la réponse photoélectronique unique dans ces analyses pour chacun des canaux d’acquisition des expériences, afin d’obtenir la forme, le « modèle » de la forme d’onde due à la photoélectron. Le gabarit était bien adapté avec la combinaison linéaire d’un composant rapide, un gaussien, et un composant lent, fait de la convolution d’un gaussien avec une exponentielle.
Le modèle a été utilisé pour appliquer un filtre assorti à la forme d’onde, pour obtenir un signal plus lisse ; sur ce signal, un algorithme de recherche de pics a été appliqué afin de stocker tous les pics trouvés dans la forme d’onde, en particulier leur heure d’arrivée et leur proéminence.
L’étape suivante consistait à déterminer la distribution des afterpulses après coup. Une afterpulse secondaire est créée à partir d’électrons dans une avalanche qui sont piégés puis relâchés peu de temps après par des défauts de silicium. Pour ce faire, seuls les événements ayant un photoélectron dans le temps de déclenchement prévu ont été pris en compte. Dans ces formes d’onde, tous les pics avant le vrai signal du laser, le « pic primaire », devaient être sombres et non corrélés.

Ceux qui suivent doivent être à la fois des afterpulses et des bruits sombres. Comme le bruit sombre doit être réparti avec la même probabilité le long de la forme d’onde, la soustraction des pics avant le primaire de ceux après qu’il a retourné la distribution de temps des afterpulses après ; ce processus a été répété pour tous les événements sélectionnés ReD, donnant le nombre moyen d’afterpulses secondaires en termes de délai à partir du pic primaire, étant donné que le pic primaire contient un photoélectron.
L’intégration temporelle de cette distribution a retourné la probabilité d’avoir une afterpulse secondaire, compte tenu d’un photoélectron dans le pic primaire.

Cette valeur était inférieure à celle trouvée dans la littérature. Ceci est probablement dû au réglage de l’algorithme du localisateur de pics, qui détient certains seuils dans la proéminence, la hauteur et la largeur des pics ; certains pics dus aux afterpulses postérieures tombent en dessous des seuils, de sorte qu’ils sont sautés et non stockés. Néanmoins, cette « inefficacité » du pointeur pourrait être évaluée, ce qui permettrait de corriger la distribution du temps de afterpulses.
La dernière partie du travail a été la caractérisation des crosstalks optiques.
Celles-ci sont dues à l’accélération des porteurs de charge lors d’une avalanche dans l’une des diodes d’avalanche composant le SiPM. Cette accélération donne une émission de photons uniforme, qui peut tirer un ou plusieurs pixels environnants,

ajoutant un ou plusieurs photoélectrons à la charge reconstruite dans le SiPM. Le principal problème est que ce bruit corrélé est simultané au bruit primaire. On a donc utilisé une approche totalement différente. Une simulation de Monte Carlo jouet a été réalisée, dont la sortie aurait été comparée avec celle de l'ensemble de données.

Le seul paramètre restant à contraindre était la probabilité de crosstalk, de sorte que le chi-carré a été utilisé comme statistiques de test. L'entrée est le nombre d'événements à zéro photoélectrons dans la réponse photoélectronique unique.

Ceci renvoie l'occupation moyenne sur ces canaux ; la distribution des hauteurs des pics dans la réponse photoélectronique unique serait le Poissonien de cette occupation, sans aucun bruit corrélé. Ensuite, chaque photoélectron de ceux donnés par le Poissonien peut donner lieu à une afterpulse et/ou à une crosstalk.
.Chaque crosstalk peut produire une autre crosstalk et/ou une afterpulse. Chaque afterpulse peut produire une crosstalk et/ou une afterpulse.

La condition pour arrêter la boucle est que le nombre de photoélectrons s'arrête pour augmenter, ce qui se produit réellement en raison des faibles probabilités. La probabilité de discussion croisée était d'environ 10 %, en accord avec ce qui a été trouvé dans la littérature. Le travail est terminé et est disponible pour la collaboration.
Au cours de la deuxième année, à côté des séminaires organisés à APC, j'ai également participé à un GEANT4 International School 2018 à Trento et l'International School of Statistics 2019 à Paestum. Les travaux relatifs à la supernova ont été présentés lors d'une conférence en Italie de la Société italienne de physique et aussi au groupe GdR des neutrinos.

La caractérisation du bruit corrélé a été montrée au début de la troisième année, dans un exposé à l'Université de Cagliary, lors du Symposium de physique de la haute énergie.

Au début de la troisième année, j'ai pu entrer en contact avec la collaboration DEAP et commencer une analyse de la matière noire avec leurs données, grâce aux accords entre DarkSide et DEAP collaborations. Dans la condition d'effectuer un quart de travail mensuel à distance sur leur expérience en cours d'exécution DEAP-3600 je pourrais commencer à rechercher un candidat de particule de matière noire très différente de WIMPs, appelé habituellement MIMPs, qui en raison de leurs masses très élevées et de croiser-section peut finalement traverser l'atmosphère et la terre morts-terrains et atteindre le détecteur de matière noire sous terre, donnant une signature particulière, un « chemin » de reculs nucléaires d'environ 10 keV d'énergie déposée chacun, tous principalement dans une ligne droite.
Ma première tâche ici fut d'écrire une simulation de Monte Carlo jouet en ROOT pour évaluer la vitesse et la position du MIMP à l'entrée du détecteur, après diffusion à travers les atomes dans l'atmosphère et la Terre, pour toutes les directions possibles du MIMP, et les masses MIMP et les sections transversales d'intérêt. Entre-temps, le reste du groupe de travail a mis au point un générateur dans RAT, et plus précisément

en utilisant GEANT4, pour simuler les MIMPs une fois qu'ils entrent dans le détecteur. Les deux simulations ont ensuite été réunies en une seule.
Avec cet outil, j'ai lancé des simulations de MIMPs, afin de sélectionner les variables d'intérêt que nous pouvons regarder, donc celles qui décrivent le mieux le signal particulier d'un MIMP.
Les principaux sont essentiellement le nombre de photoélectrons « qPE », la solidité du signal de scintillation « fprompt », le nombre de hits identifiés dans la forme d'onde, « SubeventN ». La distribution des MIMPs à différentes sections et masses a été évaluée pour toutes ces variables. Une fois qu'il a été confirmé que ce que nous simulions était en fait ce que nous attendions, j'ai commencé la validation de la simulation de Monte Carlo, avec un accent particulier sur la variable SubeventN, qui n'a jamais été utilisée auparavant à des valeurs élevées. Pour ce faire, j'ai comparé la distribution de SubeventN pour les empilements dus aux bétas et gammas dans un petit ensemble de données avec ce qui a été donné à partir des simulations GEANT4. Cela a été fait en supposant des statistiques de Poissonian et aussi grâce au modèle de fond déjà publié de la collaboration. La validation a donné un désaccord entre les données et la simulation en dessous de quelques pour cent jusqu'à 10 MeV d'énergie déposée, confirmant que nos simulations étaient dignes de confiance. Puis, en utilisant les mêmes statistiques utilisées pour la validation, j'ai évalué l'accumulation prévue de données de base au cours des trois années de prise de données que nous allons débloquer, en supposant une incertitude conservatrice de 10%, selon la validation de Monte Carlo effectuée. Ces étapes m'ont permis de définir trois régions d'intérêt (ROI), chacune avec ses coupes de sélection et ses acceptations relatives de MIMP. L'arrière-plan gauche total après les coupes de sélection était inférieur à un événement inférieur à 10 MeV. A plus haute énergie, aucune simulation de Monte Carlo n'a pu être réalisée en raison de problèmes techniques liés à la simulation d'un si grand nombre d'événements. Au-dessus de 10 MeV, l'arrière-plan est dominé par les muons entrant dans le détecteur. La coupe de veto de muon du détecteur a diminué leur nombre prévu de quelques centaines jusqu'à environ 19; encore trop pour débloquer cette région. En outre, l'absence de simulations fiables de muons à des énergies aussi élevées ne permettait pas d'optimiser les coupes de sélection dans les autres variables comme cela a déjà été le cas à une énergie moindre. Ainsi, après que la collaboration ait été convenue, nous avons ouvert le « sideband » des muons et des événements marqués par le veto des muons, qui n'auraient de toute façon pas fait partie de l'analyse. De cette façon, nous pourrions voir la distribution des événements équivalant à environ 8 jours de vie. Cela a permis de définir des coupes personnalisées et de sélection simple également dans cette région d'énergie, portant finalement à moins d'un événement aussi la région de haute énergie. L'analyse a été examinée et approuvée par la collaboration et est maintenant entièrement prête pour la levée de l'insu des trois années de données, qui seront effectuées au cours des prochains mois.

Università degli Studi di Cagliari *Universitè de Paris*

PHD DEGREE

Cycle XXXIII°

Dark matter search and neutrino physics in Liquid Argon

Scienti c Disciplinary Sectors

FIS/01 -FIS/02

PhD Student: Michela Lai

Coordinator of the PhD program Prof. Paolo Ruggerone
Coordinator of the PhD program Prof. Fabien Casse

Supervisor Dr Walter Marcello Bonivento
Supervisor Dr Davide Franco

Final exam. Academic Year 2019 – 2020
Thesis defence: February 2021 Session

Acknowledgments

These three years have not been easy for me. This is far to be a complaint, as I think this is how a Ph.D. course is expected to be. Still, I have been helped by a few people, that I'd like to thank here.
The first ones are my supervisors, Walter and Davide, who had to help me passing from AdS/CFT theories to the experimental way-of-thinking and the dark matter world. No need to hide it was a long shot, but in the end, I know I made the right choice. I hope this thesis will remind me of this any time in the future I will doubt myself. Without the teachings of Davide and the support of Walter, I would not have learned and done so much in three years.

I want to thank the coordinators of both the Ph.D. courses, with specific care for Paolo, whose help and support was outstanding, and brought to the birth of my favourite fan club, and also Alessandra, on the Paris side, who guided me through the difficulties of the bureaucracy in a foreign country and made this joint Ph.D. possible.
A great acknowledgment is due to INFN and the University of Cagliari, who fully founded my Ph.D., and to the collaborations that I joined, DarkSide and DEAP. In such a reach environment my knowledge on the dark matter search could flourish.

An aside comment must be reserved for Shawn and Shivam, together with Ashlea and Nirmal, of course. Our "MIMP team" really changed my feelings for a research career, as I felt like I was inserted in an active, positive, and passionate working group. The MIMP work could have not seen the light without my team-mates. I learn every day with both of you.
A heartly thank you also to Alessandro. We worked together for a very poor time, but I learned something at any minute. I hope we can continue in the future.
I can't help thinking to my partners in physics in the offices. Break times in Paris with Andrea were a relief when we talked about neutrino physics as well as we talked about red pandas. On the Cagliari side, the relief was given by both office mates and a few people from the labs on the ground floor. I can't count all the lunches and the teas we had in these years, but they all were helpful to me. On the same path, let me thank my first fan, who actually became a friend in the meantime. I can't look forward to celebrating your Ph.D. too, even if I have to take a flight to Sweden.
An unexpected thank you goes also to my student, Lorenzo. You trusted me when you wanted to do your bachelor thesis with me. Helping you in your path was a pleasure. I hope we will continue working together in the future.

And I also hope I will be able to lead any other student that will work with me with the same serenity I had with you.

These years have been weird and full of tests, most of them not related to physics. Physics is never trouble in itself, and this is why I'm still here, playing with particles whose existence is still to be proved. In these tests, there is a small audience of people from which I got help, which is honestly incredible as I usually don't like asking for it.
So I want to thank my parents, Laura and Francesco, as well as my brother Matteo, for being there for me, even when I was pretty far. You saw me changing in these years. Growing up, some might say. But whatever the trouble, if I was the tightrope walker, you were my safety net.
Another very expected thank you goes to my partner in crime. I honestly missed our travels in these years. But I did not miss you, because you were there. I clearly remember one phone call we had when I was abroad. The 80 % of the days were not really good when I was far from home, but that one specifically was extremely cold. As always, you got my trouble and you showed me the solution. Problem-solving is the strongest point of physicians, isn't it?

And finally, thanks to my partner in life. Life is strange, and most of the time quite harsh. So I don't know how much what we are living now will last. But I wanted to put it written here, because "scripta manent". Thank you for believing in me, even when I stopped doing it. Thank you for sleeping by my side, while I had to work in the night time, as the days were often not long enough. Thank you for the calls, the skypes, the flights. Thank you for simply being around and simply calm me in this way. And sorry if I spent too much time with my laptop. These three years have not been easy for me, but it would have been much harder without you.

Finally, thanks to you, who are reading this thesis. I hope you will find it helpful. You probably are a physician, so you know the mantra: if you have questions, just ask.

Abstract

French version

Plusieurs observations astrophysiques, tant galactique que cosmologique, montrant qu'il y a une "masse manquante" dans l'Univers observable, peuvent être expliquées en supposant une matière non lumineuse, donc appelée "matière noire". L'un des candidats les plus prometteurs est le Weak Interacting Massive Particle (WIMP), une particule massive non relativiste, capable d'une interaction gravitationnelle et d'une interaction faible avec la matière baryonique. Le présent travail est axé sur le potentiel physique en plus de la recherche des WIMPs des détecteurs de matière noire remplis d'argon liquide, comme DarkSide et DEAP-3600. L'argon liquide est une cible optimale grâce à ses rendements élevés de scintillation et d'ionisation. DEAP-3600 est un détecteur monophasique qui exploite uniquement le canal de scintillation, tandis que DarkSide-20k et Argo, les futures expériences à l'échelle des tonnes du programme DarkSide, sont des chambres de projection temporelle (TPCs) biphasiques qui examinent les signaux de scintillation et d'ionisation. La grande masse (3.3 tonnes) de la cible de DEAP-3600 a permis d'effectuer une analyse pour rechercher des Multi Interacting Massive Particles (MIMPs), une possible alternative aux WIMPs, à des masses supérieures à 10^{16} GeV et avec une section efficace indépendante du spin matière noire-argon d'environ 10^{-22} cm^2. Ce travail est la phase préparatoire à l'ouverture de 3 années de collection de données. Du présent aux futurs détecteurs de matière noire, DarkSide-20k et Argo seront caractérisés par une sensibilité extraordinaire aux faibles reculs d'énergie. Ceci est principalement la conséquence de la haute résolution énergétique des photodétecteurs choisis, les photomultiplicateurs de silicium (SiPMs). Les SiPMs personnalisées ont été fabriques pour la recherche de la matière noire dans DarkSide-20k; par conséquence, les SiPMs ont été ici caractérisées, avec un accent sur leurs bruits corrélés : les afterpulses et les optical crosstalks. La même sensibilité à basse énergie apporte également un fort potentiel de détection des neutrinos de supernova par coherent elastic neutrino-nucleus scattering (CEvNS) dans l'argon en exploitant le signal d'ionisation. L'étude de sensibilité correspondante est ici réalisée et il montre que l'émission de neutrinos sera détectée pour toute supernova galactique, avec une bonne précision dans la reconstruction des principaux paramètres de l'éclatement, c'est-à-dire l'énergie totale des neutrinos et leur énergie moyenne.

Abstract

English version

Several astrophysical observations, both on a galactic and cosmological scales, showing that there's a "missing mass" in the observable Universe, can be explained assuming a non-luminous kind of matter, hence called "dark matter". One of the most promising candidates is the Weakly Interacting Massive Particle (WIMP), a non-relativistic massive particle, gravitationally and weakly interacting with baryonic matter. The present work is specifically focused on the physics potential besides WIMP search of dark matter detectors filled with Liquid argon, like DarkSide and DEAP-3600. Liquid argon is an optimal target thanks to its high scintillation and ionization yields. DEAP-3600 is a single-phase detector, exploiting the scintillation channel only, while DarkSide-20k and Argo, future tonne scale experiments from the DarkSide program, are dual-phase Time Projection Chambers (TPCs), looking at both scintillation and ionization signals. The large mass (3.3 tons) of the DEAP-3600 target has allowed me to perform an analysis to search for Multi Interacting Massive Particles (MIMPs), a dark matter candidate alternative to WIMPs, at masses above 10^{16} GeV and with argon-dark matter spin-independent cross-section of about 10^{-22} cm^2, fully setting up the upcoming unblinding of three years of data taking. Going from the present to the future dark matter detectors, DarkSide-20k and Argo will be characterized by an extraordinary sensitivity at low energy recoils. This is mainly consequence of the high energy resolution of the chosen photodetectors, Silicon Photomultipliers (SiPMs). Custom SiPMs have been designed for the dark matter search in DarkSide-20k; hence, SiPMs have been here characterized, with a focus on their correlated noises, namely afterpulses and optical crosstalks. The same sensitivity at low energy brings also to a strong potential in detecting supernova neutrinos via coherent elastic neutrino-nucleus scattering (CEvNS) in argon by exploiting the ionization signal. The related sensitivity study is here performed showing that the neutrino emission will be detected for any galactic supernova, with a good accuracy in reconstructing the main parameters of the burst, namely the total energy of neutrinos and their average energy.

Contents

1 Introduction **9**

2 Introduction to the dark matter **12**
2.1 Evidences of dark matter . . . 12
2.2 Dark Matter candidates . . . 19
2.3 WIMP detection . . . 33
2.3.1 Direct detection assumptions . . . 35
2.3.2 Backgrounds . . . 40
2.3.3 Overview of the detection techniques . . . 44

3 Liquid Argon detectors **55**
3.1 The case of Liquid Argon . . . 55
3.1.1 From Atmospheric to Underground Argon . . . 55
3.1.2 Scintillation process . . . 56
3.1.3 Electroluminescence in Gas Argon . . . 66
3.2 DEAP-3600 . . . 67
3.2.1 The inner detector . . . 70
3.2.2 Cryogenic system . . . 72
3.2.3 Electronics . . . 75
3.3 DarkSide-20k . . . 80
3.3.1 Photoelectronics . . . 82
3.3.2 Inner Detector . . . 85
3.3.3 Cryogenics System . . . 89
3.3.4 Veto Detector . . . 92
3.3.5 Data Acquisition . . . 95
3.3.6 Computing . . . 96
3.4 The ReD experiment . . . 98

4 Multi-scattering dark matter particles in DEAP-3600 **104**
4.1 Introduction . . . 104
4.2 MIMP models . . . 105
4.2.1 Elementary MIMP . . . 106
4.2.2 Composite MIMP . . . 108
4.3 Sensitivity of DEAP-3600 . . . 109
4.4 Propagation through the overburden . . . 111
4.5 Expected signal of MIMPs in DEAP-3600 . . . 116
4.6 Backgrounds . . . 128
4.6.1 Pile-up background . . . 128
4.6.2 Expected pile-ups in the available dataset . . . 130

4.6.3 Other backgrounds 132
4.7 Validation of the Monte Carlo simulation 133
4.7.1 MonteCarlo validation at low energy 134
4.7.2 Validation with Americium Beryllium run 138
4.8 Set up of the data unblinding 142
4.8.1 Selection cuts and acceptances 143
4.8.2 Muon unblinding 150
4.9 Conclusion 153

5 Characterization of SiPM correlated instrumental noise 156
5.1 Silicon PhotoMultipliers 157
5.1.1 Single Photon Avalanche Diode 157
5.1.2 From SPADs to SiPMs 159
5.1.3 Noise in a SiPM 160
5.1.4 FBK-NUV-HD LF SiPMs 161
5.2 SiPM Single Electron Response 166
5.2.1 Integration Charge 166
5.2.2 Prominence 169
5.3 Characterization of afterpulses in ReD 179
5.4 Optical Crosstalk characterization 184
5.5 Conclusion 188

6 Sensitivity to detection of core-collapse supernova neutrinos in DarkSide-20k and Argo 191
6.1 Overview 191
6.2 Core Collapse Supernovae 194
6.3 Supernova neutrino signal and detector response 200
6.3.1 Expected Backgrounds 202
6.3.2 Toy Monte Carlo simulation 203
6.3.3 Event selection 204
6.4 Determination of the Supernovae Neutrino Detection Significance 208
6.5 Conclusion 214

7 Conclusion 216

8 List of Figures 248

9 List of Tables 266

1 Introduction

There are several evidences, both at galactic and cosmological scales, for a "missing mass" in the Universe, an additive and non-luminous matter component, called "dark matter". The visible and baryonic matter is only about 15 % of the whole mass in the Universe: the rest is dark matter. Even if there's mainly agreement with its abundance, still a direct detection is missing.
Together with a clear discovery, a direct detection may also shade light on the nature of dark matter particles. Since the 50', a wide spectrum of candidates have been purposed, mainly non-baryonic, and hence not included in the Standard Model. One of the most promising candidate are "WIMPs", which would interact not only gravitationally but even weakly with baryonic particles. WIMPs are expected to have a mass in the range $(1 - 10^5)$ GeV and an elastic WIMP-nucleon cross-section below $\sigma_{\chi-n} \approx 10^{-46}$ cm^2 for WIMP mass of 20 GeV/c^2. Several Earth based experiments have been designed and built for WIMP search. Indeed, assuming that the dark matter is distributed all around the Milky Way, as the Sun moves around the galactic centre and the Earth around the Sun, an apparent "wind" of dark matter is expected to recoil in the detector target mass. The eventual recoil releases an energy below 100 keV, so a very low energy threshold is needed. Moreover, the low cross-section implies that the detector sensitivity increases with the increase of the target mass and the suppression of the local background. Dark matter experiments designed for direct detection are usually set underground, where the rocks shield the detector from cosmic rays.
Noble liquids are a particularly suited target for WIMP search: they have both a high scintillation and ionization yield, which determines a high number of photons and electrons released after the WIMP scattering on the noble liquid nucleus; moreover, they are easy to purchase and to scale to larger volume. Liquid argon, specifically, offers a unique technique to discriminate the recoils due to an eventual WIMP from the electrons/positrons and photons from local radioactivity, which are the most abundant background component.
In my Ph.D thesis the aim is to fully exploit the physics potential of a liquid argon dark matter detector, beyond the WIMP search. This allowed me to work with two different collaborations, DEAP and DarkSide, both searching WIMPs in liquid argon. Indeed, according to the agreement between the two experiments, people from DarkSide collaboration like me can access and analyze data from DEAP-3600 experiment, a single phase detector with 3.3 ton of target mass, if a monthly shift of data taking is performed. This agreement is connected to the joining of the two collaboration to the

Global Argon Dark Matter Collaboration (GADMC), together with ArDM and MiniCLEAN experiments. The first aim of GADMC will be the built of DarkSide-20k, a 50 ton dark matter detector filled with high radiopure liquid argon, taken from underground and further distilled. This low radioactivity level, together with the new technologies developed to suppress the background level, will allow for the highest sensitivity ever achieved in liquid argon, down to WIMP cross-section of 7.4×10^{-48} cm^2 at 1 TeV/c^2 with a decade of run. The ultimate GADMC aim is the built of Argo, with 400 ton of target mass.
Indeed, after a wide introduction on the dark matter evidences and detection techniques in Chapter 1, Chapter 2 is entirely dedicated to the direct detection in liquid argon, with a detailed description of the detectors which I have worked with in these three years: DEAP-3600, DarkSide-20k and Argo, with a quick overview on ReD, related to the DarkSide-20k and Argo photodetection.
Chapter 3 deals with the detection in DEAP-3600 of a dark matter class of candidates different from WIMPs, called "MIMPs", expected to scatter more than once in the target volume, differently from WIMPs. This is a consequence of the higher cross-section in which they are expected, above 10^{-30} cm^2 for the elastic dark matter-nucleon cross-section. Furthermore, their high mass, about 10^{16} GeV, assures a effectively collinear path along the detector volume. The study is based on three years of data taking in the experiment. At this stage of the analysis the signal region of the data is still blind. The unblinding will performed in the next months. Indeed, after characterizing the expected signal in the detector with a custom developed Monte Carlo simulation, the selection cuts to reject the expected backgrounds are optimized, finally bringing to an expected background level of less than 2 events.
Chapter 4 and Chapter 5 deals with the upgrades and the physics potential at low mass of the future detectors DarkSide-20k and Argo.
One of the main new technologies foreseen in GADMC detectors is the choice of the photosensors, as the Photomultipliers Tube exploited already in DarkSide-50, the running detector from DarkSide collaboration, and DEAP-3600, will be exchanged for solid state photodetectors, Silicon Photomultipliers (SiPMs). Custom SiPMs have been developed, fulfilling the requirements for dark matter search in DarkSide-20k, in terms of the low radioactivity of its materials, the active detection surface, the thermal noise and correlated noise level. Specifically, Chapter 4 is focused on the characterization of the correlated noise, namely afterpulses and optical crosstalks, in these SiPMs. The only running dark matter experiment equipped with them and based on liquid argon is ReD, a small TPC set in Naples, whose data are here exploited

to perform the characterization.
Mainly thanks to the high energy resolution, the single photon sensitivity and the use of double phase TPC technology, future GADMC detectors will have an extraordinary sensitivity at low energy, promising for outstanding constrains on WIMP search for masses below 10 GeV/c^2. For the same reason, these detectors will be sensitive to neutrinos performing coherent elastic scattering on liquid argon nuclei with an incident energy of about 10 MeV. Specifically, neutrinos from a core-collapse supernova are focused in that energy region. These phenomena are rare, about 2–3 per century in spiral galaxies, releasing in $\approx$ 10 s an energy of about 10^{46} J, the 99 % of which is released via neutrinos. Hence Chapter 5 describes the sensitivity study of GADMC future detectors to the neutrino emission from a core-collapse supernova, in terms of both the discovery potential according to the supernova distance and the information on the supernova global emission that can be retrieved from this measurement. Thanks to the foreseen outstanding sensitivity, the two detectors are going to be inserted in the new program of the Supernova Warning System (SNEWS 2.0).

2 Introduction to the dark matter

2.1 Evidences of dark matter

The existance of a non baryonic "dark matter" has origin in the '30s, from the comparison with the visible light and the mass in galactic clusters. The first measurement was performed by Fritz Zwicky who measured the velocity dispersion of galaxies in Coma cluster, thanks to the redshift of the galaxies [1]. The velocity dispersion is related to the cluster total mass through the virial theorem; he found that the newtonian mass was at least ten times greater than the one inferred from the light of the cluster. A similar result was obtained by Smith in 1936 [2] for the Virgo cluster and one year later by Zwicky itself [3] with a review of the same measurement performed in many known galactic clusters. This "missing mass" issue brought the first hypothesis on a new kind of matter, stars probably, with a shallow interaction with the light, and hence called "dark matter".

Specifically these results were expressed in terms of the mass-to-light ratio, M/L, which is the fraction of luminous mass over the total mass from an astrophysics object. The same parameter can be applied to a nearby galaxy to study M/L variation from the center to the galaxy's edge. Babcock (1939), for instance, studied the light from M31, the Andromeda Galaxy, the spiral galaxy closest to the Milky Way [4]. From the spectra, he evaluated that the rotational curve at the edge of the galaxy was much higher than the keplerian one, in analogy with Zwicky's and Smith's observations on clusters of galaxies. Again, the missing mass problem arose not only on a galactic cluster scale but also in a single galaxy, showing that, whatever the reason of this disagreement, its effects were more evident on the edge of galaxies. Two explanations were purposed: either a strong dust absorption in the arms of spiral galaxies either the presence of a dark matter population, with a very high mass-to-light ratio, equivalent to about 20 in M31. Later, radio observations in the 21-cm H emission confirmed this result, also pointing out an evident change of the M/L parameter according to the distance from the center of the galaxy, where it was found to be M/L ≈ 2 [5] [6]. A stronger confirm of this result was given by Rubin & Ford (1970 [7]) and Roberts & Rots (1973 [8]), who using respectively optical and radio data, derived the rotational curve for Andromeda Galaxy up to a radius of 30 kpcs. As shown in Figure 2.1.1, the radial velocity first increases linearly, as expected if it is assumed that most of the mass lies in the galactic bulge; then, instead of decreasing as prescribed by newtonian dynamics, the radial velocity stays almost constant. Now, the radial velocity returns the radial mass distribution along M31, while photometric data gives the light distribution. In the

periphery of a spiral galaxy, the expected M/L ratio was ≈ 1, due to old, metal-poor stars. In contrast, the high radial velocity in the periphery of M31 brought to M/L > 200, hundreds of times the one that would have followed from the newtonian radial curve. These observations found their final output at the First European Astronomy Meeting, held in Athens in 1972 [9]: the only way to make the rotational and photometric data agree is to assume that there is a population of bodies, spherically distributed all around galaxies, with a very high Mass-to-Light ratio. At that time, this sphere was called "corona", not to be confused with the stellar halo. This agreement did not solve the "missing mass" issue but just shifted it into a new brand question, related to the nature of this unknown matter. After 40 years from Zwicky measurement, the dark matter paradigm was eventually accepted by the scientific community.
Successive technologies confirmed the first observations, wiping out the first uncertainties on the dark matter existence. Observations in the HI line at 1420 MHz on both other galaxies [10] and the Milky way confirmed a show flat rotation curve, up to ≈ 60 kpc in our Galaxy [11] [12]. These observations implied a dark matter halo mass in the range of $1 - 2.5 \times 10^{12}$ $M_\odot$, with a central density of 0.1 $M_\odot$ pc^{-3} [13].
In addition to this, X-ray observations with Einstein satellite allowed to confirm the estimate of the masses of Coma, Virgo and Perseus clusters done with the virial theorem [14] [15].
Further confirmations of the results of the electromagnetic spectrum come by exploiting the gravitational lensing effect. It was already known in the last century that the masses of galaxies, clusters of galaxies and eventually stars bend the light from farther objects, focusing the light as a "lens" and allowing for the enhancement of the image. According to the mass of the gravitational lens, the image can eventually be distorted, with the addition of light arcs, Einstein rings, multiple images; in this case, the phenomenon is tagged as "strong lensing". The "strong lensing" is observed in rich galaxy clusters and allows for the determination of the cluster mass to compare with X-ray data and the virial theorem output.
The distortions of the light decrease with the mass of the gravitational lens; weak lensings can then be used to determine the distribution of the dark matter in clusters and superclusters, which is how clusters of galactic clusters are usually referred to. For instance, the weak lensing allowed for the determination of the mass-to-light ratio of the most luminous known X-ray cluster, RXJ 1347.5-1145, equal to 200 ± 50 in Mass solar units [17].
In general, gravitational lensing gives strong evidence in favor of the dark matter model, contrary to Modified Newtonian Dynamics (MOND) theories. These, first proposed in [18], aim to solve the tensions in the radial curves

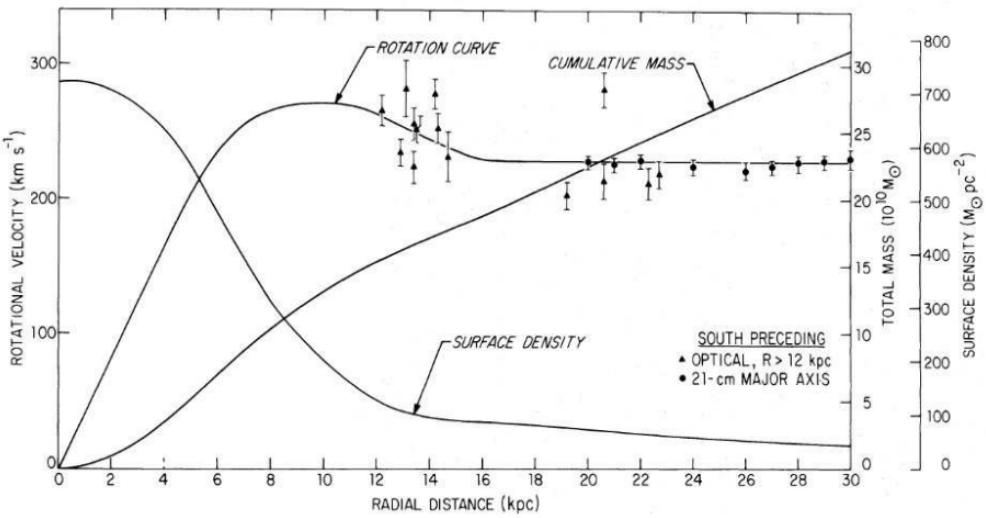

Figure 2.1.1: Rotational curve for M31, the Andromeda Galaxy, from optical and 21-cm line observations compared to the expectation from the surface density [16].

by properly change Einstein's general relativity without introducing a non-specified, still totally new kind of matter, characterized by a mass-to-light ratio of a few hundred. A notable example in favour of the dark matter hypothesis is 1E 0657-558, the "Bullet Cluster", shown in Figure 2.1.2 [19] [20] [21]. This is a pair of galactic clusters, in which the smaller one passed through the heavier one almost perpendicularly to the line-of-sight. The X-ray observation of baryonic gas compression shows that the hot gases have been stripped away by the ram pressure during its motion. On the other hand, the bullet cluster is also a weak gravitational lens, so that the galaxies in the background follows the equipotential curves of the gravitational force. What is counterintuitive is that the lens is not focused on the X-ray hot gases, in coincidence with the luminous mass, but stands approximately where the smaller cluster was before being attracted by the heavier one. This observation implies that most of the mass is not in the hot gas but is a collisionless, non-baryonic component (dark matter hypothesis), or somehow, the gravitational laws need a fine-tuning on this specific scale (MOND). As more observations have been done in several clusters, each showing a quantitatively different disagreement of the distance between the gravitational and the baryonic centers, a universal modification of the general relativity seems unlikely. In this sense, assuming a "dark matter" model, differently from the MOND approach, promises for a general, universal solution of the discrepancies found among several objects and physics scales.

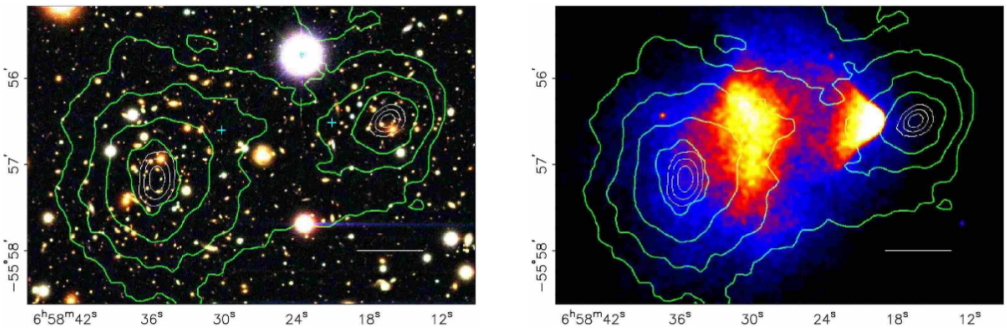

Figure 2.1.2: Merging 'bullet' cluster 1E0657-558, both in optical (left) and X-ray (right). In both panels, green contours are the equipotential gravitational curves of the cluster, found using weak lensing of distant galaxies. The contours of the gravitational potential coincide with visible galaxies but are far from the location of the X-ray gas (the dominant baryonic component of clusters). This is straightforward to explain with the assumption of a non-baryonic matter component, which would mainly not interact during the merging, besides the gravitational force. The disagreement was also observed in other clusters, with a quantitatively spread of the distance between the gravitational and the luminous mass centers of gravity. This non-universal disagreement is then easier to explain with a different mass distribution/abundance instead of a universal modification of general relativity [22].

Once that the existence of dark matter is assumed, the consequent question is on its composition. The most natural model for dark matter particles are neutrinos, as they are abundant in the universe and still not-luminous. The so cold "hot dark matter" model (HDM), where "hot" stands for relativistic, came out. Still, the matter distribution between the galaxies was not in agreement with a relativistic particle, as it would have smoothed the perturbations in the early Universe. Furthermore, as explained in Section 2.2, neutrinos have a too low mass to account for the whole present dark matter abundance.

Hence the dark matter particle moved from a relativistic and hot to a non-relativistic, "cold" scenario. If no modified gravity theory is assumed, the missing mass seen in the galaxies and galactic clusters must be composed of non-relativistic and non-electromagnetic interacting particles. In first approximation, it is assumed that the dark matter is uniformly distributed around the galaxy center. The gravitational effects of this "dark matter halo" are remarkable mostly on the edge of the galaxies, filling the missing mass in the arms and consequently increasing the local radial velocity. It would fill the voids in the cosmic web on a super-galaxy scale, keeping gravitationally bound the galactic clusters as Coma and Virgo clusters, that would otherwise break up [23].
On the cosmological side, it was clear from observations of the red-shift from Type Ia supernovae that the Universe expansion was accelerated [24] [25] [26]. This implies that there must be an additional contribution to the universe mass-energy, together with the radiation and the matter -baryonic and not-baryonic one- acting like an "anti-gravity" suppling the acceleration of the Universe expansion [27] [28]. The existence of this "dark energy" is easily parametrized by the Λ cosmological constant at first inserted in the Einstein equation.

The Λ Cold Dark Matter Model (ΛCDM) is today the most robust description of the distribution of the baryonic matter, dark matter and dark energy in the universe, even without any assertion of the properties of the latter two. The Cosmic Microwave Background provides a strong constraint on the ΛCDM model. First predicted by Alpher and Herman [29], it was first observed by Penzias and Wilson in 1965 at Bell Labs [30] and later by space telescopes like WMAP [31] and finally Planck, whose temperature map is shown in Figure 2.1.3.
According to the Big Bang model, at first, the Universe's density was so high that photons could not freely travel, emitted and re-absorbed by a plasma of free charged particles. Only three-hundred thousand years ago the Universe

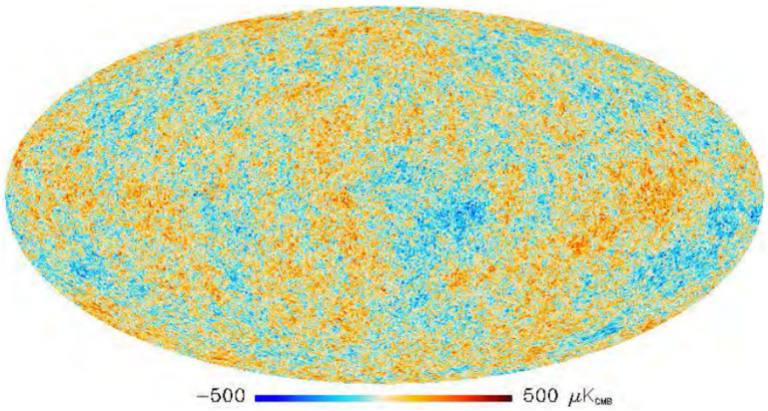

Figure 2.1.3: Cosmic Microwave Background from Planck(2013) [32]. The signal is mainly isotropic but shows slight temperature variations, of the scale of 10^{-5}. This is due to the local fluctuations of the cold photons-matter plasma which preceded the recombination process.

expansion and hence its cooling allowed for the binding of protons and neutrons into nuclei: this is called the "recombination" era. Then, photons were free to propagate: the CMB is the energy they released in their last scattering before freely propagate, so the light from the "last-scattering surface". Due to the cosmic expansion, this light is redshifted and corresponds to an average temperature of 2.7 K. The first full observation was performed by COBE satellite, soon followed by balloons, ground-based experiments and other satellites.
The CMB radiation shows to be mainly uniform in any direction, with local anisotropies of the scale of 10^{-5} radians. The CMB anisotropies are due to the fluctuations in the cold photons-matter plasma, which preceded the recombination process. The photon-matter plasma's local gravity determined the trapping of photons in gravitational wells, where the wells could be of different sizes. The radiation pressure from each well, on the other hand, struggled against the gravity, determining an oscillation of the plasma. In analogy with the sound as a pressure wave, these are usually called "acoustic fluctuations". What we see today is the snapshot of the radiation leaving the potential well and freely propagating. The multipole expansion of the CMB Fourier transform is shown in Figure 2.1.4, where l is the wavenumber, inversely proportional to the oscillation's wavelength. The Y-axis is the amplitude of the oscillation mode, which is also proportional to its temperature variance from the CMB mean one. Fluctuations at low l also mean high wavelength, so at wider angles. The first peak is at l = 200, equivalent to about 1 degree. Its position is related to the curvature of the universe, with

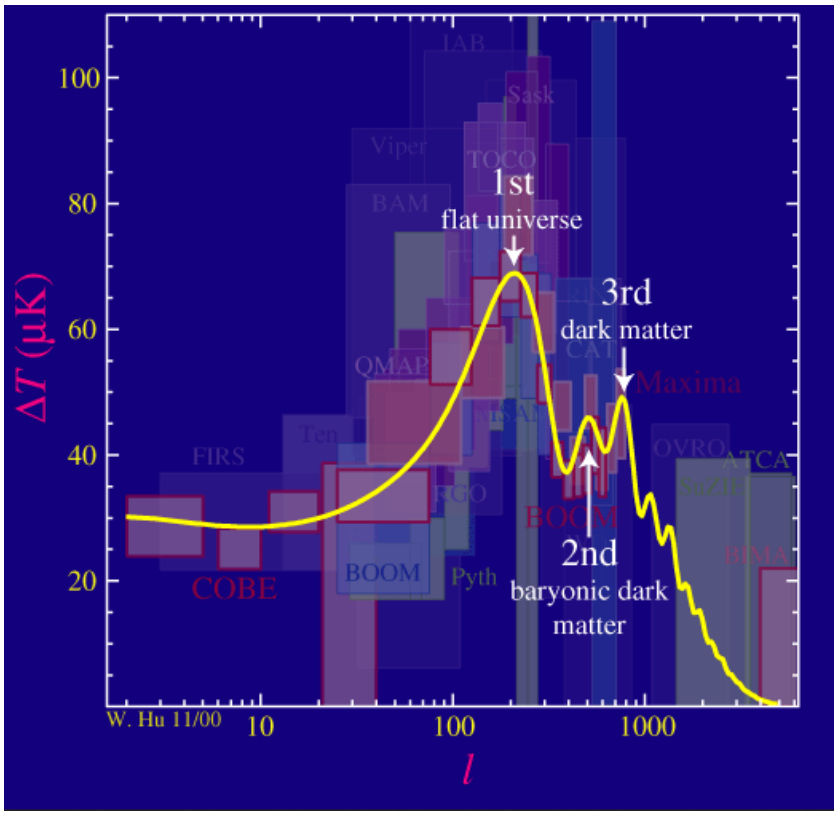

Figure 2.1.4: Multipole expansion for the Cosmic Microwave Background. l is the acoustic peaks' wavenumber: low l corresponds to high wavelength and then wider angles. The first peak is related to the universe curvature, which is almost null. The relative height of the second peak compared to the first one relies on the baryonic contribution. The third and following odd peaks are second-order contribution, so from the dark matter, which does not interact with photons [33].

the peak going at smaller degrees -higher l - with the curvature's increase. The actual position of the peak shows a universe mainly flat, assuming a fixed matter density, confirming the Λ contribution, the "dark energy" in the universe expansion. The contribution to the baryonic component of the non-luminous matter is instead given by the relative height of the second harmonic compared to the first one. The more are the free nucleons in the plasma, the more the radiation pressure is depressed and the oscillation is deeper. Since the spectrum is proportional to the absolute value of the temperature variance, odd peaks increase with the increase of the depth of the gravity well and hence with the baryonic matter, while even peaks result to be related only to how the plasma rarifies. The more the baryonic matter, the higher the first peak, while the second is not affected. Hence, the second peak's relative height to the first one constrains the density amount of baryonic matter. Finally, the other odd peaks are second-order contributions, due to the matter component which does not interact with the photons in the plasma, i.e., the dark matter [34]. The values for the three components are $\Omega_m = 0.27 \pm 0.02$ for the global matter density, $\Omega_b = 0.041 \pm 0.002$ for the baryonic component with a resulting 73 % for the dark energy [9].
Simulations assuming the ΛCDM were performed in the last twenty years. The most accurate one is the Millennium Simulation, from Max Planck Institute [35] [36] [37], with about 10 millions of cold dark matter particles following the stating ΛCDM power spectrum and the semi-analytical model for the simulation and the evolution of the galaxies [38] [39] [40]. The photometric properties, masses and sizes of superclusters, the clusters of galaxies and the cosmic web given by the simulation found an extraordinary agreement with observations, making the Millennium simulation the very starting point for any further study on the clusters and galaxies formation. Similarly, Navarro et al. in 2010 [41], within the Aquarius Project, performed a detailed simulation of the dark matter halos in galaxies. By simulating six halos for different galaxy sizes, with the highest resolution reached of 4.4 billions of stars per halo, they modelled the dark matter halo density profile $\rho(r)$, whose derivative follows a power law in the radius, $d\ ln\rho(r)/d\ lnr \propto r^{\alpha}$, where the shape parameter α may vary among the galaxies.
To resume, the ΛCDM fully describes the evolution of the universe, in agreement with cosmological and astrophysics observations. What is still missing is the nature of the dark matter particle.

2.2 Dark Matter candidates

Although the astrophysical observations have put some constraints on the dark matter nature, the range of candidates is still broad. As described in

the previous section, the ΛCDM deals with the composition of the Universe in terms of the baryonic matter, radiation, dark matter and dark energy, but weakly constrains the composition of the latter two. In principle, there might be more dark energies and more dark matter species.
A tiny percentage is due to MaCHOs, Massive Compact Halo objects, terms by which baryonic stars emitting no electromagnetic signals are grouped. Some examples are brown dwarf stars, non-rotating neutron stars, non-accreting black-holes. Measurements mainly based on gravitational micro-lensing [42] set an upper limit on their potential contribution to the dark matter halo, equal to 1.7×10^{-7} for the optical depth [43].

Within baryonic candidates, active neutrinos, like any other relativistic particle, are excluded from accounting for the whole dark matter content for two reasons. First of all, a relativistic particle would have smoothed the perturbations in the early Universe, preventing the formation of large scale structures that brought to the galaxies we see today. More direct evidence against any Hot Dark Matter candidate, here resumed from [44] [45], is given by the current energy density of the dark matter. After Planck analysis in 2018 of the CMB, the dark matter energy density is evaluated to be [46]

$$\rho_{DM} = 1.26 \times 10^{-6} GeV/c^2/cm^3 = 0.7 \times 10^{-11} eV^4 \tag{2.2.1}$$

where c is the speed of the light in the vacuum; in the last step the density is re-written in Planck natural units. This density is a relic one, coming from the early stages of the Universe, where the dark matter was in thermal equilibrium with neutrinos, electrons, protons and light elements formed during Big Bang Nucleosynthesis. As the Universe cooled down, dark matter particles became too heavy to be produced in the thermal bath. Furthermore, their annihilation rate became too slow, compared to the Universe expansion rate. Hence their density stopped changing, and that is the density we measure today. The temperature at which this decoupling happens is of "freeze-out", T_{fo}.
Both the energy density ρ and the number density n in the early universe strongly depends on the temperature. Specifically, assuming a Bose-Einstein (Fermi-Dirac) distribution for dark matter particles, the two parameters are

$$n = \int \frac{d^3\vec{p}}{(2\pi)^3} \frac{g}{e^{\frac{E-\mu}{k_B T}} \pm 1}, \tag{2.2.2}$$

$$\rho = \int \frac{d^3\vec{p}}{(2\pi)^3} \frac{gE(\vec{p})}{e^{\frac{E-\mu}{k_B T}} \pm 1}, \tag{2.2.3}$$

where μ is the chemical potential, $k_B = 8.6 \times 10^{-5}$ eV/K, and g is the number of quantum internal states. By integrating on the energy E of the dark matter particle with mass m_χ and taking the relativistic limit T >> m_χ, the integrals can we written as polylogaritms function $Li_n(z)$, where z = $e^{-\mu/k_B T}$; furthermore, if also k_B T >> μ, z $\approx$ 1 and Li_n (1) = ζ(n), the Zeta Riemann function. In this limit the number and energy density are then given by

$$n = \left[\frac{3}{4}\right] \frac{\zeta(3)}{\pi^2} g \left(\frac{k_B T}{\hbar c}\right)^3 \tag{2.2.4}$$

$$\rho = \left[\frac{7}{8}\right] \frac{\pi^2}{30} g (k_B T)^4 \left(\frac{1}{\hbar c}\right)^3 \tag{2.2.5}$$

where the terms in [ ] are introduced for fermions only. The pressure p is proportional to the mass density, $p = w\ \rho$, with w = 1/3 for relativistic particles. The number of internal degrees of freedom is a sum over the fermion populations and the boson popoluations, each with g_i degrees of freedom at a temperature T_i,

$$g_*(T) = \sum_{bosons} g_i \frac{T_i^4}{T^4} + \sum_{fermions} g_i \frac{7}{8} \frac{T_i^4}{T^4} \tag{2.2.6}$$

where the "*" underlines that non -relativistic states are actually negligible compared to the populations at T_i >> T. Hence g_*(T) is defined as the number of effective relativistic degrees of freedom at temperature T. From the definition of the pressure and the energy density also follows the density of entropy of quantum states s, equal to

$$s = \frac{p + \rho}{k_B T} = \frac{2\pi^2}{45} g_{*,s} \left(\frac{k_B T}{\hbar c}\right)^3 \tag{2.2.7}$$

where $g_{*,s}$ is the number of relativistic intristic degrees of freedom contributing to the local entropy

$$g_*(T) = \sum_{bosons} g_i \frac{T_i^3}{T^3} + \sum_{fermions} g_i \frac{7}{8} \frac{T_i^3}{T^3} \tag{2.2.8}$$

The entropy density of the CMB photons, with temperature T = 2.75 K is, from Equation 2.2.7,

$$s_\gamma = 1.1 \times 10^{-11} \left(\frac{eV}{\hbar c^2}\right)^3 = 1.44 \times 10^3 cm^{-3}. \tag{2.2.9}$$

The entropy per unity of comoving volume is a conserved quantity. Hence the expected entropy from the CMB radiation must rely to the relic dark matter density; this is the case, through the abundance Y, defined as the ratio of the number density over their entropy, $Y = n/s$. Then it is straightforward to rewrite the relic abundance in terms of the abundance at the temperature of freeze-out,

$$\rho_{DM} = m_\chi c^2 s_\gamma Y(T_{fo}). \tag{2.2.10}$$

The measured energy and the entropy density from the CMB are given in Equation 2.2.5 and Equation 2.2.9 respectively; it results that the abundance that a dark matter candidate with mass m_χ must have to agree with CMB observations is

$$Y(T_{fo}) \approx \frac{1.26}{1.44}\frac{eV}{m_\chi c^2}. \tag{2.2.11}$$

Now it happens that neutrinos would have an abundance $\mathrm{Y}(\mathrm{T}_{fo}) \approx 1$, which prevent them to fulfill all the dark matter needed. In fact, the freeze out temperature for neutrinos can be obtained by comparing the expected neutrino abundance at the freeze-out temperature T_{fo} with the relic one in Equation 2.2.11. In a thermal bath, neutrinos are in equilibrium via electroweak interactions, with a thermally averaged cross section times relative velocity of $< \sigma v > \approx G_F^2 T^2$ where G_F is Fermi constant, in natural units. Then, from Equation 2.2.4, the production or annihilation rate $\Gamma \approx \mathrm{n}_\nu < \sigma v > \approx G_F^2 T^5$. The expansion rate of the universe is given by the Hubble factor, which shows dependence by the temperature in the early universe,

$$H \approx 1.66\sqrt{g_*(T)}\frac{(k_B T)^2}{M_{pl} c^2 \hbar} \tag{2.2.12}$$

where $g_*(T)$ is the number of relativistic degrees of freedom and the Planck mass is $\mathrm{M}_{pl} = 1.22 \times 10^{19}$ GeV/c^2. The ratio Γ/H returns an estimate of the interactions between neutrinos and Standard Model particles in a given time, which translates to a given temperature,

$$\Gamma/H \approx G_F^2 T^3 M_{pl} \tag{2.2.13}$$

in Planck natural units. The freeze out of neutrinos happened at $T_{fo} \approx (G_F^2 M_{pl})^{-3} \approx 1MeV$. The corresponding number density and entropy density is given by Equation 2.2.4 and Equation 2.2.7 respectively. This brings to an abundance of neutrinos at freeze-out of

$$Y_{fo} = \frac{135\zeta(3)g}{8\pi^4 g_{*,s}(T_{fo})}. \tag{2.2.14}$$

Equation 2.2.14 gives today's expected abundance of neutrinos, after their freeze-out, which happened when the universe cooled down to $\approx$ MeV. Equation 2.2.11 is the abundance a particle should have to give the observed energy and entropy density in the CMB today. The ratio of the two is then the relic abundance of neutrinos today,

$$\Omega_\nu h^2 \approx 0.2 \times \frac{g}{g_{*,s}} \frac{m_\nu}{eV}. \tag{2.2.15}$$

The early universe can be approximated as a gas of neutrinos in thermal equilibrium with photons and electrons. For a species of neutrinos, g = 2 , as well as for photons; for electrons g = 4. The resulting multeplicity is $g_{*,s} = 2 + 4\ 7/8 = 11/2$, for photons and electrons. Then $g/g_{*,s} \approx 0.36$. The only way to have that all the dark matter is composed by neutrinos, so $\Omega_\nu h^2 \approx 1$, would be having $m_\nu > 10$ eV. Nevertheless, the current upper bound for neutrino mass is at 1.1 eV at 90 % C.L. [47], which implies that neutrinos can contribute less then 7 % of the whole matter in the universe. Further measurements will eventually push down the neutrino mass upper limit, together with their contribution to the dark matter.

An aside comment must be reserved to sterile neutrinos. This may consist of one or more additive neutrino flavor which does not present any interaction with Standard Model particles out of gravitational force, but may oscillate into the three active neutrinos. Alternatively, sterile neutrinos can consist of right handed (left-handed) neutrinos (antineutrinos).

The production mechanism in the early Universe is likely to be the oscillation of active neutrinos into sterile neutrinos, at temperature of about 100 MeV. In this way they had never been in thermal equilibrium, but just close to it. The resulting sterile neutrino density is [48]

$$\Omega_{\nu_s} = 0.2 \frac{sin^2 2\theta}{10^{-8}} \left(\frac{m_{\nu_s}}{3keV}\right)^{1.8} \tag{2.2.16}$$

where θ is the mixing angle and $m_{\nu s}$ the sterile neutrino mass. The resulting contour is shown in Figure 2.2.1 for null lepton number asymmetry , L = 0. The region at the right of this contour is always excluded by overclosure. On the other hand, it is also possible that L $\neq$ 0, with a resulting enhancement of the sterile neutrino abundance. Strong constraints can be set on this dark matter candidate by looking at the small-scale structure in the universe, which would be suppressed by too fast, and then too much light, candidates.

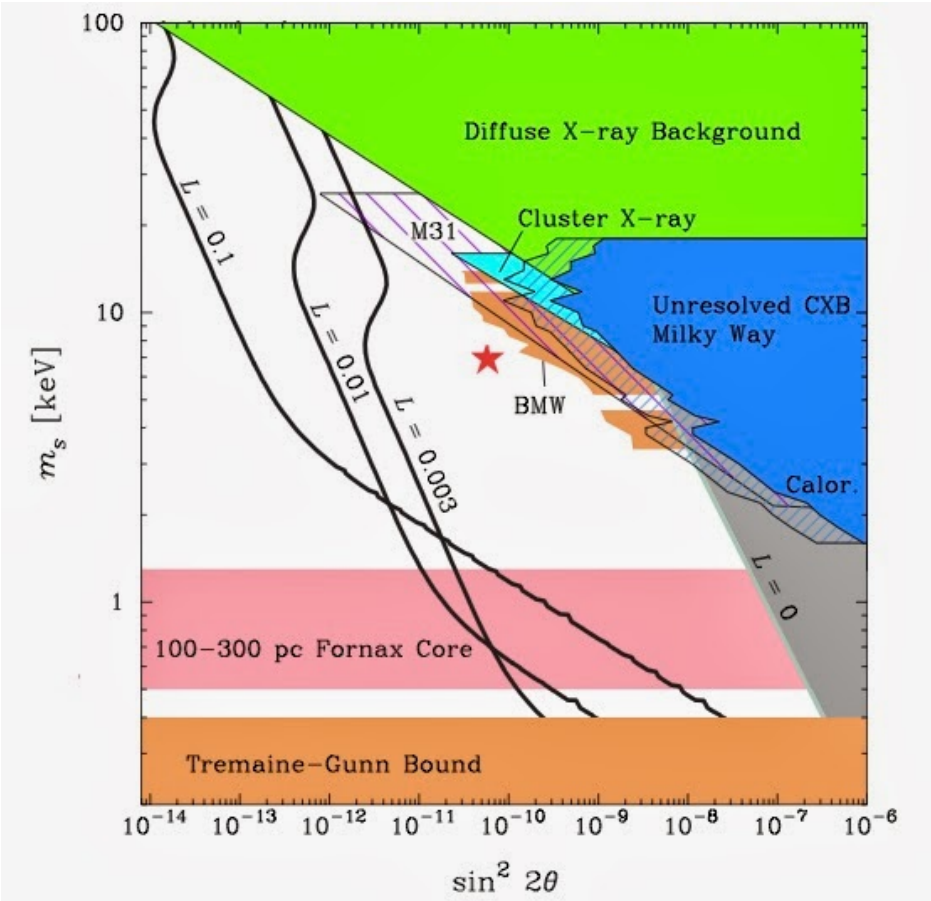

Figure 2.2.1: Constrains on the sterile neutrino as dark matter candidate, mainly coming from observations on small-scale galactic structures. Red curves show theoretical predictions for sterile neutrinos constituting all the dark matter with lepton numbers L=0, 0.003, 0.01 [49].

Once that the limits of the HDM model are pointed out still a wide amount of dark matter candidates are available. In Figure 2.2.2 a simplified subdivision according to the mass ranges is given.

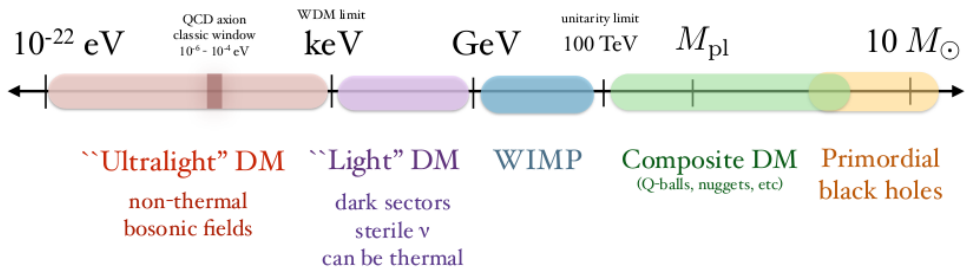

Figure 2.2.2: Dark matter main models, according to the mass of the dark matter particle [44].

The most massive dark matter object modelized would be a black hole, called primordial, as such high masses imply its decoupling from Standard Model particles well before the recombination era. Massive Primordial Balck holes (PBH), which can also be considered MACHOs, can release photons by an eventual accretion disk. Thus CMB observations allowed the exclusion of PBHs above 50 $M_\odot$ [50]. On the other hand, PBHs lighter than about 10^{-18} $M_\odot$ (solar mass) would be evaporated in a time shorter than the age of the universe [51]. PBHs are searched mainly via astrophysical observations: microlensing, gravitational waves, eventual accretion disk on the PBH and the dynamic related to compact baryon objects. An updated overview of the constrained PBHs is given in Figure 2.2.3.

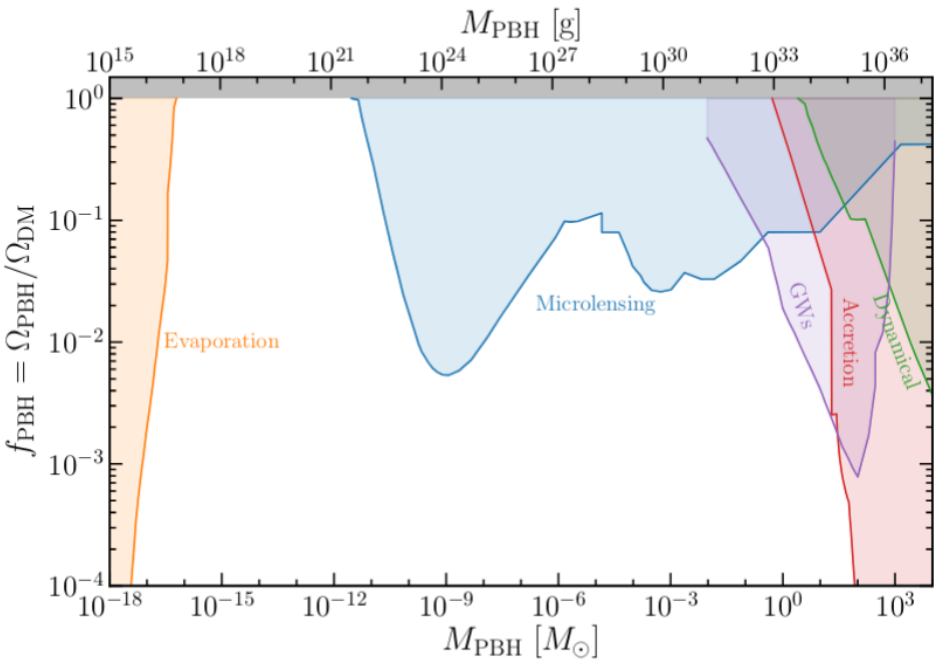

Figure 2.2.3: Constraints on the fraction of dark matter to which PBHs may account for, according to their mass, expressed both in grams and Solar Mass units [52].

Below 10^{16} g, superheavy dark matter particles can contribute to the whole dark matter halo in our galaxy. If they weakly interact with baryonic matter and have masses above 100 TeV scale, they are called "WIMPzillas" [53], referring to their lower-mass counterpart, WIMPs. WimpZillas arise in SUSY theories, where the break of supersymmetry happens at large scale [54] [55], in theories with discrete gauge symmetries [56]; finally also string and M theory allows for WIMPzillas candidates [57]. WimpZillas could not be produced thermally; instead, the most reliable mechanism is via gravitational particle production, just after the inflation [58]. The main detection strategy comes from astrophysical observations of Ultra High Cosmic Rays, whose decay would be due to the decay of WimpZillas [59].
Parallel to WIMPzillas, at higher cross-section strongly interacting massive particles, SIMPs, are also modeled [60] [61]. In the same space of parameters are also theorized composite states of dark matter, like Q-balls, solitons with a baryonic matter appearing first in SUSY theories [62] and "dark matter nuggets", as "nuclei" made of N dark matter nucleons [63]. An overview of SIMPs detection state-of-art is shown in Figure 2.2.4.

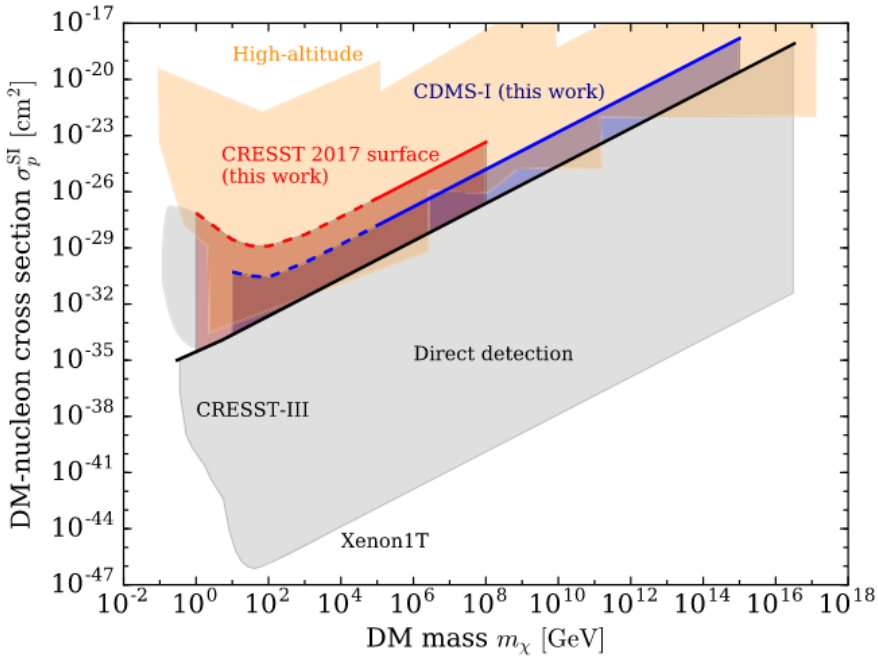

Figure 2.2.4: Constraints on strongly interacting dark matter from direct detection experiments, based on the nuclear scattering of dark matter particles on baryonic nuclei [64]. The orange regions were excluded by high-altitude experiments, such as RSS [65] and SKYLAB [66], fully reviewed in [67]. The grey shaded is bounded from below by constraints from Xenon1T [68] and from the left by CRESST-III [69] and the CRESST 2017 surface run [70] [71]. The black line denotes the previous cross-section reach from [72]. The shaded blue area shows the additional region of parameter space excluded by the reanalysis in [64] of the CDMS-I limits [73].

One of the most promising dark matter candidates are WIMPs, which stands for any elementary weakly interacting massive dark matter particles which thermally decoupled from baryonic matter. Hence it is a non-relativistic, "cold" candidate, which can make up the entire dark matter in the universe by itself. As the detectors on which the analysis showed in the present thesis are mainly designed for the detection of WIMPs, a straightforward description on their thermal freeze-out is here given.
The number density for non relativistic particles in thermal equilibrium at a temperature T follows a Boltzmann distribution,

$$n_\chi^{eq} \approx g \left(\frac{m_\chi c^2 k_B T}{2\pi\hbar c} \right)^{3/2} e^{-m_\chi c^2/k_B T}. \tag{2.2.17}$$

Assuming that the dark matter particles were in thermal equilibrium, their

annihilation rate Γ must be equal to the universe expansion rate, given by Hubble constant H. The latter one is given in Equation 2.2.12. The annihilation rate is proportional to the cross section times the velocity of WIMPs averaged on the temperature,

$$\Gamma = n_{\chi}^{eq} < \sigma v > (\hbar c)^2 = H. \tag{2.2.18}$$

The abundance at freeze out can then be written in terms of the annihilation cross section,

$$Y_{fo} = \frac{n_{\chi}^{eq}}{s} = \frac{H}{s < \sigma v >} \approx \frac{\sqrt{g_*}}{g_{*,s}} \frac{(\hbar c)^3}{< \sigma v > \hbar k_B T_{fo} M_{pl} c^2} \tag{2.2.19}$$

The annihilation rate drops down as the T goes below m_{χ}; still the drop is exponential, so the freeze-out temperature would not have been much below m_{χ}. For a quick extimation, it can be set $T_{fo} k_B \approx m_{\chi} c^2/10$. The abundance at freeze out for a thermal relic is given in Equation 2.2.11. Then the annihilation cross-section is estimated to be

$$< \sigma v > \approx \frac{\sqrt{g_*}}{g_{*,s}} \frac{10(\hbar c)^3}{eV M_{pl} c^2 \hbar} \approx 1 \times 10^{-26} cm^3/s. \tag{2.2.20}$$

This result, which is in agreement with the benchmark parameter [74], gives the minimum annihilation rate a thermal relic must have to not occur into an overbundance.
Two great implications follows from the relic abundance. A good explanation is given by considering the annihilation process of two WIMPs into Standard Model fermions, mediated by a generic V, with mass m_V, coupling g_{χ} and g_f respectively with dark matter and fermions. Looking at the s-channel, in the non relativistic limit, and assuming $m_{\chi} >> m_f$, the related cross-section in the center of mass frame is

$$\sigma = \int d\Omega_{cm} \frac{c|\vec{p}_f||M^2|(\hbar c)^2}{16\pi^2 E_{cm}^3 |\vec{v}_1 - \vec{v}_2|}. \tag{2.2.21}$$

If the fermion mass is assumed to be negligible, c $|\mathbf{p_f}| \approx E_{cm}$ /2 ; Mandlestham variable is $s = E_{cm}^2 \rightarrow 4\, m_{\chi}^2 c^2$ in the limit in which k_B T $<< m_{\chi} c^2$. Then the cross-section can be written as

$$\sigma = \int d\Omega_{cm} \frac{c|M^2|(\hbar c)^2}{32\pi^2 s |\vec{v}_1 - \vec{v}_2|} \longrightarrow < \sigma v > \approx \frac{c|M^2|(\hbar c)^2}{32\pi (m_{\chi} c)^2}. \tag{2.2.22}$$

A good estimation of the matrix term can be given. Assuming that the two Dirac-fermions have a single flavor/color and a vector mediator with mass

m_V, the spin-averaged matrix element in the non-relativistic limit is

$$|M^2| \approx g_\chi^2 g_f^2 \frac{32(m_\chi c^2)^4}{(m_\chi^2 c^4 - m_V^2 c^4)^2}, \tag{2.2.23}$$

where $g_\chi^2 = 4\pi\alpha_\chi$ and $g_f^2 = 4\pi\alpha_f$ are the vector-WIMP and vector-fermion couplings respectively. It follows that in the non-relativistic limit, the WIMP annihilation cross-section into two fermions mediated by a vector V is

$$< \sigma v > \approx g_\chi^2 g_f^2 \frac{m_\chi^2 c^4 (\hbar c)^2 c}{\pi (m_\chi^2 c^4 - m_V^2 c^4)^2}. \tag{2.2.24}$$

This result has two main outcomes. Whatever is the ratio between the WIMP and the mediator mass, the cross-section is upper bounded by

$$< \sigma v > \lessapprox \frac{g_\chi^2 g_f^2 (\hbar c)^2 c}{\pi (m_\chi c^2)^2}. \tag{2.2.25}$$

This means that by comparing to the expected cross-section from thermal freeze-out in Equation 2.2.20, the higher WIMP mass is

$$m_\chi \lessapprox 20 - 100 TeV \tag{2.2.26}$$

which is known as perturbative unitarity bound [75], and reflects that a heavier dark matter particle decoupled via freeze-out could not annihilate away enough to compare with the present dark matter abundance. More detailed bounds, with more assumptions on the dark matter candidate, can be found in [76].
A second consequence follows from Equation 2.2.25. If it is assumed a mass $m_\chi \approx 1$ TeV and leaving the coupling α^2 unconstrained, with $\alpha_f \approx \alpha_\chi$, the minimum annihilation cross-section is that of Equation 2.2.20. A comparison brings to

$$\alpha \approx 0.03. \tag{2.2.27}$$

This result is astonishing, as it corresponds to the weak coupling constant. The straightforward consequence is that thermal dark matter particles are very likely to have a weak interaction with baryonic matter, besides the gravitational one. This " WIMP miracle" made Weakly interacting massive particles one of the most promising dark matter models and justified from a theoretical point of view a wide stage of experiments aiming to detect WIMPs in laboratories. The ways the WIMP model is probed will be listed in the next section.

As m_χ drops below the GeV scale, the minimalist approach becomes not sufficient, and a mediator M for the Dark matter- SM particle interactions must be taken into account. The first approach would be considering a weak-scale mediator, like Higgs or an electro-weak gauge boson. Assuming $m_V \approx 100$ GeV, Equation 2.2.24 and for a mediator heavier than the WIMP, $m_V > m_\chi$ gives

$$< \sigma v > \approx \frac{m_\chi^2}{GeV^2} \frac{\alpha_\chi \alpha_f}{\alpha_w^2} \frac{1}{10^9 GeV^2} \tag{2.2.28}$$

where natural units were applied for convenience. For weak gauge couplings, $\alpha_\chi \alpha_f = \alpha_w^2$ the cross section goes below the one needed by the observed thermal relic abundance when $m_\chi <$ GeV (Lee-Weiberg bound [77]). New mediators below the weak scale are therefore needed to have dark matter candidates thermally produced and below the GeV mass scale.
The Standard Model offers by itself a possible candidate as mediator: the photon. This possibility can be counterintuitive, as electromagnetic interactions should allow for detecting dark matter at some frequency. Still, there is always the possibility of a very poor coupling, far from any astrophysical detection. Also, this would not be in contrast with the Lee-Weinberg bound, as that works only when $m_V > m_\chi$, which is not the case with the photon.
The annihilation cross-section, with two dark matter particles going into two fermions, $\chi\bar{\chi} \to f\bar{f}$ is

$$< \sigma v > \approx \frac{\pi \alpha_{em}^2 Q^2}{m_\chi^2}. \tag{2.2.29}$$

in natural units. The comparison with the thermal relic cross-section brings to Q $\approx 10^{-3} m_\chi$, where m_χ is in GeV; this is why this is called "millicharged dark matter". In the pre-recombination era, a millicharged DM particle is expected to scatter off the free charged particles in thermal equilibrium with a Rutherford cross-section. This process allows today to set very stringent limits, as these scatterings eventually would have determined the suppression of the growth of dark matter halos [78]. Further exclusion limits are set by the observations of the CMB anisotropies [79] [80]. Additional limits can be placed from supernova remnants [81], at electron colliders [82] [83], from cosmic rays observations [84], in direct detection experiments based on noble liquids [85].

Alternatively to the photon, dark mediators can be introduced, with the condition that their coupling with SM particles must be sufficiently small as, otherwise, it would have been already detected. The models purposed here are several, and compose a secluded particle sector, the "secluded sector" or "dark sector" [86] [87], which can eventually be connected to the SM

sector through some "portals" in which interactions between dark matter and Standard Model particles can bring to an excess/loss of energy or entropy in the system. Portals can be, for instance, due to vectorial mediators, such as dark photons [88], or scalar field coupled to a doublet Higgs boson [89], the so-called "Higgs portal".
The dark sector as well as sterile neutrinos are the main examples for Warm Dark Matter (WDM) candidates. The lowest mass for a candidate to be produced thermally just before the recombination era follows from the mass distribution at galactic scales. The smallest measured massive structure has a length scale of 10 – 20 Mpc. Such a wide anisotropy must have started growing at a very early stage of the Universe, at a redshift of z $\approx 10^7$. At this time, the photon temperature was of the order of keV. Therefore if dark matter was in thermal equilibrium with radiation, it had to satisfy $m_{DM} >$ keV; otherwise, it would be relativistic and would have smoothed the mass anisotropies. It follows that dark matter with $m_{DM} <$ keV was not produced thermally: this is referred to as the Warm Dark Matter (WDM) limit [90] [91].
Dark matter candidates below the WDM limit are usually referred to as ultra-light bosonic dark matter. Their lowest mass is set at $m_{DM} \approx 10^{-22}$ eV. In fact, at such low energy, dark matter particles are fully described as a coherent field, with a wavelength,

$$\lambda_{DM} = \frac{2\pi}{m_{DM} v} \approx 0.4 kpc \left(\frac{10^{-22} eV}{m_{DM}} \right) \tag{2.2.30}$$

in natural units. This massive bosonic field satisfies the classical wave equation $\Box\phi + m_\phi^2 \phi = 0$, which has a Jeans length, below which any perturbation is suppressed. Observations on dwarf galaxies, with a half radius of about 1 kpc, required that $m_\phi > 10^{-22}$ eV. Dark matter at about $m_\phi \approx 10^{-21}$ is called Fuzzy DM [92] [93].

A peculiar example of a scalar boson is the axion, one of the most interesting dark matter candidates. A wide review is given in [94]. The reason for this interest is that axions naturally arise as pseudo-Nambu Goldstone bosons when the U(1) Peccei-Quinn symmetry, introduced to solve the CP-violation lackness in QCD, is broken. The axion is expected to interact with the electromagnetic field [95],

$$L_{A\gamma\gamma} = \frac{g_{A\gamma\gamma}}{4} F_{\mu\nu} \tilde{F}^{\mu\nu} = g_{A\gamma\gamma} \mathbf{B} \cdot \mathbf{E} \phi_A. \tag{2.2.31}$$

Equation 2.2.31 allows for three processes:

- axion decay in two photons, A $\rightarrow \gamma + \gamma$;
- photon coalescence into axion, 2 $\gamma \rightarrow$ A;
- Primakoff conversion, $\gamma \leftrightarrow A$.

Requiring that axions are produced by the break of the Peccei-Quinn simmetry determines a relation between the axion mass and its coupling with the electromagnetic field,

$$g_{A\gamma\gamma} = (0.203(3)k - 0.39(1)) \frac{m_A}{GeV^2}. \tag{2.2.32}$$

The value of k is not fully constrained by the theory, as it depends by the exact way in which the symmetry is broken [96]. For instance, in DFSZ models [97] k = 8/3, while in KSVZ k = 0 [98]. A wider values for k has been also purposed, giving the yellow diagunal band shown in Figure 2.2.5. Furthemore, the condition in Equation 2.2.32 can be relaxed, keeping the same phenomenlogy; then the electromagnetic coupling is not related to the axion mass, and a wider space of parameters must be scanned. In this case these bosons are referred to as "Axion Like Particles (ALPs). A first way to look for axion and ALPs is the emission spectra of stars, active galaxies [99] [100] and eventually supernovae [101] [102], mainly looking at deviations from the expected emission due to conversion to/from axions, possible in presence of a strong magnetic field [103]. Earth-based experiments are usually divided in three main categories:

- the light-shining into a wall detectors, such as ALPS-II [104]
- Haloscopes, such ADMX, which look for microwave photons into which axions eventually converted to [105];
- Helioscopes, which look for X-ray photons from the ALPs conversion in the Sun core [106].

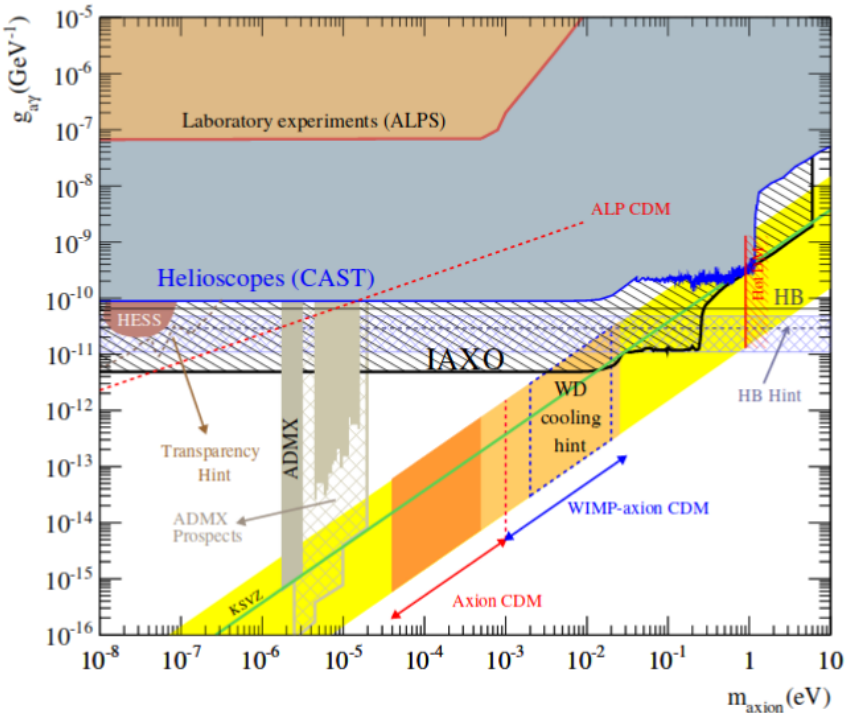

Figure 2.2.5: Updated axion and ALPs exclusion plot. The yellow band refers to the space of parameters in which Axions are expected. By relaxing any constraint on the mass-coupling ratio, the Axion-Like-Particle candidate follows [107].

In summary, even if indirect observations constrain the amount of dark matter, still our knowledge about its nature and eventual composition is lacking. As already stated, WIMPs rise to the top among all dark matter candidates both for theoretical and experimental reasons. In the next section, a review of the ways dark matter is searched nowadays is given, focusing on the direct detection of WIMPs.

2.3 WIMP detection

WIMPs are one of the most promising dark matter candidates, not only because of the "WIMP miracle" but also because an eventual detection would eventually also probe SUSY theories [108]. Furthermore, experiments aimed for WIMP detection show also sensitivity to different dark matter candidates and still-not probed Standard Model physics.
Schematically, dark matter can be tested via three methods, resumed in Figure 2.3.1. Indirect detection experiments look for an excess of the Standard

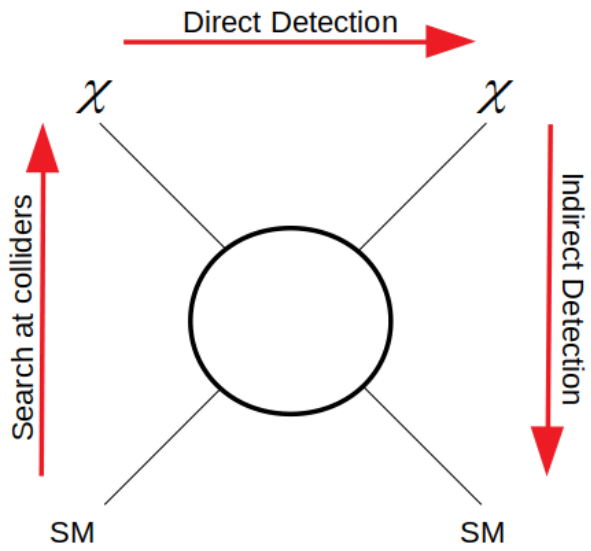

Figure 2.3.1: Scheme of the dark matter detection strategies. The direct detection (horizontal lines) looks for the scattering of dark matter particles on baryon atoms, so the input and output is a particle from the Standard Model. At colliders the annihilation between baryons can produce dark matter particles. Finally, indirect detection looks for the signal from the decay of the annihilation of dark matter particles.

Model particles, like high energy photons, electrons, protons, positrons, produced by the decay of dark matter particles [109] or their self-annihilation [110]. Among all the available signals, neutrinos and γ keep information on their incoming direction; furthermore, neutrinos differently from γ rays, are not affected by the absorption of the interstellar medium. γ ray astronomy exploiting imaging Cerenkov telescopes are then exploited, looking for abundances from stellar or galactic objects, which may highlight the contribution from dark matter decay products. In the TeV energy range the most stringent exclusion limits has been set by MAGIC [111], HESS [112] and VERITAS [113] while Femi-LAT telescope [114] is sensitive to lower energies, 20 MeV-300 GeV. These observations did not bring to any significant abundance from the fluxes expected from the Standard Model only, so limits on the annihilation cross-section were set. At lower energies, 0.1-10 keV, X-ray observations, like by XMM-Newton and Chandra satellites, also may be analyzed in terms of a dark matter candidate annihilation/decay. For instance, an unexpected line at 3.5 keV was observed by both satellites [115] [116], which may be due to the decay of dark matter particles; nevertheless, alternative explanations, not including physics beyond the Standard Model,

were suggested.
The neutrino detection is Earth-based. The main examples are Ice Cube, ANTARES and Super-Kamiokande, all designed and mainly focused on the neutrino physics; up to now, no hint of neutrinos from dark matter annihilation was observed, allowing for constrains on dark matter annihilation cross-section into neutrinos [117] [118] [119].
Alternatively, dark matter particles can be eventually searched at Large Hadron Collider (LHC), in experiments like CMS and ATLAS. Proton-proton collisions at a center-of-mass energy of 7 TeV produce a hadron shower, in which a lack in the transferred momentum and energy would represent a potential dark matter signature.
Finally, direct detection experiments look for the signal from dark matter particles, scattering on Standard Model particles. WIMPs, in this sense, are also very attractive from an experimental point of view, as the energy and cross-section ranges are accessible from Earth-based detectors. As the present thesis is focused on the physics potential of detectors designed for the direct detection of WIMPs, this section will focus on this specific dark matter candidate. At first, the expected WIMP rate is reviewed, followed by a complete overview of the direct detection experiments designed for the WIMP search.

2.3.1 Direct detection assumptions

Even if direct detectors designed for WIMPs can also be exploited to search for other dark matter candidates, it is worth pointing out the assumptions underneath the WIMP direct detection:

- WIMPs are uniformly distributed in the galactic halo, in thermal equilibrium with the baryonic matter. As our solar system moves in the Galaxy, this results in an apparent WIMP wind, which can be eventually directly detected. In the frame comoving with the Sun, their velocity distribution f(v,t) is then a Maxwell-Boltzmann distribution, centered at the velocity of the Sun $v_{\odot}$ = 220 km/s and truncated at the galactic escape velocity v_{esc} = 544 km/s [120].

- They are single elementary particles; their number density is the ratio of the galactic halo density in which they are distributed with the assumed WIMP mass.

- their dimensions are negligible compared to Standard Model nuclei, so they are treated as point-like particles with no excitation spectrum.

- WIMPs are electrically neutral and weakly interacting.

- they equally couple to neutrons and protons.
- the interaction with Standard Model particles is local.
- the cross-section only dependence on the recoil energy is enclosed in a "form factor" which takes into account the finite dimensions of the target nucleus. For spin-independent interactions, the interaction potential is also independent of the incident angular momentum.
- WIMPs typical recoil energies are O(10 keV), not enough to produce Standard Model particles from their scattering in the detector, neither to excite internal degrees of freedom of nuclei. Hence their scattering is assumed to be elastic.
- again due to the non-relativistic WIMP velocities, the transferred momentum q will be too small to discern the nucleus structure, so scattering coherently with it. As far as q $r_N << 1$, where r_N is the nucleus radius, this assumption is a good approximation. Its breakdown at higher energies is kept into account by including a momentum dependent form-factor, as shown later in this section.
- as the transferred momentum is much larger than the inverse of the typical inter-atom space, any bulk effect is negligible, and the scattering process can be analyzed as on a single baryon atom.
- the scattering is described by a s-wave (l = 0), so it is isotropic in the center of momentum frame [121].

These assumptions shape the WIMP-nucleus differential cross-section. The interaction with the nucleus is point-like only on the WIMP side. The nucleus finite dimensions are taken into account by the form factor, which is the Fourier-transform of the centers-of scattering density in the nucleus, if the s-wave assumption holds,

$$F(\vec{q}) = \int \rho(\vec{r}) e^{i\vec{q}\cdot\vec{r}} \tag{2.3.1}$$

Furthermore, to take into account the loss of the coherence at high transferred momentum, the form factor will be energy dependent. Hence the cross-section at a momentum $\vec{q}$ is related to that at zero-momentum transfer by $\sigma(q) = F^2(\vec{q}\,)\ \sigma(0)$. By explicitly expressing the spin-dependent and independent components, the differential cross section is

$$\frac{d\sigma}{dE} = \frac{m_A}{2\mu_A^2 v} \cdot (\sigma_0^{SI} F_{SI}^2(E) + \sigma_0^{SD} F_{SD}^2(E)). \tag{2.3.2}$$

The spin-independent term at zero momentum transfer is given by the sum of the neutron and the protons contribution in the nucleus,

$$\sigma_0^{SI} = \sigma_p \frac{\mu_A^2}{\mu_p^2}[Zf^p + (A-Z)f^n]^2, \tag{2.3.3}$$

where the f are the WIMP couplings to protons and neutrons, usually assumed to be equal, $f^n = f^p$, which brings to an A^2 enhancement. The Helm form factor [122] is the standard assumption for the target nuclei, so modeling it as a homogeneous cave sphere with a finite thickness,

$$F(q) = 3\frac{j_1(q \cdot r_n/\hbar)}{(q \cdot r_n/\hbar)^2} exp(-\frac{1}{2}(\frac{qs}{\hbar})^2) \tag{2.3.4}$$

The Lewin-Smith parametrization [123] assumes a = 0.52 fm, a skin thickness s = 0.9 fm; the effective radius r_n is then

$$r_N = \sqrt{c^2 + \frac{7}{3}\pi^2 a^2 - 5s^2} \tag{2.3.5}$$

where c = (1.23 $A^{1/3}$ - 0.60) fm. This choice of the parameters allows for a good agreement with muonic spectroscopy data. In Figure 2.3.2 the squared form factor for different target nuclei is shown.

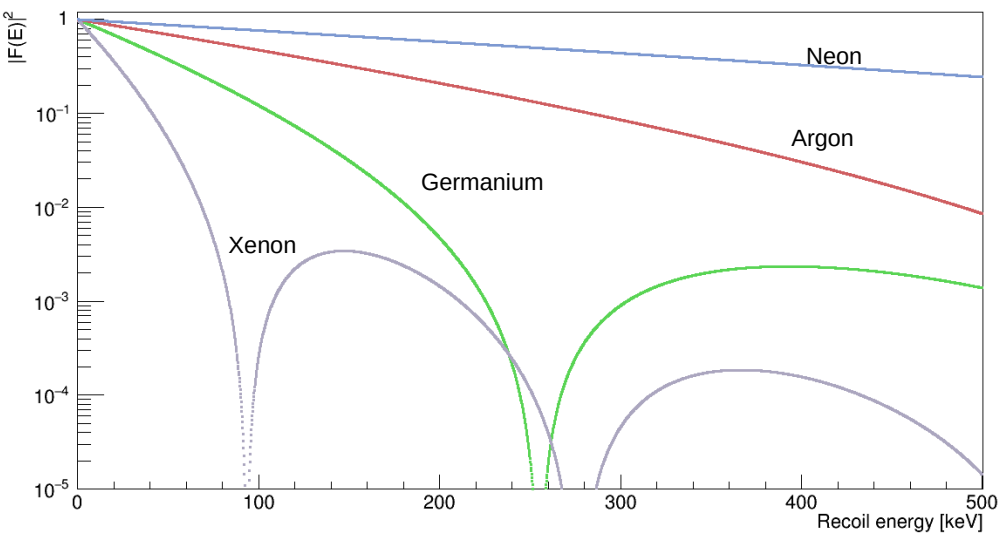

Figure 2.3.2: Squared Helm form factor for different nuclei, assuming Lewin-Smith parametrization.

The spin-dependent contribution is written in terms of spin structure function,

$$\sigma_0^{SD} = \frac{32}{\pi}\mu_A^2 G_F^2 \cdot [a_p < S^p > + a_n < S^n >]^2 \frac{J+1}{J} \tag{2.3.6}$$

where G_F^2 is the Fermi coupling constant, $a_{p,n}$ the effective proton/neutron couplings, J the total nuclear spin; finally $< S^{p,n} >$ stands for the expectation values for neutrons and proton spins.

An alternative approach is to consider in more detail the WIMP-nucleons interaction in the context of Effective Field theories (EFTs). In this case the nucleus is not treated as a point-like particle, but holds a finite dimension. The couplings, both in the spin dependent and independent component, are exchanged for six possible nuclear response-functions, which brings to 14 operators; the spin response function is split in transverse and longitudinal components, due to the not-point like modelization of the nucleus. Four vectors compose all EFT operators:

- i $\vec{q}/m_N$, the transferred momentum normalized with the nucleon mass;
- $\vec{v}^{\perp}$, the WIMP-nucleon relative velocity;
- $\vec{S_N}$, the target nucleus spin;
- $\vec{S_\chi}$, the eventual WIMP spin.

In EFT, the standard spin-dependent and independent scattering shown in Equation 2.3.3 and Equation 2.3.6 is described by the operators

$$O_1 = 1_\chi \cdot 1_N, O_4 = \vec{S_\chi} \cdot \vec{S_N}. \tag{2.3.7}$$

Examples of reanalysis of WIMP limits at the light of EFT can be found in [85] [124] [125] [126].

Once that these assumptions hold, also some expectations on the WIMP signal in the detector follow. WIMPs are expected to perform elastic scattering on baryonic nuclei; hence these recoils are targeted as "nuclear recoils". WIMPs with masses of (10-1000) GeV/c^2 would eventually return nuclear recoils within the range (1-100) keV [123]. As the probability of interaction is small, they are assumed to scatter at most once in a detector. Single scatter events from nuclear recoils are then the expected signal for a WIMP, whatever is the employed technology to detect it. The differential rate of events is the convolution of the flux f(v,t) of WIMPs, with mass m_χ, velocity v and density in the halo ρ_0 with the differential cross-section $d\sigma/dE$, which

is proportional to the probability to scatter with a baryon atom with mass number A and mass m_A,

$$\frac{dR}{dE}(E,t) = \frac{\rho_0}{m_\chi m_A} \int v \cdot f(\vec{v},t) \cdot \frac{d\sigma}{dE}(E,v) d^3v. \tag{2.3.8}$$

The recoil energy spectrum was widely analyzed in [123]; from here it follows that the recoil energy spectrum can be written in terms of the WIMP mass m_χ and the WIMP-nucleon cross-section at zero-momentum transfer σ_0,

$$\frac{dR(E_{rec})}{dE_{rec}} = \frac{c_1 N_A \rho_0}{2\sqrt{\pi}\mu_1^2} \sigma_0 |F(q)|^2 v_0 \frac{A^2}{E} exp(-c_2 \frac{E_{rec}}{Er}) \tag{2.3.9}$$

where μ_1 is the reduced mass for a $^1_1$H nucleus, N_A is the Avogadro number, v is the velocity of the Earth relative to the galaxy, E is the consequent WIMP kinetic energy. Given the mass number A and the target mass M_T, it is finally defined r = $\frac{4M_\chi M_T}{(M_\chi+M_T)^2}$. In Figure 2.3.3 the recoil spectrum for a WIMP mass $m_\chi = 60$ GeV/^{2} and $\sigma_0 = 10^{-44}$ cm^2 is shown, for a few target nuclei.

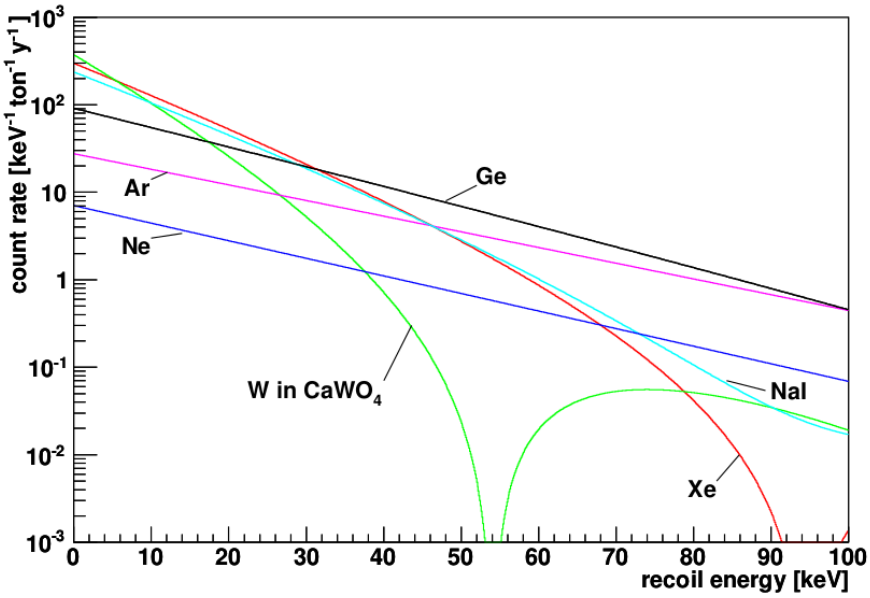

Figure 2.3.3: Recoil energy spectra for WIMP $m_\chi = 60$ GeV/^{2} and $\sigma_0 = 10^{-44}$ cm^2, for Argon, Xenon, Neon, Germanium and Tungsten, contained in $CaWO_4$ crystals [127].

Three main detection strategies are applied. One is to look for the energy dependence of WIMP recoils, so time-integrating Equation 2.3.8. In this

case, background suppression and rejection techniques must be applied, as the sensitivity of the detector will decrease with the increase of background events in the WIMP energy Region of Interest (ROI).
Alternatively, the time dependence of Equation 2.3.8 is searched in the observed events; in fact, an annual modulation is expected to be observed as a consequence of the Earth revolution motion. In summer, the Earth revolution agrees with the solar system motion in the Milky Way, resulting in an effective stronger "WIMP wind" scattering in the detector, with a peak at about June 2nd; on the other hand, the minimum is expected to occur in December. Hence the number of WIMP events giving a signal above threshold in the detector will have the same modulation, differently from any background events [128].
Finally, also a daily modulation on the direction of the incoming WIMP is a strong signature. In fact, background events from the detector or the Earth are not expected to come from the Cygnus constellation, as for dark matter particles. So detectors sensitive to the recoiling track of the incoming particle can then select an eventual WIMP signal [129].

2.3.2 Backgrounds

The main obstacle in rare-events search is the significant amount of background, which might suppress the detector sensitivity to the poor signal. A quick review of the expected background in WIMP direct detection experiments is here given.

To shield the detectors from cosmic rays, they are set underground to exploit the natural shield of the rock. Still, muons produced from the interaction of cosmic rays with the atmosphere can reach the detector, inducing an energy deposit much higher than the one expected from WIMPs. In addition, muons scattering on the detector materials may produce neutrons by spallation, which would finally fall in the WIMP ROI. Hence, dark matter detectors for WIMP search are built underground: the more the detector's depth, the lower the muon flux on it. In Figure 2.3.4, the depth of several laboratories hosting dark matter experiments is compared, together with the respectively measured muon flux.

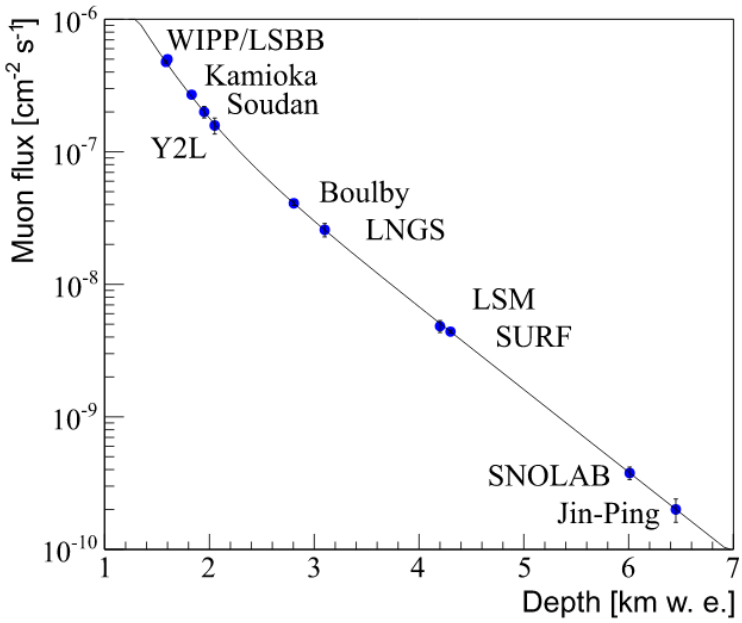

Figure 2.3.4: Muon flux as a function of depth in km water equivalent (km w.e.), for underground laboratories in which dark matter search is performed: the Waste Isolation Pilot Plant (WIPP) in the USA, the Laboratoire Souterrain à Bras Bruit (LSBB) in France, the Kamioka Observatory in Japan, the Soudan Underground Laboratory in the USA, the Yand Yand Underground Lab (Y2L) in Corea, the Boulby Underground Laboratory in the U.K., the Laboratori Nazionali del Gran Sasso (LNGS) in Italy, the Laboratoire Souterrain de Modane (LSM) in France, the Sanford Underground Research Facility (SURF) in the USA, the SNOLAB in Canada and finally the Jin-Ping laboratory in China [130].

Another source of background are γ rays, coming from ^{238}U and ^{232}Th radioactive chains, as well as from radioactive isotopes as ^{40}K, ^{60}Co and ^{137}Cs, present in the materials surrounding the active target. The interactions with electrons are mainly via photoelectric effect up to O(100) keV and Compton scattering up to O(10 MeV). All the materials surrounding the target are selected with stringent requirements of radiopurity. The natural radioactivity coming from the rock is passively shielded with dense material, such as lead; alternatively, a large water tank can be employed. A muon tank also helps for muon-induced events, as muons perform the Cerenkov process in the ultrapure water. Residual γ rays background can be then rejected by rejecting events from the outer region of the target volume. Multi-scattering events are rejected, as WIMPs are expected to scatter at most once in the detector.

Finally, some detectors also allow for good discrimination between electron recoils, due to γ and β, and nuclear recoils, due to WIMPs and neutrons.

Neutrons are a dangerous background, as they mimic the signal from WIMPs. Cosmogenic neutrons are produced by spallation of muons on the rocks surrounding the detector or on the detector itself. These neutrons, produced up to a few GeV [131], are then moderated by detector materials down to a few MeV of kinetic energy, entering the WIMP ROI; in addition to these, radiogenic neutrons [132] are produced from the radioactivity of detector materials in (α, n) processes and spontaneous fission and can show up into the active volume with an energy of a few MeV. As only neutrons performing more than one scattering can be rejected, the optimization of the radiopurity level of the detector materials is fundamental. Passive shielding with a water veto also contributes to the reduction of neutron events in the active volume. Furthermore, the removal of events in coincidence with muons in the water veto helps for cosmogenic neutron rejection; similarly, materials with a high neutron capture probability, like Gadolinium, can be employed in order to reject any events in which a neutron is in coincidence with the γ released by the neutron capture. Finally, liquid scintillators can be set as a shield to directly tag neutrons [133].

αs released by (α, n) processes are produced at higher energies than those expected from WIMPs. Still, due to the attenuation of materials which the particle passes through, their recoil still may fall in the WIMP ROI. As the mean free path is of a few millimeters, αs are usually entirely suppressed by the definition of a fiducial volume.

Dark matter detectors with an energy threshold of a few keV are also sensitive to neutrinos interactions. The main neutrino source is solar neutrinos, which can have interactions both in charged and neutral current for ν_e and neutral current only for the other flavours, with a neutrino-nucleon cross-section of 10^{-45} cm^2 at WIMP masses below 10 GeV/c^2 [134]. At higher WIMP masses, the main neutrino contribution comes from atmospheric neutrinos [135] and the diffuse supernovae neutrino background (DSNB), which is the cumulative cosmic neutrino emission, mainly due to core-collapse supernovae [136]. The cross-section is much lower than that of solar neutrinos, reaching about 10^{-49} cm^2 at 100 GeV/c^2. Neutrino-electron elastic scattering may be rejected as electron recoils if the experiment can discriminate them from nuclear recoils. Still, neutrinos at energy $\approx$ MeV mainly perform coherent elastic scattering with the target nucleus. This process was first observed by the COHERENT experiment [137], confirming what is expected

from the Standard Model. This means that, at cross-section low enough, a broad background of CEνNs events will suppress the detector sensitivity to WIMPs, as their signal will also be a nuclear recoil, as well as for dark matter particles. The cross-section and WIMP mass at which the detectors will be overwhelmed by this background is called "neutrino floor" [138] [139] [140].

An aside comment is reserved for internal background, which strongly depends on the dark matter search's technology.
Solid-state scintillators based on crystalline targets are grown from high purity melts. Impurities are naturally removed during the growing process, as their ionic radius does not match with the crystalline grid structure [141] [142]. On the other hand, contamination due to radon decay products deposited on the detector's surface impacts the detector sensitivity. In fact, αs and βs released by the radon chain usually deposit only a fraction of their energy on the crystalline, so that their recoil falls in the WIMP ROI. Besides reducing the α surface events, also a custom position reconstruction, allowing to reject events close to the surface, is optimized.

For noble gases, the main internal background usually comes from unstable isotopes of the target nucleus. For instance, ^{40}Ar is usually contaminated by ^{39}Ar. This is produced by cosmic rays performing spallation on ^{40}Ar; it β decays with an endpoint of 565 keV and a rate of about 1 Bq/kg, for Argon extracted from the atmosphere (AAr, atmospheric Argon). This background is reduced by using Underground Argon (UAr), with a radioactivity smaller by a factor of $\approx 10^3$ [143]. The other common noble liquid employed in direct dark matter search is Xenon. It has more than one unstable isotopes, all produced by cosmic activation during detector installation and operations; still, they all decay in a short time, before the start of the data taking. An exception is the ^{136}Xe, with a lifetime of 2.2×10^{21} y [144] making its activity almost negligible.
Further contamination is due to ^{85}Kr, produced by nuclear fission and then released in the atmosphere; this is usually removed by cryogenic distillation [145] or by chromatographic separation [146], eventually reaching a contamination of a few parts per quadrillion [147].
Radon is a product in ^{238}U and ^{232}Th decay chains, present in the detector materials. Due to this high volatility, it can diffuse up to the liquid target. Besides the choice for materials with low radon release, cryogenic radon traps are usually employed to remove it.

2.3.3 Overview of the detection techniques

The energy from the elastic scattering of WIMPs on a target nucleus goes into phonons, scintillation light and ionization electrons. Direct detection experiment can then look to one or more of these signals. In this section, a review of the direct detection techniques is given, by taking as reference the leading related experiments.

Crystals, mostly NaI(Tl) and Cs(Tl), are employed to detect the scintillation light at room temperature. The add of the thallium increases the number of luminescence centers and hence the light emission efficiency; also it shifts the peak emission wavelength from 415 nm to 580 nm, which is an advantage as the crystal transparency and the photodetection efficiency of the employed photosensor, for instance, photomultipliers tubes (PMTs), increase with the wavelength. Furthermore, the high scintillation efficiency and the high density brings to a high energy resolution, of about 8% for 1 MeV energy recoils, and to a lower energy threshold compared to the other technologies. The main drawback is the lack of any particle discrimination, even between nuclear and electron recoils, besides rejecting events scattering in coincidence in more crystals. Hence making the crystals grown in the most radiopure powder is a fundamental requirement.

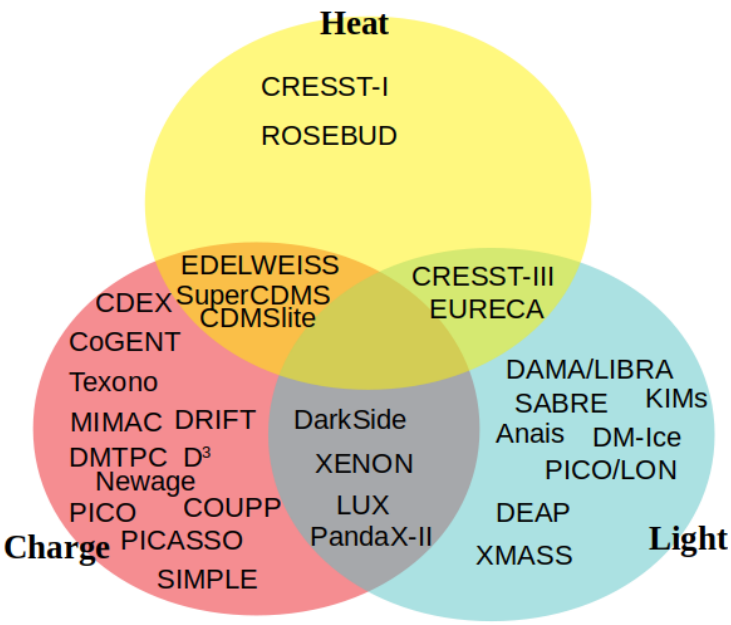

Figure 2.3.5: Representation of the main detectors for each detection strategy: the ionization charge, the scintillation light, the heat (phonons).

DAMA, at LNGS underground laboratories, is an experiment based on a target of NaI(Tl) crystals [148] as detector. The signal from the dark matter is expected to result in a rate of events showing an annual modulation, due to the Earth revolution motion. Indeed DAMA and its upgrade DAMA/LIBRA found an annual-modulate single-hit rate of events in the energy range (2-6) keV, using a total exposure of 1.33 tons year. The maximum matches with the expected one on July the 2nd within 2 σ [128]; the collected signal has a significance of 9.3 σ after a data taking lasting 14 annual cycles [149]. If the signal is from a dark matter source, it can be interpreted in several ways. First of all, the elastic WIMP scattering may occur on the iodine or on the sodium [150]. Also the same data were analysed assuming spin-dependent [151], inelastic scattering WIMP interactions [152], and also WIMP scattering on electrons [153] as no discrimination between nuclear and electron recoil is available. Nevertheless, the detections from other experiments excluded DAMA's signal. Several interpretations followed [154], some of which were also refuted, leaving a still-not fully understood signal.
The best cross-check can come from experiments using the same target as DAMA. The Anais experiment [155], with 25 kg of NaI(Tl) as a target, was precisely designed to this scope; after two years of data-taking, it already excluded any annual modulation down to an energy threshold of 1 keV [156]. In addition to this, DM-Ice-17, with its 17 kg of Na(Tl) crystal target, set 2457 m underground at the South Pole, after about 4 years of data taking, excluded the annual modulation observed by DAMA within the range (4-20) keV [157]. SABRE detector [158] [159] will also host a target of highly pure NaI(Tl) surrounded by an active liquid scintillator veto. This will allow for a better understanding of DAMA's signal, while the veto tagging will allow for further background rejection. Two twin detectors will be set, one in the northern hemisphere at LNGS and the other in the southern hemisphere, in the Stawell Underground Physic Laboratory (SUPL); in this way, any seasonal contribution to the modulation observed by DAMA can be investigated [160]. Further results are expected from PICO-LON [161]. Finally, also KIMs experiment [162] contributed to excluding DAMA results with its same target, also counting on a very high background suppression and by discrimination of electron recoils from nuclear recoils. With 2967.4 kg·day of exposure, no nuclear recoil was found [163].

Germanium detectors show a very low energy threshold, down to about 500 eV, due to the very low contamination level, making them sensitive to WIMP of masses of few GeV/c^2 when the detector is operated in ionization mode, in the gas phase. The energy resolution is about 0.15 % at 1 MeV, allowing for a full background reconstruction, which can eventually help its

discrimination. A full separation between nuclear and electron recoil is in general not available, but the rise-time of the signal on the acquired waveform can discriminate surface events from bulk events.
A first interesting result was found in the CoGeNT experiment, where after three years of data taking the signal rate's annual modulation was found, consistent with WIMP expected one within 2.2 σ [164]; still the signal amplitude was 4-7 times higher than expected. Further re-analysis, out of the collaboration, with a reviewed background model, brought to the exclusion of any annual modulation [165].
Texono [166] and the more recent CDEX experiments in China show the capability to reach an extraordinary low energy threshold, down to 177 eV for an electron recoil, down to masses of 2 GeV/c^2. A single-element 994-gram (CDEX-1B) of p-type point contact (PPC) is run surrounded by a solid passive shielding system. In the prototype, a 10 kg germanium detector (CDEX-10), consisting of three detector strings with three germanium crystals each, is directly immersed in the liquid nitrogen. This technology allowed to set competitive limits both in terms of the recoil energy spectrum and the rate annual modulation [167].

Cryogenic bolometers add to the detection of phonons either the charge either the scintillation light; this generally allows for the discrimination of electron recoils and nuclear recoils by looking at the energy dependence of the energy loss in heat. Phonons produced in the crystal lattice are tagged as thermal and not thermal. The first are due to the thermal variation with the medium after the recoil, and are hence measured by the local rise of the temperature. Athermal phonons are not in equilibrium with the medium and allow for the position reconstruction and information on the deposited energy. If a drift field is applied, electron-hole pairs are produced, enhancing the phonon yield. The detectors are kept at a temperature of (10–100) mK with a thermal bath: at cryogenic temperatures, the heat capacity is lower for many materials, resulting in a higher increase of the temperature for a higher energy recoil. For instance, germanium at 20 mK shows thermal increase of about 1 μK for nuclear recoils of a fee keV.
The first example of a cryogenic bolometer is given by CDMS [168] and CDMS II experiments [169], with a target of 230 g of ^{19}Ge and 100 g of ^{11}Si, respectively. They look both at the phonons and the ionizaton electrons, so nuclear recoils and electron recoils are discerned. The event's topological reconstruction is given by the arrival time on the photosensors and the relative charge distribution. In particular, CDMS-II excluded the annual modulation in germanium observed by CoGENT experiment [170]. The successor SuperCDMS uses 15 Ge crystals, each with 0.6 kg and sensitive to nuclear

recoil below 1.4 keV of deposited energy, for a total of 577 kg/day. WIMPs were excluded down to $1.2 \cdot 10^{-42}$ cm^2 for a WIMP mass of 8 GeV/c^2 [171]. Still from CDMS collaboration is the CDMSlite detectors, which uses a single germanium crystal as the target and is focused on the reach of the lower threshold available, down to 56 keV for an electron recoil [172]. In total SuperCDMS and CDMSlite set the most stringent limits for WIMPs below 10 GeV/^{2} [173] [174].
EDELWEISS collaboration detectors are cryogenic bolometers too, all set at Laboratoire Douterrain de Modane (LSM). In EDELWEISS-II, due to the choice of the photosensors, who are not sensitive to athermal phonons, no topological reconstruction is available; still, the interleaved structure of the photosensors allows for good discrimination of surface events, up to a discrimination power of 10^4 [175]. In EDELWEISS-III, a set of inter-digitized electrodes will allow selecting only interactions within a fiducial volume, so rejecting the surface background events. This experiment, the last built from the collaboration, is equipped with 4 advanced high-purity germanium detectors operating at 18 mK in a dilution refrigerator; this allows for identifying nuclear recoils from electron recoils. This brought to set the first WIMP exclusion limits down to 10^{-42} cm^2 for WIMP mass of 10 GeV/c^2 [176]. Furthermore, the detector showed its main physics potential in sub-GeV dark matter searches, thanks to the very low resolution achieved, down to 60 eV [177] [178].
CRESST-III experiment, set at LNGS, looks at both the phonons and the scintillation light from a target of 23.6 g of $CaWO_4$ crystals [179]. The detector first run was held from May 2016 to February 2018; the consequent analysis showed its sensitivity at very low dark matter mass, with the best stringent limit in the mass range (0.16 - 1.8) GeV/c^2 [180].
Finally, the expertise from CRESST, EDELWEISS and ROSEBUD collaborations are converging in EURECA experiment [181], in which the physics potential for dark matter search of cryogenic bolometers is expected to find is highest expression [182].

Superheated fluids can also be a suitable target for WIMP search, hold in bubble chambers, as in COUPP [183] and PICO [184] or droplet detectors, as in PICASSO [185] and SIMPLE [186]. When the incident particle scatters in the fluid, it creates a local phase transition in the medium [187]. The event is photographed with CCD cameras with $\approx$ mm of resolution. The background rejection from γs and βs is straightforward, as they cannot produce nucleation, differently from αs, neutrons and WIMP induced recoils. Here further rejection techniques are optimized. COUPP experiment showed an α rejection efficiency of about 99 % by looking at the intensity of acoustic emis-

sion, higher in α recoils than in nuclear recoils [183]. PICASSO experiment exploits the rise-time and the frequency of the acoustic signal [185]. The energy threshold is of a few keV for a nuclear recoil, but it can be changed by varying the temperature and the pressure of the superheated fluid. The usual targets are CF_3I , C_2ClF_5, C_3ClF_8 and C_4F_{10}, so the detectors are sensitive also to the spin-independent interaction, thanks to the fluorine.
Born from the joint PICASSO and COUPP experiments, PICO set the strongest exclusion limits on the spin-dependent WIMP-proton cross-section. In 2017 PICO-60, filled with 52 kg of C_3F_8, with an exposure of 1167 kg day and an energy threshold of 3.3 keV, set the most stringent limit in the WIMP-proton spin-dependent cross-section, down to 3.4×10^{-41} cm^2 at 30 GeV/c^2 for the WIMP mass [188]. The next detector, PICO-40L, with 40 litres of C_3F_8 target, is still under construction and is designed to operate in a background-free condition for a data-taking lasting a few years [189].

The DRIFT-II experiment [190] searches for dark matter particles by looking at their recoil track in the active volume, 0.3 m^3 of a low-pressure mixture of CS_2, CF_4 and O_2. The 33.2 g of fluorine allows for sensitivity to spin-dependent WIMP interaction. A first interesting result was published in 2014, with a background-free analysis for the spin-dependent interactions, outstanding among directional detections but still not competitive with the results from bubble chambers. The following analysis in 2016 allowed to exclude WIMPs down to 2.8×10^{-37} cm^2 at 100 GeV/c^2 for spin-dependent interactions [191]. Future dark matter analysis are also foreseen in MIMAC, a micro-TPC matrix aiming to detect the nuclear recoils together with their recoiling track [192] [193], and from Newage [193] and D^3 [194] experiments. Also DMTPC experiment [195] will use a TPC with a charge amplification region; in this case, the detector will be of m^3 scale, with a target of CF_4 at 50 Torr. The primary ionization electrons are drifted into this region, where the signal is then amplified with a gain of 5×10^4. Scintillation photons from ion recombination are also seen by CCD cameras, allowing for the topological reconstruction of the event.

Dark matter detectors based on noble liquids usually exploit liquid Argon (LAr), as the experiment DEAP-3600 [196], or liquid Xenon (LXe), as XMASS detector, with its 832 kg of active mass [197]. The inner vessel of a single-phase noble liquid detector is shown in Figure 2.3.6.

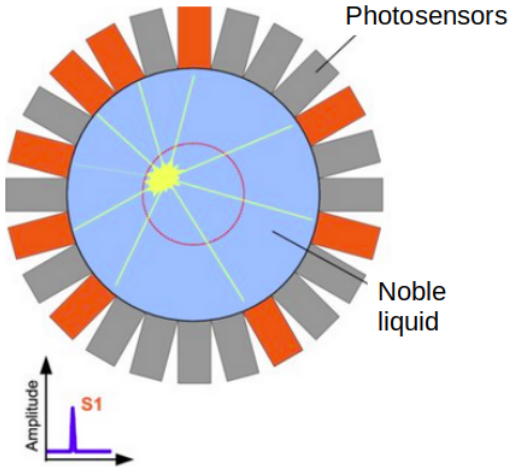

Figure 2.3.6: Representation of the inner vessel of a single-phase noble liquid detector. The shape is usually spherical and is usually completely filled with the noble liquid, which is observed by a dense array of photosensors. Only the scintillation photons are collected in these detectors.

In single-phase noble liquid detectors, the target is contained in a spherical inner vessel, surrounded by shields vetoing external backgrounds and looked by an array of photosensors. When the WIMP eventually scatters on the noble liquid nucleus phonons, excitons and ionization electrons are produced. An array of photodetectors, usually Photomultipliers Tubes (PMTs), look and record the scintillation signal, converting it in a current signal that is then digitized, amplified, and stored as a waveform. Noble liquids are transparent to their own scintillation light, which then fully reach the photosensors. Also, the technology in an experiment is easily scalable for larger target masses. Specifically, Xenon is rarer than Argon, so it is, in general, more expensive to provide. On the other hand, Xenon has a negligible amount of internal radioactivity, as its unstable isotopes decay either in a few weeks or in about 10^{22} years, so too soon or too late to show up during the detector runs. Opposite to Xenon, Underground-Argon has a radioactivity of 0.9 mBq/kg, due to the beta-decays of ^{39}Ar.
The two elements show a complementarity on the WIMP search. While LAr based detectors only search for spin-independent WIMP interactions, LXe also has stable isotopes with non zero spin, so can set limits on both the spin-dependent and independent WIMP interactions. As it will be underlined in the next chapter, Liquid Argon can still allow for a lower background level in the ROI, due to the very high rejection power of electron recoils, up

to 10^{-10} in DEAP-3600 [198]. Both the LAr and LXe have a singlet and a triplet scintillation state, where the nuclear recoils excite more likely the single state. Still, only in Argon, the triplet state's time-decay is three orders of magnitude longer than the singlet state, while in Xenon it is 4 ns and 22 ns [199]. So, only in LAr the scintillation signal from a nuclear recoil will be much faster than that from an electron recoil. DEAP-3600, with its 3.3 tons of Atmospheric Argon, recently set the most stringent limits in LAr for spin-independent WIMP interactions for masses above 10 GeV/c^2 [200].
In order to achieve a better topological reconstruction and gain sensitivity to lower WIMP masses, double phase noble liquid detectors are employed, using both liquid and gas phases. Examples for Xenon are detectors from XENON collaboration, as XENON-1T and XENONnT, while on the Argon side stand detectors from DarkSide collaboration, like DarkSide-50. The target is contained in a TPC, as shown in Figure 2.3.7

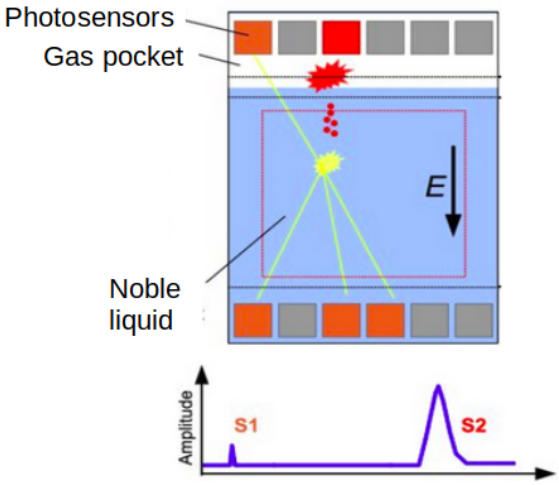

Figure 2.3.7: Representation of the inner vessel of a double phase noble liquid detector. The shape is usually cylindrical: when an incident particle scatters on the noble liquid, the scintillation signal is observed: the "S1" signal. Then, a vertical potential drifts the ionization electrons up to an extraction grid, by which they are injected into the noble gas pocket. Here they are accelerated, giving a second amplified signal, called S2.

When the WIMP scatters into the noble liquid phase, the released photons are detected by photosensors, while the ionization electrons are drifted up to the extraction grid by a vertical potential of O(100) V/cm. At the extraction grid, electrons are drifted into a gas pocket, above the liquid phase,

where they are accelerated by a potential of O(kV/cm) until their emission by electroluminescence [201]. The photosensors are set in two arrays, at the top and the bottom of the cylindrical TPC cryostat, while high reflective panels are set on the inner walls to optimize the photon collection.
LUX experiment, at Sanford underground laboratory in the USA, has an active mass of 250 kg of LXe; in 2016, with an energy threshold of 1.1 keV for a nuclear recoil and an exposure of 3.35×10^4 kg day, they excluded WIMP down to 1.1×10^{-46} cm^2 for WIMP masses of 50 GeV/c^2 [202]. Then the collaboration merged with ZEPLIN experiment [203] into the new LZ experiment, with 7 active tonnes of LXe fiducial mass and a projected sensitivity of 1.5×10^{-48} cm^2 for WIMP masses of 40 GeV/c^2 [204].
The LUX exclusion limit was also more stringent then the one reported recently by PandaX-II [205], which operates with 580 g of LXe in the China Jinping Underground Laboratory; also their future detector PandaX-4T promises for a minimum sensitivity of 6.0×10^{-48} cm^2 for WIMP masses of 40 GeV/c^2 [206]. XENON collaboration is certainly one of the leading experiments in the dark matter search. The radiopurity of the LXe, the high exposure and the design of the double phase chamber allow for setting the most competitive exclusion limits. In the last WIMP analysis, XENON-1T, with about 2 ton of active mass set at LNGS and 279 days of data taking, set the most stringent limit in the spin-independent WIMP-nucleus elastic scattering above 6 GeV/c^2, down to 4.1×10^{-47} cm^2 at 30 GeV/c^2 [207]. In the next detector XENON-nT, with 5.9 ton of active mass and the exposure goal of 20t y, the expected sensitivity to spin-independent WIMP-nucleon interactions reaches a cross-section of 1.4×10^{-48} cm^2 for a 50 GeV/c^2 mass WIMP [208]. An interesting excess of electron recoils from the background model was found in the last XENON-1T analysis, with only 0.67 ton-year of exposure. The analysis focused on the low mass dark matter search, showing an extraordinary low expected background level, only $76 \pm 2_{stat}$ events/(tonne $\times$ year $\times$ keV) in the range 1 –30 keV, and was then mainly sensitive to bosonic dark matter, solar axions and measurements on the neutrino magnetic moment. The excess over the expected background was found below 7 keV, mainly prominent at 2 – 3 keV. If related to the discovery of solar axions or neutrino magnetic moment, this result would be in strong disagreement with astrophysics constraints. It was also shown that the observed signal can be produced through the Migdal effect: as the dark matter particle would eventually scatter on the noble liquid nucleus, the electron cloud does not catch up immediately, and this can bring to an excitation or ionization signal, which would enhance the detector sensitivity to light dark matter, in the GeV mass range [209] [210]. Still the most likely interpretation is that the excess is due to β decays of tritium, specifically to a tritium concentration

in Xenon of $(6.2 \pm 2.0) \times 10^{-25}$ mol/mol [211].

On the LAr side, DarkSide detectors are the leading representative of the physics potential in the dark matter search. The last dark matter searches were published in 2018 [212], with the data from DarkSide-50. The detector, set at LNGS, runs with about 50 kg of UAr as the active target, shielded by a boron scintillator veto for the neutron rejection, all contained in a cylindrical water tank. Thanks to the very high control on the background level, reached mainly thanks to the high power discrimination of electron recoils from nuclear recoils, the experiment set the most stringent limit in 2018 on WIMPs above 20 GeV/c^2 in 2018. In the same year, the collaboration set the best stringent limit for WIMP masses in the range (1.8 – 10) GeV/c^2; this was obtained by looking only at the S2 signals, which is amplified in the gas pocket. This result was a consequence of the high quality of calibrations of the S2 signals, for both nuclear and electron recoils, who pushed the energy threshold down to 0.6 keV for a nuclear recoil [213]. Even if shortly after beaten by DEAP-3600 exclusion limits on the high mass side and by SuperCDMS on the low mass side, DarkSide-50 results are still an extraordinary plot-twist in the direct detection of dark matter, as it pointed out that the quality of the analysis and the low background level in the ROI can make a small target mass competitive with tonne-scale detectors. This outstanding result brought to the design of the future tonne-scale dark matter detectors of the collaboration, DarkSide-20k and Argo, with 50 ton and 400 ton of Argon extracted from underground(UAr) as active masses, respectively. Other experiments based on liquid Argon recently joined the same project, giving rise to the Global Argon Dark Matter Collaboration (GADMC).

In summary the WIMP search has not come to an end yet. Nevertheless, the several detection technologies developed in the last two decades assure that any eventual discovery will count on an independent cross-check; at the same time, different technologies and strategies also imply different mass regions and WIMP interactions at which detectors are sensitive too, assuring a "complementarity" between dark matter detectors. Finally, when the detectors will reach the neutrino floor and then be sensitive to coherent scattering from atmospheric and solar neutrinos, there would be no way to discriminate them from a WIMP eventual signal, in terms of the energy spectrum. The only detection strategies available then will be based on the time dependence of Equation 2.3.8, so on the annual modulation of the WIMP rate or on the daily modulation of the WIMP incoming direction. The WIMP exclusion plot updated to July 2019 is shown in Figure 2.3.8, for the spin-independent interaction.

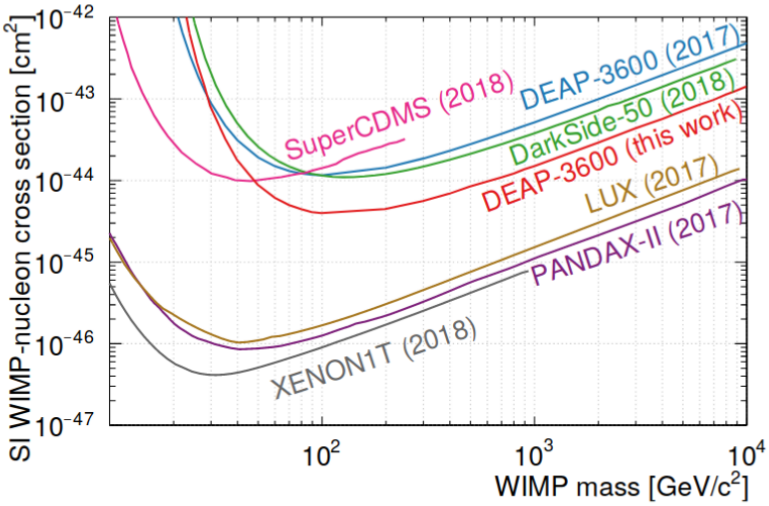

Figure 2.3.8: Updated exclusion plot in the WIMP mass- Spin-independent cross-section, only shown for the leading experiments [200].

3 Liquid Argon detectors

3.1 The case of Liquid Argon

The present chapter focuses on the dark matter direct detection in liquid argon, both in a single-phase and in a double phase detector. ^{40}Ar, compared to liquid Xenon, is a much lighter target; this implies that it is more sensitive to lower WIMP masses. It is liquid at 82.7 K below 0.4 bar, where it has a density of 1.4 g/cm^3. This temperature is close to that of liquid Nitrogen, which is indeed exploited for the cryogenic system. While Xe target is sensitive to both the spin-dependent and independent WIMP-nucleon cross-section, Argon can contribute only to the spin-independent interaction side. Furthermore, while liquid Xenon is intrinsically pure, liquid Argon presents a radioactive isotope,^{39}Ar, which β-decays with a Q-value of 565 keV. For the Argon taken from the atmosphere, the radioactivity is measured to be 0.9 Bq/kg. Looking for rare events implies as a first requirement the lowest background achievable; hence the Atmospheric Argon (AAr) was replaced with the argon peaked from underground (UAr), three order of magnitude more radiopure.
One of the greatest background rejection techniques ever developed for the dark matter direct detection is the Pulse Shape Discrimination, which allows for the rejection of most of electromagnetic background. This, as will be further explained later, is due to the electronic configuration of Argon. Finally, while the Xenon has limited production and indeed costs thousands of dollars per kilogram, the Argon costs a few dollars per kilogram, excluding the costs for the extraction from underground.

3.1.1 From Atmospheric to Underground Argon

The experience in DarkSide-50 experiment shows that the Argon extracted from underground (UAr) is three order of magnitude more radiopure than the one from the atmosphere (AAr), exploited in its first very run and whose activity was recently measured to be (1.01 $\pm$ 0.08) Bq/kg [214]. Hence the DarkSide Collaboration developed two projects, Urania and Aria, to extract and further purify the Argon, which will fulfil the DarkSide-20k and Argo TPCs.
The Urania project will extract and purify the UAr from the CO_2 wells at the Kinder Morgan Dow Canyon Facility in Cortez, Colorado. The foreseen maximum extraction rate is of 330 kg/day. The argon here was found to have a very low concentration of ^{39}Ar, below (1.4 $\pm$0.2)$\times$ 10^3 that of AAr. Once that it is extracted, the UAr is purged from the CO_2, the CH_4, the

N_2, the ^{85}Kr traces, thanks to three cryogenic distillation columns. The final product will be collected in a tank to check the purity level of the UAr, expected to be about 99.99 %. Then it will be sent at Aria plant, in Italy for further purification, thanks to appropriate cryogenic vessels shipped by boat, to minimize the cosmic rays flux in the UAr.
The Aria plant, in the south-west Sardinia, will perform the chemical purification of the UAr extracted in Urania plant. The purification will be performed in Seruci-I, a 350 tall distillation column, which will perform cryogenic distillation of Argon isotopes thanks to their tiny difference in volatility [215]. According to the present literature, the volatility of ^{39}Ar relative to ^{40}Ar is 1.0014 $\pm$ 0.0001, and this is constant at cryogenic temperatures, from 84 K to 100 K [216]. The foreseen UAr processing rate will be O(1 ton/day); this will remove all chemical impurities, including eventual traces of N_2, O_2 and ^{85}Kr left after Urania purification, with a separation power greater than 10^3 per cycle. Furthermore, Seruci-I will be able to provide further isotopic separation of UAr at a rate of 10 kg/day, with a ^{39}Ar depletion factor of 10 per pass. The method is now tested at Seruci-0 prototype column, where the first run was held in 2018, to measure the separation power between ^{28}N and ^{29}N.
Finally, before filling any dark matter detector, the radiopurity level of the UAr from Aria will be tested in DArT (Depletion Argon Test) [217] [218], a small single-phase radio-pure TPC with about 1 kg of active mass, set inside the ArDM active volume, so that the ArDM will work as active veto against internal and external radiation. According to Geant-4 based simulation, the foreseen measurement uncertainty will be of about 7 % in a week of running.

3.1.2 Scintillation process

In the present section the scintillation process in liquid Argon is described in detail. When a particle scatters on the argon atom, it will scatter either on the bound electron either on the nucleus, so giving an "electron recoil" or a "nuclear recoil" respectively. Electron recoils are performed by beta, gamma and muons; nuclear recoils are due to neutrons, αs and eventual WIMPs. A fraction k of the energy will be loss in heat, i.e. in the thermal motion of argon nuclei which are hit by the recoiling particle [219]. The left fraction goes into Argon ions Ar^+ and Argon excitons Ar^*, where the ratio α between excitons and ions is equal to about 0.21 for electron recoils and 1 for nuclear recoils [220]. Excitons have a valence electron in the first excited state, which can be shared with a ground state atom, giving a excited dimer or "excimer", in a timescale of a few picoseconds. This process is called "exciton self trapping", and give a metastable state, which decays and releases a UV photon at 128

nm,

$$\begin{aligned} Ar^* + Ar &\rightarrow Ar_2^* \\ Ar_2^* &\rightarrow Ar_2 + h\nu. \end{aligned} \tag{3.1.1}$$

Argon ions, on the other hand, may bound into a charged dimer Ar_2^+ with a ground state atom, by sharing its valence electron. This ion dimer can then capture a free electron, giving an exciton Ar^{**} and a ground state atom. After de-exciting through a vibrational mode, so non radiatively, the exciton finally relaxes via exciton self-trapping [220],

$$\begin{aligned} Ar^+ + Ar &\rightarrow Ar_2^+ \\ Ar_2^+ + e^- &\rightarrow Ar^{**} + .Ar \\ Ar^{**} &\rightarrow Ar^* + phonons \\ Ar^* + Ar &\rightarrow Ar_2^* \\ Ar_2^* &\rightarrow Ar_2 + h\nu. \end{aligned} \tag{3.1.2}$$

This process is called "recombination". In absence of any applied potential, the recombination probability is close to one, so every freed electron is captured by argon ions, as in single-phase liquid argon detectors. If a drift potential is applied, as in TPCs, the recombination probability decreases with the increase of the electric field [221]. In total, the number of scintillation photons released is the sum of the produced excitons and of the fraction of ions which recombines [222],

$$N_{S1} = N_{ex} + r(E_{rec})N_{ions} \tag{3.1.3}$$

where the number of visible quanta $N_{dep} = N_{ex} + N_{ions}$ is the ratio of the recoil energy, E_{rec}, and the work function W, equal to 19.5 eV in LAr [220],

$$N_{dep} = \frac{E_{rec}}{W}. \tag{3.1.4}$$

The recombination probability r dependence from the recoil energy was optimized by the comparison of the Monte Carlo simulation with DarkSide-50 data, for a drift field of 200 V/cm. The fit function is

$$r(E_{rec}) = erf(E/p_1)(p_2 \times e^{-\frac{E}{p_3}} + p_4). \tag{3.1.5}$$

$r(E_{rec})$ was optimized for the parameters p_1= 3.77,p_2 = 0.277,p_3= 113, and p_4= 0.665, as shown Figure 3.1.1.

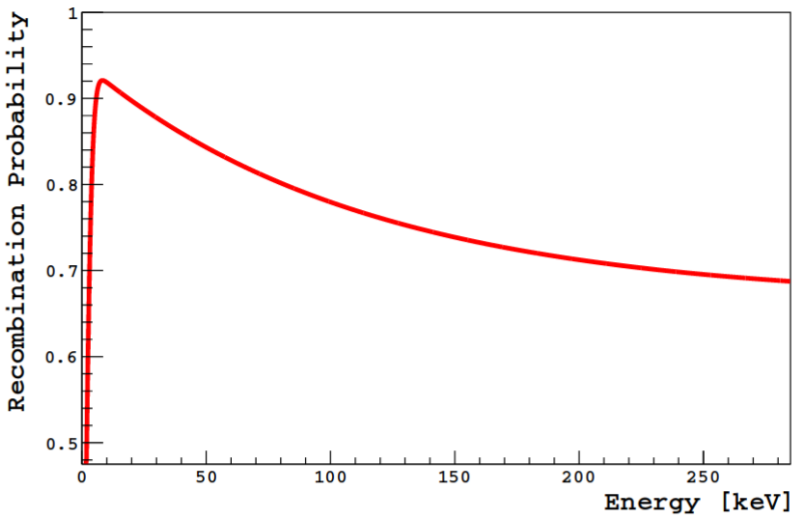

Figure 3.1.1: Recombination probability in liquid argon, for a drift field of 200 V/cm [223].

Finally the S1 light is given in photoelectrons (PE), the number of electrons produced in the hit photosensor by photoelectric effect,

$$S1 = g_1 \cdot N_{S1}. \tag{3.1.6}$$

In DarkSide-50 the photosensors were Photomultipliers tubes (PMTs) with a collection efficiency g_1 of 0.157 ± 0.001. This determined a scintillation light yield with a drift potential of 200 V/cm of about 6 PE/keV above 100 keV of recoil energy, with a peak at $\approx$ 15 keV of 7.6 PE/keV, where the energy dependence is determined by that of the recombination probability.

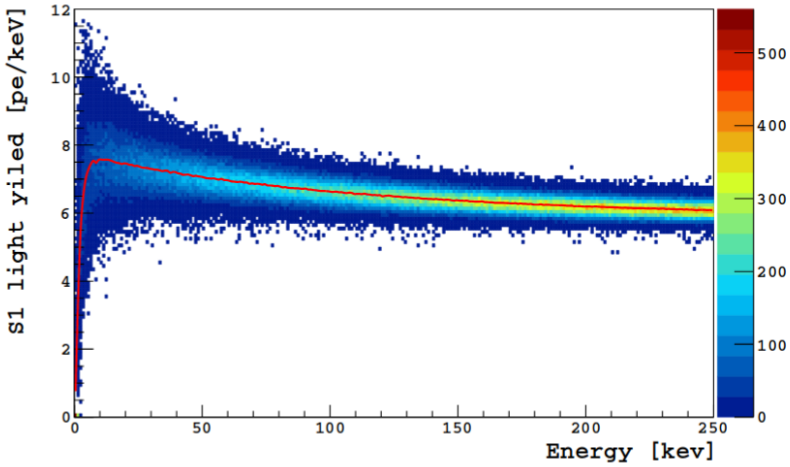

Figure 3.1.2: Mean light yield (in red) from DarkSide-50 data. On average the light yield was measured to be 6 PE/keV with a drift potential of 200 V/cm, with a peak below 30 keV up to 7.5 PE/keV [222]

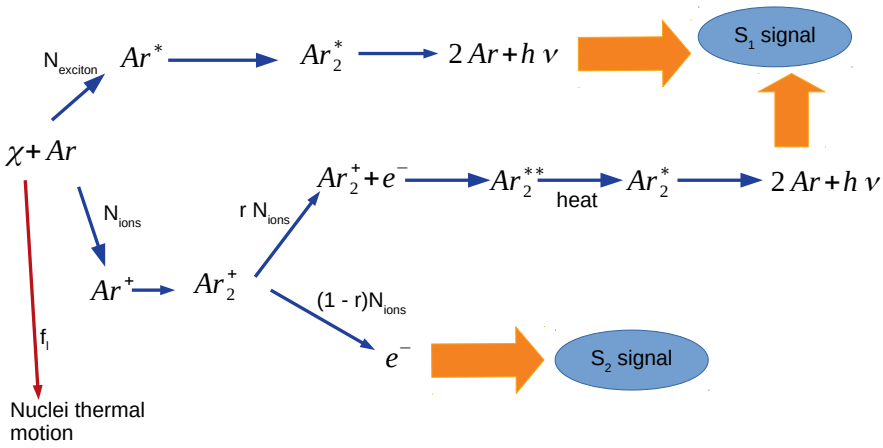

Figure 3.1.3: Scheme of the origins of the signals due to a particle scattering on liquid argon. The fraction f_L of the recoil energy goes in thermal motion. The left energy may excite or ionize argon atoms. In the first case, it will bound in a quite unstable excimer, which may be either in a triplet or a singlet state, according to the spin configuration. Whatever the case, a photon peaked at 128 nm is released. The ions also can recombine with electrons, bringing to a very excited argon dimer, which first decays vibrationally and only then radially, again either from a triplet or a singlet configuration. Both processes - exciton self-trapping and recombination- contribute to the S1 signal, both in a single and in a double phase liquid argon detector. Finally ions which do not recombine also correspond to electrons which are not captured. In a double phase chamber a drift field is applied to collect them and produce the S2 signal in the gas pocket.

Whatever is the process that brings to the excimer Ar_2^*, four molecular excited states are available. In fact, the "core" of each Argon atom and the valence electron in the excited shell behave as a Rydberg state, both with a 1/2 spin. Then the sum of the two atoms can give rise either to a singlet state either to a triplet state,

$$\begin{array}{ll} \frac{1}{\sqrt{2}}\left(|\uparrow\downarrow\rangle - |\downarrow\uparrow\rangle\right) & \textit{Singlet State} \\ \left.\begin{array}{l} |\uparrow\uparrow\rangle \\ \frac{1}{\sqrt{2}}\left(|\uparrow\downarrow\rangle + |\downarrow\uparrow\rangle\right) \\ |\downarrow\downarrow\rangle \end{array}\right\} & \textit{Triplet State} \end{array} \tag{3.1.7}$$

The two states are spectroscopically equivalent, with an emission peak at 128 nm, but show to have a quite different time decay in liquid argon. Indeed the singlet state as well as the ground state has spin equal to zero, so the transition is allowed at dipole approximation and happens in 6 ns on average; the transition from the triplet state is instead forbidden, and then its time decay is three order of magnitude larger, about 1.5 μs [224]. Both channels can excite the singlet or the triplet state with the same likelihood. Neverthless it is observed that at high ionization density some collision processes can suppress the exciton-self trapping and then reduce the number of released photons [219]. The main ones are:

$$\begin{aligned} \textit{Penning collision: } Ar_2^* + Ar_2^* &\rightarrow 2Ar + Ar_2^+ + e^- \\ \textit{Biexcitonic collision: } Ar^* + Ar^* &\rightarrow Ar + Ar^+ + e^- \\ \textit{Photoionization: } Ar^* + Ar_2^* &\rightarrow Ar + Ar_2^+ + e^- \end{aligned} \tag{3.1.8}$$

These processes depend on the density of the ions after the recoil and, together with the recoil energy given to nuclei thermal motion, constitute the total energy loss in a recoil in liquid argon and, more generally, in any noble liquid. For both the contributions, it was observed that the energy loss is negligible for electron recoils, differently from nuclear recoils. Indeed the relative scintillation yield - defined as the ratio between the visible light from a nuclear and from an electron recoil at the same energy- is a good estimation of the nuclear scintillation efficiency L_{eff}, or "Monte Carlog factor", which is the ratio of the visible energy on the recoil energy,

$$L_{eff} = E_R^{vis}/E_R. \tag{3.1.9}$$

The contribution due to the length of the recoil track was widely investigated by Lindhard [225], while the ionization density dependence, which sums the contributions from processes in Equations 3.1.8 is fully described by Birk's law to noble liquids [226]. The two models found a good agreement with Mei's model, which is up to today the most reliable model for the quenching in noble liquids [219].

When an argon recoils after a particle scattering, it releases energy along its recoil track. Its energy loss is due to both excitation/ionization of electrons and translational motion of atoms. The first contribution is called electronic stopping power, and gives the full amount of visible light. The thermal motion, on the other hand, goes into internal excitation and hence is not detected; this is usually tagged as "nuclear stopping power". The total

stopping power is then

$$\left(\frac{dE}{dx}\right)_{tot} = \left(\frac{dE}{dx}\right)_{el} + \left(\frac{dE}{dx}\right)_{nuc}. \tag{3.1.10}$$

As only the first term gives the visible contribution, the fraction f_n returns the reduction factor of the visible light due to the thermal motion,

$$f_n(E_R) = \frac{\int_0^{E_R} \left(\frac{dE}{dx}\right)_{el} dE}{\int_0^{E_R} \left(\frac{dE}{dx}\right)_{el} dE + \int_0^{E_R} \left(\frac{dE}{dx}\right)_{nuc} dE} \tag{3.1.11}$$

An alternative way to show f_n is given by Lindhard et al. [225], in terms of the reduced energy $\varepsilon = 11.5\ \mathrm{E}_R(\mathrm{keV})\ \mathrm{Z}^{-7/3}$, for a noble liquid with Z electrons and mass number A,

$$f_n = \frac{kg(\varepsilon)}{1 + kg(\varepsilon)}, \tag{3.1.12}$$

where $\mathrm{k} = 0.133\ \mathrm{Z}^{2/3}\ \mathrm{A}^{-1/2}$ and $\mathrm{g}(\varepsilon) = 3\ \varepsilon^{0.15} + 0.7\ \varepsilon^{0.6} + \varepsilon$. This factor in the wider Mei's model resumes all the dependence of the quenching factor by the length of the recoil track, as heritated from Lindhard model [219].

The dependence of the scintillation efficiency on the ionization density is described by the Doke-Birks model. The relation between the electron stopping power and the ion density is expected to not be linear. In fact, on one side the number of excitons increases with the likelihood of being trapped and give excimers and hence is proportional to the ionization density. On the other side, the biexitonic quenching and the Penning collision are proportional to the density of free excitons produced and hence, to the ionization density itself. Hence the production of excitons determines a saturation of the specific fluorescence dS/dx, which is harder as the collision exciton probability k increases,

$$\frac{dS}{dx} = \frac{A\frac{dE}{dx}}{1 + kB\frac{dE}{dx}}. \tag{3.1.13}$$

where A and B can be determined experimentally. It follows that the fraction of scintillation light which survives to the suppression due to ionization density is

$$f_l = \frac{1}{1 + kB\frac{dE}{dx}}. \tag{3.1.14}$$

kB was measured for liquid argon to be 7.4×10^{-4} MeV^{-1} g cm^{-2} [227]. Since the two contributions are independent of each other, the total scintillation efficiency is written as

$$L_{eff} = f_n \cdot f_l. \tag{3.1.15}$$

The contribution of the saturation law allowed for a better agreement with experimental data in [228] [229] [230]; this agreement made the Mei interpolation as the best model describing the quenching in noble liquids.
In DarkSide-50 experiment a measurement on the scintillation efficiency was performed, by comparing the scintillation light from an Americium-Berillium (^{241}Am^{9}Be) source with a Geant-4 based simulation custom-developed for the detector, called G4DS. The Americium-Berillium is a neutron source, also releasing gammas at 4.4 MeV (97 % BR) and a 3.2 MeV plus a 4.4 MeV gammas (3 % BR). A cut on f_{90} allowed for the selection of the nuclear recoils only, whose S1 signal was then compared with the expectations from both Lindhard model and Mei model, both integrated into G4DS simulation. It was found that both were in tension with the dataset above 550 PE, about 90 keV. Hence, the kB factor from Birk's saturation law was freed. The fit converges at kB= $4.66^{+0.86}_{0.94} \times 10^{-4}$ MeV^{-1} g cm^{-2}. This modified-Mei model was then implemented in G4DS as quenching model in liquid argon. The comparison with the Lindhard and the original Mei model is shown in Figure 3.1.4, together with measurements from the literature.

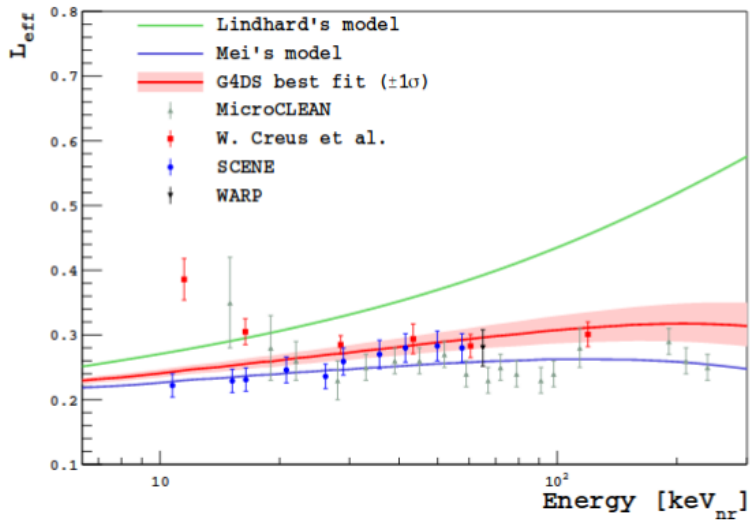

Figure 3.1.4: Comparison between the Lindhard model, the Mei model, the modified-Mei model developed from DarkSide collaboration with the experimental data from SCENE [231], MicroCLEAN [232], W.Creus et al. [233] and WARP [234]. Beside MicroCLEAN and W.Creus at al. at low energy, the modified-Mei model shows agreement with the measurements available in the literature and is now the favourite effective quenching model in liquid argon.

The essential contribution of the Birk's saturation law is clear from the disagreement of Lindhard's model with data. The modified Mei-model shows the best agreement with both WARP and SCENE measurements and also with W.Creus et al. above 20 keV. Further confirmation of this effective G4DS fit went from ARIS measurements [235]. Equation 3.1.9 implies that only a fraction of the recoil energy from a nuclear recoil will be detected, while the loss for an electron recoil is negligible. Hence, to be able to compare the two recoils, the notations keV$_{nr}$ and keV$_{ee}$ are introduced to refer respectively to the recoil energy released in a nuclear recoil and its "electron equivalent", the recoil energy an electron recoil would have to return the same amount of visible energy,

$$E_{rec}[keV_{ee}] = L_{eff} E_{rec}[keV_{nr}]. \tag{3.1.16}$$

Processes in Equation 3.1.8 mainly suppress the triplet state excimers, which has a much longer time decay respect to singlet states; furthermore, they are proportional to the ionization density of the projectile particle, so it increases with the particle stopping power. Since nuclear recoils have higher stopping power, triplet states are widely suppressed in recoils due to WIMPs

or neutrons. This means that the scintillation light from a nuclear recoil is mainly due to the deexcitation of singlet states. The effect is further enhanced by the higher exciton to ion ratio in nuclear recoil, compared to electron recoils.
The scintillation pulse will result to be much faster in nuclear recoils, due to the quick time decay of Argon excimer's singlet state. Hence the fraction of the prompt light will help for the discrimination of nuclear recoils from electron recoils, i.e. the rejection of electromagnetic background in the WIMP search. This rejection technique is called Pulse Shape Discrimination (PSD), and the related optimized parameter in DarkSide-50 is the f90, the fraction of the scintillation light in the first 90 ns. In DEAP-3600 the rejection power of electron recoils at 15 keV, with a scintillation yield of 8 PE/keV and at null drift field, is 1×10^{10}, as projected from the measurements performed in [236]. This means that only one electron recoils after at least 10^{10} is mismatched as a nuclear recoil, and is not rejected [237]. The PSD power slightly decreases when the drift potential is turned on, as the recombination probability decreases and then the exciton to ion ratio slightly decreases for nuclear recoils. In DarkSide-50, at 200 V/cm, the selection cut at 90 % of WIMP acceptance with f90 parameter was measured to have a discrimination power $> 1.5 \times 10^7$ for ^{39}Ar decays in the 8.6 -65.6 keV energy range [224].

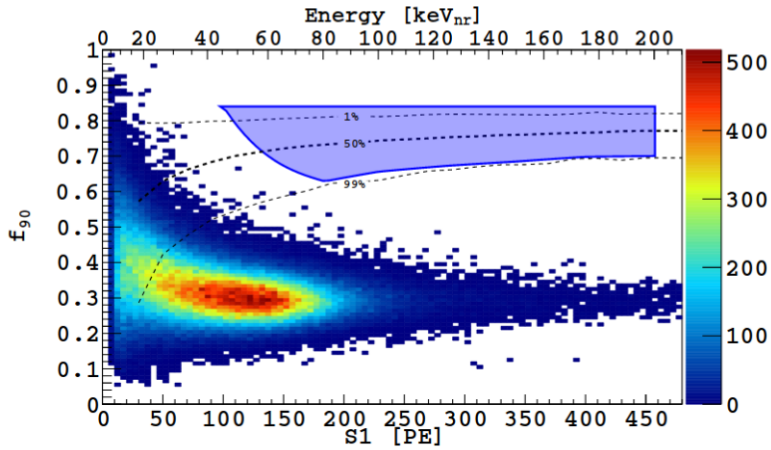

Figure 3.1.5: Distribution of the f90 parameter versus S1, in 532 days of data taking in DarkSide-50 [212]. Events at $f_{90} = 0.3$ are electron recoils, hence scattering events from γs or βs. The main contribution comes from ^{39}Ar β decays. At $f_{90} = 0.7$ nuclear recoils are expected, as they have a higher singlet state likelihood and then a faster scintillation signal. Nuclear recoils are neutrons and eventually WIMPs, which are specifically expected in the blue area. The three dotted lines show the f90 cuts at which 1 %, 50 % and 99% of the WIMPs would "survive", i.e. of WIMP acceptance, obtained thanks to calibrations with the neutron AmBe source.

3.1.3 Electroluminescence in Gas Argon

Single Phase detectors based on Liquid Argon only look at the scintillation light and operate without any drift field. In these conditions, the recombination probability is close to 1, so essentially all the visible energy is released via the S1 light. One example of a LAr single-phase detector is DEAP-3600, which will be fully described in the next section.
If a drift field is applied, up to a gas pocket above the liquid argon phase, also an S2 signal will be available. A grid set at a potential of O(kV/cm) extracts electrons from the liquid phase to the gas phase, where a slightly higher potential accelerates them. Accelerated electrons excite gas argon atoms, who release light according to the analogue of the exciton-self trapping process in gas argon, called electroluminescence.
S2 signal is proportional to the number of electrons which do not recombine in the liquid argon, and that reach the gas pocket,

$$S_2 = g_2 Y_{S2}(1 - r(E_{rec}))N_{ions} \tag{3.1.17}$$

where g_2 is the collection efficiency for a photon generated in the gas pocket, which was measured to be 0.163 in DarkSide-50, while Y_{S2} is the electroluminescence yield, which returns 273 photons per drifted electrons on average [222]. This will result in a S_2 light yield of 23 PE/e- [213].
The signal is much slower than the scintillation pulse in liquid argon, lasting about 3.4 μs [238]. Hence the S2 signal can be identified by looking for pulses with a very low f90, smaller than 0.15 [213]. In the standard WIMP analysis, the S_1 light allows for the rejection of the electromagnetic background. This, together with the radio-pure level achieved allowed DarkSide-50 experiment to put the strongest WIMP exclusion limit above 20 GeV/c^2 in Liquid Argon in 2018 [212].
On the other hand, the enhancement of the S_2 signals respect to the S_1 signal means that at very low energy the S_1 pulse may not be detectable, while S_2 actually is. In DarkSide-50 the S1 trigger asks for 2 or more PMTs seeing at least 0.6 PE within 100 ns; specifically below 10 keV$_{nr}$ this trigger may fail. Hence a dark matter search of low mass WIMPs was performed by triggering on the S_2 signal. Even if the PSD is not available, the very low background level reached and the very high quality of the calibration performed at low energy allowed to search for WIMPs down to 0.6 keV$_{nr}$, setting the world strongest exclusion limit in the WIMP mass range 1.8 –10 GeV/c^2 [238]. The same low mass approach allowed for the sensitivity study on supernova neutrinos described in Chapter 6. The favourite energy variable for S_2 both in the low mass analysis and the core-collapse supernova neutrinos is the number of drifted electrons N_{e-}, to which the S2 signal is just proportional, giving on average 23 PE for each drifted electron.

3.2 DEAP-3600

DEAP-3600 is an example of a single-phase dark matter detector based on liquid argon. It has an active mass of 3287 kg of Atmospheric Argon, so it counts on the largest mass target among the running detectors filled with liquid argon. In the present section a full description of the detector, shown in Figure 3.2.1, is given.
The cryostat is an acrylic vessel (AV) sphere with a radius of 85 cm and 5 cm of thickness. It can contain up to 3600 kg of Liquid Argon. The LAr is observed by 255 8-inch-diameter Hamamatsu R5912-HQE high quantum efficiency (HQE) Photomultipliers Tubes (PMTs), coupled to the vessel through acrylic Light guides (LGs), each 45 cm long. The space between the LGs is filled with filler blocks (FBs), made of layers of high-density polyethene and polystyrene. The inner AV surface is coated with a 3 μm thick layer of the organic wavelength shifter 1,1,4,4-tetraphenyl-1,3-butadiene (TPB,$C_{28}H_{22}$),

deposited in situ [239].
The inner detector is contained in a stainless steel pressure vessel, a sphere with a cylindrical neck on the top, which allows access to the inner detector volume. The neck is made of stainless steel and acrylic and contains a cooling coil which uses Liquid Nitrogen (LN_2) to cool the LAr. A glove box at the top of the neck allows for operations in the detector in a radon-free environment.
The outer vessel is immersed in a 7.8 m diameter shield tank filled with ultrapure water and instrumented with 48 Hamamatsu R1408 PMTs, all working as active muon veto.
The detector design and the components were chosen to minimize the backgrounds. These include:
(i) electromagnetic recoils, mainly the beta decays from ^{39}Ar;
(ii) nuclear recoil events induced from radon (^{222}Rn and ^{220}Rn) and progeny (^{210} Po, ^{212} Po, ^{214} Po, ^{216} Po)
(iii) nuclear recoil events from radiogenic and cosmogenic fast neutrons.
The AV is filled with about 3.3 tons of Atmospheric Argon. The measured activity is 0.9 Bq/kg, from the β decays from ^{39}Ar, up to 565 KeV. The rejection is performed via PSD, with a projected discrimination power of 10^{-10} for DEAP-3600. Furthermore, the choice to set the High Quantum Efficiency PMTs coupled to the vessel via the LGs allows for a very high light collection and low electronic noise: both are fundamental to achieve a good PSD.
Nuclear recoils due to αs from Radon (Rn) decay chain are too energetic to fall in the WIMP ROI. However, if they occur in the neck only a fraction of the scintillation light will be measured. Radon daughters can also bound to the TPB and return a surface α events. The mitigation strategy is mainly based on the control of exposure to lab air during production of components, surface treatment after construction, cryogenic purification of the argon. Radon (^{222}Rn and ^{220}Rn) and progeny in the LAr target itself are reduced by carefully selecting materials for their low radioactivity. The main sources are the inner surface acrylic vessel and the TPB layer, where αs release most of their energy, O(1) MeV, so that only a small fraction of O(10) keV reaches the detector photosensors.

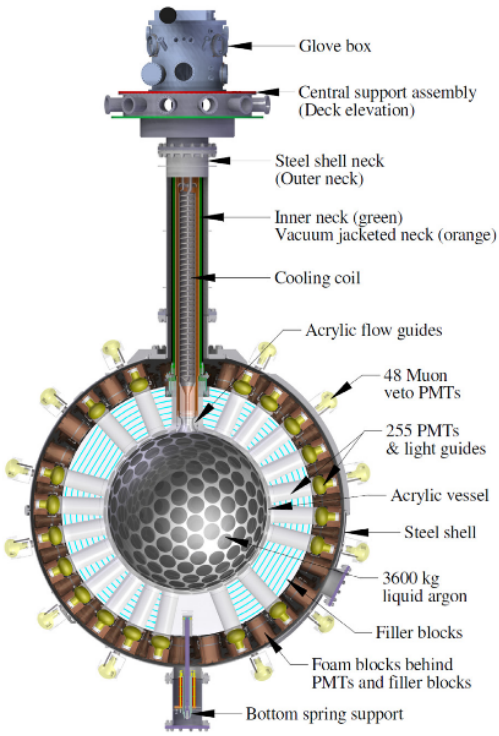

Figure 3.2.1: DEAP-3600 detector design showing the inner vessel, the LGs, the PMTs and the filler blocks, out to the stainless steel outer vessel, together with its neck. The representation does not shown the TPB coating and the ultra-pure water veto, in which the outer vessel is immersed [196].

The acrylic for the cryostat was chosen, produced and assembled to minimize the exposure of the acrylic precursors to radon and other contaminants. Still, the final assembly steps were performed underground at SNOLAB, where the ^{222}Rn level is approximately 130 Bq/m^3 . The main rejection of the left α background is finally performed via volume fiducialization. To reach a background level of less than 0.2 events/ year, a rejection of 10^3 αs must be achieved.
Also radiogenic neutrons with a few MeV kinetic energy can fall in the WIMP ROI. The mitigation is mainly performed by the choice of radiopure materials to reduce their production rate and with hydrogenous shielding, like the acrylic, to thermalize those that are produced near the LAr. The primary source is the borosilicate PMT glass which is moderated by the acrylic LGs and polyethene filler blocks. Cosmogenic neutrons from the rock wall at SNOLAB are also passively-shielded by the water tank.
In addition to this, the water tank is an active shield for muons, who release Cherenkov light in the ultra-pure water. In the WIMP search cosmic ray

muons, with a flux of 0.27 m^{-2} day^{-1} [240], are tagged with an efficiency above 80 %, in order to reach the targeted 0.2 background events in 3 years of exposure

3.2.1 The inner detector

The inner detector is composed of all the elements from the LAr out to the steel shell, as shown in Figure 3.2.2.
The LAr is contained in the acrylic vessel. It was built in three pieces - the neck, the collar and the truncated sphere- due to the limited envelope of the mine-shaft leading underground. The average vessel radius is 846 mm when cold and 7 mm larger at room temperature. The neck, with an inner diameter of 255 mm, is designed to provide mechanical support of the AV from above and access for the purification system cooling coil. The acrylic used to construct the AV was also employed for the flow guide assembly. These were milled at the University of Alberta in a controlled room with a radon level of 0.3 mBq/m^3.

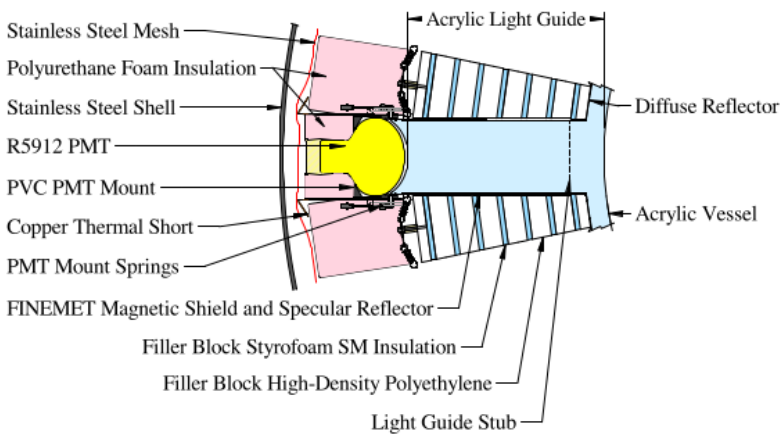

Figure 3.2.2: Cross-section of the inner detector, from the acrylic vessel to the stainless steel shell. The light from the LAr is brought by the acrylic light guide to the PMT, which is thermally isolated. Filler blocks help with thermal gradient between the photosensors and the inner vessel, together with the passive neutron suppression [196].

The Light guides connect each PMT to the LAr. They are 45 cm long and 19 cm of diameter, for a total AV coverage of 76 %. Although about 80 % of photons emitted in the LAr are trapped in the LGs by total internal reflection, an additional specular reflector is loosely wrapped around the

LGs, to increase light collection and allow for optical isolation between LGs. The specular reflector is a 50 μm mylar foil sputter-coated with 100 nm of aluminium, using a 99.999 % high purity target, to satisfy the radiopurity requirements for dark matter search.
The inner vessel surface between LGs are covered with a 98 % reflective white Tyvek base layer, followed by a layer of black Tyvek and finally a layer of polyethene foam backing. These layers optimize the light collection and reduce the leakage of photons produced outside the active volume into the LAr volume. The layers of the inner vessel are shown in Figure 3.2.3 during their installation.

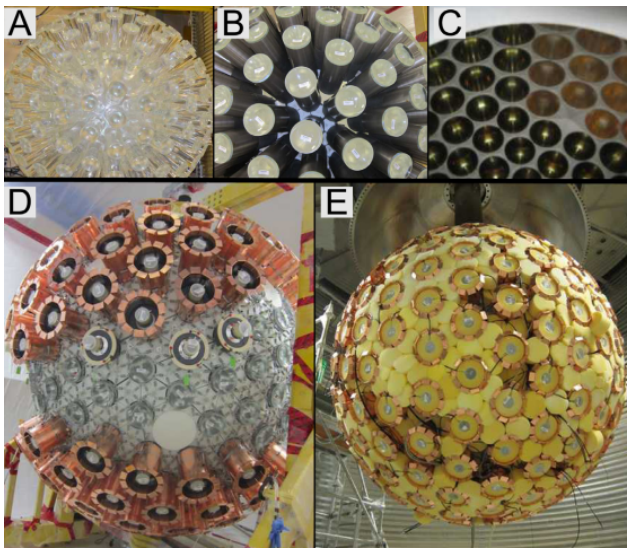

Figure 3.2.3: Assemblying of the inner detector. In (A) the acrylic vessel was connected to the light guides, to which in (B) reflectors and magnetic shielding was applied. In (C) the view from the inside of the inner vessel is given, to show the Tyvek (white) and the PMT installing. The installation of the filler blocks is shown in its preliminary stage in (D) and completed in (E) [196].

The photodetection in the inner detector is performed by 255 Hamamatsu R5912 8-inch-diameter HQE PMTs. These PMTs are characterized by a high photon detection efficiency, with a nominal value of 32 %, low dark noise rate and good time resolution. They operate at bias voltages between 1.5 kV and 1.9 kV. The single photoelectron response (SER) was determined in situ and returns an average charge of 9.39 pC with an RMS among all the PMTs of 0.16 pC. The dark noise at room temperature has a mean of 5.80 kHz and an RMS of 0.78 kHz. At about 270 K, just after the cooldown, quite close

to the PMT operating temperature, the dark noise has a mean of 0.24 kHz and an RMS of 0.06 kHz. A in situ measurement of the dark noise rate at the true operating conditions, when the vessel is filled with LAr, is impeded by the high radioactivity from Atmospheric Argon. PMTs show also a correlated noise, the afterpulses, due to residual gas in the vacuum tube which is ionized by accelerated electrons. The mean probability is measured to be 7.1 % and a RMS of 1.8 % [196].

3.2.2 Cryogenic system

The cryogenic system is composed by a liquid Nitrogen (LN_2) cooling system and a LAr purification loop. The cooling coil, shown in Figure 3.2.1, is filled with LN_2 , to keep the LAr between a temperature of 84-87 K and a pressure of 13-15 psia.
A 3750-L storage dewar located above the detector, in the Cube Hall staging area, injects the LN_2 in the cooling coil. Then boil-off nitrogen gas is returned to the dewar, where it is recondensed by three 1-kW Stirling Cryogenics SPC-1 cryocoolers. During operations, only two of them are operated, while the third one is kept for backup. Temperature and pressure readings are taken under control through an Emerson DeltaV slow control system, which also allows for valve automation, emergency shut-sown and isolation of critical components.
The cooling coils are composed of two helices: the outer one, with a 5.50-inch diameter, 35 turns at 3.34-inch pitch; the inner one, 84 inch long and with a diameter of 0.75 inch. It is designed to provide up to 1 kW of cooling, even when fully submersed in LAr. The LN_2 is delivered to the coil bottom through a vacuum-jacketed supply line passing through the centre of the helix. This supply line curls upwards at the bottom, transitioning into the return helix, forcing a convective two-phase flow heat transfer. At the bottom of the cooling coil flow guides (FGs) help for the convective motion of the LAr, blocking photons due to scintillations in the LAr filling the neck.
The cryogenic system is designed to purify the argon target to sub-ppb levels of electromagnetic impurities - namely CO, CO_2, H_2, H_2O, N_2 and O_2, CH_4 - and to reduce the radon level down to 5 μBq. The main components are shown in the diagram in Figure 3.2.4: the process pump, SAES getter, radon trap, condenser column, boiler. The system is designed for a nominal flow rate of 4.9 g/s of argon and has in input argon gas at 300 K coming from the bulk of liquid storage tank.

The first stage is the KNF Neuberget 150.1.2.1.2 double diaphragm process pump, which receives in input the argon gas and maintains a forward

pressure of 30 psi at the top of the system. The double diaphragm is an extra barrier between the lab air and the gas in case of a pump failure; also, it keeps monitored the pressure between the two diaphragms. The chemical purification is then performed by the SAES Mega-Torr PS5 MGT15 hot metal getter, custom-developed for DEAP-3600 to avoid components with thoriated welds. It is designed to accept high parity gas argon, at 99.999 % level, at a maximum flow rate of 7.4 g/s. A safety interlock system prevents overheating and the ignition of gas argon below the needed purity level. Radon and radioactive impurities are instead removed by absorption in a custom-built charcoal-trap, designed to take in input gas at 300 K from the getter, pre-cool it to 100 K and then send it to a charcoal column.

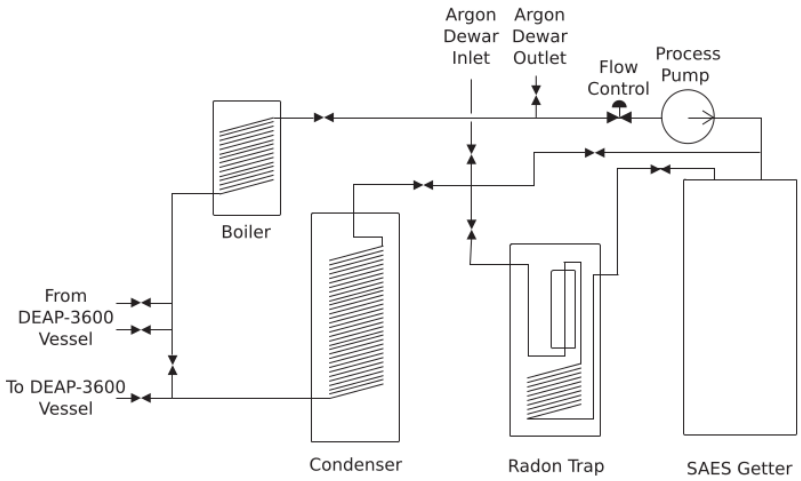

Figure 3.2.4: Flow diagram of the cryogenic system in DEAP-3600. The argon gas is first injected in the loop via a flow control valve and a double diaphragm process pump. Then the argon is chemically purged in the SAES getter and then radon-purified in the radon trap. The condenser liquefies the argon from the radon trap to the inner vessel, while the gas argon is delivered to the boiler. Finally, the liquid argon from the vessel is also delivered to the boiler, where it is recirculated in the cryogenic loop [196].

The trap is placed between the detector and the active purification system, to minimize the probability of mixing between the radon eventually released from the purification system itself and the LAr. The trap performances are optimized at low temperature, but also argon needs to be kept in the gas phase; hence the inlet is surrounded by a copper block partially immersed in LN_2, equipped with tunable cartridge heaters, to prevent argon freezing. The charcoal cartridge is a cylinder with 12-inch height and

3-inch diameter, filled with 610 g of Saratech charcoal, with very low radon releasing. The charcoal is contained in stainless steel wool and 50 μm VCR filter gaskets, one at the top and one at the bottom, to prevent the release of particulates. The cartridge is surrounded by a bake-out heater. The whole radon trap is inserted in an 8-inch-diameter cylinder, insulated by a multi-layer foil, and finally housed within a 10-inch vacuum space.
The custom condenser column liquefies gas coming from the radon trap and then delivers it to the detector. The condenser is composed by a stainless steel coil, which is a 39-ft long, 0.5-inch-outer diameter stainless steel tube, contained in an 8-inch-diameter cylinder and immersed in LN_2 . Either liquid or gaseous argon can be delivered to the AV. In the current configuration, with gas in the detector neck, gas is returned to the boiler inlet. To avoid direct exposure of the heating elements to the argon, the vaporization of the LAr is performed by a 1.5- kW heater coiled around the stainless steel flow line returning from the AV. Gas released by the boiler goes through the flow control valve into the KNF pump at the top of the loop.
The cryogenic system is operated in three main configurations:

- Filling mode. The gas is constantly drawn from the storage, purified, and injected into the detector. The gas can both be liquefied before reaching the AV or being injected as gas and then liquefied by the cooling coil. The maximum injection rate is between 4.9 g/s.

- Recirculation. After filling or during data taking breaks, the gas argon is recirculated, purified and liquefied.

- Storage recirculation. Purified gas in output from the radon trap bypass the detector and is stored in a 3750-L dewar. This is the default mode of the cryogenic system.

According to the original design of the detector, the LAr should have filled the whole AV and the neck, for a total active volume of 3.6 tons. Unfortunately during the filling of the detector, due to a leak at the connection between the process flange and the inner vacuum-jacketed neck, LAr entered the space between the inner acrylic neck and the outer vacuum jacket, filling equally this space and the inner neck. Hence it got in touch with the acrylic. The acrylic is sealed with 2 butyl-O-rings and an additional cryogenic seal, designed to contract and steal when slowly cooled. But on 17 August 2016, the sudden cooling due to the direct contact with LAr determined the failure of the butyl seals: clean, radon-scrubbed LN_2, in circulation to purge the steel shell volume, could then enter the AV, mixing with the LAr in it. This determined a sharp decrease in the observed long time constant for argon

scintillation and a spike of the pressure in the AV. This incident required to fully boil the LAr volume. After having fixed the leakage, clean gas argon was injected and liquefied in the AV. To minimize the probability of LAr reaching the butyl seals again, the LAr level is set at 771 mm from the centre, leaving gas argon in the neck and in the top of the AV. A final level of 3.3 tons of LAr was chosen and kept since completing the second fill in November 2016.

3.2.3 Electronics

The whole structure of the Data Acquisition (DAQ) system is shown in Figure 3.2.5. The signals from PMTs are sent to the Digital trigger module (DTM), which decides whether the event has to be triggered or not. Triggered signals are then sent to two different models of digitizers, CAEN V1720s and CAEN V1740. The digitized waveform is then read, filtered and written in the disk. The DAQ takes as input the signal from the three photodetection systems:

- the 255 PMTs looking at the inner veto;
- the 48 Hamamatsu R1408 8-inch PMTs in the muon veto;
- the 4 Hamamatsu R7600-300 PMTs looking at the events in the neck, and so composing the neck veto.

The PMTs are supplied by a WIENER MPOD crate with ISEG high voltage modules via 27 custom Signal Conditioning Boards (SCBs). Each SCBs read the signal from 12 PMTs. 22 SCBs are dedicated to inner detector PMTs, 4 to the muon veto PMTs, 1 to the neck veto PMTs. The foot of the PMT terminates with a 4.7 nF capacitor, put in series with a 75 Ω resistor, and are connected to the SCBs by cables with 75 Ω impedance and 20 meters of length.
Each SCB has 12 identical channels, in which waveforms from PMTs are shaped and amplified. Each channel has three outputs:

- the high gain channels, designed to achieve a high signal to noise ratio for single photoelectrons and to shape the pulse to better match the V1720 digitizer, at 250 MS/s of sampling rate
- the low gain channels, designed for pulses which would saturate the high gain channel; it shapes the signals to be wider, to better match the V170 digitizers, at a sampling rate of 62.5 MS/s
- the summing channels are added to create an analogue sum (ASUM) for each SCB. The shaping and the gain are similar to that of low gain channels, but matching the 45 MS/s of the ADC on the DTM.

Together with the inputs from the PMTs each SCB receives a "test pulse". The test pulse is produced by the DTM and is sent to all 12 channels, with a 0.2 ns of delay between the channels. This allows for the extraction of the timing offsets between different digitizer channels.
In the detector, two different digitizers are employed, according to the required gain. The high gain CAEN V1720 has a sampling rate of 250 MS/s, 8 channels at 12 bits, connected to high gain SCBs with MCX cables. V1720s can store data either as full waveforms or in Zero Length Encoding (ZLE). The ZLE algorithm records data only if a minimum number of samples drops below a threshold ADC value. Considering that in these digitizers the noise level is ≈ 1.2 ADC, and the typical SPE pulse is 50 ADC, an ADC threshold of 5 ADC below the baseline of 3900 ADC is set. The low gain CAEN V1740 waveform digitizers have a sampling rate of 62.5 MS/s, 64 channels at 12 bits, and are connected to the SCBs through MCX cables. These digitizers do not allow for ZLE recording but only for full-waveform mode.

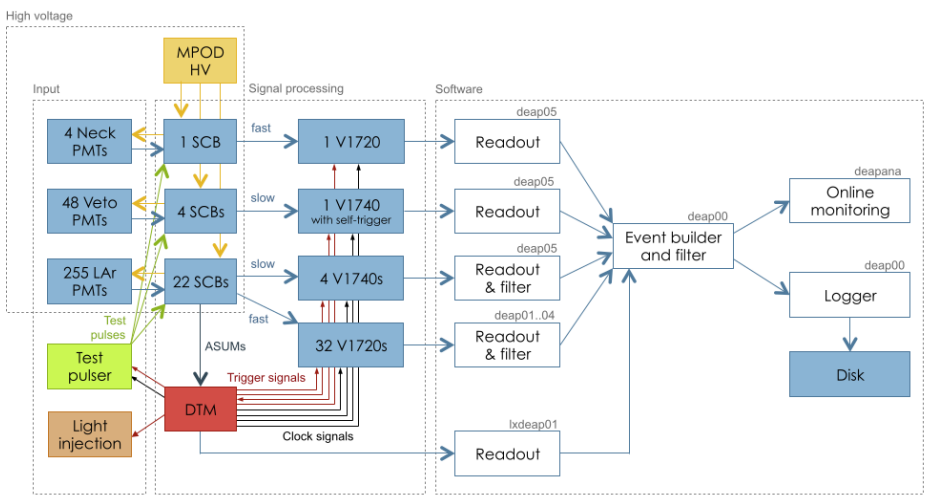

Figure 3.2.5: Flow diagram of the DAQ system. The SCBs takes in input the signal from the three photodetection systems: the neck, the inner vessel and the Veto PMTs. The DTM checks if those signals fall in the ^{39}Ar region and hence whether to trigger or not. The triggered signals are sent to the digitizers, which finally send the waveform to the reconstruction and filter software and then store the digitized waveform in the disk [196].

The waveforms from muon veto PMTs are connected to a V1740 running in self-trigger mode: they don't ask for the DTM input but they "decide" whether the signal in the water is enough to be triggered. The 48 PMTs are

divided into six groups of 8 PMTs each; if any channel in a group sees a signal above 15 ADC, that group is "active". If at least three groups are active, the self-trigger condition is fulfilled. A signal is then sent to the DTM.
Finally neck veto PMTs are connected to a CAEN V1720 digitizer running in ZLE mode only. All the digitizers are read-out through optical links by CAEN A3818 cards. Each card has in input four optical links, and two V1720 are daisy-chained on the same link so that each card can read either eight V1720 digitizers or four V1740 digitizers.

The DTM hardware is based on a TRIUMF-designed 6U VME motherboard with an ALTERA Stratix IV GX field-programmable gate array (FPGA). The motherboard is connected to three daughterboards via FMC standard connectors. Each daughterboards is composed by a 24-channel ADC card to digitize the ASUM channels from the SCBs, a 12-channel NIM I/O card with 8 outputs and 4 inputs, and a master clock distribution board, for the synchronization of the digitizers. The main trigger algorithm used in DEAP-3600 is the "physics trigger", in which the waveforms from the 22 ASUMs from all the 255 inner-detector PMTs are summed up. Two rolling integrals are evaluated, up to 177 ns and up to 3100 ns from the trigger time. The total charge in the prompt window (E_{prompt}) and the ratio of energy in the prompt and late windows (F_{prompt}) are calculated and compared in Figure 3.2.6. The space of parameters is divided into six regions. Events in region "X" are discarded, while the other five are counted as separated trigger sources. The lower bound of region E is set above the ^{39}Ar endpoint. The standard trigger setup exploits the physics trigger, a periodic trigger and the muon veto self-trigger, already described. The physics trigger is set to not read out the 99 % of the events in region A and C, dominated by the ^{39}Ar decays. This will have a key role in the dark matter search set in Section 4. Digitizers are instead read-out from region A, B, D and E. Either cases, the summary information, as the time event, the E_{prompt} and F_{prompt}, are stored. The periodic trigger runs at 40 Hz, with test pulses sent at 1 Hz, while the left 39 Hz are employed to monitor the PMT, as later described in the present section. The veto PMTs are only read out when the muon veto self-trigger fires.

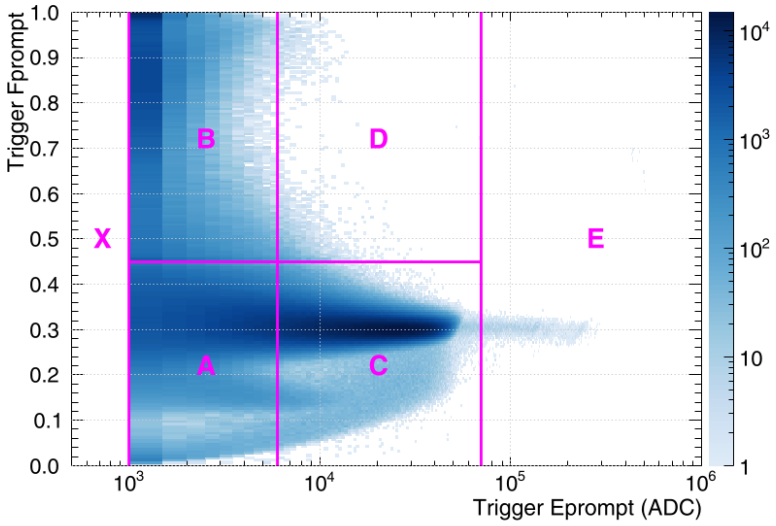

Figure 3.2.6: The space of parameters E_{prompt} and F_{prompt} for a typical physics run, evaluated by the DTM. Events in region X are discarded, while specific trigger conditions are applied in region A, B, C and D. Usually 99 % of the events in region C are "pre-scaled", which means that only DTM information are kept. The lowest energy bound of E is the ^{39}Ar endpoint [196].

The readout software receives the information from the digitizers and the DTM, drops out the unnecessary information, and stores the left in a single event into the disk. In total seven computers running Scientific Linux 6.6 handle the readout; four of them analyze the data from the V1720 digitizers in the inner veto, with additional PCs for the DTM data, the inner veto V1740 digitizer, the muon and neck vetos data, and a master. The V1740 information is needed only when the V1720 digitizers saturate, at about 100 PE; only in that case, the V1740 information is stored. Otherwise it is filtered out. The filtering is also applied to the V1720 waveforms, to further reduce the amount of data written to the disk. Specifically, once that the number of PE carried by a given pulse is correctly identified thanks to the Single PhotoElectron response, the waveform information is dropped and only the main information is kept. This summary information assures a sub-ns timing resolution of the peak position, as well as the pulse charge, height, baseline with its RMS. After all the filtering, the data rate decreases from 7GB/s to 6 MB/s.
The DAQ system is based on the MIDAS package and was developed by TRIUNF and Paul Scherrer Institute. The shift is usually performed in remote

via a web interface which also interfaces with DEAP's CounchDB database. In this way, the shifter selects only the run type, and then the database retrieves the DAQ parameters required by that run type. In case of hardware or network malfunctions the current run is stopped and an alarm -via SMS, e-mail and Slack chat- is sent to the shifter. If he/she does not fix the issue within 15 minutes and restart the new run, the PMTs are ramped down. In absence of unexpected power outage, the data-taking uptime is greater than 95 %.

An Apache CounchDB [241] database is used to calibrate and analyze data, evaluate data quality and fix external parameters. The ranges of validity for the parameters are evaluated for each run number. Furthermore, information from the DeltaV slow control system is transferred to a PostgresSQL database.
Raw detector data are transferred as ROOT files from the DAQ storage computers to the main analysis cluster. The low-level analysis applies all the calibrations, as the PMT gains, for instance, to translate the DAQ units into physics units; also the data quality plots are generated and kept available online. The second stage analysis calculates the high-level information for each event, as the number of photoelectrons, the position and the number of hits. The high-level variables are finally stored in a new ROOT file. The analysis software is kept in a Git repository on a self-hosted GitLab server, which provides to the user a web interface and automatic builds and tests after each commit (GitLab-CI).

The detector simulation is developed in RAT, a software framework for simulation and analysis of liquid scintillator experiments, based on Geant-4 [242] version 4.9.6 and ROOT [243] version 5.34. The simulation in RAT was validated using DEAP-1 data [244], the prototype of the experiment [245]. These simulations allow for the definition of the detector materials, based on their radio purity, background rejection optimization, the definition of the light yield and studies on the systematic effects. The full detector geometry is implemented, included the SNOLAB Cube Hall in which the detector is set. Some optical parameters of the simulation come from ex-situ measurements; the main ones are the wavelength-dependent light attenuation of the acrylic [246], the wavelength-dependent reflectance of the reflectors surrounding the AV, the light yield [247], the time profile and the temperature dependence of the alpha scintillating in the TPB [248].
In addition to the standard libraries in GEANT-4, a few extension packages were included. Nuclear recoils from an arbitrary rough surface are simulated from a custom simulation to study the background coming from the AV inner

surface [249]. The argon scintillation simulation is based on [219], together with SCENE measurements of the nuclear recoil quenching factors and PSD distributions [221]. The hadron physics processes for muon and gamma-induced neutron events are simulated as suggested in [250]; below 20 MeV Geant-4 provides high precision data-driven neutron models. Finally, the energy spectrum and rate of neutrons from the inner detector are calculated thanks to SOURCES-4C code [251] and cross-checked with NeuCBOT [252], getting 30 % level of agreement.

3.3 DarkSide-20k

DarkSide-20k (DS-20k) detector comes from the joined resources of collaborations working with LAr-based detectors, including ArDM, DarkSide, DEAP-3600 and MiniCLEAN, all composing the Global Argon Dark Matter Collaboration (GADMC). The detector assembling and installation is foreseen in the 2024, but the full design is frozen and is shown in Figure 3.3.1. The detector active mass will be of about 50 tons of UAr, observed in a Time Projection Chamber, so both via S1 and S2 signals. An outer detector filled with 700 tons of atmospheric argon will allow for the background rejection. All the technology and the physics potential of DS-20k will be rescaled in the next detector from the GADMC, Argo. 400 tons of UAr are foreseen as target mass for Argo, of which 300 tons as fiducial mass. Thanks to its high exposure, Argo will be able to search WIMPs of mass above 1 GeV/c^2 down to the neutrino floor.
While the design of Argo still needs to be frozen, the DarkSide-20k one is finalized and is fully described in the present section.
The core of the detector will be the inner detector, composed by the LAr Time Projection Chamber (TPC), filled with UAr, already employed in DarkSide-50. The TPC will have an octagonal plant and a height of 350 cm, hosting 49.7 t of LAr. The volume is contained in an ultrapure PMMA acrylic vessel. The photodetection won't be performed by PhotoMultipliers Tube (PMTs) as done in DarkSide-50, but by Silicon PhotoMultipliers (SiPMs), fully covering the top and the bottom TPC surfaces. The acrylic vessel will be surrounded by the veto detector, filled with Atmospheric Argon, separated in two layers by a Gd-loaded PMMA shell. The veto detector allows for both passive and active shielding from radiogenic neutrons. The whole detector will be contained in a cryostat made of layers of plastic sustained by a stainless-steel structure, inspired by ProtoDUNE-outer cryostat design [253] [254]. The cryostat will moderate cosmogenic and radiogenic neutrons from the rock surrounding the experiment. Finally, as in DarkSide-50, the experiment will be set in the Hall C at LNGS, 2 km underground, 6 km

w.m.e.; the choice of the underground set assures the natural shield from cosmic rays.
DS-20k was designed to be a "background-free" experiment. This means that the background due to the materials is kept below 0.1 events over 200 t yr of exposure in the WIMP ROI. The electromagnetic background will be rejected with the Pulse Shape Discrimination, which was measured to have a rejection power greater than 10^7 in DarkSide-50. Thanks to the very low background and the possibility to perform background measurement in situ, the expected sensitivity of the experiment is down to 1.2×10^{-47} cm^2 (1.1×10^{-46} cm^2) for 1 TeV/c^2 (10 TeV/c^2) WIMPs after five years of data-taking. With ten years of run and 200 ton yr exposure the sensitivity increases to 7.4×10^{-48} cm^2 (6.9×10^{-47} cm^2) for 1 TeV/c^2 (10 TeV/c^2). With 200 t yr exposure, 3.2 nuclear recoil events are expected from the coherent scattering of atmospheric neutrinos on liquid argon, making DS-20k be the first experiment reaching such a high sensitivity.

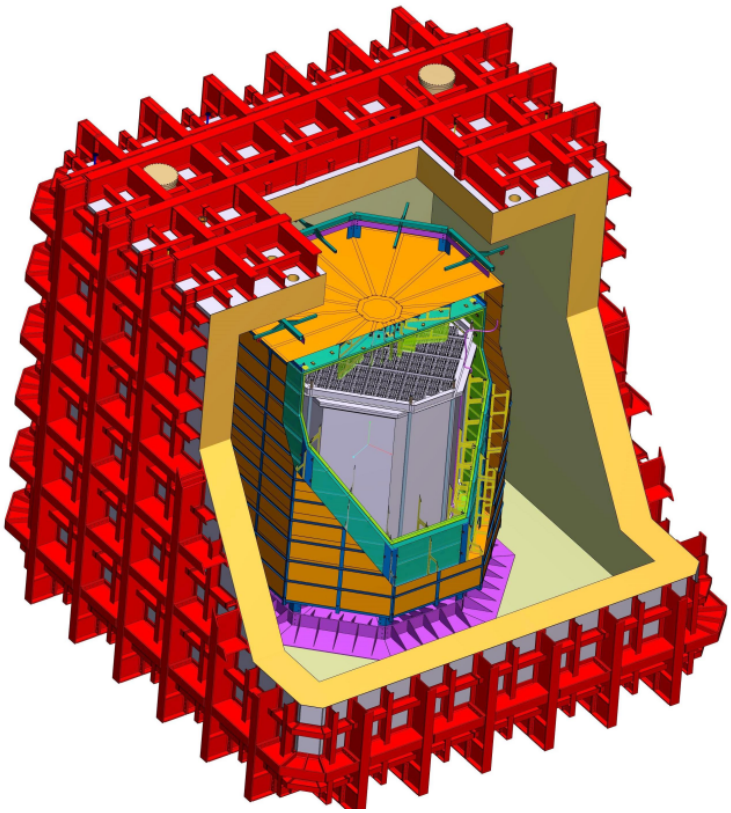

Figure 3.3.1: Rendering of the main component of DS-20k detector. In grey the PMMA acrylic vessel is shown, with the SiPM top array installed. In green, the Gd-loaded acrylic Shell (GdAS) will separate two AAr active layers, called Inner and Outer Active Buffer (IAB and OAB respectively). All of this is contained in the ProtoDUNE-like cryostat, in red, and stands on a support on the floor of the cryostat during the installation, but will then suspended by ropes when the construction will be completed.

The very low background level foreseen in DarkSide-20k will also allow for an outstanding sensitivity to neutrinos from galactic core-collapse supernovae, which is the content of the analysis performed in Chapter 6. In the present section, each component of the experiment is described in detail.

3.3.1 Photoelectronics

The photodetection will be performed by Silicon Photomultipliers (SiPMs) instead of the Photomultipliers Tubes (PMTs) used in DarkSide-50. SiPMs will be also employed in LAr based detector such as DUNE [254] and liquid xenon based detector such as NEXO [255], for the neutrinoless double-beta

decay. Specific SiPMs have been developed for the dark matter search in DarkSide-20k, described in more detail in Section 5.1.4. The main advantages are the higher photon detection efficiency and the extraordinary single photoelectron resolution. Furthermore, they are more radio-pure than PMTs and thanks to the solid-state technology are less fragile and easy to integrate into tiles. In DS-20k SiPMs are grouped in tiles of area 50 x 50 mm^2 operating as a single detector, called Photodetector Module (PDM), shown in Figure 3.3.2. The module is also composed by a cryogenic amplifier board which amplifies and shapes the signal in output from the sensor and sends it to a signal transmitter. Finally, the PDM includes the mechanical structure which holds all the components and minimizes the production of bubbles in the LAr due to the PDM heat dissipation. The tile and the front-end-board PCBs is made with an Arlon 55-NT substrate. The electronic component was assembled by FBK company, under the supervision of LNGS personnel, and tested at warm and cryogenic temperatures to test the correct working of the impedance.

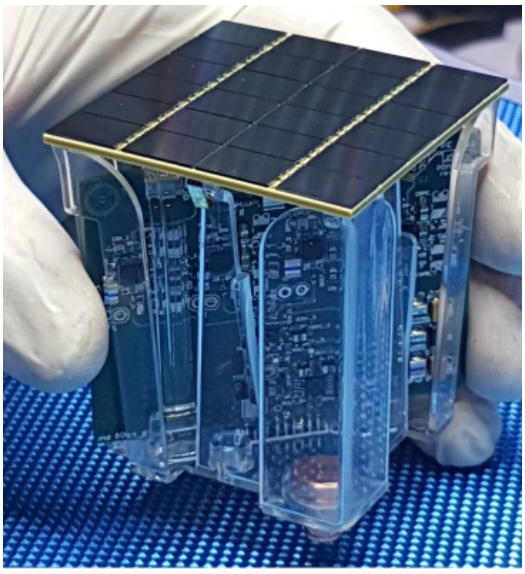

Figure 3.3.2: Snapshot of a Photodetection Module developed for DarkSide-20k, composed by a 50 x 50 mm^2 tile, together with its amplifier board and the mechanical structure.

The main challenge with SiPM readout stands in their high capacitance, 50 pF/mm^2, which brings the total capacitance above O(1) nF. The use of the charge integration amplifier determines an increase of the noise and of the rise time due to the large capacitance; hence a Transimpedance amplifier

(TIA) was preferred and optimized at 87 K [256].
The SiPM readout scheme affects both the Signal-to-Noise Ratio (SNR) and the bandwidth of the signal. For DarkSide-20k a hybrid scheme was adopted, with couples of SiPMs put in series and then connected in parallel, which is called 2s3p SiPM configuration [257]. In this way the signal and most importantly the noise gain is reduced by a factor of two, due to the decrease of the input capacitance; furthermore, the bandwidth is strongly improved respect to the parallel readout scheme, comparable to the one from a single SiPM in input.

The PDMs will be located above the anode and below the cathode, covering the bottom and top surfaces of DS-20k TPC with 4140 PDMs each. They will be grouped in Square Motherboards (SQBs), which will be the very mechanical unit in the multi-ton detector. Each SQB is composed of 25 PDMs; the modified SQBs, at the edge of the detector, will have only 15 PDMs positioned towards one corner, to optimize the photodetection in an octagonal plant detector. The first assembled motherboard was composed by 27 tiles, each made of 24 SiPMs, shipped at LNGS inside acrylic boxes, allowing for safe shipping and also for inserting a Front-End-Board without removing the tile from the box; this makes possible the characterization of the tile in liquid nitrogen. The characterization returned an SNR of 12 on average, above 8, which is the requirement for dark matter search in DarkSide-20k. After these tests, the tiles were assembled in Pisa, in a clean room, while the PDM pillars and the copper motherboard structure were built in Bologna, with a 99.997 % pure copper sold by the Luvata Company. The PDMs in the motherboard were connected by PCB strip, made of a 0.5 mm thin stack-up based on a Pyralux substrate. The mounting of the first motherboard, made of 25 PDMs, was finalized in a few days; a picture is shown in Figure 3.3.3.

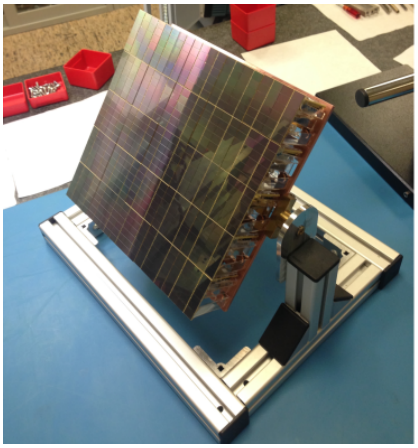

Figure 3.3.3: Square MotherBoard (SQB) made by 25 PDMs assembled at LNGS. SQBs will be the very photodetection unit in DarkSide-20k.

The DS-20k experiment will require the production of more than 10000 PDMs in 2.5 years. A large clean room, together with high technology equipment and trained personnel, is required. The GADMC selected for the DS-20k SiPM packaging facility a cleanroom to be built inside the LNGS, called "Assembly Hall", with a surface of 700 m^2 and an Rn-suppressed environment.

3.3.2 Inner Detector

The core of the experiment is the LAr TPC, which will be filled with 51.1 t of UAr (49.7 t active mass). The target is contained in an ultrapure acrylic vessel, which is then surrounded by the TPC field cage system, with the anode and the cathode above and below the acrylic vessel, coated with a commercial conductive polymer, Clevios^{TM}, which allows to not use conductive metals materials. Four millimeters thick sheets of the same ultrapure acrylic hold the Enhanced Specular Reflector (ESR) foils installed on the inner walls of the cryostat, to maximize the light collection.
All the inner surfaces of the TPC are coated with the TPB wavelength shifter, which has the absorption peak at 128 nm and the emission peak at 420 mm, so to convert the UV scintillation light to the SiPM detection efficiency peak. On the top and the bottom of the TPC are placed two arrays of 4140 PDMs, just outside the acrylic vessel. The whole inner detector is contained in the neutron veto detector, which will be described later. Here each component of the inner detector is detailed, with the foreseen specifics optimized from the Geant-4 simulations.
The DS-20k TPC will have an octagonal plant to best fit the coverage of the

PDMs, still optimizing the fiducial mass. Each SiPMs array will consist of 156 fully-populated square motherboards (SQBs), each made of 25 PDMs, and 26 modified SQBs, with only 15 PDMs set on the corner. The modified SQBs will use the same mechanical and electronic configuration as in the fully-populated SQBs. Thus the total number of PDMs is 8280. The distance from edge to edge of the octagonal active volume will be 350 cm. With this design, the total target mass will be 49.7 t; assuming as fiducial cuts 70 cm in the height and 30 cm from the walls, 20.2 t of fiducial mass are foreseen.

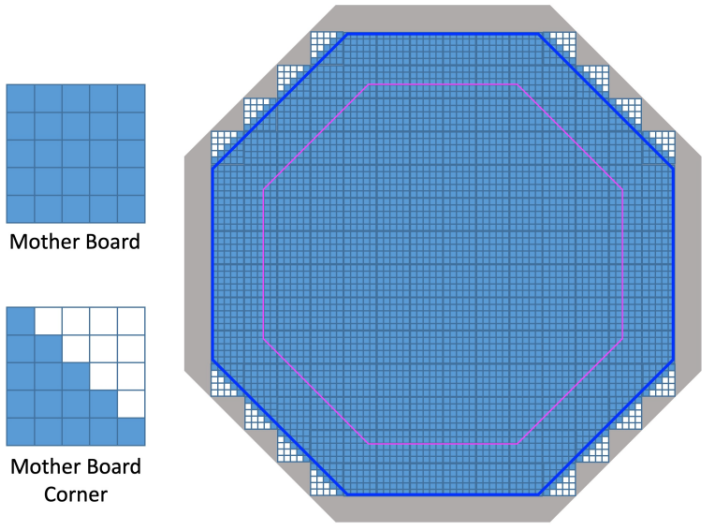

Figure 3.3.4: SQB array in DarkSide-20k. Two arrays will be installed at the top and at the bottom of the inner vessel, each consisting of 4140 PDMs. Motherboards in the corners of the octagonal plant will be modified to have only 15 over 25 supplied PDMs .

The target will be contained in an acrylic PMMA vessel, much more radiopure then any metallic vessel, with a residual neutron background less than 10^{-3} for 200 t yr of exposure. The PMMA vessel will be composed by 5 cm thick acrylic plates fused, flanged and sealed with the top and the bottom lid, who will host the anode and the cathode of the TPC. The ESR panels will be placed inside the acrylic vessel, while the PDM arrays will be just outside it, immersed in the AAr of the neutron veto detector, but isolated from any light coming from it. In this way the 97.3 % of the total argon is active; for the same reason all cables are moved outside the cryostat, to optimize the UAr purity. The indium tin oxide (ITO) which coated the photosensor arrays in DarkSide-50 will be exchanged for the Polymer coating

Clevios^{TM}. This is already used in industrial applications such as transparent electrodes for touch panels. Respect to ITO it will be easier to cover the two arrays areas with Clevios^{TM}, as it is a water-based solution. Its radiopurity is under study, with a sample of 100 g. The transparency performances are comparable with the ITO: a sample of 4 μm of thickness was measured to have 98.5 % transparency, compared to 98 % from ITO in DarkSide-50. Furthermore, Clevios^{TM} will replace the bulky copper field shaping rings, resulting in an easier built of the TPC, a decrease of the total cost and a reduction of the expected background.

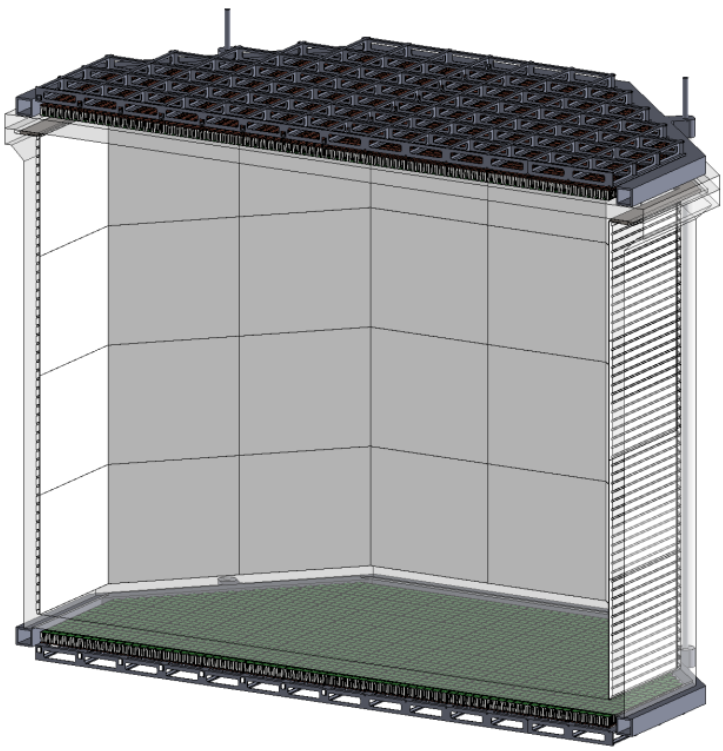

Figure 3.3.5: Representation of the inner vessel, made in PMMA acrylic, internally covered with the ESR reflectors. The top and bottom SiPM arrays, placed just outside the vessel, follow the octagonal plant of the TPC.

The PTFE reflectors in DarkSide-50 were the main source of neutron background and Cherenkov light, so they will be replaced by ESR. This is a thin layer foil with a reflectivity of 98 % at 420 nm with a thickness of only 50 μm. The ESR surface looking at the LAr volume will be coated with TPB. On the other side, the ESR foils will be held by 4 mm thick Ultraviolet Transmitting acrylic sheets, which will keep the flatness of the ESR foils.

The entire reflector panel of the TPC is shown in Figure 3.3.5.
The fields are produced by the Clevios^{TM} coating. The relative permittivity of LAr and GAr is 1.54 and 1.03 respectively. The zero of the electric potential is set at the anode. The extraction grid is then at - 3.8 kV and finally the cathode at -73.8 kV. Three different field regions result in the TPC:

- a uniform drift field of 200 V/cm from the cathode Clevios^{TM} to the extraction grid at 350 cm of height;
- the extraction field above the liquid phase of 4.3 kV/cm, along with the 3 mm between the liquid phase interface and the extraction grid;
- from the extraction grid up to the upper Clevios^{TM} layer coating, acting as anode, for a total of (7.0 $\pm$ 0.5) mm of distance, the electroluminescence field in the gas phase will be 4.2 kV/cm.

These values are based on DarkSide-50 settings but are expected to be scaled with the dimension of DS-20k. At the top boundary of the active volume, a diving bell will be installed to maintain a stable gas pocket. The diving bell is made of a 5 cm thick acrylic window, with its inner surface coated with a thin layer of Clevios^{TM}; finally, the TPC is coated with the Clevios^{TM}. The top Clevios^{TM} layer is in contact with a C-profile feature on the walls of the acrylic vessel, which will shape the field and smooth the field lines in the corner of the cathode region.
The extraction grid will be composed by stainless steel wires stretched in parallel with 3 mm spacing and fixed via small posts set into a stainless steel frame. Suitable tensions will be applied to the grid wires to minimize the sagging, which would distort the electroluminescence field. Finally at the bottom of the active volume is set a 5 cm thick acrylic window coated with Clevios^{TM} on both sides; the TPB layer coats only the top Clevios^{TM} layer. As for the top Clevios^{TM} layer, also in the bottom, the field smoothing is provided with a solid guard copper ring.
The gas pocket will be generated and maintained by both the bubbler and the gas feed-in. The bubbler is full of Pt-100 RTDs with tunable heating power to boil off the LAr. The gas feed-in introduces gas argon from the UAr cryogenic system to the TPC and regulates the pressure. The gas pocket will have about 7 mm of thickness, in which the field uniformity is fundamental for the S2 resolution; this results in a requested anode flatness, which follows by maintaining the pressure balance between the UAr in the TPC and the AAr in the Veto. The foreseen distance between the TPC acrylic vessel and the AAr surface is 2 m, which corresponds to a pressure of 4 psi. This, added to the pressure from the AAr veto and the need for a flat anode brings to a total UAr pressure of 19.6 psi.

3.3.3 Cryogenics System

Two main cryogenic systems are foreseen: one for the AAr in the veto detector and one in the UAr in the TPC. The AAr cryogenic system will be based on that of ProtoDUNE at CERN, optimized for the LNGS installation: namely, a liquid recirculation system controlled by a pressure and vacuum relief valve and a warm purification system to assure an efficient impurity trapping in the gas phase. The continuous circulation of the argon along the purification system is allowed by a system of custom-developed gas argon pumps who, together with integrated heat exchangers, allows circulation rates of 10^4 stdL/min AAr and 10^3 stdL/min UAr, removing electronegative impurities from either or both liquid and gas argon. The removal of N_2, CO_2 and O_2 will be performed by SAES hot getter. Furthermore, DS-20k purification system will operate in parallel with a continuous LAr cryogenic circulation system, whose level-zero scope will be the removal of radon from the LAr TPC.

The cryogenics will be based on that of DarkSide-50, together with improvements needed for DS-20k. From DS-50 it will heritate the long term TPC pressure stability, with an RMS of 150 μbar, which determines the S2 resolution; also oxygen contamination below 0.01 ppb was achieved, resulting in a drift electron lifetime greater than 5 ms [213]. Furthermore, during the commissioning phase and also in an incident in 2019, the cryogenic system showed immunity to total power failure, assuring the safety of UAr in the TPC. The main improvement for DarkSide-20k will be the increase of the circulation speed, up to 1000 stdL/min, required to purify LAr in a couple of turn-over times of 20 days; also the LAr condenser, which is the core of the cryogenic system, will have a cooling power of 2.2 kW, nearly twice the required one.
The UAr cryogenics system is composed of several subsystems:

- the LAr handling system
- the LAr cryogenic circulation system for radon removal
- liquid nitrogen reserve system
- the UAr purification system
- the cold box
- the gas circulation pump
- heat exchangers

- UAr recovery and storage system

all shown in Figure 3.3.6. The cryogenic system for AAr is analogue, with lower purity requirements and additional liquid recirculation. The two cryogenic systems share the same liquid nitrogen reserve loop, still keeping the two argon loops separated.
The LAr handling system delivers the radon-free UAr initially stored in the recovery storage system, which can contain the full UAr for DS-20k TPC. Two options are under study: the storage in the liquid phase or high-pressure gas phase. Either way, the handling system will be exploited to pre-purify the UAr in the gas phase before filling the TPC volume. Furthermore, in case of an emergency or at the end of the experiment, the UAr can be extracted from the TPC and stored back in the recovery system.
LAr will continuously rush with a flux of 30 L/min in the cryogenic circulation system, which is composed of a commercial cryogenic liquid pump, a LN_2/LAr heat exchanger, an absorption column, a cryogenic mass flow meter, a phase separator vessel. The Radon removal process takes place in the column, in which the atoms are extracted from the TPC before their decays, as the turn over is about 0.9 days, much shorter than Radon lifetime. The column is filled with absorbent material. The difference between the argon and the radon residence time brings to a large radon decay rate in the column. The LAr cryogenic circulation system can also be applied for the purification from other impurities, as O_2, H_20, N_2, if suitable absorbents or reagents are provided.
The LN_2 reserve system consists of a closed-loop with a LN_2 plant placed outside the Hall C and a few liquid nitrogen dewars. The cooling system supplies the condensers in the UAr cryogenics system of the inner detector, the AAR cryogenic system, and finally the recovery system if the liquid phase storage-mode is chosen. Furthermore, the system extracts the boiled-off nitrogen gas to liquify back in the LN_2 reserve system.
The UAr purification system purges the UAr in the gas phase during its circulation. From DarkSide-50 experience, a commercial Zr-based getter system is also foreseen for DS-20k.

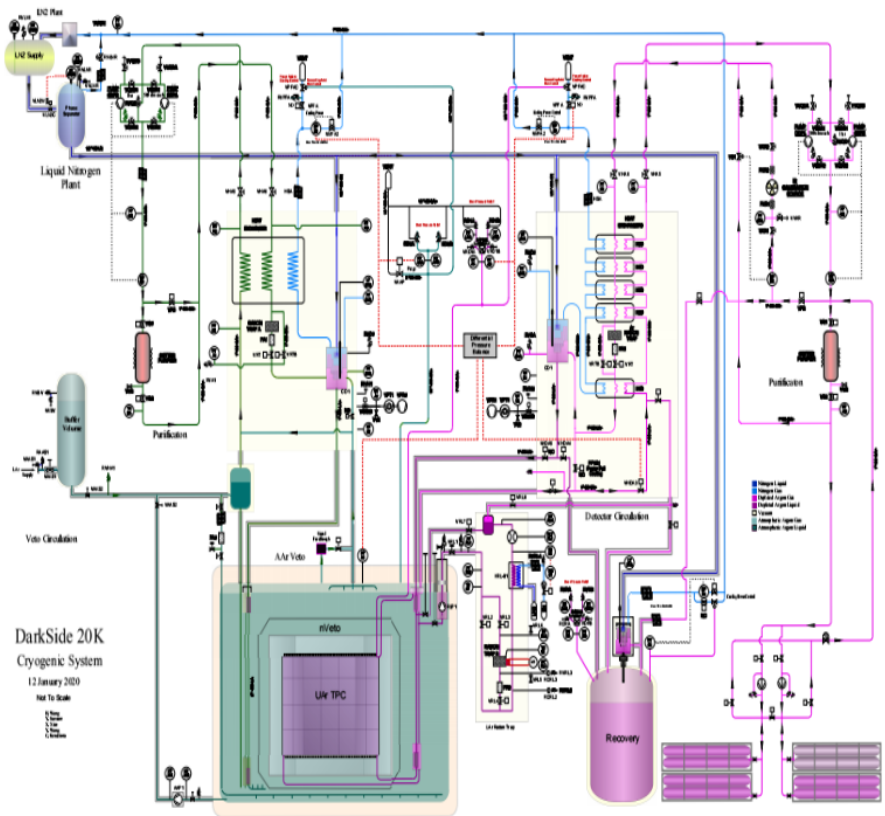

Figure 3.3.6: Rapresentation of the cryogenic system.

The main components of DS-20k cryogenics system are contained in the Cold box. Together with the condenser, five heat exchanger modules are placed in it, to pre-cool the argon gas, by the circulation of cold nitrogen gas and the release of cold argon gas. Between the two coldest heat exchanger modules the radon trap is placed, as the optimal radon trapping is achieved when the argon is still in the gas phase and at its lowest temperature. To control and monitor the system eight cryogenics valves and temperature and pressure sensors are placed. The argon circulation speed is foreseen to be up to 1000 std L/min through 1" OD stainless steel tubings. The stainless steel LAr condenser is divided into two separated volumes: the top one filled with nitrogen and the bottom one with argon. A continuous liquid nitrogen dropping is assured by the "chicken feeder", mounted at the end of the liquid nitrogen delivery tube. A mass flow meter and a control valve monitor the flow of the evaporated nitrogen gas. The control valve adjusts the evaporated nitrogen gas flow rate, which determines the cooling power of the condenser, according to the LAr TPC pressure, assuring the same stability between the

UAr and the AAr systems already proved in DarkSide-50.
The Gas circulation pump is based on DS-50 experience, where it reached a speed up to 50 stdL/min. It is composed of linear motors and reed valves. The linear motors, essentially a piston coupled to a cylinder, can provide a continuously adjustable pumping power. The reed valves direct the gas flow. The combination of the two will minimize the friction in the pump during operations so that it can have a long lifetime. During the initial fast circulation, when a good UAr purity level has to be achieved, the required circulation speed is 1000 stdL/min; to help to achieve it two individual circulation pumps will be placed in parallel, each providing a circulation rate up to 500 stdL/min.
The heat exchangers are placed close to the TPC. Outgoing LAr from the LAr TPC absorbs heat from the incoming liquid-gas mixture of purified argon here, then it boils off into gas phase, and then enters the circulation loop. A heat exchanger is placed above the TPC, to impede LAr from the TPC to enter the lowest heat exchanger in the cold box, where it would freeze. Another set of heat exchangers are set near the TPC bottom to help fast recovery during the draining stage; otherwise, they are completely passive during ordinary operations.
The underground argon recovery and storage system consists of a set of high-pressure gas containers and a vacuum insulated cryostat for liquid phase recovery coming from the TPC. The UAr cryogenics handling system is designed to deliver the liquid argon to the TPC during ordinary operations and keeps a separated liquid outlet port to eventually deliver liquid argon to the recovery system if needed. The recovery system will have its own condenser, sized to handle the full volume of the UAr when it will be fully recovered. The recovery speed must be adjusted according to the emptying speed of the AAr veto, to protect TPC acrylic vessel from high-pressure gradients, which would damage it. A custom passive cooling system based on LN_2 will be set on the recovery cryostat, to prevent releases of argon during eventual power loss.

3.3.4 Veto Detector

The veto detector is composed by three volumes: a 40 cm thick inner volume of active liquid Atmospheric Argon (AAr), the Inner Argon Buffer (IAB); a passive octagonal shell made of Gd-loaded PMMA acrylic, called "GdAS", surrounding the IAB; a 40 cm thick outer argon buffer (OAB), contained in the outer copper Faraday cage. The GdAs moderates radiative neutrons from detector materials, and enhances the neutron capture probability with the Gd doping, with the consequent releases of multiple γ rays, who recoil

in the AAr buffers. To optimize the detection, both the OAB and the IAB are segmented in 8 subdivision plates coated with a light deflector and a wavelength shifter.
The GdAs will be built by coupling two layers of Gd-loaded PMMA plates of thickness of 5 cm. Each plate will be approximately 60 $cm^2 \times 100$ cm^2. The total number of Gd-loaded PMMA plates is of about 450, half facing the IAB and half the OAB.
The read-out will be performed by 2000 SiPM tiles facing the IAB and 1000 facing the OAB, all mounted on the GdAS. The photo-detection is performed by the FBK NUV-HD SiPMs already foreseen for the TPC read-out, but the front-end-board will be optimized for the veto geometry and electronics.

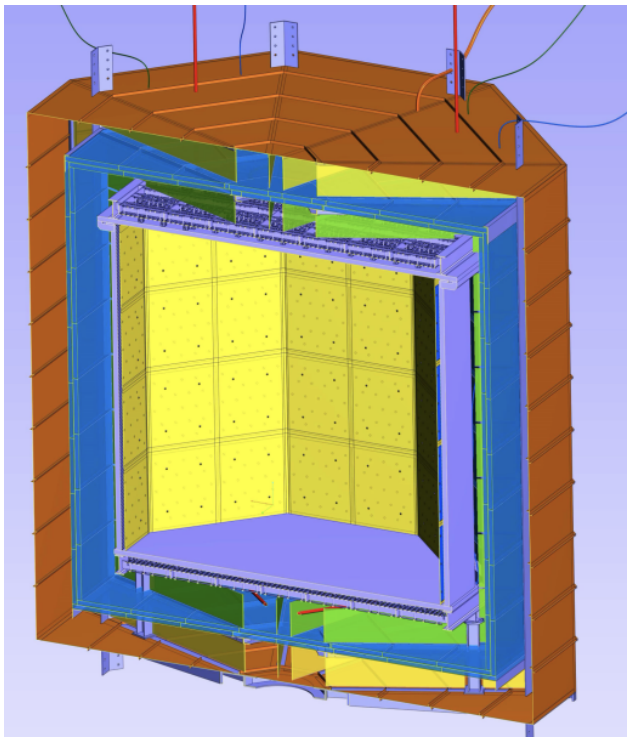

Figure 3.3.7: View of the DS-20k veto detector. Two layers of Atmospheric Argon are separated by the Gd-loaded PMMA foils composing the GdAS, in blue. The veto is contained in the Faraday cage, shown in brown. The height subdivision panels dividing the AAR inner and outer buffers are shown in green.

The FEB will be realized with a custom ASIC, which showed a linear behaviour up to more than 700 mV and an RMS noise of 0.5 mV. With an overvoltage of 8 V, the measured mean peak amplitude of the single photo-

electron is 7.1 mV, which means a linear dynamic range of 100 PE. In these tests, the SNR is 10.
Figure 3.3.8 is a representation of the prototype FEB developed for the veto detector, which, coupled to the tile, will compose the Veto Cryogenic Photodetector Module (VCPDM). Approximately 10 VPDMs will be dedicated to the IAB and 5 to the OAB. Two coupled GdAs plates, their respective VPDMs, the associated electronics and the reflectors coated with the TPB wavelength shifter compose the basic unit of the veto detector, the Veto Detector Unit. Each VDU will be assembled and tested in a test cryostat before their installation in the DS-20k veto detector.
All of the inner surfaces of the veto detector will be covered with Enhanced Specular Reflector (ESR), coated with a wavelength shifter. The Tetraphenylbutadiene (TPB) has already been employed in present DarkSide detectors, but its evaporation on such wide area may be challenging. Thus the collaboration is exploring the possibility to use instead the Polyethylene Naphtalate (PEN). It was measured to have a fluorescence lower of about a factor two [258], which still fulfill the requirement for DarkSide-20k, and has a time constant fast enough for the application in the detector. PEN is already used in the test TPCs for the optimization of the S2 signals and also in the ProtoDUNE dual-phase experiment.
The veto expected light yield was calculated by means of a custom Geant-4 simulation. The SiPM detection efficiency is tuned to reach 45 % at 420 nm. The ESR reflection probability is set at 92 %, as measured for the ESR with TPC coating. The Rayleigh scattering length of LAr is set to 55 cm at 128 nm. The LAr purity is so that the attenuation length of the scintillation light is greater than 10 m. The resulting light yield was 2.2 PE/keV in the IAB and 0.8 PE/keV in the OAB.

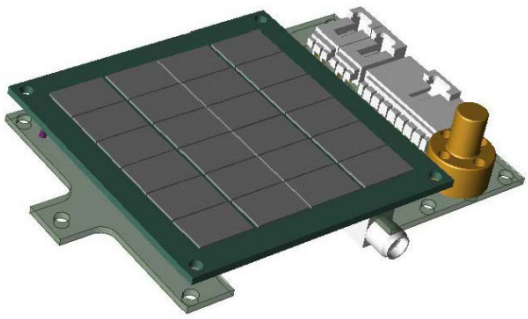

Figure 3.3.8: Design of the test front end board (FEB) coupled with the tile. In the veto a peculiar geometry for the coupling of the SiPMs tile to the FEB is foreseen, with two parallel devices for the veto detector.

3.3.5 Data Acquisition

The basic scheme for the TPC and Veto detector DAQ electronics hardware is an optical signal receiver feeding a differential signal to a flash ADC digitizer board, which is connected to a large Field Programmable Gate Array (FPGA). A digital filtering capability within the digitizer board would allow to discriminate single photoelectrons signals and to store the time and charge on the single-channel pulses. Furthermore, the digitizer board provides a down-sampled waveform at a few MHz when it receives in input the large and slow signals, such as S2 ionization-born pulses in the TPC or the typical signal from the Veto. These preprocessing operations will allow for the needed data reduction. Data from signals detected in the TPC or in the Veto detector are then sent to the front-end boards, where further data reduction can be performed.
The purposed trigger would be set asking a coincidence of 7 hits in 200 ns. In this way, nuclear recoil events at the trigger threshold, at about 15 PE along with a time window of 5 us, would result in a collection of minimum 6 PE in the first 200 ns, and then in a 100 % trigger efficiency.
The clock source of the TPC DAQ is used as a reference; then pulsed signals among all the modules will be sent to check and correct the alignment of each channel between the TPC and the Veto detectors.
The fundamental readout element purposed for DS-20k is a multi-channel board hosting several flash ADCs (fADCs) linked to an FPGA for digital signal processing. This will be connected to a host CPU for control, to monitor and format the data, which are then sent to an external computer through a 1Gbit/s - 10 Gbit/s Ethernet connection. The ADC will have 14 bits resolution and 125 MHz sampling rate. The board will handle 64 channel with a VME 64 form factor. Data from the ADCs will be sent to a large FPGA through a high bandwidth JESD. The board will host a Xilinx made Zync Ultrascale+ with a quad-core ARM Cortex A53 processor.
The chosen framework for the developing of the DAQ read-out and online control software is the Maximum Integrated Data Acquisition System (DAQ), already used by DEAP-3600. MIDAS DAQ package together with CAEN hardware will provide a suitable basement for the digitization and recording of the raw data. A collaboration between the MIDAS and the CAEN developers will ensure the compatibility of the front-end hardware with the back-end hardware and the software for the compiling and storage of the data.

3.3.6 Computing

Due to the large numbers of channels looking at the events in the TPC the digitize and the storage of the full waveform is undoable. Nevertheless, the information about the charge and the hit time will be preserved, in order to have access to the time evolution of the signals. Thanks to the filtering, compression and the data reduction, the amount of recording will be just a few times that of DarkSide-50. DarkSide-50 collects 1 $\times 10^5$ events/day from the dark matter search and 8 $\times 10^5$/day from laser calibrations. The latter has a size of about 0.1 MB, the first about 2.6 MB. This will decrease by a factor of 3-4 in DS-20k. The short-term storage required is 20 TB. The total storage required by the experiment is expected to be more than 20 PB, including the one needed by simulated and reconstructed events.

The first step for the event processing is performed in the experimental site, where the event is temporarily stored ad copied to the central computer centre (Tier-1/Tier-2). These computers allow for the preprocessing of the data and the access to older processing. Furthermore, DS-20k simulations will be stored here. Bulk data processing will be performed using cluster computing based on commercial CPUs. The final data analysis will be performed either at the Tier-1/Tier-2 computer or on commercial CPU hosted at institutes which joined the experiment. Furthermore, there's the possibility to use the Open Source Grid, as already done by many current experiments for the data reconstruction and analysis.
The amount of the short-term storage currently available at LNGS for DS-50 is 7 TB of front-end storage located in the underground laboratory, to which 710 TB sums in the above-ground computing centre for short and long term storage of DS-50 data. Data are then copied and reprocessed at CNAF and Fermilab. At CNAF 1 PB of disk storage and 300 TB of tape storage is available for DS-50 data, while at Fermilab 50 TB of disk storage and 620 TB for tape storage is available. Much of the listed resources will be also employed for DS-20k. The total amount of storage in ten years of data taking is 20 PB for the disk storage and 20 PB of tape storage. The current processing power in DarkSide-50 includes a farm of 400 cores at LNGS plus 400 job queues at CNAF and 60 batch slots at Fermilab grid system. In DS-20k 100 dedicated cores will be needed to keep a realtime reconstruction of physics data and calibration events, plus 1000 dedicated cores to produce simulated samples. Furthermore, 2000 physical cores are needed to reprocess in three months all physics events collected in one year.

The software will be based on the C++ programming language, with some

components from a higher level language like Python 3.0. The reconstruction takes in input information from both the TPC and the veto. Usually in input are taken raw data from an event, to which a set of modular tools are applied and outputs one or more sets of reconstructed objects. DS-20k will produce about 2 PB of data per year among data processing, calibrations, simulations and distributed analysis activities. Two types of data storage are planned, in order to allow efficient access to all these data. The first one is a file-based data, used for fundamental information like physics data, calibration and simulation data. The relational database resident data is used for information like detector production, installation, geometry data, condition databases, offline processing configuration. The file-based storage of C++ objects will be implemented through the use of ROOT I/O, which assures high performances. Database storage will be performed in SQL-based relational databases, as MySQL and SQLite.
The Grid middleware components and services, based on the infrastructure and software developed for the LHC Computing Grid (LCG) project, will allow for the needed computing resources, such as software installation, data access and analysis, interfaces for remote job submission and data retrieval.
The online event selection will be provided by the High-Level Software Trigger (HLST). The trigger is based on an online version of the DS-50 reconstruction software and is optimized for the DS-20k online environment, which will run on farms of Linux PCs and/or GPU farms. The HLST will also provide the required data reduction and data preprocessing.

The simulation is a GEANT4-based simulation toolkit specifically developed for DarkSide Collaboration, called G4DS. The structure of the code was built to be able to describe the time and energy response of all DarkSide detectors, including DS-20k, with eventual variations of their geometry. This actually allowed for the optimization of the design of DarkSide-20k, according to the needs of the dark matter search. G4DS provides a wide set of particle generators, geometries, physics processes and the full optical propagation of the photons giving S1 and S2 signals. In this way, the simulation describes the light response and the time response of both the signals, predicts the nuclear and electron recoil backgrounds, allows for the set of the analysis cuts together with the respective acceptances and the definition of the signal acceptance band. Furthermore, G4DS tracks events generated by FLUKA simulation, mainly cosmogenic neutrons and isotope productions, and by TALYS simulation, for the (α, n) reactions.
G4DS simulations stop when the photons are converted in photoelectrons when they reach the photosensor. Then the conversion from photoelectrons to charge signals is handled by a custom-made C++ code. This electronic

simulation takes into account dark noise as well as correlated noise, such as afterpulses and crosstalks, due to the photosensors, as well as effects in the electronics, such as saturation. The output is a waveform for each channel with the same data format of real data so that it can be processed with the same reconstruction code

3.4 The ReD experiment

The photo-detection via FBK SiPMs was performed for the first time in a double phase TPC with the ReD experiment, set in Catania, at Laboratori Nazionali del Sud (LNS). The experiment main aim is to test the sensitivity of a double phase TPC to the incoming direction of particles; in future tonne-scale experiments this will eventually allow for sensitivity to WIMPs even below the neutrino floor, as it will be able to reject events from neutrinos [259]. On the other hand the experiment gave the opportunity to characterize the correlated noise in FBK SiPMs, as performed Chapter 5

The core of ReD experiment is the 5x5x6 cm^3 TPC. Two windows of acrylic (25 mm thick) are set on the top and the bottom of the sensitive volume, each covered with 25 nm of ITO (indium tick oxide), so that they will work as electrodes. From the inner to the outer layer, the four walls of the TPC are made of: a first inner layer of acrylic (1.5 mm thick), the enhanced specular reflector ESR, then the second 1.5 mm thick layer of acrylic. As the scintillation light in Argon falls in the UV range (128 nm) and the reflection peak of the ESR is at 420 nm , all the inner surfaces are covered with TPB whose layer thickness is about 180 $\mu g/cm^2$. The whole volume is enclosed within a PTFE structure, while the field cage – who maintains the fields homogeneous and stable– is made of nine rings of copper surrounding the inner volume, set at 0.5 cm from each other. In the standard configuration the drift field is 200 V/cm, the extraction field is set at 3.8 kV/cm and the electroluminescence field in the gas pocket is 5.7 kV/cm.

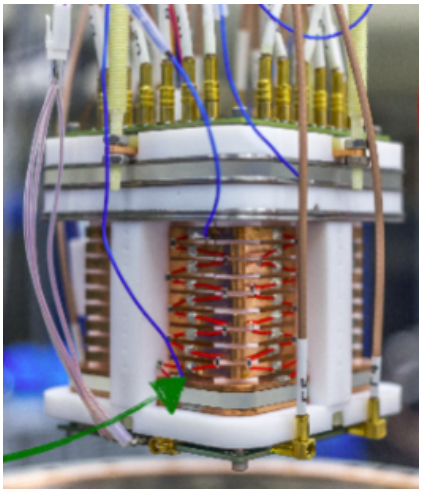

Figure 3.4.1: The Time Projection Chamber of ReD. The TPC is surrounded by a field cage of nine copper rings and is contained by a PTFE structure. It is also possible to see the two FEBs, with each cable connected to its channel.

The TPC was operated in both double and single phase. The extraction grid is set at a height of 5 cm, covered by 3 mm of liquid argon and a 7 mm layer of gas argon. The gas pocket is produced by a bubbler, by evaporation of argon in contact with a PT-100 resistor. The gas diffuses through a teflon tube into the "diving bell", which surrounds the active volume, and from there into the active volume. Finally four rods bound the PTFE structure to the cryostat main flange.
The TPC is cooled by a cryogenic system, whose scheme is showed in Figure 3.4.2. During the filling phase gas argon enters into the system, and reaches the condenser, where it is condensed by contact with a cold head connected to a cryocooler. Liquid argon then drops into the dewar, which contains both the TPC and the cryogenic liquid. After approximately twelve hours the liquid reaches a level of 30 cm. At this point the flow from the argon is stopped, and the system enters in the recirculation mode: the argon vapor from the dewar is sent into the purification system and then into the condenser again, restarting the cicle.

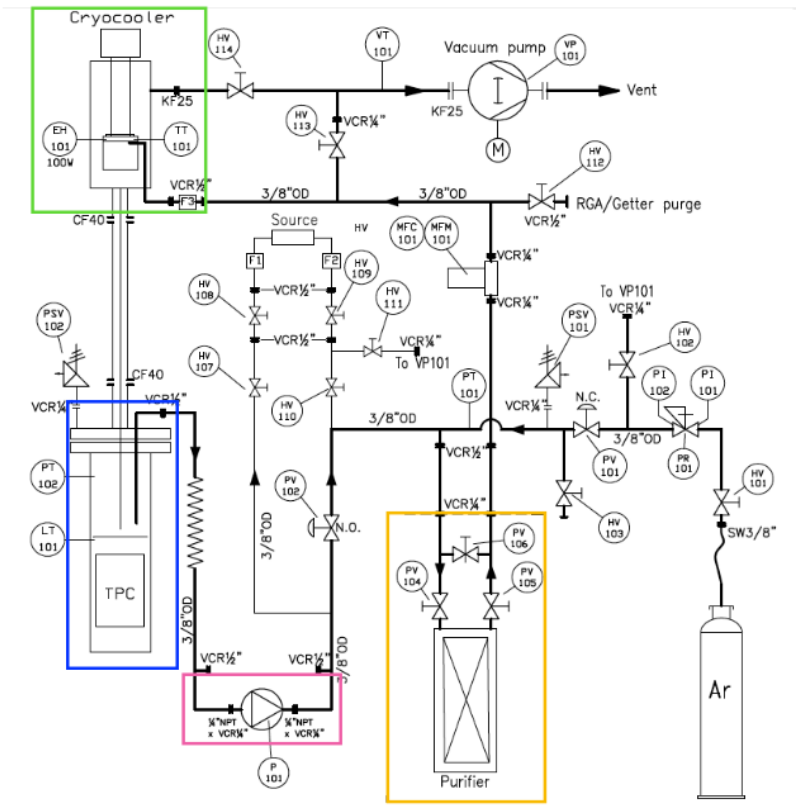

Figure 3.4.2: Scheme of the cryogenic system developed by Criotec company for ReD experiment. During the filling, commercial gas argon is purified and then condensed by means of the cryocooler. From there it drops into the dewar, which contains the active volume, until it reaches a level of 30 cm. Then the flowing of the commercial gas is stopped, and the system enters into the recirculation mode: from the TPC evaporated argon is circulated into the purifier and hence to the cryocooler, restarting the circle.

The light is seen by two tiles of 24 FBK NUV-HD-LF SiPMs of area 1.7 x 7.9 mm^2. Indeed ReD is the first experiment in which these custom photodetectors worked at LAr cryogenic temperature. Each tile is coupled to a Front-End Board (FEB), which provides the bias voltage and amplify the output signal. The bottom FEB reads the 28 SiPMs via four channels, each from the input of 6 SiPMs. On the other hand a custom FEB was developed for the top tile in order to acquire 24 channels, one for each SiPM in the tile, to optimize the x-y position reconstruction [260]. The mapping for the bottom and top channels was changed between different data taking, according to the purposes of the run. The channel mapping for the laser runs

that were analyzed in this analysis is shown in Figure 3.4.3.

0	1
2	3

4	5	6	7
9	10	8	12
14	15	11	13
18	19	17	16
23	24	22	21
25	26	20	27

Figure 3.4.3: Mapping for the laser runs which entered the present analysis (top view of the TPC). On the top, the four bottom channel, each composed by the input of six SiPMs. On the bottom, the top tile, with its 24 read-out channels. Two CAEN ADC boards, each with 16 channels, amplify and digitize all the 28 channels.

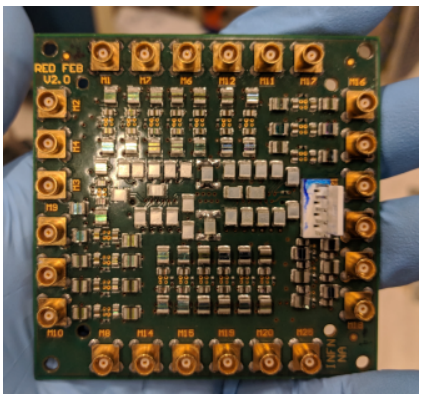

Figure 3.4.4: Top view of the FEB for the top tile, custom developed from INFN Naples together with DarkSide Bologna and LNGS. It is possibile to see the 24 read-out channels, four for side, which assured to ReD the best x-y reconstruction available.

The Data Acquisition System (DAQ) in ReD is performed by three CAEN

V1730 Flash ADC board -one for each read-out system- characterized by 16 acquisition channels, an input voltage equal to 2 V_{pp}, a resolution of 14 bit and 500 MHz as sampling rate. During the laser runs the acquisition window is 20 μs long with 6 μs of pre-trigger; for physics runs the standard S1+S2 events were acquired in a window of 100 μs, with a pre-trigger of 10 μs.
Parallel to these, three parameters are kept under control through a Slow Control System:

- the fields in the TPC, thanks to the CAEN 1471 power supply module;
- the liquid argon temperature in the crysostat, read on the Lakeshore 335 Temperature Controller;
- the level of the gas pocket, controlled by a Keithley 2280S.

The favourite DAQ software for ReD analysis is a graphical-interface software based on the experience of PADME experiment. Recently the DarkSide collaboration developed a reconstruction software, parallel to PADME and based on Python programming language, called PyReD. More details on the reconstruction variables in PyReD are given in Section 5.2.

4 Multi-scattering dark matter particles in DEAP-3600

4.1 Introduction

Present dark matter experiments based on noble liquids are designed to detect WIMPs, weakly interacting massive particles, with masses below the unitary limit at 100 TeV. Nevertheless, several models allow for dark matter particles at higher masses; they arise with weak or color interactions from grand unification theories. Specifically, strongly interacting massive particles are expected to be produced in the early universe by out-of-equilibrium production [261] [262], Hawking radiation of primordial black holes [263], pre-heating [264], gravitational production at the end of inflation [265], as for the weakly-interacting WIMPzilla [266], and are modeled as composite coloured dark matter particles [267] [268], electroweak-symmetric solitons [269], Planck-mass black holes [270]. Dark matter detectors designed for WIMP search are not sensitive to most of the high cross-section particles due to the overburden attenuation. Still, if the mass is high enough, dark matter particles can penetrate the overburden layers, reaching the detectors. Regardless of the specific model, such heavy-strongly interacting dark matter particles are expected to interact more than once in the detector and are commonly grouped under the name "MIMPs", referring to the multi-scattering interaction expected. The main target of the present analysis is the detection/exclusion of MIMPs above $M_\chi \geq 10^{16}$ GeV, as lower masses were already excluded by DAMA in 1999 [271].
Particles at such high cross-section, above 10^{-24} cm^2 for the DM-nucleus cross-section, are expected to give always a detectable signal once they enter the active volume; so the interaction rate scales with the cross-sectional area, instead of the volume. Among all the running experiments based on noble liquids, DEAP-3600 (see Section 3.2) is the one with the largest cross-sectional area, large enough to find or exclude MIMPs up to Planck Mass. After giving the theoretical framework of the assumed models in Section 4.2, the consequent mass reach and the minimum MIMP-nucleus cross-section to which the experiment is sensitive, assuming no background, are described in Section 4.3. In Section 4.4 the overburden impact on the MIMPs velocity distribution, along their path from the halo to the detector, is fully accessed through a C++ Monte Carlo simulation. Then Section 4.5 shows the simulation of the MIMPs in the detector, outlining the variables of interest for the present analysis. It follows the review of the expected backgrounds for multi-scattering particles in Section 4.6. The comparison of the background

and the signal allows for the definition of the Region of Interests (ROIs) for MIMP search. Then Section 4.7 describes the Monte Carlo simulation validation, performed thanks to both a Physics Run and an Americium-Beryllium calibration run. Finally, the selection cuts and the corresponding acceptances are listed in Section 4.8, fully setting up the upcoming unblinding of three years of data-taking.

4.2 MIMP models

Direct detection experiments looking for dark matter spin-independent interactions with baryon matter can benefit of a A^2 enhancement due to the coherence of the interaction, together with a kinematic factor μ_T^2 of the dark matter-target nucleus reduced mass. The consequent relationship between the dark matter-target nucleus cross-section $\sigma_{\chi-T}$ and the elastic dark matter-nucleon cross-section $\sigma_{\chi-n}$ is

$$\sigma_{\chi-T} = \frac{\mu_T^2}{\mu_n^2} A^2 \sigma_{\chi-n}, \tag{4.2.1}$$

where μ_n is the dark matter-nucleon reduced mass. If $M_\chi >> M_T$, the dark matter-nucleus reduced mass $\mu_T \approx A\mu_n$, giving $\sigma_{\chi-T} \approx A^4\sigma_{\chi-n}$. This is assumed for dark matter particles at $\sigma_{\chi-n} \approx 10^{-44}$ cm^2, where the typical WIMP searches are performed, and are "model-independent" as they do not depend on the potential's exact shape. This allows for the comparison of the constrains from different experiments, as they do all finally refer to the same dark matter-nucleon cross-section.
At higher cross section, $\sigma_{\chi-n} \approx 10^{-30}$ cm^2, the Born approximation, which is valid only for weak couplings, stops holding, and Equation 4.2.1 may not hold, depending on the specific model, i.e. the interaction potential [272]. When the Born approximation stops holding, the interaction is fully described by the partial wave expansion. In order to access a straightforward analytical dark matter-nucleus scaling law and show the results in terms of the elastic dark matter-nucleon cross-section, two models are considered in the present analysis. The first assumes an elementary dark matter particle with a repulsive interaction, modeled as a top-hat potential; the second one models the MIMP as a composite particle, a dark matter "nugget". The two models are explained in the present section, with a focus on the $\sigma_{\chi-T}$ to the $\sigma_{\chi-n}$ scaling.

4.2.1 Elementary MIMP

The first model considered describes MIMPs as elementary particles, holding a contact nucleon-dark matter repulsive interaction, described by a simple top-hat model with a radius r_T,

$$V(r) = \begin{cases} V_0 & r < r_T \\ 0 & r > r_T \end{cases} \tag{4.2.2}$$

The differential cross-section is given by the square scattering amplitude $f(k, \theta)$,

$$\frac{d\sigma_{\chi-T}}{d\Omega} = |f(k, \theta)|^2 \tag{4.2.3}$$

For strong couplings and high cross-sections, the partial wave expansion allows for a full perturbative description of the interaction, as it holds even when Born approximation's hypothesis is not fulfilled. The scattering amplitude for a momentum k and a scattering angle θ can be written as an expansion of Legendre polynomials,

$$f(k, \theta) = \frac{1}{k} \sum_{l=0}^{\infty} (2l + 1) e^{i\delta_l} sin(\delta_l) P_l(cos\theta) \tag{4.2.4}$$

where the wave phase shifts δ_l are determined from Schrödinger equation [272]. The consequent MIMP-nucleus cross-section is then

$$\sigma_{\chi-T} = \frac{4\pi}{k^2} \sum_{l=0}^{\infty} (2l + 1) sen^2(\delta_l). \tag{4.2.5}$$

. The top-hat potential in Equation 4.2.2 allows for an analytic solution of the partial wave expansion, $\propto r j_l(k'r)$, where j_l is the l-th Bessel function and $k'^2 = k^2 - 2\mu_T V_0$ is the effective momentum. The main contribution comes from the s-wave, at l = 0 , which describes a spherical symmetric interaction in the center-of-mass frame. In the limit of weak coupling $k' r_T << 1$ the s-wave cross-section is [272]

$$\sigma_{\chi-T}^{l=0} \approx \frac{16\pi}{9} \mu_T^2 r_T^6 V_0^2 - \frac{128\pi}{45} \mu_T^3 r_T^8 V_0^3 + o(|V_0^4|). \tag{4.2.6}$$

The first term of the expansion also matches to the first Born approximation. In fact, the dark matter -nucleon cross-section at first order would be

$$\sigma_{\chi-n}^{l=0(1)} \approx \frac{16\pi}{9} \mu_n^2 r_n^6 V_0^2 \tag{4.2.7}$$

where μ_n is the nucleon mass and r_n its radius. Assuming a charge density independent of the atomic mass nucleus, $r_T = A^{1/3} r_n$; then the ratio of the per nuclear and the per nucleon cross-section at first order given by Equation 4.2.7 brings to the A^2 scaling

$$\sigma_{\chi-T}^{l=0\,(1)} = A^2 \frac{\mu_T^2}{\mu_n^2} \sigma_{\chi-n}^{l=0(1)} \xrightarrow{\mu_\chi >> \mu_T} A^4 \sigma_{\chi-n}^{l=0(1)} \tag{4.2.8}$$

which holds for weak interactions and coincides with the result of Born approximation. It follows that at first order and low cross-section, the partial wave expansion returns the model independent A^4 scaling in the limit $\mu_\chi >> \mu_T$. Then, at higher cross-section, Equation 4.2.6 shows that this scaling breaks down by increasing or decreasing the MIMP-nucleus cross-section according to the kind of the potential, just by the sign of the interaction – whether the interaction is repulsive or attractive.
Finally the cross-section saturates at about its geometrical cross-section. In the strong coupling limit, where $k' r_T >> 1$,

$$\sigma_{\chi-T} = 4\pi r_T^2. \tag{4.2.9}$$

The scaling between the per nuclear and the per nucleon cross-section is shown in Figure 4.2.1 for a target nucleus of liquid argon,

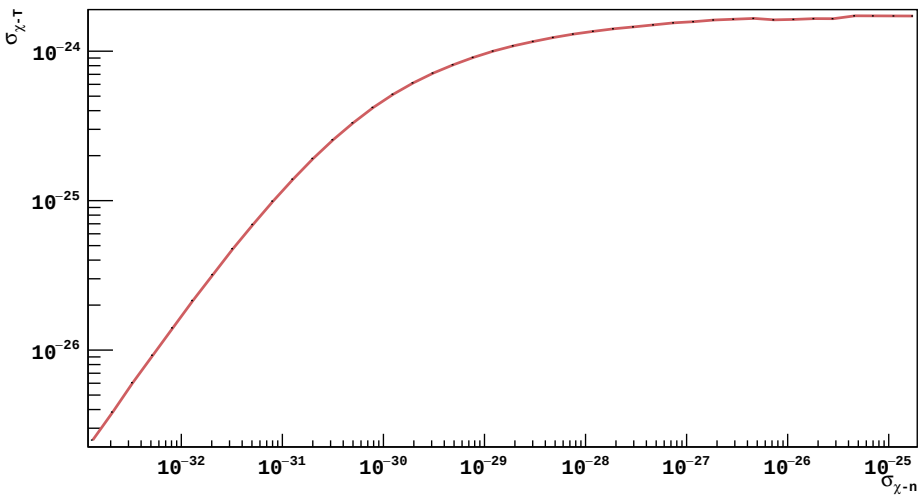

Figure 4.2.1: Scaling between the per nuclear and the elastic per nucleon cross-section for a elementary dark matter particle interacting with liquid argon through a repulsive top-hat potential.

4.2.2 Composite MIMP

The second model here considered assumes that MIMPs are composed by N_{DM} "dark nucleons", each with radius r_{DM} and mass m_{DM}. Therefore the MIMP nucleus mass is $\mathrm{M}_\chi = \mathrm{N}_{DM}\ \mathrm{m}_{DM}$, with a radius $R_{DM} = \mathrm{N}_{DM}^{1/3}\ \mathrm{r}_{DM}$. Analogously to Equation 4.2.8 in the limit $\mathrm{M}_\chi >> \mathrm{M}_T$, the scaling between nuclear and the elastic nucleon cross-section follows the A^4 scaling law at zero-momentum transfer. Then the dimensions of the dark matter nucleus and the target nucleus are taken into account by the respective form factors,

$$\sigma_{\chi-T} = \sigma_{\chi-n} A^4 |F_{DM}(q)|^2 N_{DM}^2 |F_T(q)|^2 \tag{4.2.10}$$

so that the form factors collect the loss of coherence at large transfer momentum q. Assuming elastic scattering with uniform coupling with all dark nucleons, the form factor is the three-dimensional Fourier transform of the nucleon density in the dark nucleus ρ_{DM}

$$F_{DM}(\vec{q}) = \int d^3\vec{r} e^{i\vec{q}\cdot\vec{r}} \rho_{DM}(\vec{r}) \tag{4.2.11}$$

If ρ_{DM} is uniform, the coupling is modeled by a spherical top-hat potential; then the MIMP form factor is written in terms of the spherical Bessel function j_1 [268],

$$F_{DM}(q) = \frac{3}{(qR_{DM})^3}[sin(qR_{DM}) - (qR_{DM})cos(qR_{DM})]. \tag{4.2.12}$$

The elastic dark matter-nucleus cross-section in Equation 4.2.10 depends on the squared dark matter form factor,

$$\begin{aligned} |F_{DM}(q)|^2 = \frac{9}{(qR_{DM})^6}[&sin^2(qR_{DM}) - 2cos(qR_{DM}) \\ &sin(qR_{DM}) + (qR_{DM})^2 cos^2(qR_{DM})] \end{aligned} \tag{4.2.13}$$

In the limit $qR_{DM} >> 1$, the first two terms become negligible; the $cos^2(qR_{DM})$ instead quickly oscillates with q, so that its envelope is given by the average on a full period. It follows that

$$|F_{DM}(q)|^2 \xrightarrow{\mathrm{q\ R}_{DM} >> 1} \frac{9\pi}{(qR_{DM})^4}. \tag{4.2.14}$$

On the other hand, assuming the same dark matter scattering length with neutrons and with protons, the target nucleus is modeled with the Helm form

factor with the Lewin-Smith parametrization [273] [274] [275]. In the limit $qR_T << 1$,

$$F_T(q) = \frac{3}{(qR_T)^2}[sin(qR_T) - (qR_T)cos(qR_T)]e^{(-q^2s^2)/2} \xrightarrow{\text{q R}_T << 1} 1. \tag{4.2.15}$$

So in the limit by which $qR_{DM} >> 1$ and $qR_T << 1$, Equation 4.2.10 becomes

$$\sigma_{\chi-T} = \sigma_{\chi-n}A^4\frac{N_{DM}^{\frac{2}{3}}}{(qr_{DM})^4}. \tag{4.2.16}$$

Equation 4.2.16 describes the scaling of the dark matter - target nucleon cross section, which is actually $\propto A^4$. Still the dark matter-target cross-section $\sigma_{\chi-T}$ is bound from above by the geometric cross section,

$$\sigma_{geo} = 4\pi R_{DM}^2 = 4\pi N_{DM}^{2/3} r_{DM}^2 \tag{4.2.17}$$

determining a saturation of the interaction.
In the present analysis the results will be first shown in terms of the dark matter-nucleus cross-section; only after the full unblinding of the three years of data, it will be applied to the two models here described, in order to show them in the usual exclusion curves given by the dark matter mass compared with the spin independent elastic dark matter-nucleon cross-section. Hence Equation 4.2.16 and Equation 4.2.17 ask for benchmark parameters for the dark matter nugget composition. In the present analysis it was assumed $R_{DM} \simeq 10^3$ fm, in analogy with baryon QCD nucleons. The typical momentum transfer is $q = 0.40$ fm^{-1} in liquid Argon. As MIMPs are searched above $\mathrm{M}_\chi \geq 10^{10}$ GeV, assuming $\mathrm{m}_{DM} \simeq 1$ GeV it follows $N_{DM} = 10^{10}$; also as $R_{DM} \simeq 10^3$ fm, the dark nucleon radius is $r_{DM} \simeq 1$ fm. This assumption is surely counter-intuitive, if compared with the usual nuclear structure of baryon matter; on the other hand, it should be pointed out that no electromagnetic repulsive forces are expected between dark nucleons, so no limit to the extension of the nucleus is expected. These parameters fulfill both the limits $qR_{DM} >> 1$ and $qR_T << 1$, so Equation 4.2.16 holds up to the saturation at σ_{geo} in Equation 4.2.17.

4.3 Sensitivity of DEAP-3600

In the present section, the mass reach and the minimum cross-section in absence of backgrounds of DEAP-3600 is accessed, for both the models considered. The aim is to show the a priori physics potential of the detector in the multi-scattering frontier. After listing the optimized selection cut and

the correspondent MIMP acceptance in Section 4.8, the effective mass reach and cross-section threshold will be addressed.
The instantaneous MIMP flux over a small area is given by $\phi = n \cdot v$, where n is the MIMP number density and $< v_\chi >= 300$ km/s the average velocity, calculated from the usual truncated Maxwell-Boltzmann distribution,

$$f(v) = v \cdot exp\left[-\frac{v^2 + v_0^2}{\sigma_v^2}\right] \cdot exp\left[\frac{2vv_0}{\sigma_v^2}\right] - exp\left[\frac{c_{min}2vv_0}{\sigma_v^2}\right] \tag{4.3.1}$$

where v is the MIMP velocity in the detector frame, $v_0 = 220$ km/s is the Sun velocity, also numerically equivalent to the dispersion σ_v. The galactic escape velocity $v_{esc} = 544$ km/s enters the constant c_{min},

$$c_{min} = Min\left(-1, \frac{v^2 - v_{esc}^2 - v_0^2}{2vv_0}\right) \tag{4.3.2}$$

Then the total flux Φ in the detector is given by the integration on the whole surface area A_{det} and the exposure time t_{exp},

$$\Phi = \frac{\rho_\chi}{M_\chi} < v_\chi > A_{det} t_{exp}. \tag{4.3.3}$$

The MIMP number density n is the ratio of the halo density $\rho_\chi = 0.3$ GeV/(c^{2}cm^3) and the dark matter mass M_χ. The active mass of the detector is the LAr contained in the inner vessel, a sphere of radius 85 cm for the DEAP-3600 inner vessel.
At such high cross-sections, about $\sigma_{\chi-T} \approx 10^{-25}$ cm^2, any MIMP reaching the detector will give a signal, so the number of observed events will depend only on the flux, which decreases with the increase of the MIMP mass. By asking at least 2.3 events in the exposure time $t_{exp} = 3$ years, from Equation 4.3.3 it follows that the maximum MIMP mass that can be observed in DEAP-3600 is

$$m_{\chi-max} = 3.3 \cdot 10^{19} GeV/c^2. \tag{4.3.4}$$

As all MIMPs reaching the detector will give at least one scattering, the minimum dark matter-nucleus cross-section $\sigma_{T-\chi}$ follows by asking a unitary optical depth,

$$\tau = \sigma_{T-\chi min} n \lambda_{path} = 1, \tag{4.3.5}$$

where n is the numerical target density and λ_{path} is the characteristic path length. The number density in Liquid Argon is $n = 2.1 \cdot 10^{22}$ cm^{-3}; assuming the inner vessel radius as λ_{path} brings to

$$\sigma_{LAr-\chi min} = 5.6 \cdot 10^{-25} cm^2 \tag{4.3.6}$$

In Figure 4.3.1 the sensitivity that can be achieved with DEAP-3600 assuming no background is shown. As already stated, the scaling between the per nuclear and the per nucleon cross-section strongly depends on the interaction's detail at typical MIMP masses and cross-section. Hence the limit is represented in terms of the MIMP-target nucleus cross-section. By requiring multiple interactions in the detector the shapes of the exclusion limits are determined: the detector's sensitivity is mainly independent on the mass of the MIMP particle as the cross-section decreases. Up to day, the highest explored mass is $M_\chi = 10^{16}$ GeV [272]; with only three years of data taking, DEAP-3600 will be the only running experiment scanning MIMPs up to Planck mass.

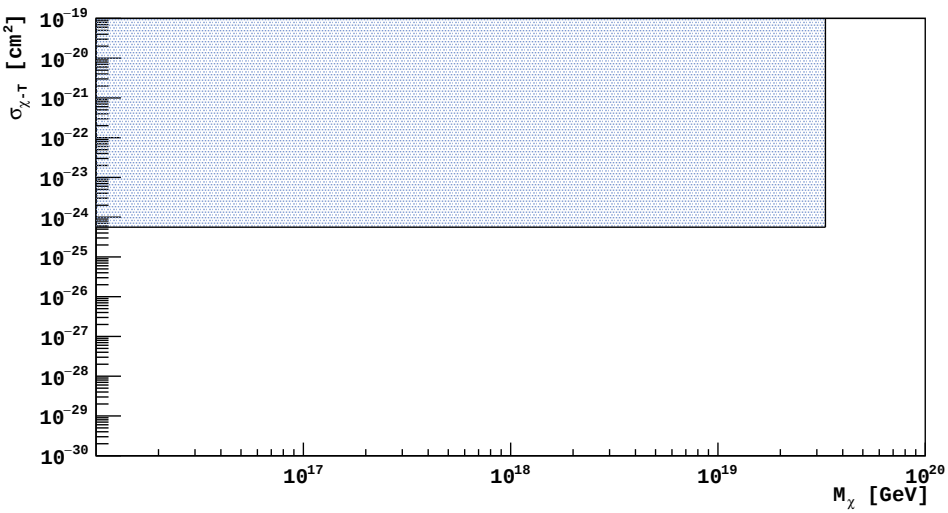

Figure 4.3.1: Sensitivity of DEAP-3600 to MIMPs with three years of data taking, assuming no background. Thanks to its wide exposure, it would be the only running experiment with a mass reach greater than Planck Mass. The lowest cross section at which DEAP-3600 is sensitive is $\sigma_{\chi-T} = 5.6\ 10^{-25}$ cm^2, assuming no background. Lower mass ranges has already been excluded [272].

4.4 Propagation through the overburden

Differently from WIMPs, dark matter particles with $\sigma_{\chi-T} \approx 10^{-24}$ cm^2 are expected to lose a non-negligible fraction of their kinetic energy during their path to the detector, due to the wide numbers of scatterings with atoms of the Earth and the atmosphere -whose ensemble is here called "overburden". The impact on the MIMP kinetic energy is studied with a custom-developed

C++ based Monte Carlo simulation. In the present section, the details of the simulations are described for MIMPs reaching DEAP-3600, set 2 km underground.
As a consequence of their very high mass, the deflection angle after each of the scatterings with the elements in the overburden is negligible,

$$\alpha_R \approx \frac{m_T}{m_\chi} \approx 10^{-15} rad. \tag{4.4.1}$$

This means that MIMPs, once extracted from the halo, will propagate down to the detector through an effectively straight line. Figure 4.4.1 shows the average incoming direction for a MIMP at SNOLAB in function of α, defined as the angle between the MIMP average incoming direction and the detector position vector from the Earth center, for one entire year, starting from 11 July.

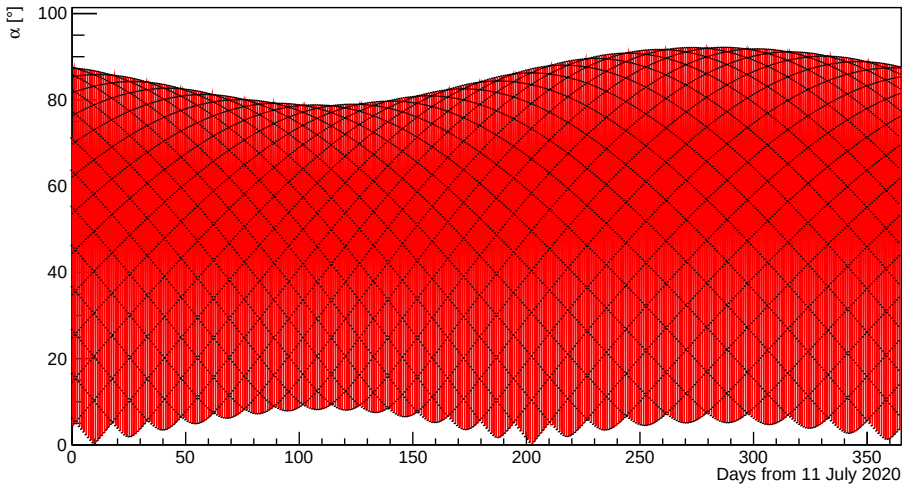

Figure 4.4.1: Average MIMP incoming direction at SNOLAB, where the angle α is defined between the MIMP average incoming direction and the detector position vector from the Earth center. For reference, the flux modulation is shown along the whole year, starting from the 11th July.

The oscillations reflect the Earth's revolution motion; on average, the MIMP flux is expected to come from overhead, at about 50° for an observer at SNOLAB.
The number of scatterings performed by the MIMPs along the overburden will be the sum of the scattterings done with each of the elements species

present in the overburden. For a single target species T, the number of performed scatterings is

$$N_T = \int_0^{L_T} n_T(r)\sigma_{T-\chi} ds \tag{4.4.2}$$

where L_T is the length of the path through the medium with the element T, $n_T(r)$ is the numerical density of the target T in that medium and $\sigma_{T-\chi}$ is the target-MIMP cross-section, which is related to the nucleon-MIMP cross-section according to the specific model hypothesis.
The total length of the MIMP path from the halo to the detector L depends on the incoming direction of the MIMP particles, as it is shown in Figure 4.4.2.

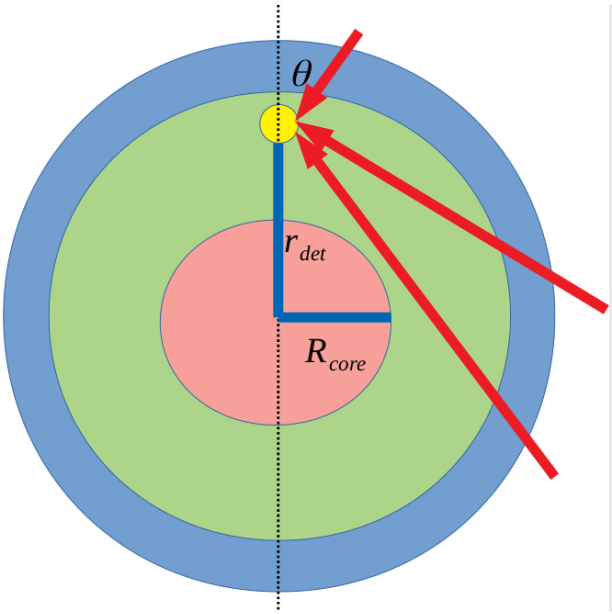

Figure 4.4.2: Propagation of the MIMPs along different paths, depending on the incoming direction in the detector frame. The overburden is divided into: atmosphere (blue), crust/mantle (green), core (red). θ is defined as the angle between the incoming MIMP direction and the detector zenith.

If θ is the angle between the MIMP average flux and the zenith of the detector, L is

$$L = -r_{det}cos\theta + \sqrt{(R_{earth} + L_{atm})^2 - (r_{det}sin\theta)^2} \tag{4.4.3}$$

in which $R_{earth} = 6.4 \cdot 10^3$ km is the Earth average radius, $r_{det} = R_{earth} - d$ is the distance from the Earth center of the detector, installed at a depth

$d = 2$ km for DEAP-3600. The atmosphere is assumed to be all focused in the closest $L_{atm} = 80$ km from the ground. The density profile is assumed as reported in [276], with a composition of 78 % of Nitrogen and 21 % of Oxygen.
The radius r from the Earth center is written in terms of the step s along the path L,

$$r = \sqrt{(R_{earth} + R_{atm})^2 + s^2 - 2s(r_{det} cos\theta + L)}. \tag{4.4.4}$$

The number density $n_T(r)$ in Equation 4.4.2 is a continuous function of the radius defined in Equation 4.4.4; the mass density profile is taken from [277]. The components of the core and the crust/mantle are listed in Figure 4.4.3, together with their abundance.
Due to the high number of scatterings in the overburden, it is worth assuming a continuous energy loss [278], whose average decreases as

$$\frac{d < E_\chi >}{dt} = -\sum_i n_i(\vec{r})\sigma_{\chi-i} < E_R >_i v \tag{4.4.5}$$

where v is the MIMP velocity from the halo; the sum runs over the atoms in the overburden, so $\sigma_{\chi-i}$ is the MIMP-nucleus cross-section, n_i is the local density of the i-th element, on which on average a recoil energy $< E_R >_i$ is deposited.

Element	Atomic number	Mass fraction Core	Mass fraction Mantle
Oxygen, O	16	0.0	0.440
Silicon, Si	28	0.06	0.210
Magnesium, Mg	24	0.0	0.228
Iron, Fe	56	0.855	0.0626
Calcium, Ca	40	0.0	0.0253
Phosphor, P	30	0.002	0.00009
Sodium, Na	23	0.0	0.0027
Sulphur, S	32	0.019	0.00025
Nickel, Ni	59	0.052	0.00196
Aluminum, Al	27	0.0	0.0235
Chromium, Cr	52	0.009	0.0026

Figure 4.4.3: List of the elements composing the mantle and the core. The core is assumed to be uniform, while the mantle also includes the crust [279].

The average recoil energy can be written as

$$< E_R >_i \sigma_i(v) = \int_0^{E_i^{max}} E_R \frac{d\sigma_i}{dE_R} dE_R \tag{4.4.6}$$

where, assuming a model-independent scaling on the cross-section,

$$\frac{d\sigma_i}{dE_R} = \frac{m_i \sigma_n^{SI}}{2\mu_{\chi,n}^2 v^2} A_i^2 F_i^2(E_R). \tag{4.4.7}$$

It follows that Equation 4.4.6 can be written as

$$\sigma_i(v) < E_R >_i = \frac{\mu_{\chi-i}^4 v^2}{\mu_{\chi-n} m_i} \sigma_n^{SI} A^2 \int_0^1 2x F_i^2(x E_i^{max}) dx = \frac{\mu_{\chi-i}^4 v^2}{\mu_{\chi-n} m_i} \sigma_n^{SI} A^2 C_i(m_\chi, v). \tag{4.4.8}$$

Hence, the average energy loss in Equation 4.4.5 is

$$\frac{d < E_\chi >}{dt} = \frac{v^2 \sigma_n^{SI}}{\mu_{\chi-n}^2} \sum_i n_i \frac{\mu_{\chi-i}^4}{m_i} A_i^2 C_i(m_\chi, v). \tag{4.4.9}$$

As MIMPs are not relativistc, E_χ = m_χ $\mathrm{v}^2/2$; hence the velocity attenuation after a step dx is

$$\frac{dv}{dx} = -\frac{v^2 \sigma_n^{SI}}{\mu_{\chi-n}^2} \sum_i n_i \frac{\mu_{\chi-i}^4}{m_i} A_i^2 C_i(m_\chi, v). \tag{4.4.10}$$

One example of the simulation is shown in Figure 4.4.4, for a MIMP entering the detector from different directions (the zenith is at $\theta = 0$), with mass M_χ = 10^{16} GeV and cross-section $\sigma_{\chi-T} = 2.6 \times 10^{-18}$ cm^2.

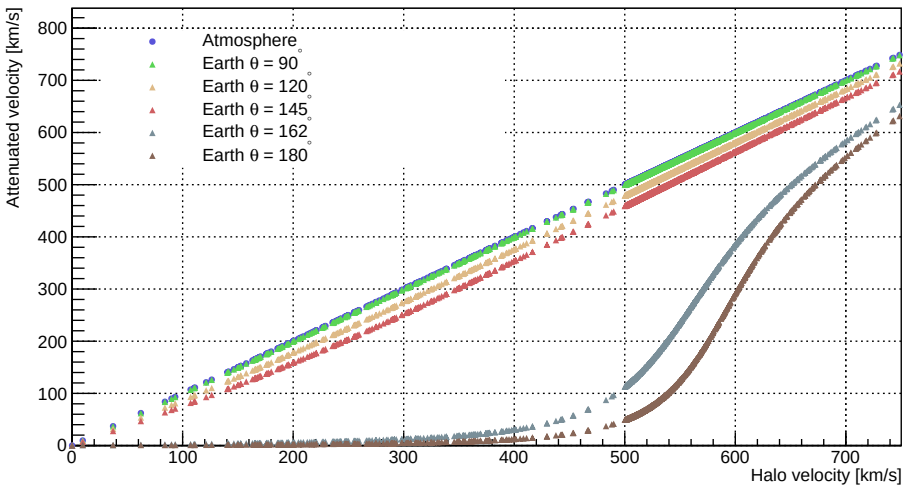

Figure 4.4.4: Attenuation of a MIMP particle coming from different directions (the zenith is set at $\theta = 0$) in DEAP-3600 with mass $M_\chi = 10^{16}$ GeV and cross-section $\sigma_{\chi-T} = 2.6 \times 10^{-18}$ cm^2 after passing through the atmosphere (blue) and the mantle (green).

The impact from the atmosphere only is negligible, as the elements in the atmosphere are much lighter than MIMP masses. For the same reason, most of the impact of the overburden is felt from MIMPs at high θ, passing through the Earth core. The output is the velocity after the overburden attenuation: this will be the input to the GEANT4 simulation, reproducing the MIMP path in the detector.

4.5 Expected signal of MIMPs in DEAP-3600

The analysis is based on both the background and the MIMP signal's knowledge, whose expectations are based on Monte Carlo simulations. The present section deals with the expected signal given by the scatterings of a MIMP in the detector. In general, the expected path is an almost collinear path of recoils, with a negligible deflection after each scattering, thanks to the very high ratio between the incident and the target particle masses. The average argon recoil energy per scattering is $E_{rec,1} \approx m_T v_\chi^2 \approx 40$ keV$_{NR}$, which is quenched to about 11 keV$_{ee}$ [235]. The average number of scatterings is

$$< N >= \sigma_{\chi-T} n_{LAr} R, \tag{4.5.1}$$

where $R = 85$ cm is the radius of the inner vessel and $n_{LAr} = 2.1 \cdot 10^{22}$ cm^{-3} the number density of liquid argon; then the average number of scatterings

follows from the MIMP-nucleus cross-section, $N = \sigma_{\chi-T} \cdot 1.8 \cdot 10^{24}$ cm^{-2}. The consequence is that the shape itself of the expected signal strongly depends on the cross section, while is independent on the MIMP mass. Three main regimes are expected, according to the number of expected scatterings:

- at $\sigma_{\chi-T} \approx 10^{-24}$ cm^2 and below it, O(1) scatterings are expected, giving a deposited energy of O(10) keV$_{ee}$;
- at $\sigma_{\chi-T} \approx 10^{-23}$ cm^2, O(10) scatterings are expected, all distributed quite uniformly along the acquisition window, and giving a deposited energy of O(100) keV$_{ee}$;
- at $\sigma_{\chi-T} \approx 10^{-22}$ cm^2 and above, O(100) scatterings are expected, giving a deposited energy of O(1) MeV$_{ee}$.

Whatever the number of scatterings, all of them are expected to be distributed in about 6 μs, which is the time required by a particle with an average velocity v_{DM} =300 km/s to pass through the inner vessel.
A custom-developed GEANT4 generator simulates the detector's response to the multi-scattering dark matter particle; its output was compared with the aforesaid described expected signal. The generator takes in input the dark matter-nuclear cross-section, the velocity, and the particle's position as it enters the detector. A velocity of 220 km/s was set in input in the present analysis simulations. The simulation here performed assumes an elementary MIMP-so no form factor assumed- while the Helm form factor describes the target nucleus. After entering the detector, the position is updated assuming that the MIMP propagates through a straight line: the direction is kept from the input, while the displacement of the MIMP is the local average path length, calculated from the scattering cross-section of the elements composing the local material. The key in the generator, as no WIMP or MIMP particle is stored in the PDG, is to simulate the scattered nucleus, instead of the dark matter particle scattering on it. Here specifically, the liquid Argon nucleus recoils, giving the scintillation light, with the vertex position and time determined by the MIMP displacement. Hence instead of a MIMP scattering along with all the Liquid Argon nuclei, the nuclei bumped by a "phantom" particle are simulated.

An example of an output waveform is showed in Figure 4.5.1, for a MIMP coming from the zenith in the lab frame, with mass $M_\chi = 10^{18}$ GeV and $\sigma_{\chi-T}$ $= 2.6 \cdot 10^{-22}$ cm^2 .

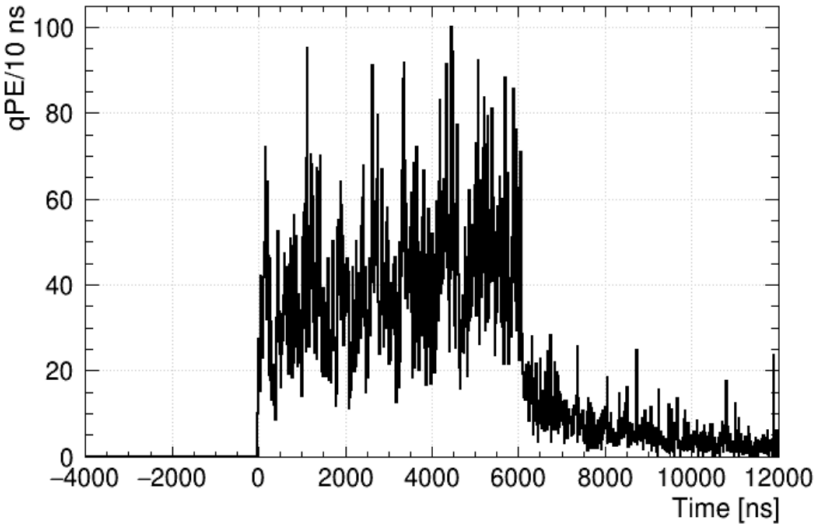

Figure 4.5.1: Waveform for a simulated MIMP event in DEAP-3600, with $\sigma_{\chi-T} = 2.6\ 10^{-22}$ cm^2 and $M_\chi = 10^{18}$ GeV. The MIMP passes through the inner vessel in 6 μs; then a tail of afterpulses follows.

At such high cross-section Equation 4.5.1 returns about 400 expected scatterings. All the pulses are acquired in the same acquisition window, so as the same triggered event, and are uniformly distributed in the first ≈ 6 μs from the trigger. For the waveform here showed the equivalent recoil energy of the triggered event would be approximately 3.5 MeV, assuming a quenching of 20 %. The scintillation light from this event is expected to be widely uniformly distributed through all the PMTs looking at the inner vessel, as the 3.7 MeV comes from a collinear path crossing the whole detector. Furthermore, Figure 4.5.1 shows that not all the pulses are distinguishable: they mostly "merge", so that the hundreds of pulses return only about a dozen of higher peaks. Given the peculiar shape of the expected signal, with more pulses uniformly distributed along the waveform, but triggered as a single event with a very uniform light distribution, the selection cuts based on the variables optimized for WIMP search does not match with the ones to apply to reject MIMPs for the foreseen background.
Whereas WIMPs nuclear recoils can be discriminated from betas and gammas in liquid argon thanks to the pulse shape discrimination, the same rejection power is not foreseen for a MIMP event, due to the distribution of the pulses along the acquired waveform. Then, in principle, all nuclear and electron recoils are a potential background. Still, MIMPs are expected to perform more than one scattering in the detector, so any variable looking at the number of "pulses" along the waveform will discriminate MIMPs from any

single-scatter event, whatever the kind of recoil (nuclear or electron recoil). Still, it is possible that two or more background recoils happen in the same acquisition window –what is called "pile-up event". Custom selection cuts will be optimized to minimize the pile-up impact on the detector sensitivity. In Section 4.6 the expected backgrounds beside single-scatter events are fully listed.
In the present analysis the detector potential in the MIMP search is addressed by only exploiting the variables already stored in the database and the already implemented DAQ specifics. The variables chosen as the ones which best describe MIMPs in DEAP-3600 are:

- **qPE**, which is the number of photoelectrons in the first 10 μs after the trigger time. The photoelectron counting is performed as the ratio of the charge in input in a PMT pulse with the Single PhotoElectron Response (SER) charge [280]. No afterpulse-correction is applied, as the energy range of the analysis goes above the energy at which the afterpulse-removal algorithm was validated. The qPE variable in the present analysis is related to the scattering regime and hence to the MIMP-nucleus cross-section.

- **Fprompt** is defined as the ratio of the prompt light in the scintillation signal normalized to the total number of photoelectrons. The prompt window, which optimizes the rejection of the WIMP signal from the background, starts 28 ns before the trigger and ends after 150 ns,

$$Fprompt = \frac{\sum_{-28ns}^{150ns} PE(t)}{\sum_{-28ns}^{10\mu s} PE(t)}. \tag{4.5.2}$$

  A very low Fprompt is expected for multi-scattering particles; specifically, Fprompt is expected to decrease with the increase of the number of scatterings and hence of the cross-section; it thus is expected to help with the discrimination from nuclear recoil background.

- **FmaxPE**, which calculates the fraction of photons collected in the brightest PMT. As already stated, the scintillation light from a MIMP is expected to be uniformly distributed through all PMTs, giving a very low FmaxPE, compared to any other localized background.

- **ChargeTopRing** and **ChargeSecondRing**, which return respectively the charge collected in the first and the second top ring of PMTs, the closest to the neck. As for FmaxPE, the uniform light distribution from a MIMP will return a meager fraction of the light in the highest

PMTs. It is therefore defined the **Charge Top Ratio**, as the sum of ChargeTopRing and ChargeSecondRing normalized to qPE.

- **SubeventN**, which gives the number of main peaks along the waveform. The respective GEANT4 processor *MultiEvent* builds a binned waveform from the pulses of all PMTs and calculates the (discrete) derivative of the waveform. When the derivative is at least 3 ADC/ns above the baseline, a peak or "subevent" is triggered. It is assumed to start three bins before the trigger time and it ends when the derivative goes below 0.25 ADC/ns and the current voltage is closer than 2 ADC to the baseline. The following potential pulse must also present a "significant" derivative to be tagged as subevent, i.e. it must not be smaller than 5 ADC from the recognized previous one.

As they were designed for WIMP search only, the chosen variables are not optimized for MIMPs; still, as it will be shown in the next sections, they allow for a good background rejection power. MIMPs were simulated with the GEANT4 generator at different masses and cross-sections, spanning the space of parameters to which DEAP-3600 is expected to be sensitive, shown in Figure 4.3.1. An example is given in Figure 4.5.2, where four thousands of MIMPs at $\sigma_{\chi-T} = 2.6 \times 10^{-22}$ cm^2 are compared for $M_\chi = 10^{16}$ GeV and $M_\chi = 10^{19}$ GeV, by looking at their distribution on the qPE vs FPrompt plane. The number of photoelectrons qPE and the fraction of the prompt light Fprompt matches with the expectation at $\sigma_{\chi-T} = 2.6 \cdot 10^{-22}$ cm^2. The number of photoelectrons is, on average, 27000 qPE; as the implemented light yield is 7.1 qPE/keV$_{ee}$, this brings to an overall recoil energy of about 3800 keV$_{ee}$, and so to about 400 scatterings, as expected at high cross-sections. Also, assuming that the scatterings are uniformly distributed along the 6 μs employed by the MIMP to cross the detector, the fraction of scatterings in the prompt window will be 150 ns/ 6 μs = 0.025, each with a fraction of prompt light of 0.7; hence the total MIMP event will have Fprompt = 0.018 on average.

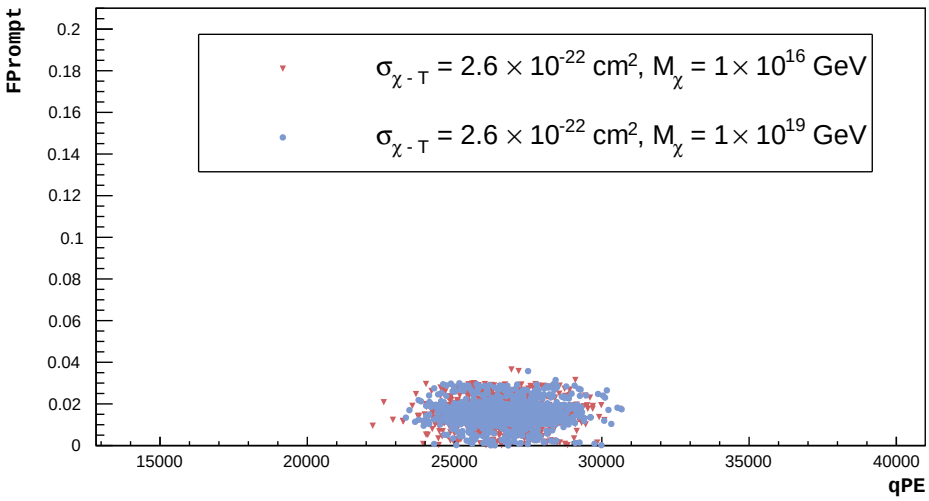

Figure 4.5.2: Distribution in the qPE vs Fprompt plane of MIMPs at the same MIMP-nucleus cross-section $\sigma_{\chi-T} = 2.6 \times 10^{-22}$ cm^2 and different mass, $M_\chi = 10^{16}$ GeV and $M_\chi = 10^{19}$ GeV.

Furthermore, the comparison of two MIMP populations reminds that due to the very high MIMP mass the shape of the signal –and hence the stored variables– does not depend on the MIMP mass, but only on the cross-section. Once that the detector response independence to the MIMP mass is confirmed, the MIMP-nucleus cross-section's role is analyzed. The distribution of MIMPs for cross-section going from $\sigma_{\chi-T} = 10^{-24}$ cm^2 to $\sigma_{\chi-T} = 10^{-22}$ cm^2 is showed in terms of all the listed variables, for $M_\chi = 10^{18}$ GeV. Figure 4.5.3 shows the comparison in the qPE-Fprompt plane. The number of reconstructed photoelectrons qPE matches the expected average number of scatterings for any simulated cross-section, increasing as the MIMP-nucleus cross-section increases. For instance, MIMPs at $\sigma_{\chi-T} = 5.2 \cdot 10^{-22}$ cm^2, at high cross-sections, scatter about 900 times with LAr, giving a triggered event of about 50000 qPE. On the other hand, events at low cross-section are observed at about 60 qPE , as O(1) scatterings are expected.

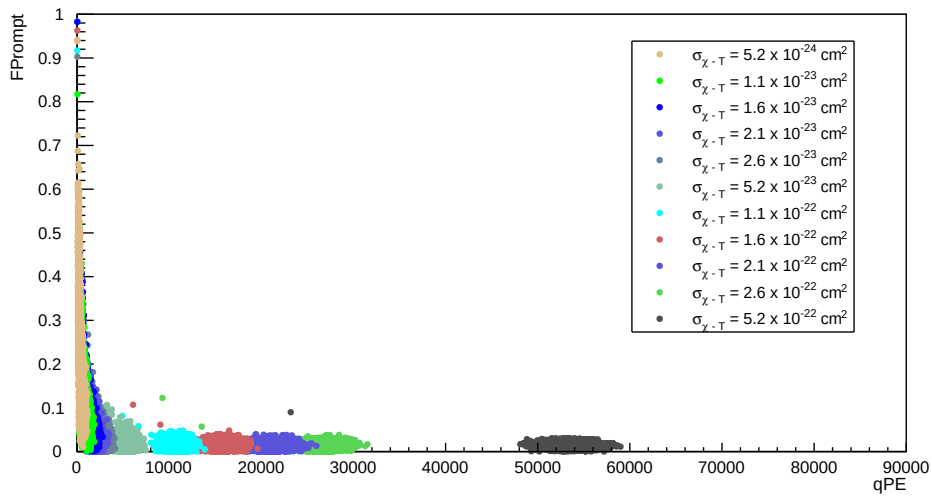

Figure 4.5.3: Comparison of MIMPs in terms of qPE and FPrompt variables. The cross-sections shown go from $\sigma_{\chi-T} = 10^{-24}$ cm^2 to $\sigma_{\chi-T} = 10^{-22}$ cm^2, while the mass is $M_\chi = 10^{18}$ GeV. For each cross-section, qPE agrees with the number of expected scatterings, assuming average recoil energy of 8-12 keV$_{ee}$ for each scattering, and hence increases with the cross-section. FPrompt, on the other hand, decreases with the increase of the cross-section, as the number of scatterings which fall out of the prompt window increases.

FPrompt variable was designed and optimized for the single scatter dark matter search. It still shows a monotone decrease, as the cross-section increases. In fact, as the number of scatterings increases, and as they are uniformly distributed along the waveform, also the number of pulses after the first 150 ns increases, lowering the fraction of prompt light. Going to lower cross-sections, the number of scatterings decreases to a few ones, and the Fprompt increases up to the usual nuclear recoil band, at $Fprompt \approx 0.7$.

A uniform distribution of the light in the PMTs is generally expected from a MIMP, as it gives scintillation light through the whole detector. This contrasts with events from single scatter background from inner vessel radioactivity, who will return a less heterogeneous light distribution. Hence FmaxPE variable is expected to help with background rejection in any energy range. In Figure 4.5.4, the distribution of FmaxPE is shown in terms of the number of photoelectrons qPE. The trend of FmaxPE reminds that of the Fprompt variable: as the number of scatterings decreases to O(1), at low cross-sections, at $\sigma_{\chi-T} < 10^{-23}$ cm^2, FmaxPE spreads at a higher value, as expected. On the other side at qPE $\approx$ 3000 and above, the fraction of light

stands at least below 0.05, decreasing as the cross-section increases.

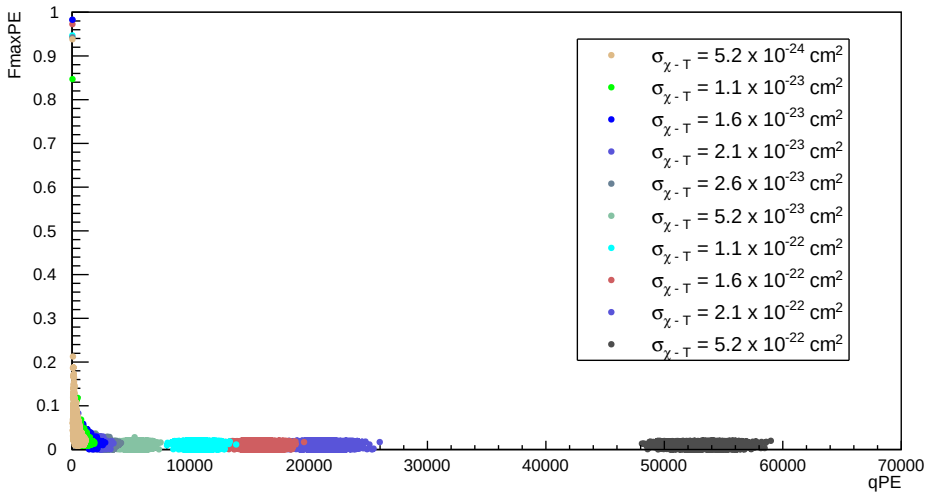

Figure 4.5.4: FmaxPE distribution for MIMPs at different cross-sections. FmaxPE shows a behaviour analog to Fprompt: a monotone but non-linear increase with the cross-section decrease, with a spread at FmaxPE higher than 0.1 only at low cross-sections, below 4000 qPE.

The uniform distribution of the scintillation light in a MIMP event also determines a very low fraction of Top Charge Ratio. For MIMPs this is approximately 3 % of the total qPE, as shown in Figure 4.5.5.

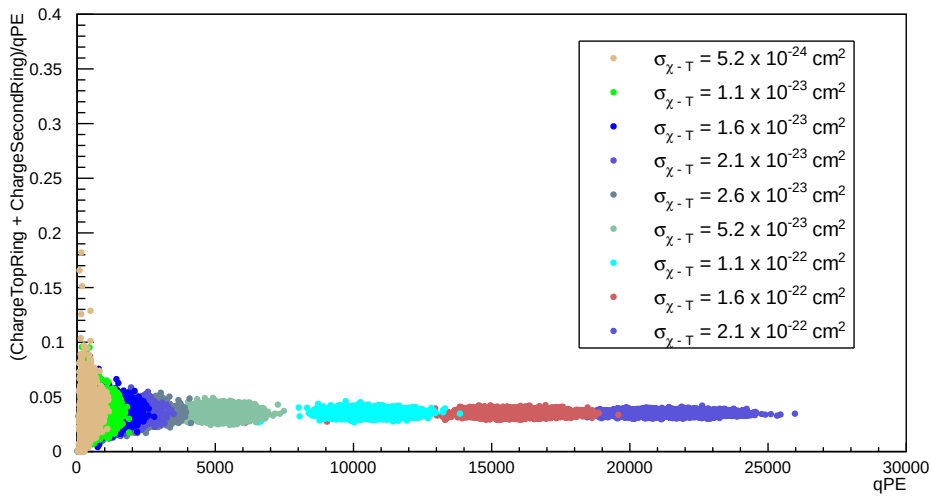

Figure 4.5.5: Distribution of Top Charge Ratio, the fraction of charge in the first and second top PMT rings normalized to qPE, for MIMPs at different cross-sections. At high energy, above the LAr endpoint, Top Charge Ratio is below 0.05, while at lower energies, it spreads up to 0.1.

As already noticed with Fprompt and FmaxPE variables, also in Top Charge Ratio the multi-scattering regime determines a unique response of the detector, giving a Top-Charge Ratio of maximum 0.05 above $\approx$ 3000 qPE and hence above $\sigma_{\chi-T} = 2 \times 10^{-23}$ cm^2. On the other hand, at low cross-section MIMPs show a wider distribution, due to the loss of the multi-scattering shape as it approaches the single-scatter limit. A cut on this variable will allow for the rejection of background events scattering in the Gas Argon pocket, who return a much higher charge fraction in the top rings.

The number of peaks across the waveform is the main evidence of the multiple scatterings; hence MIMPs are also studied in terms of the variable SubeventN. This was originally defined to reject pile-ups background in the standard WIMP analysis; in the multi-scattering analysis, this is instead the key variable to discriminate dark matter particles from single-scatter backgrounds and pile-up backgrounds, with a Monte Carlo tuned selection cut that will be shown in Section 4.8. For reference, in the waveform shown in Figure 4.5.1 SubeventN is equal to 10, while more than 400 scatterings are simulated. This can be compared with the waveforms of MIMPs at lower cross-sections. At $\sigma_{\chi-T} = 2.6 \times 10^{-24}$ cm^2, where a bunch of scatterings is expected, shown in Figure 4.5.7, the number of scatterings usually corresponds to the value of SubeventN. At $\sigma_{\chi-T} = 2.6 \times 10^{-23}$ cm^2, instead, SubeventN is not equal to the number of scatterings but is still proportional to it; hence

in Figure 4.5.6 about 60 scatterings are simulated, but SubeventN = 13.

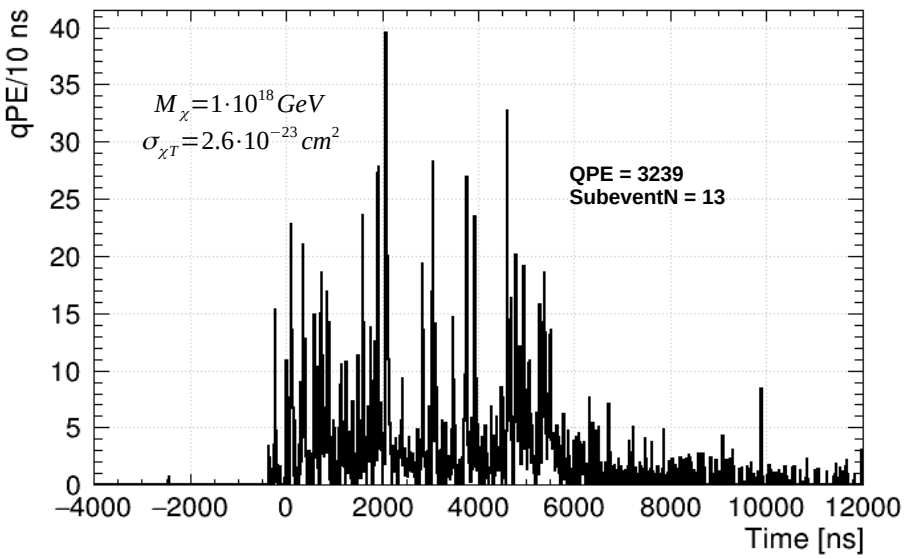

Figure 4.5.6: Waveform for a simulated MIMP event in DEAP-3600, with $\sigma_{\chi-T}$ = 2.6 $\times 10^{-23}$ cm^2 at M$_\chi$ = 10^{18} GeV. SubeventN returns the number of highest peaks along with the acquisition gate, recognized by the waveform derivative's significance. Only if the peak has a derivative above 5ADC/sample, it is stored as Subevent. For O(10) scatterings, the value of SubeventN does not match with the number of scatterings, but is proportional to it.

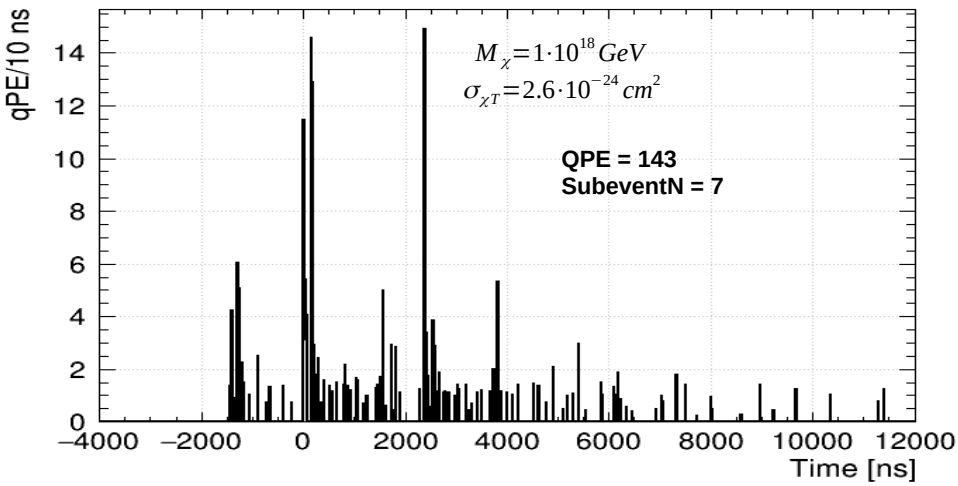

Figure 4.5.7: Waveform for a simulated MIMP event in DEAP-3600, with $\sigma_{\chi-T} = 2.6 \times 10^{-24}$ cm^2 and $M_\chi = 10^{18}$ GeV. At such low cross-section SubeventN mainly matches with the number of scatterings.

A more clear picture of SubeventN response to MIMPs is given by Figure 4.5.8 where its distribution is shown for a wide range of cross-sections and hence of qPE.

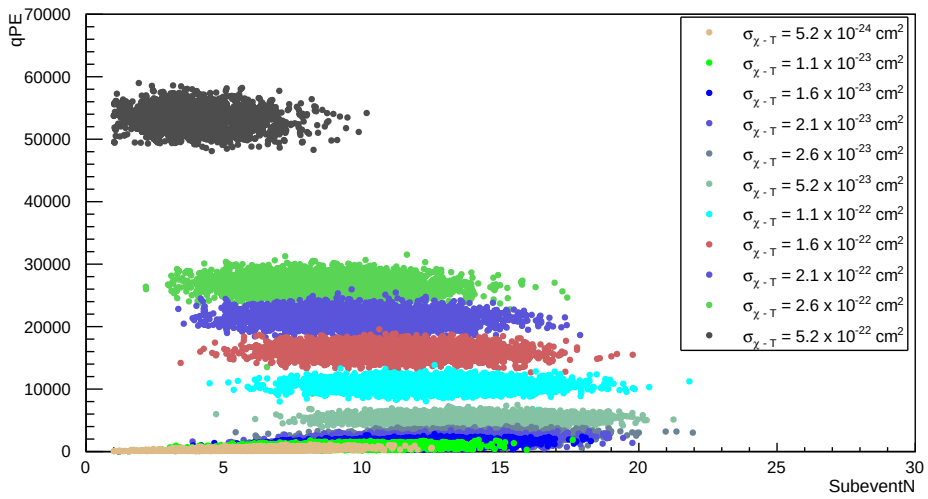

Figure 4.5.8: Distribution of SubeventN for a wide range of cross-sections and hence of deposited energy. The variable SubeventN shows not-monotone behaviour. Going from about $\sigma_{\chi-T} = 10^{-24}$ cm^2 up to about $\sigma_{\chi-T} = 10^{-23}$ cm^2, it increases with the cross-section and the number of scatterings. Then it starts decreasing with the increase of the cross-section. This is a consequence of the MultiEvent processor tuning, which looks at the peaks along the waveform and saves peaks as "subevent" only if their derivative is significant.

In presence of a bunch of recoils in the same waveform, the MultiEvent processor, which stores SubeventN variable, set SubeventN = n, where n is the number of recoils. So, if each pulse on the MIMP signal would be distinguished by the MultiEvent processor, the number of SubeventN would be directly proportional to the number of scatterings in the detector and then to qPE. Instead, Figure 4.5.8 shows a clear saturation. In fact, SubeventN increases going from $\sigma_{\chi-T} = 10^{-24}$ cm^2 to $\sigma_{\chi-T} = 10^{-23}$ cm^2, so up to about 50 scatterings. Then, as the number of scatterings, the number of reconstructed subevents decreases, as their significance is too low compared to the previous stored subevent. In Section 4.6, the distribution of the expected backgrounds in the variables here listed will be addressed. Then, in Section 4.8, the selection cuts to reject backgrounds from MIMPs are listed, finally giving the effective minimum cross-section to which the present analysis is sensitive too, i.e. including the backgrounds.
The variable SubeventN has never been exploited at such high energies and a high number of subevents in any previous analysis; hence, before applying selection cuts on SubeventN, the variable must be validated. In Section 4.7,

the simulation's output is compared with true datasets, finally validating the variable up to 10 MeV.

4.6 Backgrounds

In the standard WIMP analysis, all the events giving more than one pulse along the waveform are rejected: pile-ups are excluded, while new cuts are introduced to reject electromagnetic backgrounds, alphas and neutrons from natural radioactivity. In the present analysis, the table is turned, so events with only one pulse are excluded by just asking $SubeventN > 1$, while the background giving more than one pulse has to be characterized. In this section the expected backgrounds at $SubeventN > 1$ and $Fprompt < 0.4$ – as MIMPs are expected to have a low Fprompt– are listed, together with the main cuts to reject them.

4.6.1 Pile-up background

A pile-up in a dark matter detector is the superposition of two or more recoils in the same acquisition window. In Figure 4.6.1 an example of a pile-up due to two βs from ^{39}Ar decays is shown.

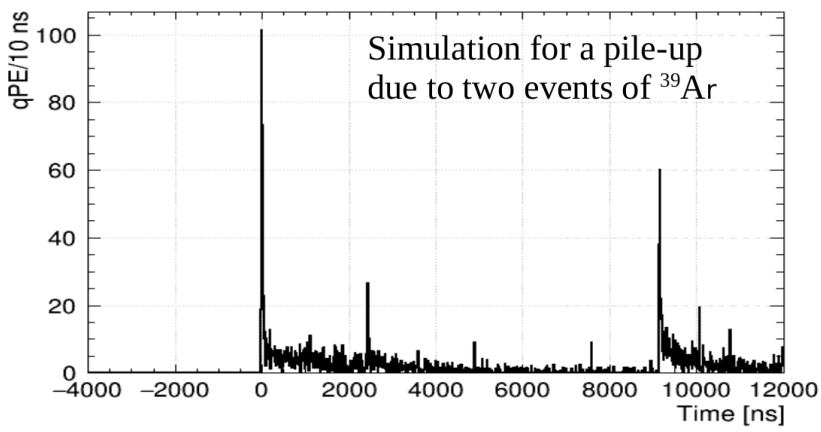

Figure 4.6.1: Waveform from a simulated pile-up from two ^{39}Ar recoils.

The number of expected pile-up events of a recoil B after a pulse due to a recoil A is here calculated. If the data taking lasts T seconds, for an acquisition gate of length W, the number of expected events of A kind is

$$n_A = R_A \cdot T, \tag{4.6.1}$$

where R_A is the rate of A events. Then, a recoil of type B follows in the same acquisition gate, thus giving a pile-up of second order. The probability is given by

$$P_B = Poisson(\lambda_B, 1) \tag{4.6.2}$$

where $\lambda = W \cdot R_B$ is the number of expected B events in the acquisition gate. The number of expected pile-ups of kind $A + B$ is then

$$N_{A+B} = n_A \cdot P_B. \tag{4.6.3}$$

In Table 4.1, all the rates R_i for the main electromagnetic sources in DEAP-3600 are given [281].

Decay Source	Rate [Hz]
^{39}Ar	3287
^{40}K	472
^{226}Ra	227
^{232}Th	51

Table 4.1: List of assumed rates for the main EM background sources in DEAP-3600 [281]. The main contribution comes from the LAr bulk with ^{39}Ar βs and the ^{232}Th and ^{235}U chains in the PMTs.

An example of the pile-up distribution is given for Run 022677, who will be also exploited is Section 4.7 to validate the Monte Carlo simulation. In Figure 4.6.2 the pile up events at $SubeventN > 1$ and $Fprompt < 0.4$ are shown, for reference. The poissonian statistics together with the aforementioned rates allows to estimate the number of expected pile-up for each pile-up "order", which is the number of recoils in the pile-up, which in principle corresponds to the value of the SubeventN variable. For instance, the SubeventN distribution of pile-ups from about three hours of data taking is given in Figure 4.6.3.
This can be compared with the signal expectation given in Figure 4.5.8 in the same variables. At low value of SubeventN, the MultiEvent processor fully reconstructs the number of observed pulses along the waveform, while the high number of overlapping pulses in the MIMP waveforms determines the observed saturation at high cross-section. Then, selection cuts on the SubeventN variable set according to the qPE range will allow for the necessary rejection of MIMP signal from pile-up background. For this reason, the evaluation of the expected pile-ups in three years of data taking is performed in Section 4.6.2, to determine the selection cuts shown in Section 4.8.

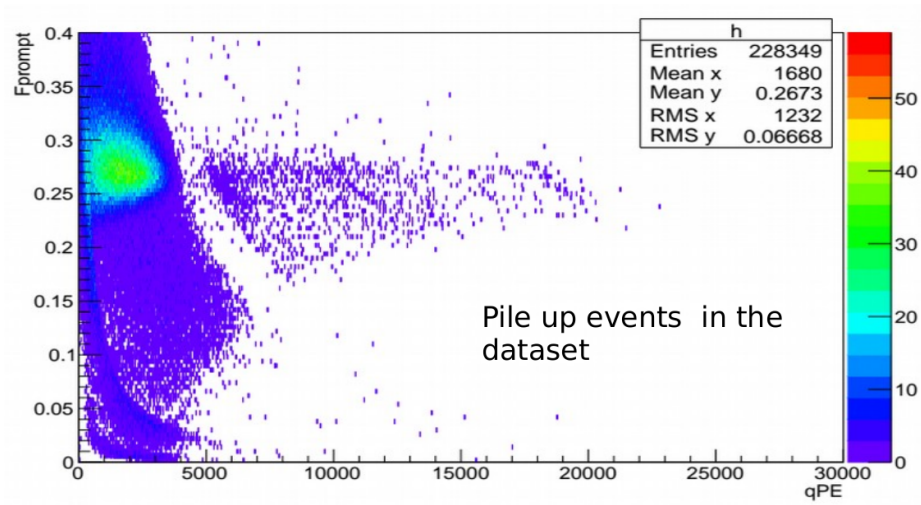

Figure 4.6.2: Pile-up events from Physics Run 022677. The performed cut are $Fprompt < 0.4$ and $SubeventN > 1$. As expected from statistics, the main pile-up source is ^{39}Ar due to high activity.

4.6.2 Expected pile-ups in the available dataset

In Section 4.7, the pile-ups in a Physics run and in an Americium-Berillium run will be reconstructed, allowing for the validation of the $SubeventN$ variable. On the other hand, this will allow for the understanding of the two key points with pile-ups: the contribution of the pile-ups between two or more γs is negligible compared to the one with ^{39}Ar βs; this means that a pile-up with M scatterings will have at least M -1 βs in it. Furthermore, and trivially, the more the trigger rate of a background source, the higher the pile-up order in which it appears.
In Figure 4.6.4 the measured EM single scatter background from 247 days of data-taking is reported [281]. An experimental estimate of the trigger rate for each energy range can hence be given; then, Equation 4.6.3 returns the number of the expected pile-up of nth order, where n stands for the number of recoils falling in the same acquisition window. The pile-ups will follow the Poissonian statistics, which allowed for the Monte Carlo validation in Section 4.7. For the present analysis, three energy regions are identified, according to the maximum order of pile-ups expected to be triggered in three years of data taking, with a total lifetime of 835.195 days (see Section 4.8).
Below 2.6 MeV$_{ee}$, the electromagnetic background is dominated by ^{39}Ar, which may pile-up with itself or with γs from the natural radioactivity from the inner vessel, with the prominent peaks due to ^{40}K at 1.4 keV and ^{208}Tl at 2.6 MeV. Due to the very high trigger rate, of about 2.5×10^3 Hz, the

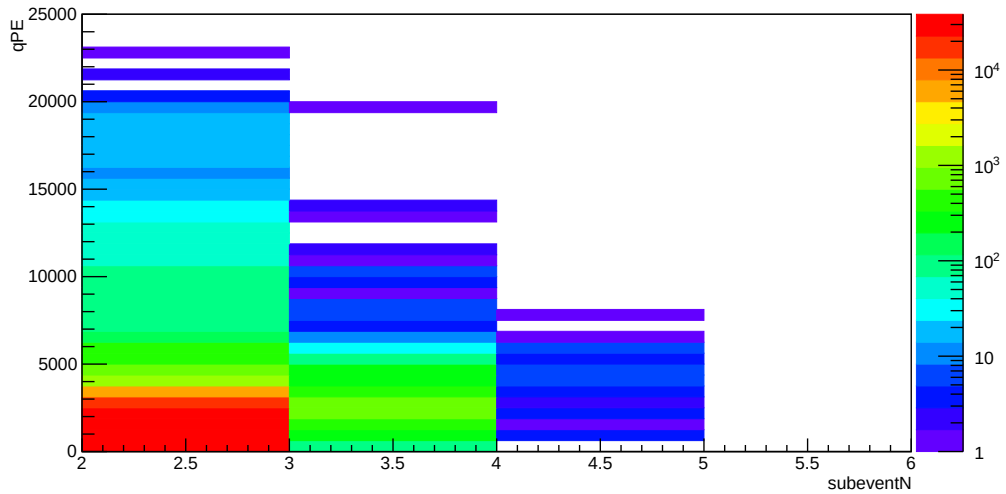

Figure 4.6.3: Pile-up events in the qPE-SubeventN plane from Physics Run 022677, lasting about three hours. A major cut at SubeventN > 1 and Fprompt < 0.4 is applied, to show the pile-up events which overlap on the MIMP signal in Fprompt variable. The maximum qPE reached in three hours is below 25000; in three years of data taking pile-ups are expected up to about 10 MeV, as it will be better explained in Section 4.6.2

.

highest order of expected pile-up is at n = 6, so with six events from ^{39}Ar in the same acquisition window. Then at n =7 , 0.71 pile ups events would be expected to be triggered, below 18000 qPE. After the ^{208}Tl peak at 2.6 MeV the electromagnetic radioactivity strongly decreases and is characterized by the summation of the 2.8 MeV γ with γs at 583.2 keV, 860.6 keV or 1093.9 keV, until a plateau is reached at 4 MeV. Hence the second energy range goes from 2.8 MeV to 4 MeV: the highest order of expected pile-ups is at SubeventN = 4, and above it 0.19 pile-ups events are expected. Above 4 MeV the background goes to a plateau of neutron capture γs, where neutrons are due to materials activity. Their rate is constant up to 70k qPE, and then it decreases of one order of magnitude. From 4 MeV to 10 MeV 0.07 events are expected at SubeventN = 4, so the highest order of expected pile-up is 3. Table 4.2 resumes these estimations, together with the respective uncertainties. The percentual errors can be retrieved from the Monte Carlo validation performed in Section 4.7; in the low energy range, up to mainly the ^{39}Ar endpoint the agreement with the Monte Carlo led by the Poisson statistic brings to an uncertainty of 0.4 % on average, which increases up to about 1 % at higher energies. An overall conservative uncertainty on the pile-up

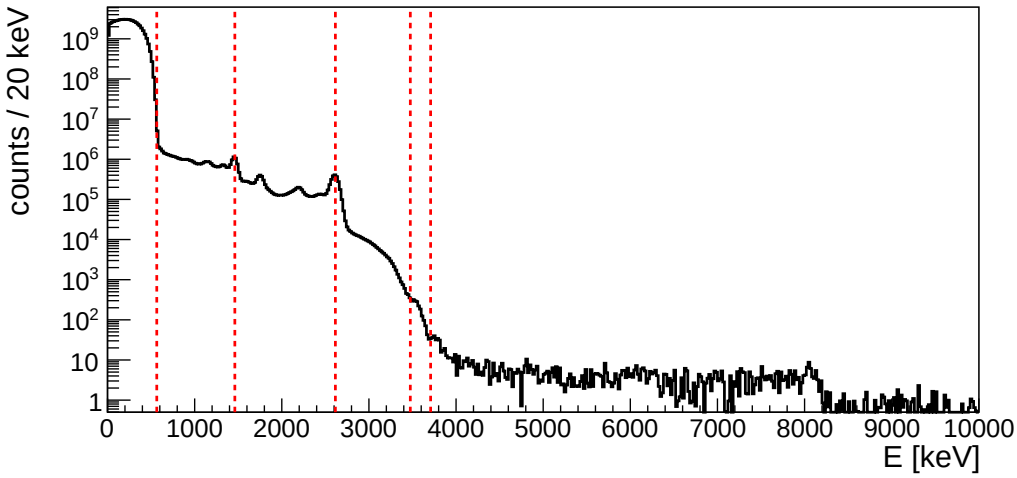

Figure 4.6.4: Electromagnetic background in DEAP-3600, for a lifetime of 247 days [281]. The more the trigger rate of an event, the higher the maximum pile-up order. Thanks to the Monte Carlo validation, an upper bound on the expected number of pile-ups in three years of data taking is set. Pile-ups due to ^{39}Ar and γs from inner vessel are expected up to SubeventN = 6 below 2.8 MeV and up to SubeventN = 4 below 4 MeV. Then up to 10 MeV, the highest order of pile-up is at SubeventN = 3.

background is hence set at 10 %.

4.6.3 Other backgrounds

The main cut will be applied on the SubeventN variable to reject pile-up background, which is the dominant one for the MIMP search. Other secondary backgrounds are here listed, together with the cuts to reject them.
Events from αs scattering first in the gas argon phase may occur. They show a signal with a Fprompt below 0.2 and energy between 10000 qPE and 14000 qPE, as can be seen in Figure 4.6.4 from single-scatter events. These events can eventually return SubeventN >1 due to the slow scintillation in the gas argon. However they are expected to return a higher fraction of light in the top PMT rings than the one from the MIMP scintillation in the LAr, in which case Top Charge Ratio < 0.1. Specifically, according to Figure 4.5.5 they will be rejected by asking Top Charge Ratio < 0.06.

At high energies, above 70 kqPE some residual background is expected, mainly due to muons. The expected rate of muons in the detector is $0.736\mu/day^{-1}$. This brings to 269 events/year. The rejection method is the removal of any

Energy range [MeV]	SubeventN$_{MAX}$	Pile-ups above SubeventN$_{MAX}$
Up to 2.8	6	0.71 ±0.07
2.8 - 4	4	0.19 ±0.02
4 - 10	3	0.07 ±0.007

Table 4.2: Three energy regions are set, according to the pile-up distribution in three years of data taking. For each energy range, the expected maximum pile-up order, and hence the maximum value for SubeventN, is given for the foreseen lifetime. The left pile-up background after applying the selection cut SubeventN > SubeventN$_{MAX}$ is given. An overall 10 % of uncertainty is assumed for the residual pile-up background, according to the validation of the Monte Carlo simulation performed in Section 4.7.

event within [-1, 100] us from the muon veto (MV) trigger. This brings to the highest available muon suppression, triggering 97 % of them. For the dataset lifetime 18.5 muons over 615.5 will skip veto tagging. On the other hand, the MV trigger will essentially take any event in the veto, so also the noise, mainly coming from the PMTs. The trigger rate is measured to be 98.8 Hz. This results in 7.13 $\times$ 10^9 triggers and 8.33 days of dead-time, which is less than one percent of the total lifetime of 835.195 days. Furthermore the same cuts are not expected to affect MIMP acceptance. Indeed the maximum recoil energy of a MIMP scattering against Hydrogen is about 2 keV, and so a velocity of $\approx 2 \times 10^{-3}$ c; on the other hand, the refractive index in the water veto is equal to 1.5, giving v/c = 0.67; hence MIMPs cannot give Cherenkov light in the water veto, and will not be rejected by any muon veto cut.
Due to technical difficulties in simulating MIMPs at very high energies and cross-sections, any sophisticated cut in SubeventN above 70 kqPE cannot be applied. A tight cut in Fprompt, at $Fprompt = 0.1$ or even below, is expected to decrease the left muon background of 19 events enormously, as the Cherenkov light usually releases a very prompt signal. Due to the lack of trustworthy simulations at about some millions of qPE, in Section 4.8.2 the relative muon sideband in the dataset will be unblinded first, in order to quantify the rejection power of a Fprompt cut on the muons, and finally, give an estimate of the left background above 70 kqPE.

4.7 Validation of the Monte Carlo simulation

The present analysis is the first ever performed in DEAP-3600 to search for multi-interacting dark matter particles. The variable SubeventN was

never used at high values of subevents, but only to exclude multi-scattering backgrounds in the WIMP ROI, by just asking $SubeventN = 1$. Hence in the present section, the variable SubeventN is validated by comparing the output from the Monte Carlo (MC) simulations with true data. The GEANT4 MC simulations are based on the Coincidence generator, in which particles were shot at a specific energy, except for the βs from ^{39}Ar, which was simulated according to its spectrum, already stored in the database. Specifically, the comparison is performed for events at $SubeventN > 1$ and $Fprompt < 0.4$, where MIMPs are mainly expected, so it relates only to the pile-ups between electromagnetic backgrounds. The expected number of pile-ups will be evaluated assuming the statistics in Section 4.6.1. The Physics run 022677 is employed to validate the MC simulation up to 3 MeV. Finally, by means of an Americium-Beryllium (^{241}AmBe) calibration run, specifically Run 020412, the validation is extended up to 10 MeV.

4.7.1 MonteCarlo validation at low energy

To fully understand the distribution of pile-ups, events in Physics Run 022677, with a lifetime of 2h 48m 39.015s, are reconstructed. The distribution of the pile-up background for this run was already shown, for reference, in Figure 4.6.2, in Section 4.6. In Figure 4.7.1 the distribution of the events due to electromagnetic single scatters –at $Fprompt < 0.4$ and $SubeventN = 1$– are shown in the qPE- Fprompt plane.

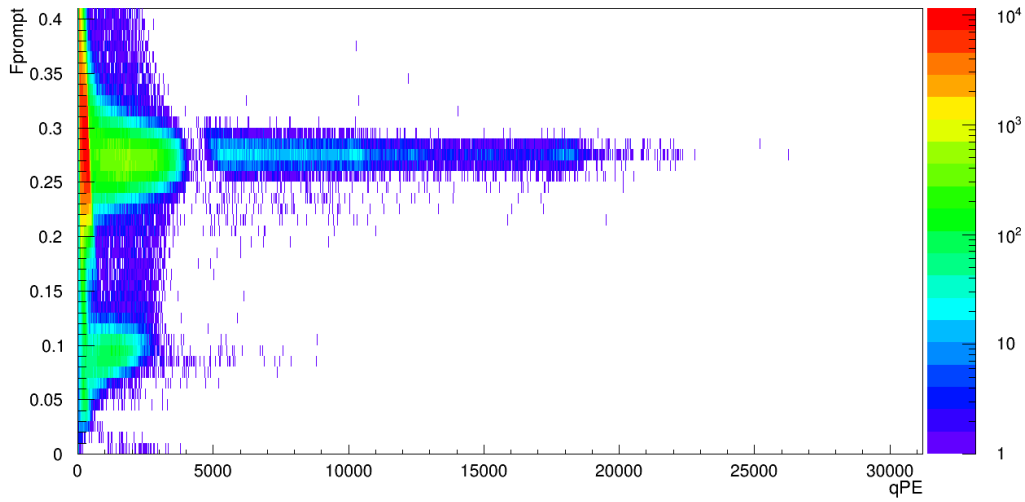

Figure 4.7.1: Electromagnetic single scatter events from Physics Run 022677. The electron recoil bands is centered at Fprompt $\approx$ 0.3, dominated by the ^{39}Ar β decays up to about 4000 qPE and then by the natural radioactivity of the materials composing the inner detector, mainly from the PMTs.

The background in DEAP-3600 due to single scatter events has already been fully reconstructed in [281] and reviewed in Section 4.6; its comprehension is the starting point to understand the background coming from pile-ups. Up to 3955 qPE, which corresponds to 565 keV, the electromagnetic band at Fprompt $\approx$ 0.3 is dominated by the ^{39}Ar β decays. Then, at higher energy, the main contribution comes from the radioactivity in the PMTs, mainly due to ^{40}K decay at about 10000 qPE and the ^{208}Tl at 20000 qPE [281]. Finally events at Fprompt $\approx$ 0.1 are mainly due to scatterings in the Gas Argon. The gap observed at about 5000 qPE and Fprompt = 0.25-0.3 reminds that for about 99 % of the events the high-level variables, like qPE and Fprompt, are not stored, so "prescaled", as these events are found by the Digital Trigger Module (DTM) to be due to ^{39}Ar, as described in Section 3.2.3.

All these events may happen in the same acquisition window, in a group of two or more. The total amount of events doing pile-up is shown in Figure 4.6.2.

To compare the dataset with the Monte Carlo simulation, the expected number of pile-ups must be first determined, for each "order" n of pile-up, where n stands for the number of recoils in the same acquisition window. In Table 4.3 the theoretical number of pile-up events is calculated as in Equation 4.6.3, referring to the rate in Table 4.1. Then GEANT4 simulations are performed

to see how the Digital Trigger Module (DTM) prescales the events, lowering the number of pile-ups seen in the dataset. Also, GEANT4 simulations returned the efficiency of the SubeventN in recognizing all the recoils composing the pile-up. The resulting number of pile-ups events that are expected to be triggered then follows. In principle, even pile-ups between electron re-

Pile-up	Theoretical Events	DTM [%]	Efficiency [%]	Expected triggered Events
$^{39}Ar \times 2$	1261214	12.8	95	163812
$^{39}Ar +^{40} K$	186538	13	5.97	1545
$^{39}Ar +^{226} Ra$	87578	13	1.4	170
$^{39}Ar +^{232} Th$	15957	80	5.44	632
$^{39}Ar \times 3$	24874	14	86	3290
$^{39}Ar \times 2 +^{40} K$	7073	12.4	4.8	45
$^{39}Ar \times 4$	327	11.4	76	30

Table 4.3: Expected pile-up events in Run 022677. The statistics determines the number of pile-ups happening in the detector; the validation follows by looking for the number of events that are actually triggered; this means taking into account the percentage which is prescaled by the DTM and the efficiency in distinguishing all the pulses and correctly tag a pile-up of n recoils at SubeventN = n.

coils and nuclear recoils may fall at Fprompt < 0.4, but their result to be negligible in 3 hours of data taking. For instance, the rate of neutrons from PMT glass is about 2.8×10^{-3} Hz from NeucBot simulations. The resulting theoretical pile-up events with ^{39}Ar is 1.11 in three hours. The DTM prescaling contributions and the efficiency of recognizing the two recoils brings to a negligible number of expected triggered events, below 0.001. For this reason, only the electromagnetic background doing pile-up is here reconstructed.
A look to Table 4.3 will outline the main characteristics of the pile-ups. In 2.8 hours of data taking $\approx 1.7 \times 10^5$ events are expected, and the highest order of pile-up observed is 4, coming from 4 βs from ^{39}Ar in the same acquisition window. Only ^{39}Ar and ^{40}K gives pile-ups of order greater than 2, which is a consequence of their rate. As a general rule, the higher the recoil rate, the higher the order of pile-ups in which it is involved. Also, pile-ups from two gammas are very unlikely to return more than one subevent, about once each thousand simulated events, and are thus negligible. The significant contributions come from pile-ups composed by ^{39}Ar recoils eventually summed with one or more γs reaching the LAr; in that case, the efficiency

in detecting all the recoils and store SubeventN = n, where n is the order of the pile-up, is strongly affected by the kind of particles whose recoils are piling up. For reference, only about 6 % of ^{39}Ar + ^{40}K pile-up events are stored with SubeventN =2, while for the left 94 % is SubeventN =1; on the other hand two events of ^{39}Ar has a SubeventN efficiency of 95 %. The expected number of triggered events were simulated for each of the pile-ups listed in Table 4.3, and then compared with the dataset from Run 022677, cut at Fprompt < 0.4 and SubeventN > 1. The result is shown in Figure 4.7.2, where the distribution of SubeventN variable from the data (in black) is compared to the MC simulation, which is the sum of all the simulated pile-ups.

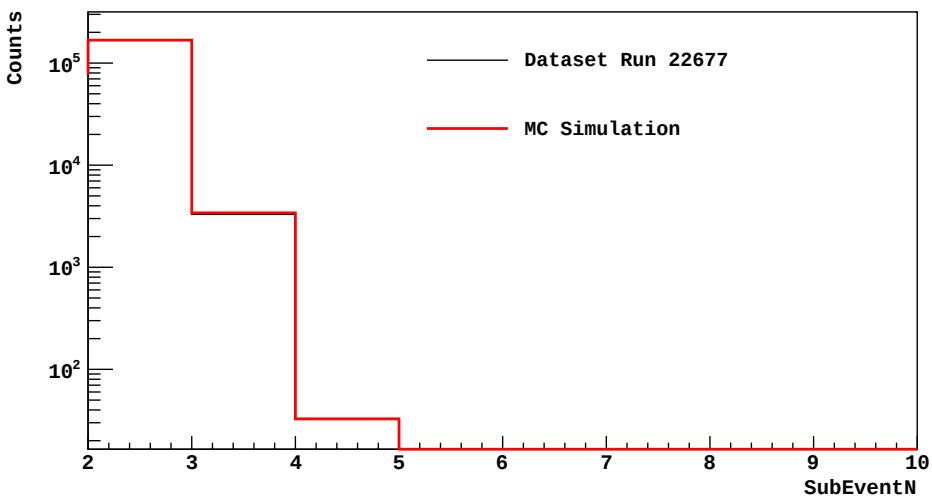

Figure 4.7.2: Comparison in the SubeventN variable between the dataset and the MC simulation. The Dataset is Run 022677 with Fprompt < 0.4 and SubeventN > 1, as only electromagnetic pile-ups are here reconstructed; the MC simulation sums all the events expected to be triggered listed in Table 4.3.

The agreement is of the order of a few percent. Specifically, at SubeventN = 2, the discrepancy between the observed events and the ones expected to be triggered is about 0.25 %. At SubeventN = 3 the discrepancy is within 0.24 %. Finally, at SubeventN = 4, 33 pile-ups events are expected, as many as observed.

The pile-up background in 2.8 hours is thus reconstructed within a few percent of error. This has two main outcomes. On the one hand, the be-

haviour of pile-ups is characterized in terms of SubeventN. This will allow for setting the selection cuts to discriminate MIMPs from pile-ups. On the other hand, this variable was not designed for MIMP search, as its non-monotonic behaviour reminds, so it needs to be validated by comparing MC simulation with the actual dataset. The validation is here performed up to 20000 qPE. In the next section, the validation will be extended up to about 70000 qPE thanks to an Americium-Beryllium (^{241}AmBe) calibration run.

4.7.2 Validation with Americium Beryllium run

The variable SubeventN is validated up to 10 MeV in the present section by comparing the Monte Carlo output and the dataset for the Run 020412, an ^{241}AmBe run. The lifetime is 3h 49m 2.868s; the neutron beam is sent from the CalE calibration tube. The dataset for single scatter events is shown in Figure 4.7.3.
Neutrons produced by the ^{241}AmBe source can either scatter in the LAr, giving a nuclear recoil, or be captured from the materials surrounding the active volume. The present dataset was cut at low energy, where the electromagnetic (EM) spectrum is dominated by ^{39}Ar β decays. In Figure 4.7.4 single scatter events from the same run at $Fprompt < 0.4$ are plotted, to highlight the main neutron capture peaks.

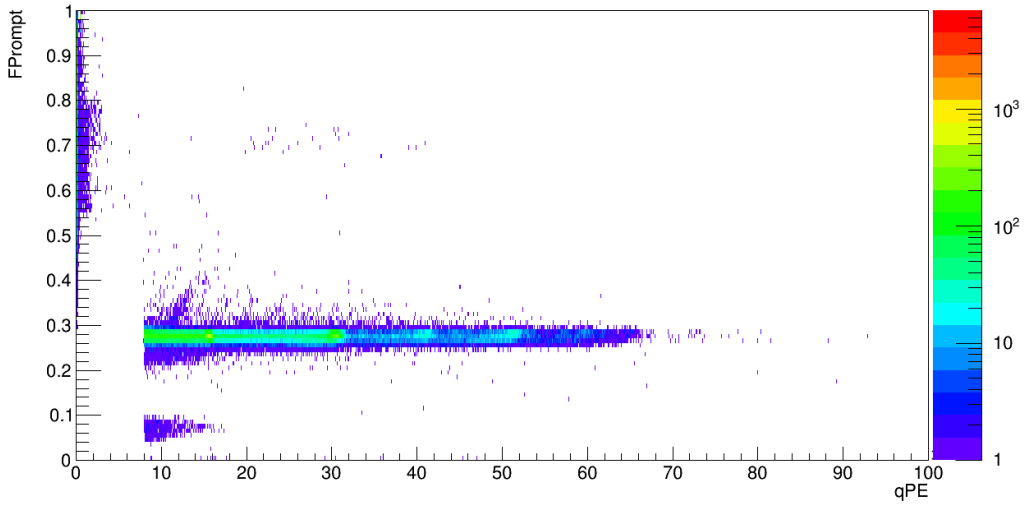

Figure 4.7.3: Single scatter events from Run 020412, in which the neutron ^{241}AmBe source is set at the calibration tube CalE, in the equator. Neutrons are captured by the materials surrounding the TPC, giving high energy γs. In the present dataset, events at qPE $<$ 8000 were cut, as there the EM background is dominated by the ^{39}Ar.

The lowest energy neutron capture γ is due to the capture in the Hydrogen, mainly in the Acrylic vessel, at 2.6 MeV. Then at 4.4 MeV follows the peak from the γ released by the ^{241}AmBe source itself. At higher energy heavier elements composing the detector can perform a neutron capture, but the main contribution is at 7.4 MeV, which can be due to capture in Iron, Nickel or Chromium.

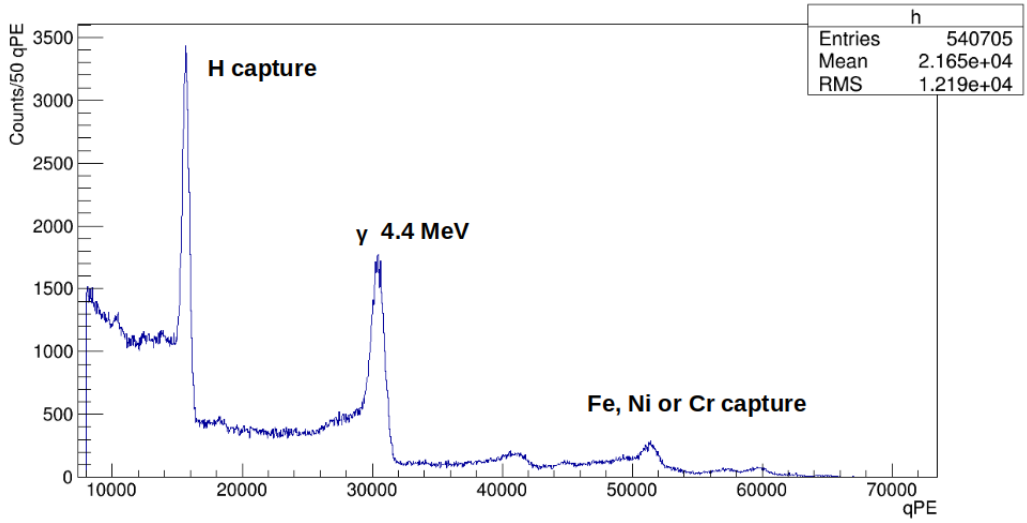

Figure 4.7.4: Single scatter spectrum at $Fprompt < 0.4$ from Run 020412. The lowest energy neutron capture γs come from H capture, which is abundant in the acrylic vessel. Then it follows the γs at 4.4 MeV released by the ^{241}AmBe source, set at CalE tube, in the equator. Finally at about 7 MeV the contribution of heavier elements as Iron, Nickel or Chromium, mainly from the vessel and the PMTs, becomes significant.

As already highlighted by the low-energy MC validation, neutron capture γs are expected to pile-up with ^{39}Ar βs, giving events at $SubeventN > 1$; furthermore pile-ups due to only γs fall at $SubeventN = 1$, while pile-ups between electron recoils and nuclear recoils are negligible at such low Fprompt. The expected number of pile-up events is calculated by Equation 4.6.3. The rate of the dominant γ sources is listed in Table 4.4, retrieved from the collaboration ^{241}AmBe data analysis and peak reconstruction. Then the

Decay Source	Rate [Hz]
H	9.82×10^2
4.4 MeV	3.85×10^3
Fe/Ni/Cr	3.46×10^2

Table 4.4: List of assumed rates for the dominant neutron capture γ sources in DEAP-3600.

number of pile-up events expected to be triggered follows by taking into

account the percentage that is prescaled by the DTM and the efficiency of the SubeventN algorithm in "seeing" the pulse from the γ, percentages that are taken from the GEANT4 simulations of the respective pile-up events. Also, as the dataset was cut at low energy, the percentage of the events above 8000 qPE is taken into account. In Table 4.5 the number of pile-up events expected to be triggered in 3h 49m of the run lifetime is calculated. The expected triggered events are simulated in GEANT4, by mean of the

Pile-up	Theoretical Events	E > 8 kqPE [%]	DTM [%]	Efficiency [%]	Expected triggered Events
$^{39}Ar + H\gamma$	482894	47	11	46	17634
$^{39}Ar + AmBe\ \gamma$	1565576	20	11	2	6951
$^{39}Ar + Fe/Ni/Cr\ \gamma$	171106	50	11	7	6648
$^{39}Ar \times 2 + H\ \gamma$	16840	55	11	40	624
$^{39}Ar \times 2 + AmBe\ \gamma$	54597	30	11	1.2	24
$^{39}Ar \times 2 + Fe/Ni/Cr\ \gamma$	5967	30	11	15	34
$^{39}Ar \times 3 + H\ \gamma$	304	50	15	53	13
$^{39}Ar \times 3 + AmBe\ \gamma$	987	70	11	1.2	1.2
$^{39}Ar \times 3 + Fe/Ni/Cr\gamma$	108	90	11	15	1.5

Table 4.5: Expected pile-up events in Run 020412. As already performed with the low-energy calibration, the number of pile-up events expected to be triggered takes into account the percentage which "survive" to the DTM prescaling and the fraction that is correctly recognized at Subevent N = n, if n is the number of recoils in the acquisition window. Furthermore GEANT4 simulations returned the fraction of events falling below 8000 qPE, where the dataset was cut.

coincidence generator, according to the expected number of triggered events. Then they are compared in Figure 4.7.5 with the dataset at $Fprompt < 0.4$ and $SubeventN > 1$.

The agreement is confirmed also with the ^{241}AmBe run, with a slightly

higher percentual discrepancy: 0.9 % at SubeventN = 2, then 2.5 % at SubeventN = 3 and finally 4 % at SubeventN =4. This is believed to be a consequence of the simulation performed, in which the neutron capture γs are simulated with a GEANT4 gun vertex, and hence at a specific energy, while Figure 4.7.4 shows a continuous spectrum. The variable SubeventN is

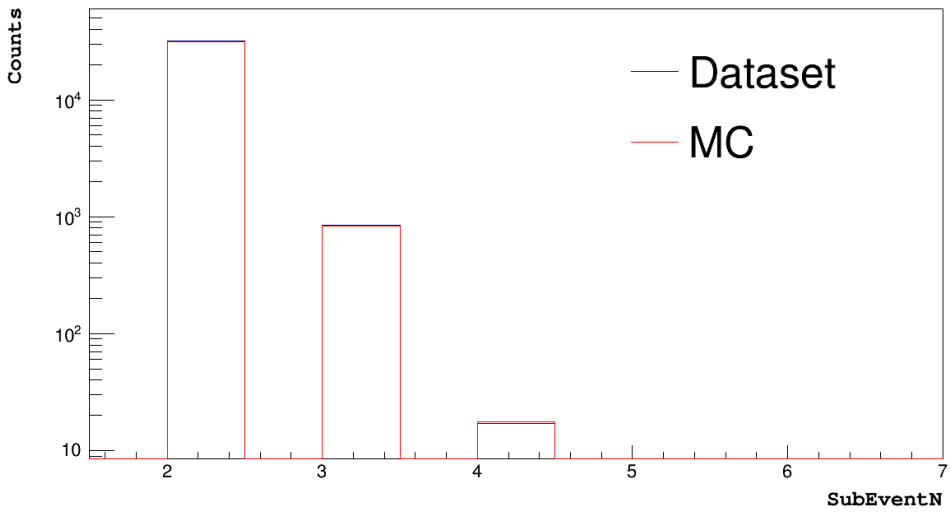

Figure 4.7.5: Distribution of EM pile-up events in Run 020412 compared to the MC simulations of the expected triggered events.

validated up to 70k qPE, as it allows for the reconstruction of the pile-ups from both the natural detector radioactivity and of the neutron capture γs from the ^{241}AmBe calibration source. This confirms the MIMP simulations' validity, which will then reproduce the eventual MIMP scattering in the true dataset with the same error. Moreover, as the present validation is based on the poissonian statistics in Section 4.6.1, the estimation on the expected background in Section 4.6, are confirmed. Now that both the MIMP signal and the background knowledge is confirmed, the selection cuts can be set as performed in Section 4.8.

4.8 Set up of the data unblinding

The selection cuts to reject the backgrounds listed in Section 4.6 are here described, followed by the consequent MIMP acceptance. Finally, the unblinding procedure is described, together with the output from one-week of data taking, where the selection cuts were tested.

4.8.1 Selection cuts and acceptances

The MIMP simulations confirmed that the energy range is directly proportional to the MIMP-nucleus cross-section through the number of scatterings, with a spread due to the quenching and light yield fluctuations. Specifically Figure 4.8.1 shows the average expected qPE for each MIMP-nucleus cross-section, for a MIMP with velocity v = 220 km/s.
The expected backgrounds change widely with the energy range and hence with the MIMP cross-section. Then, to optimize the acceptance through all the space of parameters to which DEAP is sensitive to, different sets of selection cuts are applied, counting on the MC validation performed, according to the energy range.

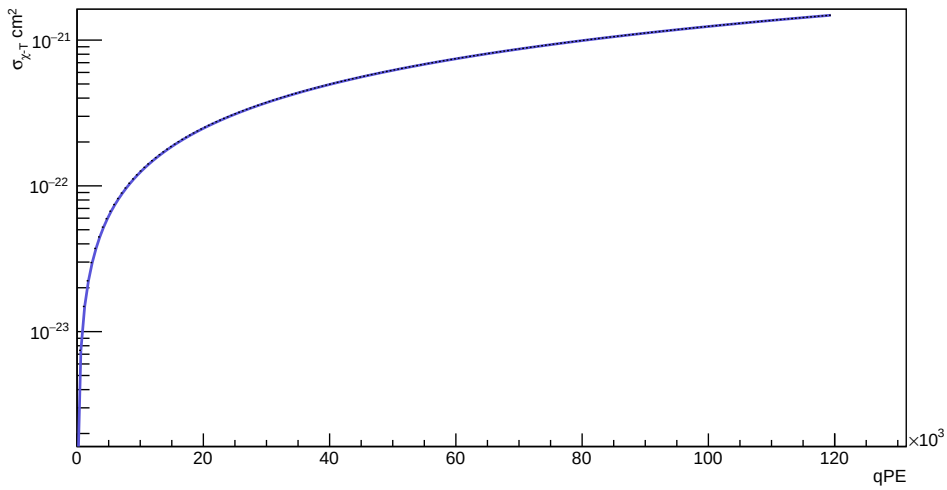

Figure 4.8.1: Average qPE expected in terms of the dark matter-nucleus cross-section. This relation will allow determining the MIMP-nucleus cross-section corresponding to each energy range.

The strongest cut is on the Fprompt, which is asked to be < 0.3 for MIMPs below 4000 qPE, and < 0.1 at arbitrary higher energies.

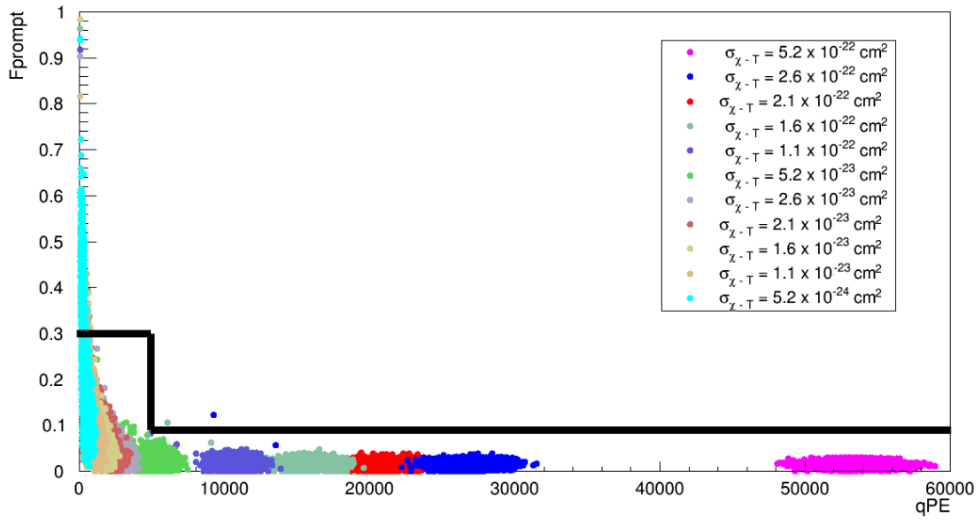

Figure 4.8.2: Selection cut on the Fprompt variable. Below 4000 qPE, Fprompt is asked to be < 0.3; then, at higher energies and cross-sections, the cut is tightened at Fprompt < 0.1.

Also, the scintillation light is expected to be uniformly distributed through all the PMTs, much more than any single scattering event. Hence a cut at $FmaxPE < 0.02$ is applied above 4000 qPE, while the cut is relaxed to $FmaxPE < 0.03$ below it.

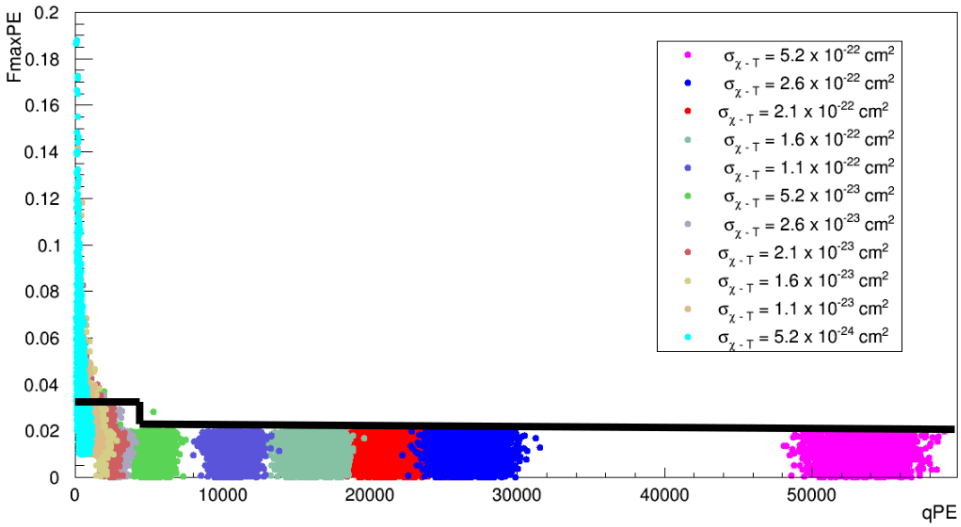

Figure 4.8.3: Selection cut on FmaxPE. As well as Fprompt the cut is stronger above the ^{39}Ar endpoint, where is FmaxPE < 0.02, while above it the condition is relaxed to FmaxPE < 0.03.

Furthermore, due to their long path of nuclear recoils across the detector, also Top Charge Ratio, the fraction of the charge in the first and the second top PMT rings will be extraordinarily low, below 5 % above 4000 qPE; the selection cut is relaxed to 0.06 at lower energies.

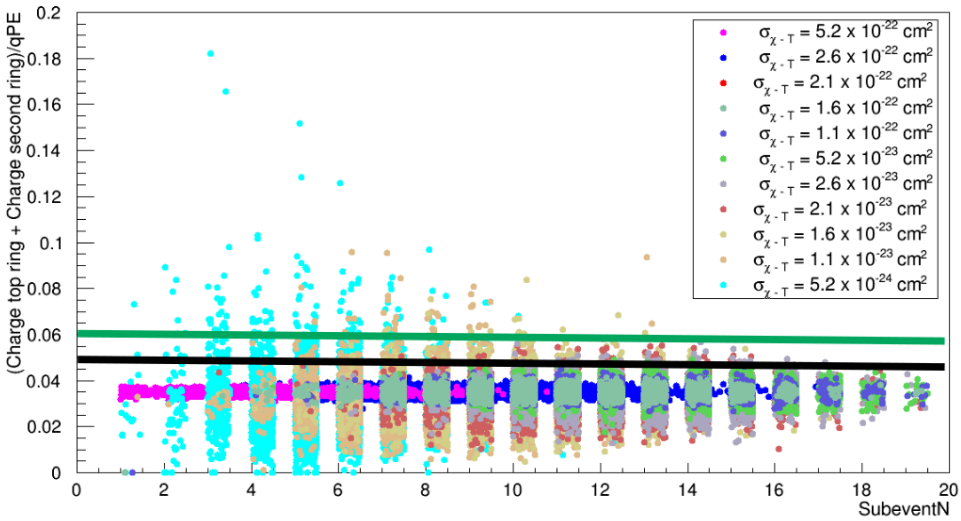

Figure 4.8.4: Selection cut on Top Charge Ratio, the sum of the charge in the first and the second top PMT rings normalized to qPE. At high energies, which means also high cross-section, the number of scatterings is higher, giving a widely uniform distribution of the scintillation light, so the MIMPs are asked to have Top Charge Ratio < 0.05 (black line); at lower energies, only a bunch of scatterings are expected, so MIMPs are asked to have Top Charge Ratio < 0.06 (green line).

The main effect of the application of this cut will be the removal of scintillation events in the Gas Argon.
As shown in Section 4.6, the main background in the MIMP analysis are the electromagnetic pile-ups. According to Table 4.2, the highest order of expected pile-ups in three years of data-taking is 6 at energies below 2.8 MeV$_{ee}$, so at qPE $<$ 20000 SubeventN is asked to be greater than 6. Then, from 20000 qPE up to 30000 qPE the highest order of pile-up is 4, so SubeventN must be greater than 4 to select MIMPs. Finally, above 4 MeV, the electromagnetic background rate decreases, allowing to select events at SubeventN > 3.

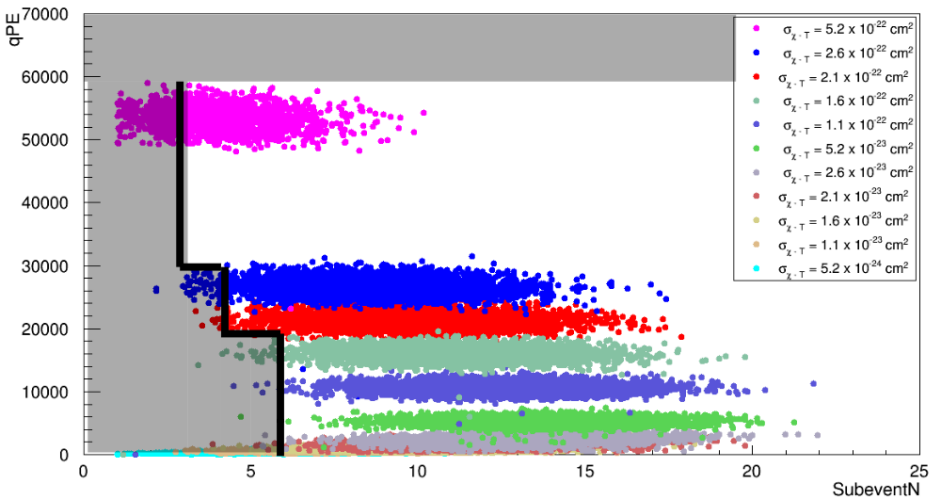

Figure 4.8.5: Cut in the qPE vs. SubeventN plane, tuned on the expected pile-up distribution in three years of lifetime.

At higher qPE the cut in SubeventN is not performed, as the ^{241}AmBe run validated the variable only up to about 70k qPE. On the other hand, the trend of the other listed selection cuts is monotone and is assumed to be the same as the highest simulated cross-section, at $\sigma_{\chi-T} = 5.6\times\ 10^{-22}$ cm^2. The muon veto (MV) cut will decrease the background level down to 18.5 events above 70 kqPE, without impacting on the MIMP acceptance. A further cut in Fprompt will be optimized to further decrease the background level in this energy range, as described in Section 4.8.2.

As a consequence of both the expected signal and the expected background, four ROIs are identified. ROI#0 extends up to 4000 qPE, corresponding to the ^{39}Ar endpoint; at such low energy the MIMP signal will be suppressed by the DTM prescaling, which will not allow the storage of 99 % of the events in that energy range and below Fprompt = 0.3. If the DTM specifics are eventually changed in future data acquisitions, the selection cuts listed in the present analysis will eventually allow for MIMP rejection from the background.
The energy range from 4 kqPE up to 70 kqPE is divided at qPE = 20000 in two different ROIs, according to the different selection cuts in SubeventN. Their acceptance for the simulated per-nuclear cross-sections is shown in Figure 4.8.6 after applying the listed cuts. The strongest cuts are that on SubeventN, which on the one hand allows for the necessary removal of the

pile-up backgrounds, but due to its not-monotone behaviour impact the acceptance in both ROI#1 and ROI#2.
Finally, ROI#3 starts from 70 kqPE; here no cuts in SubeventN can be applied due to the lack of MC simulations at such high energies. As already stated, a tight cut in Fprompt is foreseen to decrease the muon background level in this ROI. The cut will be chosen assuring an acceptance level of 95 % of MIMPs, whose behavior in Fprompt variable is monotone and can hence be extrapolated from the MIMP simulation at 5.6×10^{-22} cm^2.

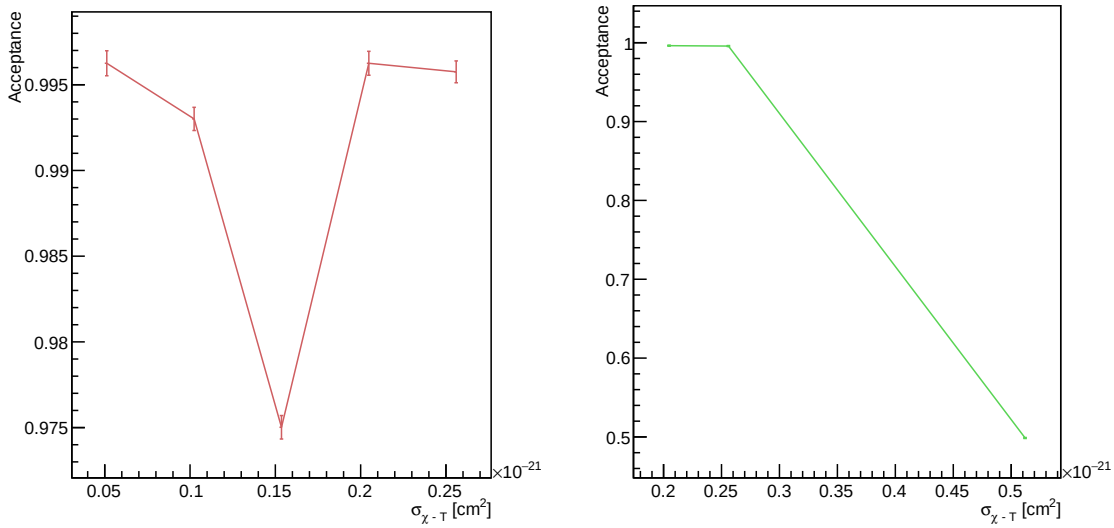

Figure 4.8.6: Acceptance for the ROI # 1 and ROI # 2 in Table 4.6. The non-monotone behaviour of the acceptance is a consequence of the selection cuts in SubeventN, necessary to reject the pile-up background from MIMP events.

The resulting background level for each of the four ROIs is listed in Table 4.6. The background shown is the maximum one, so the one left after the SubeventN cut, which removes most of the background; then, the cuts in FmaxPE, Fprompt and the Top Charge Ratio will further decrease the background level.
The "ladder cut" at SubeventN is determined by the pile-up distribution expected in three years of data taking. Indeed the cut at SubeventN > 6 goes up to qPE < 20000, extending to all the ROI#0 and ROI#1. Section 4.6 and specifically Table 4.3 shows that after the SubeventN cut, less than 0.72 background events are expected in 2.28 years of lifetime in ROI#0 and ROI#1, which we can conservatively assume to be uniformly distributed

ROI	qPE range	$\sigma_{\chi-T}$ [cm^2] range	Maximum Expected left background
0	70 – 4000	5.2 $\times 10^{-24}$ – 1.6 $\times 10^{-23}$	0.36 $\pm$0.04
1	4000 – 20000	1.6 $\times$ 10^{-23} – 2.1 $\times 10^{-22}$	0.36 $\pm$0.04
2	20000 – 70000	2.1 $\times 10^{-22}$ – 5.2 $\times 10^{-22}$	0.26 $\pm$0.03
3	70k – 4 $\times$ 10^8	5.2 $\times$ 10^{-22} – 1.0 $\times$ 10^{-18}	$<$ 18.5

Table 4.6: List of the identified ROIs for MIMPs in DEAP-3600, with both the qPE and MIMP-nucleus cross-section range. The maximum background is the number of events expected to survive the SubeventN cut, which removes pile-up events, according to the expectations given in Section 4.6, confirmed by the Monte Carlo validation performed in Section 4.7; an overall uncertainty of 10 % was assumed for the background level, one order of magnitude greater than the actual uncertainty on the background retrieved in Section 4.7. The ROI #0, at low cross-section and energy, is not accessible by the present analysis, due to the DTM prescaling, which rejects 99 % of the events below the ^{39}Ar endpoint; still, the left background and the selection cuts to reject MIMPs in this energy range is here shown, for reference. Finally, in ROI #3 the Monte Carlo simulations of MIMPs were not available due to the wide number of scatterings; also, the simulations at millions of qPE are not trustworthy. The expected background here comes from muons, which will be mainly rejected by the muon veto cut, leaving maximum 18.5 not-tagged muons. The opening of the muon sideband in the data will allow evaluating the impact of a tight cut in Fprompt on the muon rejection. In the next section this table will be updated, after the optimization of the Fprompt cut in ROI # 3.

across the two ROIs. Then, from 20000 qPE up to 30000 qPE, the cut at SubeventN > 4 leaves 0.19 background events, which sums to the 0.07 going up to 70 kqPE, giving an overall background expectation of less than 0.3 events in ROI#2.

It must also be taken into account that below 4000 qPE the signal is prescaled by the DTM as it falls below the Ar^{39} endpoint; this will further weaken the detector sensitivity by two orders of magnitude, so excluding the ROI # 0 from the present analysis. On the other side, at qPE > 70000, pile-ups with neutron capture gammas become negligible above 10 MeV, and the only residual background will eventually be the fraction of muons not tagged in the detector, up to 18.5 muons. The evaluation of the muon rejection power of a tight Fprompt cut in Section 4.8.2 will allow for the strong decrease of the background level in the ROI #3. The analysis' ceiling at 4×10^8 qPE, was determined by the larger geometrical cross-section between the two MIMP models considered, so to the geometrical cross-section of the Dark Matter nugget described in Section 4.2.2, which indeed shows saturation for the benchmark parameters chosen.

4.8.2 Muon unblinding

The present analysis was performed to have zero background after all cuts, so any found event is tagged as a potential signal. Assuming a Poisson statistics, MIMPs at a given cross-section will be rejected up to a certain MIMP mass. The lifetime for the available dataset is 835.195 days, after dead-time correction. Table 4.6 shows that from 4000 qPE to 70000 qPE the analysis is ready to be performed in a background-free condition, with an overall level smaller than 0.4 in each of the two ROIs. Below 4000 qPE the analysis sensitivity is limited by the DTM specifics, so a wide cut at Fprompt < 0.4 and qPE > 4000 will be applied. Then, at higher energies, muons are the dominant expected background. As MIMPs do not give any Cherenkov signal in the water veto, any events within [-1, 100]us from the muon veto trigger will be rejected. For the present lifetime and a measured trigger rate of 98.8 Hz in the veto, this brings to a dead time of 8.33 days, so less than 1 % of the total lifetime will be excluded from the analysis.
The present analysis was tested in one week of data taking. The analysis macro applies the listed selection cuts for each qPE range. No muon veto cuts were applied, differently from what will be done in the full unblinding. Below 70 kqPE, zero events are found after the application of the selection cuts. Above 70 kqPE if no cuts were applied, five events were found; the application of the cuts in Fprompt, FmaxPE and Top Charge Ratio as extrapolated from the ROI #3 left only one event in the ROI #3, at qPE = 1168307

and Fprompt = 0.09, which is believed to be a muon. This test confirmed that the analysis below 70k qPE is correctly designed to be background-free; above 70 kqPE, after the application of the MV cuts, it is necessary to apply the Fprompt cut at 0.1 or even below it to further suppress the background coming from muons.

Hence the unblinding of the muon sideband comes first the unblinding of the full dataset. The sideband is defined by the MV cuts already described, for a total lifetime of the sideband of 8.33 days, which would be anyway excluded by the analysis. This sideband will allow for the optimization of the Fprompt cut above 70k qPE, which will further decrease the background level in the ROI#3. On the other hand, no change in the selection cuts in the other ROIs will follow after the sideband's unblinding. This procedure will allow for fixing the background level and the acceptance in all of the three ROIs to which this analysis is sensitive to. Then the unblinding of the full dataset can be requested.

The unblinded muon sideband is shown in Figure 4.8.7, in the Fprompt - qPE plane, for the ROI#3. The total number of events above 70 kqPE is 662; 615 muon events were expected, of which a minimum of 596 is selected with these muon veto cuts.

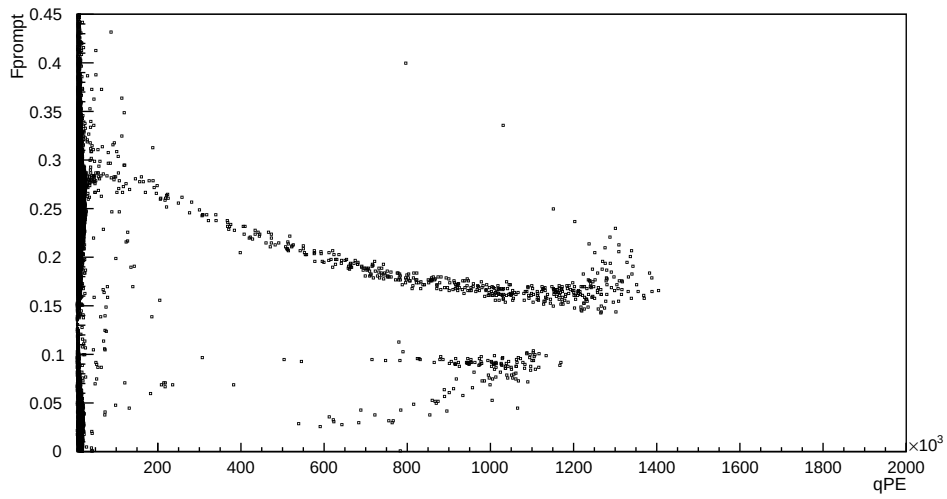

Figure 4.8.7: Distribution in the qPE-Fprompt plane of the events in the muon sideband, asking the coincidence within 100 us from the MC trigger. 662 events are found, apparently distributed in two populations. The overabundance of the events compared to the ones expected from muons -about 600- is very likely due to the lack of low-level cut and to the contribution of pathological events, due to the PMT saturation.

Considering that no low-level cuts are applied and that the background model is not completed at about 2 million qPE, equivalent to recoils of O(100) MeV, background's overabundance at the very high energy is expected. The discontinuity in Fprompt points to two different populations, with an eventual contribution of pathological events due to the PMT saturation. Still, for the present analysis is sufficient to consider all the events as a unique population, so to determine the Fprompt cut to reduce the background level in the ROI#3. A tight cut at Fprompt < 0.05 reduces the background down to 23 events, so of a factor 3.5 %. The full list of performed selection cuts that will be applied in the unblinding is listed in Table 4.7.

ROI	qPE range	Fprompt	FmaxPE	Charge Top Ratio	SubeventN
1	4000 – 20000	< 0.1	< 0.02	< 0.05	> 6
2	20000 – 30000	< 0.1	< 0.02	< 0.05	> 4
2	30000 – 70000	< 0.1	< 0.02	< 0.05	> 3
3	70k – 4×10^8	< 0.05	–	–	–

Table 4.7: List of the selection cuts that will be applied in each ROI and energy range. An overall Muon-Veto cut will be applied, removing all the events within [-1, 100] μs from the water tank trigger. As the analysis threshold is set at 4000 qPE, the ROI#0 is here not listed.

The correspondent MIMP acceptance in ROI#3 can be extrapolated from Fprompt distribution for the simulated MIMP population, shown in Figure 4.8.2, thanks to the clearly monotone decrease, and it's equal to $99.95^{0.04}_{0.01}$ %. With the application of this selection cut only in the ROI#3, together with the MV cuts, the expected background level goes from 18.5 to 0.7 left events. The resume of the ROIs of the present analysis together with their background level is finaly given in Table 4.8. Thanks to the selection cuts optimized in the present analysis, the search for MIMPs in DEAP-3600 data promises to be performed in background-free conditions, with an expected exclusion of MIMPs up to the Planck Mass.

4.9 Conclusion

In the present chapter the search for multi-scattering massive particles, MIMPs, in DEAP-3600 is fully described. After determining the expected signal in the detector, this is compared with the expected background, mainly due to electromagnetic pile-ups. The optimized selection cuts, based on already stored variables, will allow for a discovery/rejection of MIMPs down to 1.6×10^{-23} cm^2 and up to the Planck Mass, with a left maximum background level of 1.4 event through all the identified ROIs. The high quality of the results obtained in the present Monte Carlo and data driven analysis promises for an upcoming agreement from DEAP collaboration for the unblinding of the three years of data.

ROI	qPE range	$\sigma_{\chi-T}$ [cm^2] range	Maximum Expected left background
1	4000 – 20000	1.6×10^{-23} – 2.1×10^{-22}	0.36 ± 0.04
2	20000 – 70000	2.1×10^{-22} – 5.2×10^{-22}	0.26 ± 0.03
3	70k – 4×10^8	5.2×10^{-22} – 1.0×10^{-18}	0.67 ± 0.07

Table 4.8: List of the identified ROIs for MIMPs in DEAP-3600, with both the qPE and MIMP-nucleus cross-section range. The Muon Veto cut, rejecting any events within 100 us from the muon veto trigger is applied in any ROI. The analysis threshold is set at 4000 qPE. The maximum expected background is finally given after the selection cuts in SubeventN, Fprompt, FmaxPE and Charge Top Ratio in the ROI#1 and ROI#2; in the ROI#3 only the Fprompt cut at 0.05 will be applied, thanks to the optimization performed with the unblinding of the muon sideband.

5 Characterization of SiPM correlated instrumental noise

One of the key improvements in DarkSide-20k design compared to DarkSide-50 is related to the photodetection, performed by Silicon Photomultipliers (SiPMs) in substitution of Photomultipliers Tubes (PMTs). The photosensor unit, called PhotoDetection Module (PDM), is a tile made of 24 SiPMs for a total area of 25 cm^2. DarkSide-20k will be equipped with 8280 PDMs. SiPMs were developed by Fondazione Bruno Kessler, together with the DarkSide Collaboration, to fulfill all the requirements for dark matter search in tonne-scale liquid argon detectors. The first requirement in an experiment designed to be background-free in the WIMP Region of interest (ROI), from 0.7 keV_{NR} up to 200 keV_{NR}, is a high radiopurity level, with an activity lower than 1 mBq/kg from ^{238}U and ^{232}Th radioactivity chains. SiPMs have an activity smaller than 0.025 mBq/kg and than 0.003 mBq/kg from respectively ^{238}U and ^{232}Th, so they fulfill the requirement. Also, to keep the Pulse Shape Discrimination effective, the thermal noise or dark count rate (DCR) must be lower than 0.1 Hz/mm^2 [282]. For the same reason, and also to assure an efficient x-y reconstruction, the probability to observe correlated noise must be less than 60 % [282]. Finally the last fundamental requirement is a Photon Detection Efficiency (PDE) greater than 40 %. The PDE is the product of the quantum efficiency, which is in a SiPM the probability to create an electron-hole pair, and the optical coverage, defined as the ratio of the active area on the total area of the PDM. PMTs have a quantum efficiency of $\approx$ 25 % and an optical coverage of about 70 % [283]; the consequent PDE would be $\approx$ 20 %, too low for the dark matter search in DarkSide-20k [284]. On the other hand each SiPM has an area of 12 x 8 mm^2, with a dead layer of 0.5 mm between two SiPMs, so that the PDM optical coverage amounts to $\approx$ 90 % [283]; even the SiPM quantum efficiency is higher than PMT's at 87 K and is equal to 50 %. Thus the PDE in a FBK PDM is $\approx$ 45 % at 87 K [285], as required for DarkSide-20k.
However SiPMs suffer of two main drawbacks. First, the avalanche in a fired SPAD needs a few hundreds nanoseconds to fully recharge back; this implies that any scintillation pulse is slowed down, reducing the pulse shape discrimination power between an electron recoil and a nuclear recoil. As a first result in the present analysis, the SiPM time response, and specifically the recharge time was characterized. Second, and that's the focus of this analysis, SiPMs have correlated noises, together with the uncorrelated dark noise, which may affect the light yield, the energy resolution and the pulse shape discrimination, and hence need to be characterized.

In this chapter it is shown the characterization of the correlated noises in FBK NUV-HD SiPMs performing the photo-detection in the ReD experiment, which was described in Section 3.4. After a short review of SiPM's operating principles in Section 5.1 Section 5.2 is dedicated to the energy calibrations through laser runs, i.e to the response from a signal equivalent to few photoelectrons. Finally the two components of correlated noise -namely afterpulses and optical crosstalks- are characterized for all ReD channels in Section 5.3 and Section 5.4.

5.1 Silicon PhotoMultipliers

In this section the operating principles of a Silicon Photomultiplier is reviewed, starting from its smallest mechanical unit: the Single Photon Avalanche Diode (SPAD). Then the working principles of the full SPAD matrix, namely the SiPM, are described, together with the noises affecting the photodetection.

5.1.1 Single Photon Avalanche Diode

A Single Photon Avalanche Diode is a p-n junction supplied by a reverse-bias, put in series with a resistor R_Q. A representation of the SPAD is shown in Figure 5.1.1. The n and p region are respectively doped with Aluminium and Phosophorus, so they are called electron "donors" and "acceptors".

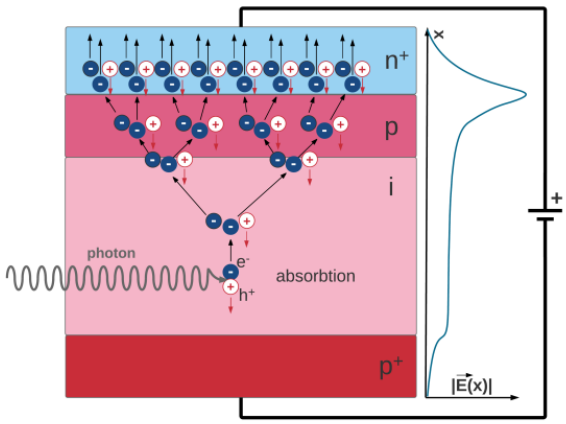

Figure 5.1.1: Illustration of an Avalanche Photodiode set in Geiger mode. The production of an electron-hole pair by photoelectric effect determines an avalanche of electrons and holes, drifted by the reverse bias respectively in the n+ and p+ doped regions [286].

The minimum energy for a photon to create a electron-hole pair by photoelectric effect is $E_{ph} = 1.1$ eV in Silicon. The reverse bias drifts electrons to the n^+ doped region and holes to the p^+ one, with a velocity evaluated to be 10^7 cm/s [287]. If the electric field is at least 5×10^5 V/cm, charge carriers are accelerated enough to create other electron/hole pairs once they scatter against crystal lattice by "impact ionization": an avalanche of charge-carriers starts. The process goes on as far as the potential V_{bias} is greater than the breakdown voltage V_{BR}, defined as the tension at which the SPAD stops to be non-conductive and the avalanche begins. When $V_{bias} > V_{BR}$ the SPAD is called to be in "Geiger mode", referring to the "discharge" in the Geiger-Muller tubes [288]; the overvoltage

$$V_{OV} = V_{bias} - V_{BR} \tag{5.1.1}$$

is one of the main parameters of the photodetector, together with the local temperature.
An equivalent circuit for a SPAD is shown in Figure 5.1.2. When the circuit is open, the capacitance C_J is charged at V_{bias}. Once that the SPAD is fired, the switch S closes and the capacitance starts discharging across the resistance R_S. As the current is flowing -i.e. the avalanche is ongoing- the SPAD is not sensitive to other incoming photons; so, the current must be stopped or "quenched". Passive quenching is performed by the resistor R_Q, which limits the current seen by the SPAD and thus lowers its voltage below the breakdown voltage, stopping the avalanche. Then the capacitance recharges back to V_{bias}, bringing the SPAD back to the photon-sensitive condition, at the overvoltage V_{OV}.

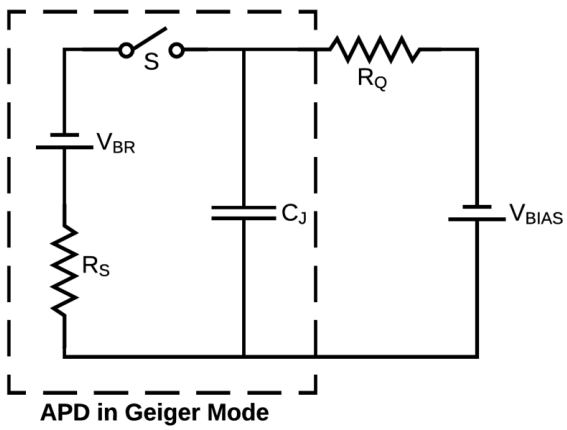

Figure 5.1.2: Equivalent circuit for a SPAD coupled with its quenching resistor R_Q. When the circuit is closed, the capacitance -at first charged to V_{bias}- discharges through the whole circuit. R_Q quenches the flowing current below the breakdown voltage: the switch opens. Then the capacitance recharges back to V_{bias}. As usually $R_Q >> R_S$, the recharge is expected to be much slower than the discharge process [286] [289].

5.1.2 From SPADs to SiPMs

The signal from a SPAD is binary, so any information about the total number of incident photons on the same SPAD is not available. SPADs are set in an arrays of hundreds-thousands, composing the SiPM; if the average number of photoelectrons per SPAD is $<< 1$, the number of fired SPADs is proportional to the intensity of the radiation. SPADs are set in parallel, as represented in Figure 5.1.3, which means that the current from a SiPM is the sum of the currents coming from all fired SPADs. For the same reason, when one or more SPADs are fired, the corresponding quenching resistor brings all SPADs down to V_{bias}, and then they all recharge back to V_{OV}.

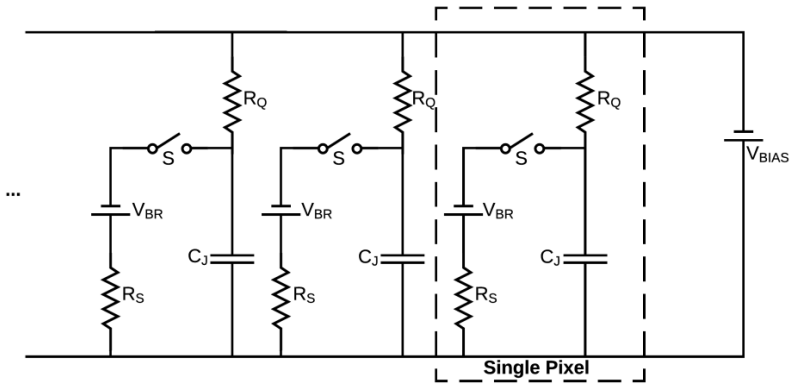

Figure 5.1.3: Equivalent circuit for a SiPM. SPADs -or pixels- are set in parallel, all charged to the same V_{bias}. When one of the SPAD's circuit closes, its quenching resistor R_Q decreases not only its SPAD's potential, but consequently the potential through all the pixels, whose capacitance then recharges back to V_{bias} [286] [289].

5.1.3 Noise in a SiPM

SiPMs are affected by uncorrelated noise (dark rate) and correlated noise, namely afterpulse and optical crosstalks, whose characterization in ReD experiment is the main result from this analysis.
The uncorrelated background or dark noise is due to electron-hole pairs which are thermally generated, with a probability proportional to the temperature. The dark count rate (DCR) is one of the main parameters for a SiPM, and it increases with the overvoltage. If one SPAD is fired by dark noise, the signal will mimic the one from 1 PE.
Afterpulses are due to electrons in the primary avalanche which are captured and then released by impurities of the silicon lattice. As the afterpulse avalanche happens in the same SPAD, the device might be not fully recharged; hence, the charge carried from the afterpulse is between 0 to 1 PE and increases with the time delay of the afterpulse. Their contribution affects the pulse shape discrimination power, as it introduces delayed charge in both nuclear recoils and electron recoils.
When the charge carriers are accelerated by the bias voltage in the SPAD avalanche, their isotropic photon emission may fire the closest SPADs. If this happens, a second avalanche, simultaneous to the primary one, starts: this is the optical crosstalk. The contribution of this noise will eventually increase the number of reconstructed photoelectrons, and so increase the energy smearing. A representation of the ways an optical crosstalk can be

produced is shown in Figure 5.1.4, which is a side view of two SPADs or pixels, sustained by the Silicon substrate. Once that one SPAD is fired, giving the "primary avalanche", about 10^7 near-infrared photons are released, able to cross substantial distances in the Silicon. If they cross the isolation trench and fire an avalanche in the high field region of a neighboring pixel, they are "Direct CrossTalks" (DiCTs), a simultaneous signal respect to the primary avalanche. On the other hand, if the photon reaching the second pixel has first been reflected in the Silicium substrate, the non-depleted region, O(10) ns of delay are expected between the primary avalanche and the crosstalk, which is then called "Delayed CrossTalk" (DeCT). The same primary avalanche can also fire an afterpulse in its own pixel, beside the crosstalks production. Furthemore, crosstalks themselves can give rise to afterpulses in their SPAD.

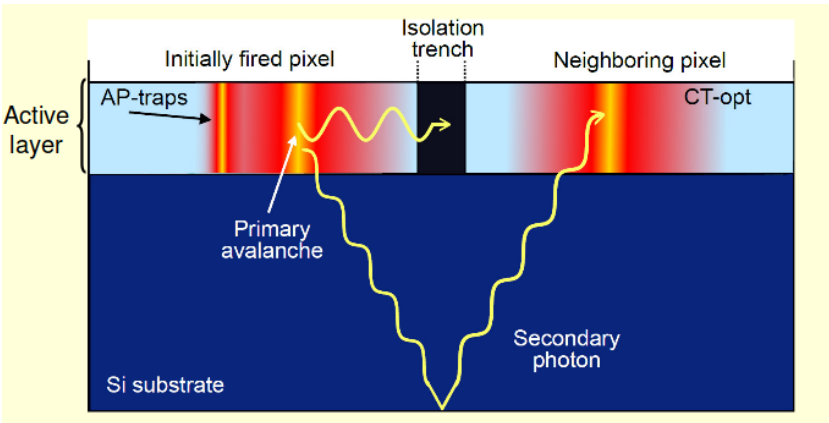

Figure 5.1.4: Illustration from a side view of correlated noises from a SPAD. Once that one pixel is fired, giving the "primary avalanche", the acceleration of charge carriers releases near-infrared photons according to a isotropic spatial distribution. The emitted photons eventually reach one close pixel, giving an Optical Crosstalk, which is Direct or Delayed depending on whether the photon is directly absorbed in the active region after passing through the isolation trench or it is first reflected by the Silicon substrate, with a resulting delay of O(10) ns. The same primary avalanche can also -but not necessarily- determine an afterpulse in the primary pixel, if one or more charge carriers has been trapped and then released by defects in the Silicon lattice [290].

5.1.4 FBK-NUV-HD LF SiPMs

In the present analysis the characterization of afterpulses and optical crosstalks is performed in the Near-Ultraviolet High Density Low Field SiPMs from Fon-

dazione Bruno Kessler, specifically designed to cover all the 14 m^2 of the top and the bottom arrays of DarkSide-20k TPC. The SiPMs installed in ReD are 11.7 x 7.9 mm^2, with a SPAD active surface of 25 x 25 μm^2, for a total SPAD density of 147888 SPADs per SiPM. The Low Field model, differently from the High Field one, is triple doped to have a higher field strength in the avalanche region. At LAr temperature the breakdown voltage for the Low Field model is 27 V, as it is shown in Figure 5.1.5.

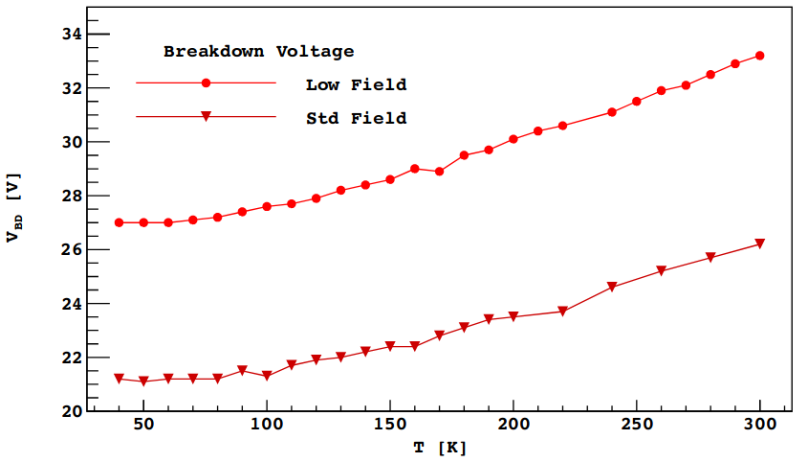

Figure 5.1.5: Breakdown Voltage for FBK-NUV-HD Low Field and High Field SiPMs measured at cryogenic temperatures [285].

In ReD SiPMs are operated at an overvoltage $V_{OV} = 7$ V. As can be sensed from Figure 5.1.6 , this implies a current amplitude of ≈ 4 μA from each fired SPAD. The quenching resistor is equal to 10 MΩ, giving a characteristic recharge time of about 2 μs at 87 K, as can be seen in Figure 5.1.7.

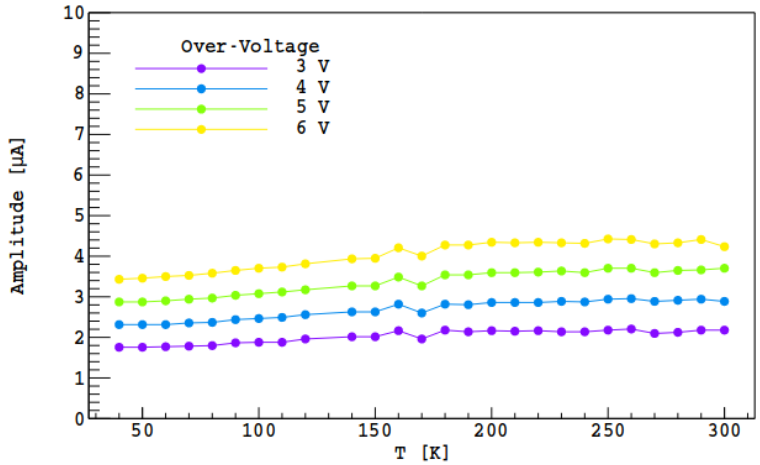

Figure 5.1.6: The amplitude of the average signal from a SPAD increases with the overvoltage. For any overvoltage a slight increase with the temperature is observed [285].

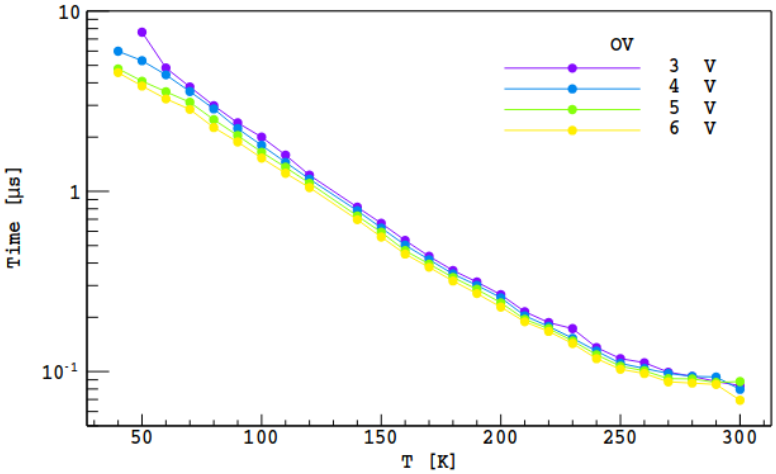

Figure 5.1.7: The characteristic recharge time is determined by the quenching resistor, equal to 10 MΩ in FBK-NUV-HD LF SiPMs [285].

The gain is the number of charge carriers developed in an avalanche, and strongly depends on the temperature and on the applied overvoltage. This is shown in Figure 5.1.8 for the SiPMs in analysis for a wide range of temperatures. In ReD the gain is about $7 \cdot 10^5$ electrons for each SPAD.

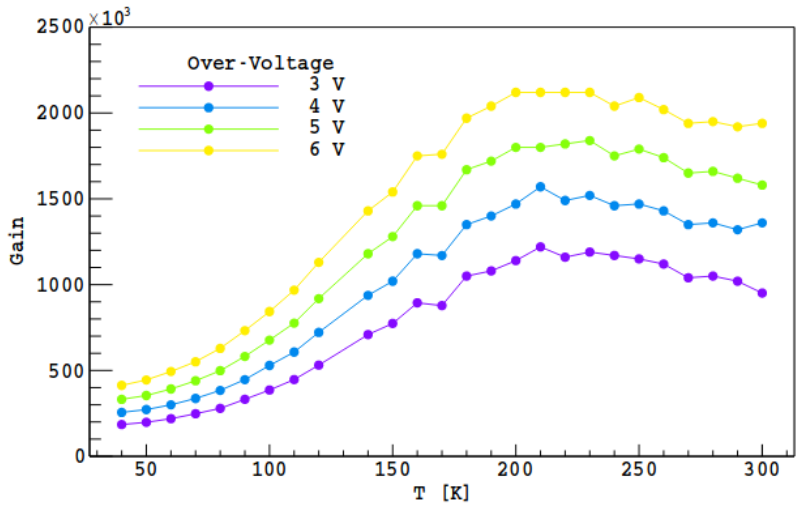

Figure 5.1.8: The gain is the number of charge carriers accelerated in an avalanche. It strongly depends on the overvoltage and the temperature [285].

Furthermore, the SiPMs developed from FBK company shows to have the dark count rate required for dark matter search in DarkSide-20k, equal to 0.04 cps/mm^2, which means 3.7 Hz per SiPM.

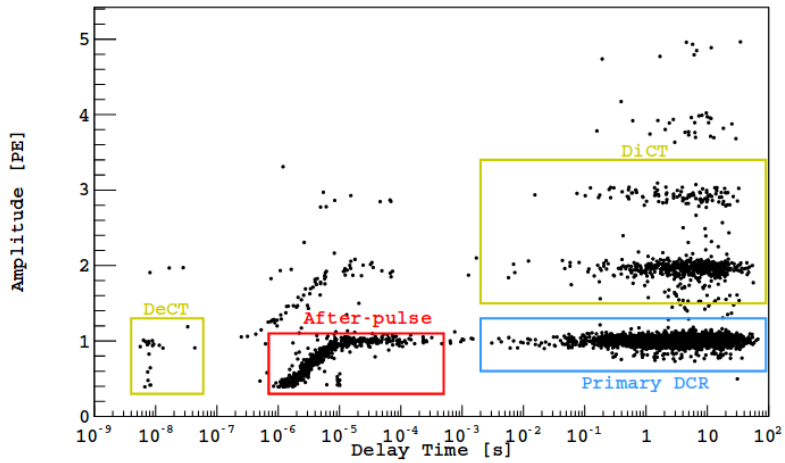

Figure 5.1.9: Distribution of correlated and uncorrelated noise in terms of the delay time, in absence of light at 77 K. After the primary pulse, the small population of Delayed Crosstalks is focused at a few nanoseconds. Then the afterpulses, together with the optical crosstalks induced are scattered at a few microseconds, with an amplitude that goes up to a maximum of one entire photoelectron. Finally the dark count rate is recognized between a few milliseconds up to O(100)s, together with their induced optical crosstalks, whose amplitude is proportional to the number of fired SPADs [285].

In Figure 5.1.9 are plotted 5000 events of dark noise together with correlated noise in absence of light at 77 K. The populations described in the previous paragraph are underlined, to have an overview of their distribution in terms of the time delay from a primary pulse. At a few nanoseconds the Delayed Crosstalks shows up, until O(10) ns. Afterpulses are distributed from about one microsecond and until about one millisecond, with a carried charge which increases up to one photoelectron. Finally the dark noise from thermally generated photoelectrons starts after a few milliseconds. For each listed signal, there's a population of direct optical crosstalks, which increases the amplitude of the signal from 1 PE up to a few PE. For instance, the population just above the afterpulses are the direct (and delayed) optical crosstalks induced from the afterpulse avalanche: indeed, they have the same time distribution. In the same way the direct crosstalks induced by the primary dark count rate mimic the time distribution of the primary dark noise, extending until 4 photoelectrons.
The present analysis has the purpose to characterize afterpulses and optical crosstalks in FBK-NUV-HD-LF SiPMs operated at an overvoltage of 7 V at a temperature of 87 K.

5.2 SiPM Single Electron Response

In the present section the energy variables in the reconstruction code PyReD (see Section 3.4) are described: the integration charge and the prominence charge. Both are calibrated looking at their Single Electron Response (SER), which allows to determine the relationship between the energy variable and the input waveform.
The SER for FBK-NUV-HD-LF SiPMs was studied in ReD from the pulsed light of a Hamamatsu PLP-10 diode laser connected to the TPC through optical fibers. The external trigger was set at 100 Hz, each pulse lasting 50 ps with a wavelength of 403 nm. The laser runs analyzed were selected from the 7th data acquisition Campaign, which took place in Naples between December 2018 and January 2019. Among all the runs, here are analyzed only the ones in which both the tiles were connected to the laser beam and in which no gas pocket was present, in order to guarantee the best uniformity through the data. The focus will be set on the ReD top tile, where each SiPM corresponds to one read-out channel.

5.2.1 Integration Charge

The number of photoelectrons seen by the SiPM is usually defined from the integral of the acquired waveform. The consequent distribution from ReD laser runs is shown in Figure 5.2.1 for Channel 27, in the top tile. Each peak is due to events to 0, 1, 2...N photoelectrons. The distribution, called Single (Photo)Electron Response (SER), is then fitted with the function

$$f(x) = \sum_i A_i \cdot Gaus(\mu_i + offset, s_i) \tag{5.2.1}$$

$$\begin{aligned} \mu_i &= gain \cdot i; \\ s_i &= \sqrt{\sigma_0^2 + i \cdot \sigma_1^2} \end{aligned} \tag{5.2.2}$$

where the *gain* is the integral of the waveform – expressed in ADC x TDC– corresponding to one photoelectron. A_i is the amplitude of the gaussian related to i photoelectrons, centered at μ_i plus an offset. The resolution s_i of each gaussian is composed by the smearing σ_0 of the pedestal and the intrinsic resolution σ_1 of the single photoelectron.

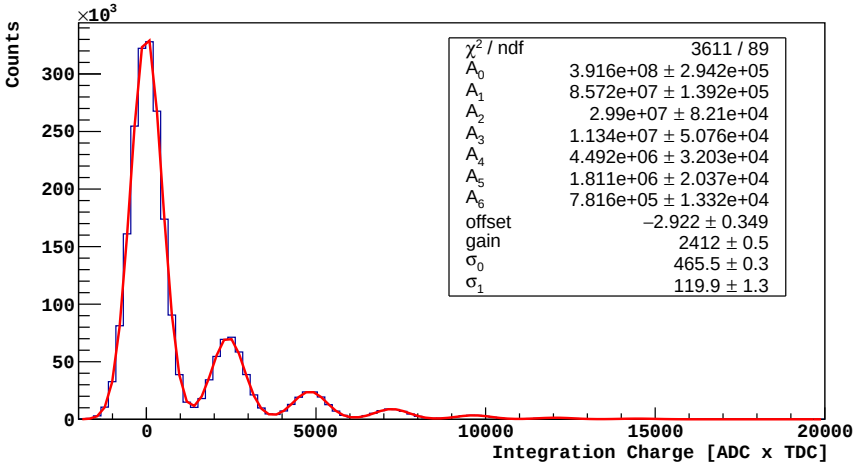

Figure 5.2.1: SER for ReD Channel 27, in the top tile. Each peak corresponds to the events with 0,1,2.. photoelectrons in input to the SiPM, and is fitted with a gaussian whose average is a multiple of the "gain", as can be seen in Equation 5.2.2

The number of photoelectrons is reconstructed using the relation

$$nPE = \frac{charge - offset}{gain}, \tag{5.2.3}$$

as confirmed by the SER calibration curve, where the A_i are indeed directly proportional to the number of injected photoelectrons; an example is given in Figure 5.2.2 for Channel 27.

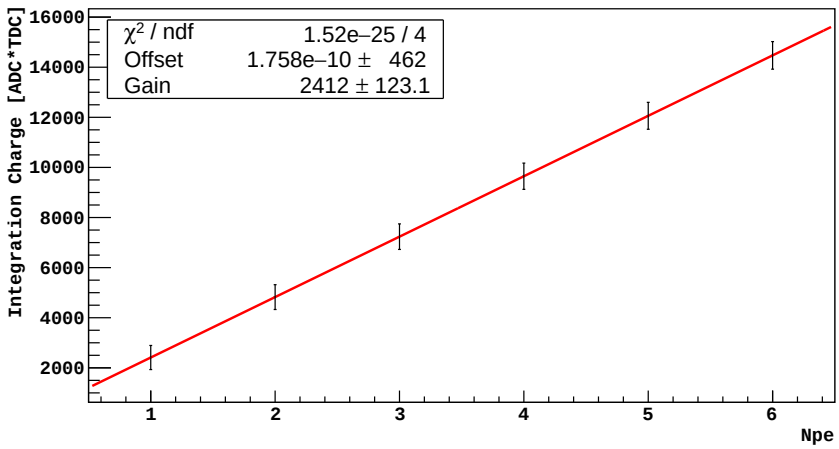

Figure 5.2.2: Calibration of the Integration Charge for ReD Channel 27 in the top tile. Each photoelectron gives a waveform with an integral of $(2.4 \pm 1) \times 10^3$ ADC x TDC.

It follows that the gain is here defined as the waveform integral corresponding to 1 PE. The gain for each ReD channel in the top tile is given in Figure 5.2.3.

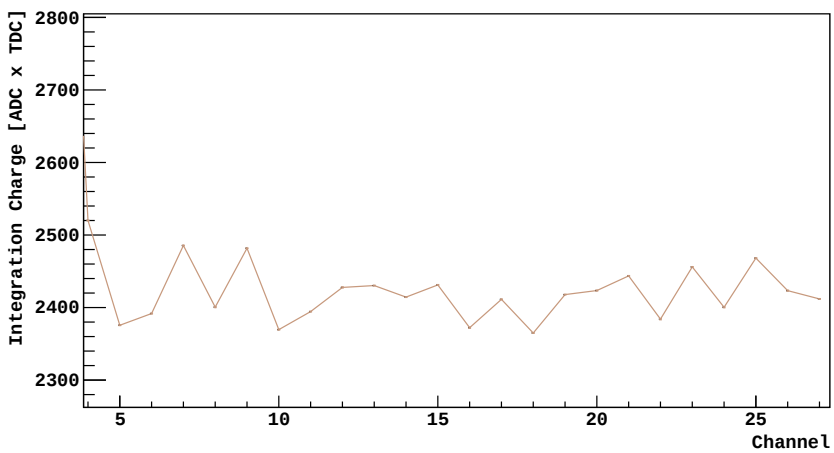

Figure 5.2.3: Gain for the integration charge for each ReD channels in the top tile, on average equal to 2400 ADC x TDC.

The relative SER resolution is the ratio between the uncertainty s_1 and the average integration charge μ_1 at 1 photoelectron. For instance, the SER

resolution in Channel 27 is 20 %; the SER resolution for all top channels is listed in Figure 5.2.4.

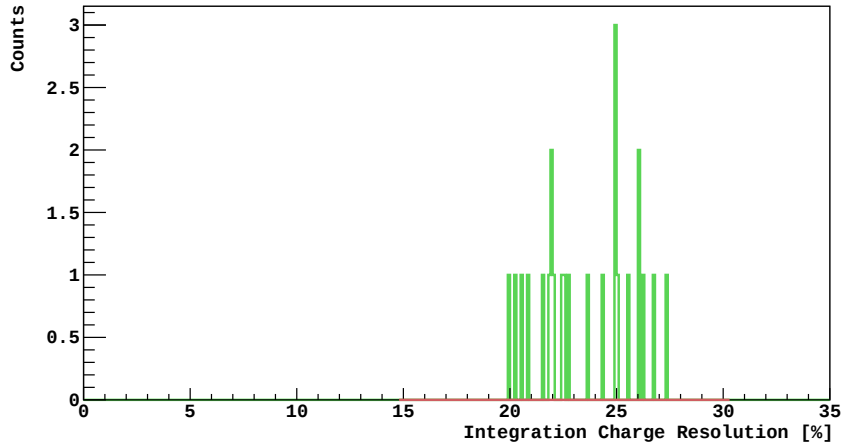

Figure 5.2.4: Percentage SER energy resolution for all ReD channels, calculated as the ratio between the smearing of the peak at one photoelectron in the SER and the gain. On average the SER resolution in ReD top channel is 24 %.

5.2.2 Prominence

Parallel to the integration charge, the number of photoelectrons can be reconstructed by using the matched filter and the "prominence", which is related to the height of the peaks along the filtered waveform. In this subsection the signal processing which allows for the definition of the prominence is described, before showing its calibration through all ReD channels.
The matched filter is the optimal linear filter which maximizes the signal-to-noise ratio (SNR) in presence of stochastic noise [291]. Originally applied to signal radar [292], today it is employed also in more advanced studies, as digital communications and gravitational waves detection [293]. Given an input waveform, which is the sum of a white noise and a signal, if the shape or "template" of the signal is known, the matched filter auto-correlates the template with the input waveform, to look for the template along the waveform. The template here is the time-response to a single photoelectron in input. An example of a waveform from a laser pulse is shown in Figure 5.2.5. As the trigger is set on the laser, the pulse is seen 6 μs after the begin of the acquisition window, which lasts 20 μs. The amplitude of the electronic noise is evaluated to be ≈ 3 ADC.

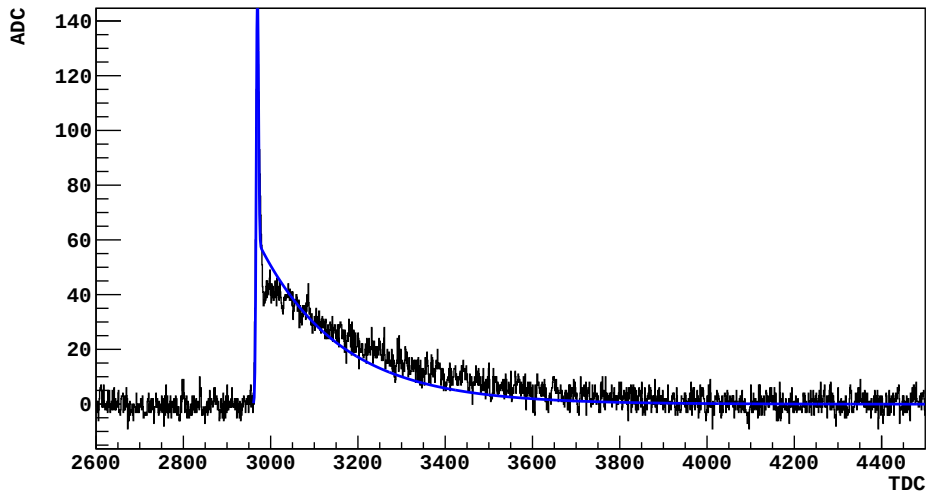

Figure 5.2.5: Laser pulse from Channel 15 due to one photoelectron. The fit function is the sum of a fast component -which determines the rise of the signal and is described by an exponential- and a slow component, which is characterized by the recharge time of the SPAD and it is fitted with the convolution of a gaussian and an exponential. The digitizer has a sampling rate of 500 MHz, so each TDC sample corresponds to 2 ns.

This signal is modelled as the sum of a fast component f_{fast}, which is a gaussian, and a slow one g_{slow}, provided by the convolution of a gaussian and an exponential,

$$f_{fast}(x) = \frac{1}{\sqrt{2\pi}\sigma} exp\left(-\frac{x^2}{2\sigma^2}\right) \tag{5.2.4}$$

$$g_{slow}(x) = \frac{1}{2\tau} exp\left[-\frac{1}{\tau}\left(x - \frac{\sigma^2}{2\tau}\right)\right]\left[1 + erf\left(x - \frac{\sigma}{\tau}\frac{1}{\sqrt{2}}\right)\right] \tag{5.2.5}$$

$$s(x) = f_{fast}(1 - p_s) + p_s g_{slow}. \tag{5.2.6}$$

The same model was applied to ReD top channels, in order to determine the template used by the matched filter.

The reconstruction of ReD channel with both the integration charge and the prominence algorithm previously described was performed in the high-level programming language Python; the software, called PyReD, will also be the model for the reconstruction software of future DarkSide detectors. At the time of this analysis, PyReD database was updated only with the raw data from one FEB, so only the templates of the first 12 top channels

were analyzed according to the mapping given in Figure 3.4.3. Their fit parameters are listed in in Figure 5.2.6.

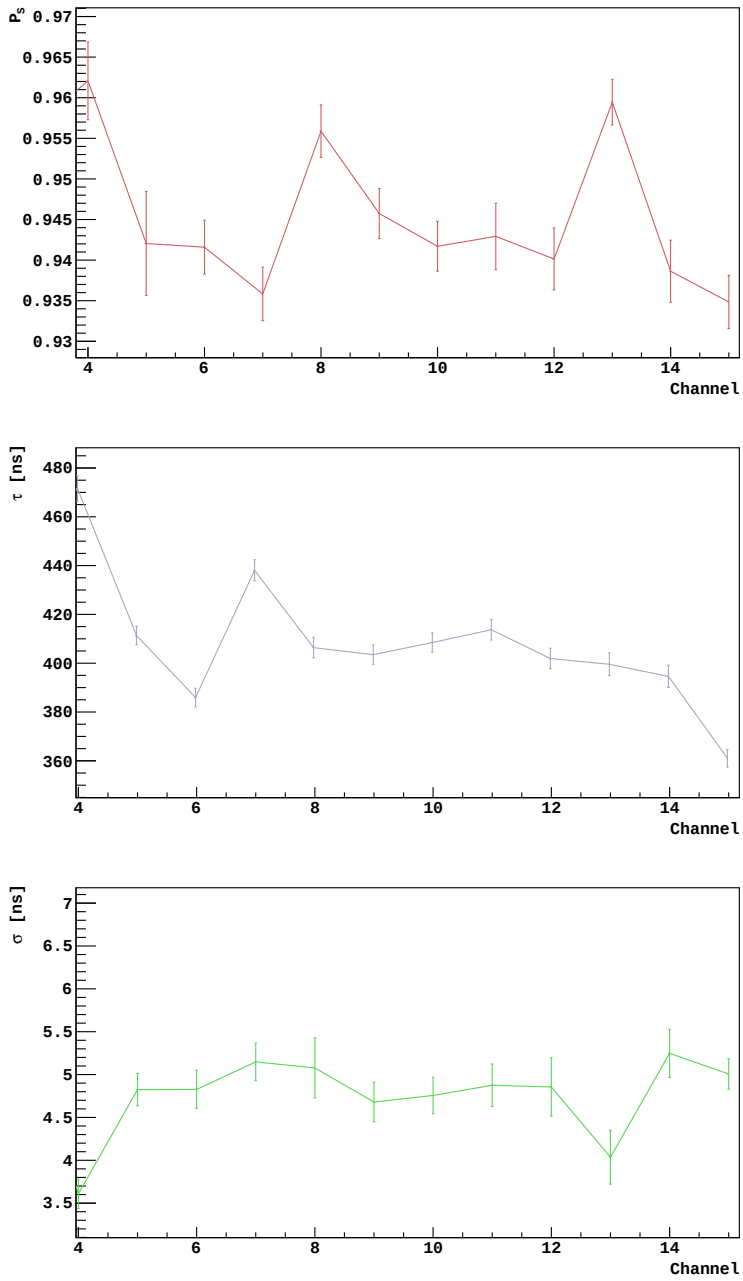

Figure 5.2.6: Fit parameters for the first twelve channels in the top tile. On average $\sigma \approx 4.5$ ns, $\tau \approx 400$ ns and $p_s \approx 0.94$.

The template is used with the matched filter. The hypothesis beyond matched filter application is that the waveform in input is the linear combination of a signal f –the one due to the photoelectrons, here– and the stochastic noise n,

$$s(t, |A, t_0) = A \cdot f(t, t_0) + n(t) \tag{5.2.7}$$

where the signal s is determined by two nuisance parameters, namely the scaling factor A and the time t_0 at which the pulse starts. The matched filter optimizes the Signal-to-Noise ratio by convolving the waveform itself with the time-reversed signal or "kernel" f(-t),

$$s_{filtered} = s(t, |A, t_0) \otimes f(-t) \tag{5.2.8}$$

According to Equation 5.2.6 the autocorrelation is the linear combination of a slow and a fast component with the waveform, where each component is the matched filter for the corresponding component in Equation 5.2.6,

$$\begin{aligned} Filtered_{Wf} &= (1 - p_{slow}) * F_{fast} + p_{slow} * F_{slow}; \\ F_{slow} &= Flip\left[LFilter\left(\frac{1}{\tau}, \left\{1, \frac{1}{\tau} - 1\right\}, Flip(Wf)\right)\right] \\ F_{fast} &= GaussianFilter(Wf, \sigma). \end{aligned} \tag{5.2.9}$$

The fast component of the template is a Gaussian. The matched filter for a gaussian signal uses as template the conjugated time reversed of a gaussian, which is still a gaussian. The result is that the Gaussian-Filter smooths the peaks assuming for each a gaussian shape with the smearing σ.
The slow component of the matched filter is based on the digital filter $LFilter$, from Python' Scipy library. It acts in three steps:
-the waveform is time-reversed (flipped) and stored as an array $x[n]$;
-the digital filter $Lfilter$ takes $x[n]$ in input and returns for each point $y[n]$, given by

$$y[n] = \frac{1}{\tau}x[n] + (\frac{1}{\tau} - 1)x[n-1] \tag{5.2.10}$$

-the output is finally flipped back to the original time order.

Figure 5.2.7 shows the output from a toy Monte Carlo simulation, to see the effect of the matched filter.

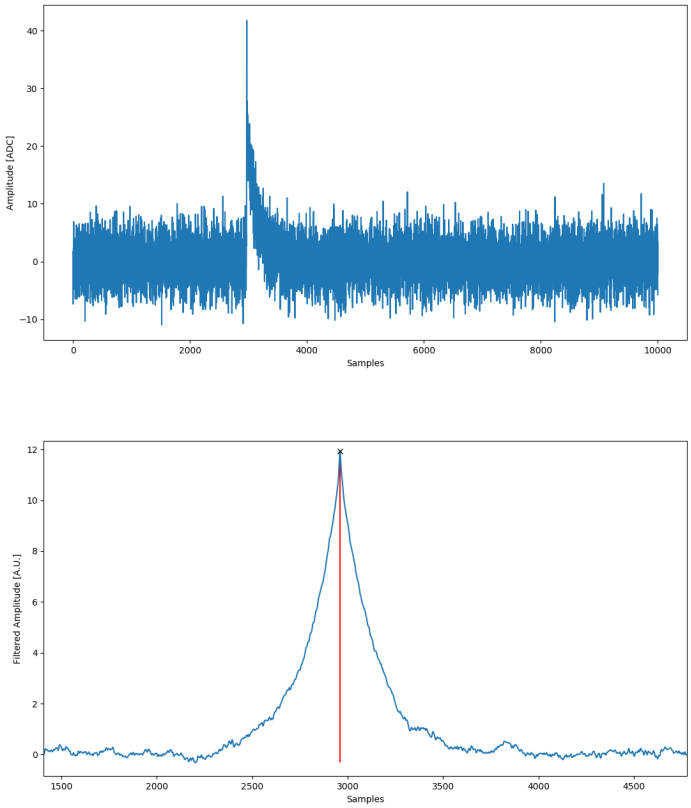

Figure 5.2.7: Simulated waveform in ReD from 2 simultaneous photoelectrons before (top) and after (bottom) the application of the matched filter. Notice how the electronic noise is strongly suppressed, while the information on the relative amplitudes of the pulses are kept, together with their arrival time. The peak-finder algorithm provides for each peak the time and the "prominence", which is shown in red and is defined as the height of the filtered peak after subtraction of the local baseline and close dominant peaks.

Pulses are generated on the waveform according to the parameters listed in Figure 5.2.6, reproducing the response to a laser pulse for each ReD channel; then the waveform is filtered with the template for the specific channel.

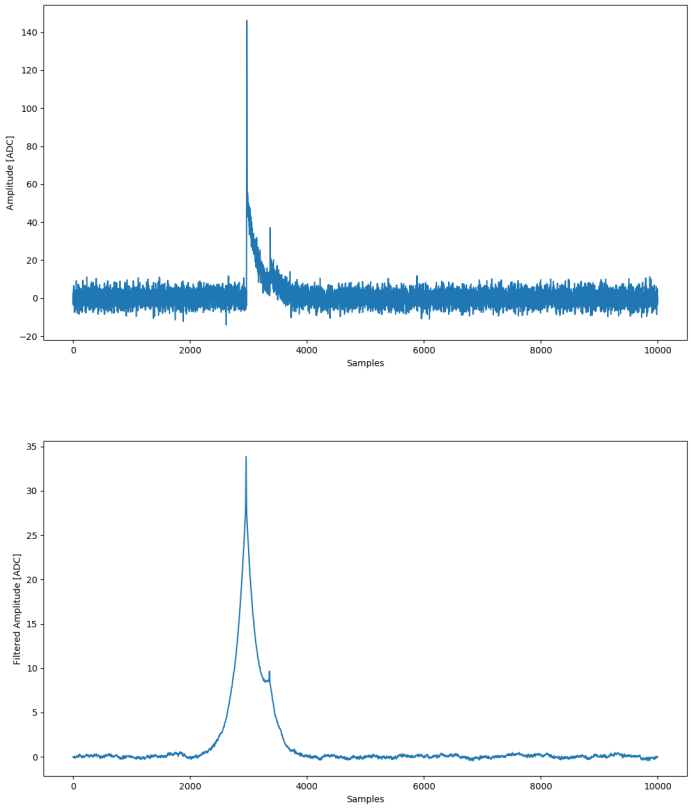

Figure 5.2.8: Simulated waveform in ReD from 5 photoelectrons followed by one afterpulse before (top) and after (bottom) the application of the matched filter. Notice how the electronic noise is strongly suppressed, while the informations on the relative amplitudes of the pulses are kept, together with their position.

Afterpulses are investigated using simulations and exploiting the filtering. For instance Figure 5.2.8 is the simulation of a laser pulse from 5 photoelectrons followed by an afterpulse at a time delay of 800 ns. This waveform was then filtered with the matched filter in Equation 5.2.9 with a strong increase of the signal to noise ratio. The peak-finder algorithm -from Python' Scipy library- was then applied on the filtered waveform, storing for each peak its position and "prominence", defined as the height of the filtered peak after subtraction of the "local" baseline and of close dominant peaks. The peak finder is based on three parameters, which define the criteria to identify and store a peak:
- a minimum height from the baseline, here set at 4 in the filtered waveform;

- a minimum prominence, here set at 3;
- a minimum distance from the previous peak, here set at 1 sample.
An example of how the peak-finder works is shown in the simulation in Figure 5.2.9, on the filtered waveform from height photoelectrons in a laser pulse. N overlapped peaks return a prominence equivalent to N photoelectrons, thanks to the SER calibration.

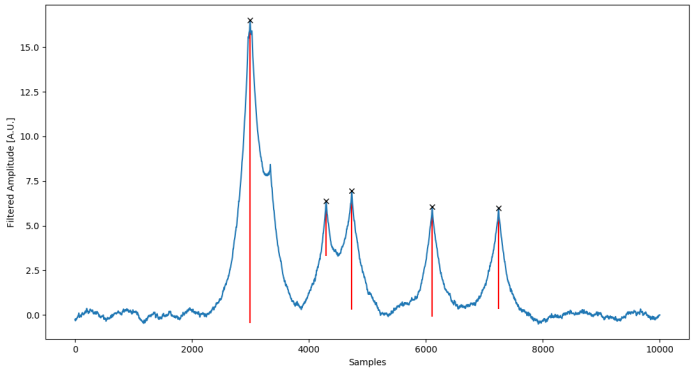

Figure 5.2.9: The peak found by the peak finder algorithm are drawn in red, along a simulated and filtered waveform from eight photoelectrons. The second peak was not found as it was below the prominence threshold at 3. Also any peak with a filtered amplitude less than 4 would not be seen, as it would be below the height threshold. Finally all the ripples left after the filtering are also suppressed by asking a minimum distance of 1 sample between two peaks.

These conditions on one hand allow to exclude any residual electronic noise but, on the other hand, also mean that some peaks may be skipped, for any of the three conditions listed above. Hence the peak-finder efficiency for each channel in ReD was determined for increasing values of the time delay. Thousands of laser events with one photoelectron followed by an afterpulse were simulated, for any time-delay of the afterpulse from the primary pulse. As can be seen in Figure 5.2.10 for Channel 15, all peaks separated by at least 500 ns are always found by the peak-finder, while two peaks separated by less than 100 ns can't be distinguished, mainly because the second one pile-ups on the shoulder of the first one, keeping a prominence below threshold. For this reason in this analysis the peak-finder algorithm was applied to only look for afterpulses, and not Delayed Optical Crosstalks, whose typical delay is O(10) ns.

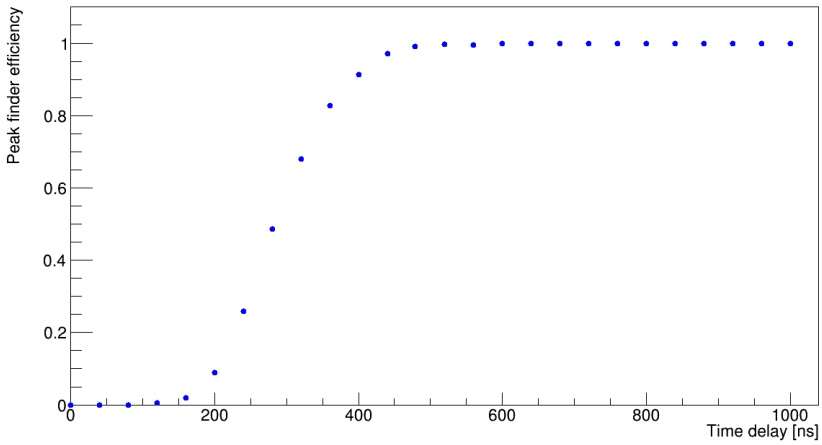

Figure 5.2.10: Peak finder efficiency in terms of the afterpulse time delay in Channel 15. Any peak with a time delay of at least 500 ns will be "seen" by the peak finder. Below 150 ns the algorithm is completely inefficient. For this reason this technique was applied to find afterpulses, but not delayed optical crosstalk, whose time delay is O(10 ns).

A definition of charge can be derived from the prominence, as the larger the prominence of a peak, the larger the number of photoelectrons related to that avalanche. As already done for the integration charge, also the prominence charge needs a custom SER calibration. In Figure 5.2.11 the prominences for all the found peaks on the filtered waveform are summed up for each laser event, for Channel 14 in the top tile. The consequent calibration of the variable is then shown in Figure 5.2.12, in analogy with what performed with the integration charge.

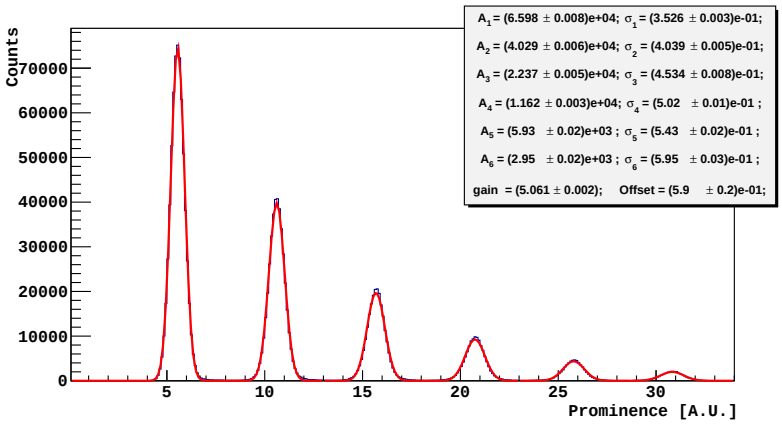

Figure 5.2.11: SER for the prominence charge in Channel 14, in the top tile. Events at zero photoelectron are not counted, as the height and/or the prominence would be below threshold. Each photoelectron returns a peak prominence of about 5.1. The energy resolution is $\sigma_1/gain = 7\%$.

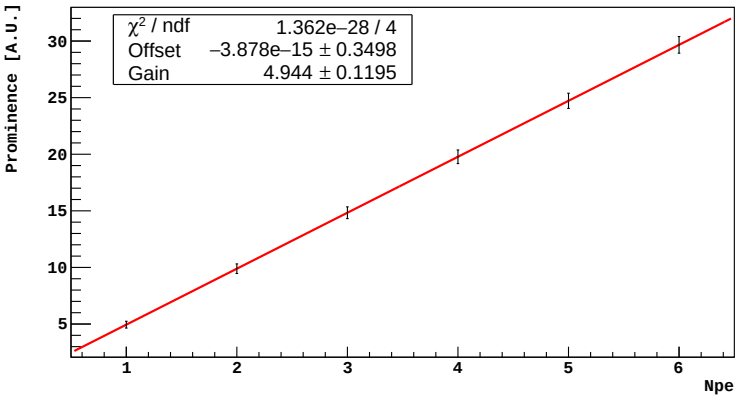

Figure 5.2.12: Calibration for the Prominence variable. The errors are the standard deviations of the gaussian in the SER figure.

Events at zero photoelectrons are not found by the peak-finder in the top channels, as their height and/or the prominence is below threshold. One single photoelectron returns a prominence of about 5 in the top channels, as shown in Figure 5.2.13.

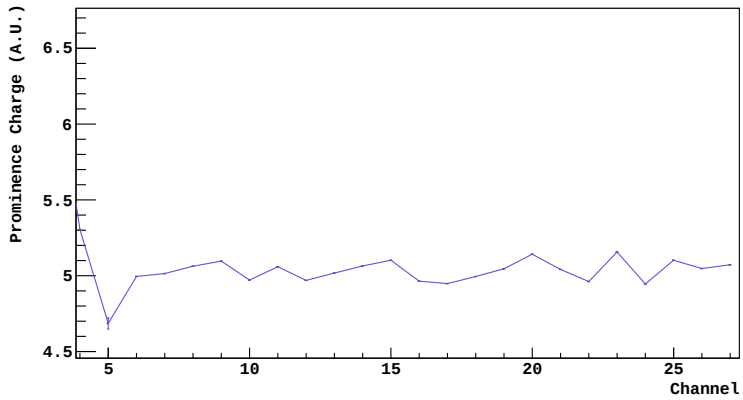

Figure 5.2.13: Gain for the prominence charge, for all ReD top channels. On average a peak of 5 as prominence corresponds to 1 PE.

The distribution of the resolution for the prominence charge is shown in Figure 5.2.14. The resolution in the top channels using the Prominence variable is on average 6.5 %.

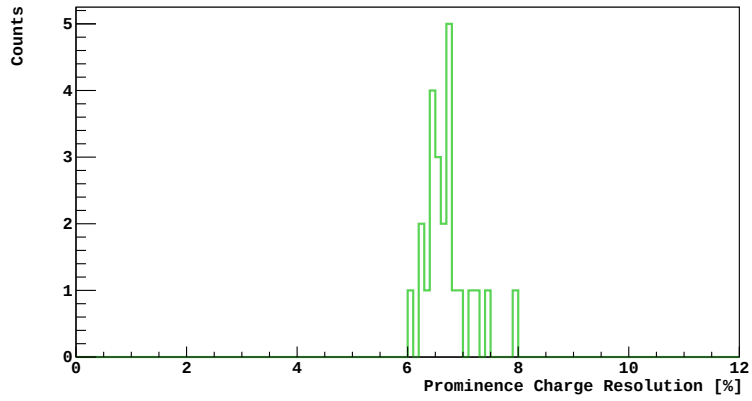

Figure 5.2.14: Resolution for the prominence charge in top tile. The charge defined from the prominence shows to have a resolution of about 6.5 %.

In the following subsections the correlated noise for all ReD top channels are determined, by the use of both the peak-finder and the prominence charge and the integration charge.

5.3 Characterization of afterpulses in ReD

An afterpulse is a delayed avalanche occurring during the SPAD recharge time and resulting on a pulse on the tail of the primary avalanche. By means of the signal processing algorithm described in Section 5.2.2, the probability for an afterpulse to occur was determined in each ReD top channel. Also, their distribution in terms of the time delay from the primary pulse and the energy carried for a given time delay were characterized, as they will allow for the determination of crosstalk probability, in the next section.
The laser run analyzed are the ones selected from Campaign 7, in which no gas pocket was created by the bubbler and in which both the tiles were connected to the laser signal. Thanks to the matched filter, the waveforms from laser runs are filtered, as already explained in Section 5.2.2. The peak-finder algorithm then looks for all the peaks along the waveform, due to primary avalanches, dark noise, afterpulses and optical crosstalks. The channel, the time and the prominence of each peak are stored in branches in TTree-s of ROOT package.
The parameter of interest is the probability P_{AP} to have an afterpulse, given 1 PE in the primary pulse. Indeed the happening of an afterpulse in one SPAD is an event independent from any afterpulse in different SPADs, so the probability $P_{AP,N}$ to have an afterpulse given N photoelectrons in the primary pulse is

$$P_{AP,N} = N \cdot P_{AP}. \tag{5.3.1}$$

For this reason only the events in which the peak-finder found 1 PE in a peak corresponding to the expected trigger time, at 5920 ± 40 ns, were considered, and this peak was tagged as primary pulse. Then all the other peaks identified in the same event are dark noise and afterpulses. Specifically dark noise is not correlated to the primary pulse, so it occurs with the same probability before and after it; on the other hand, no afterpulse is expected before the primary pulse. Thus, a scanning through all the peaks found before and after the primary up to 10 μs was performed. All the peaks before the primary pulse must be uncorrelated noise, while after the primary must lie both afterpulses and uncorrelated noise. An example of the peaks distribution is shown in Figure 5.3.1 for Channel 27. Here, 50403 events are found to have the primary peak with 1 PE in the expected trigger time; hence, for each of these events, the scan of the found peaks is performed, storing them before and after the $Peaktime = 0$, according to their relative time position respect to the primary peak, which is not stored. It is observed that before O(10) ns of time delay from the primary peak, the number of found peaks drops down; this happens because the peaks are below the prominence threshold, as they pile-up with the primary peak, so they are skipped by the peak finder. Hence they

are not stored, both before and after the primary pulse. Then, after about 50 ns of time delay, the distribution of the found peaks is clearly asymmetric, as before the primary pulse, at Peak time < 0 only uncorrelated noise occurs, while at Peak time > 0 it sums with afterpulses.

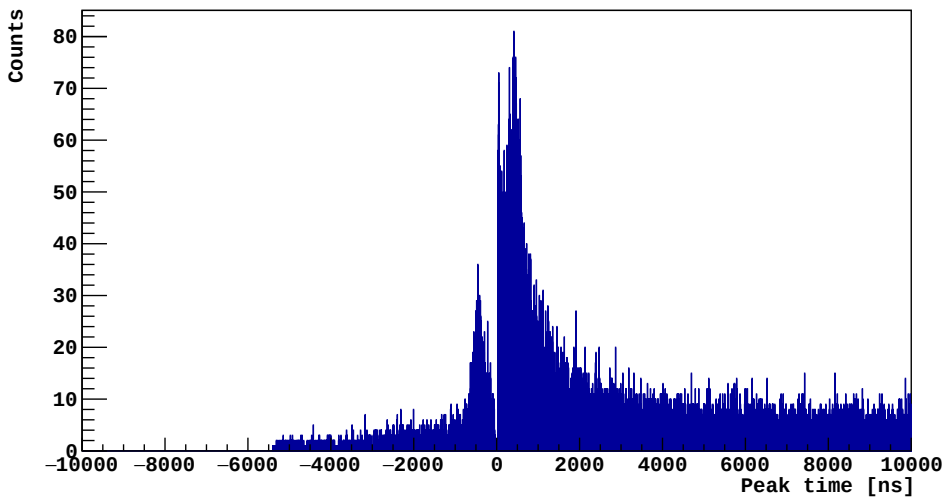

Figure 5.3.1: Peaks found before and after the primary avalanche in 5043 events from Channel 27, where the primary pulse carries 1 PE in the expected trigger time, at 5920 ± 40 ns. For each events, the primary peak is not stored. The primary peak time is taken as zero; then all the found peaks in that event are stored according to their arrival time respect to the primary pulse. Dark (uncorrelated) noise is distrubuted with the same probability before and after the primary peak, while afterpulses can lay only after the primary avalanche. The drop below about 50 ns is due to the prominence of the peaks nearby the primary pulse, which results to be below the peak-finder prominence threshold.

The dark noise is estimated in the region before the peak, the one not affected by afterpulses. As dark noise is uniformly distributed before and after the primary, the subtraction of the peaks before the primary with the ones after it returns the distribution of the afterpulses in terms of the time delay from the primary pulse. For Channel 27 this distribution is shown in Figure 5.3.3, (blue curve). The integration of this afterpulse distribution along the acquisition window returns the afterpulse average probability to occur, given 1 PE in the primary avalanche. Figure 5.3.2 returns the afterpulse probability for all ReD channels in the top tile.

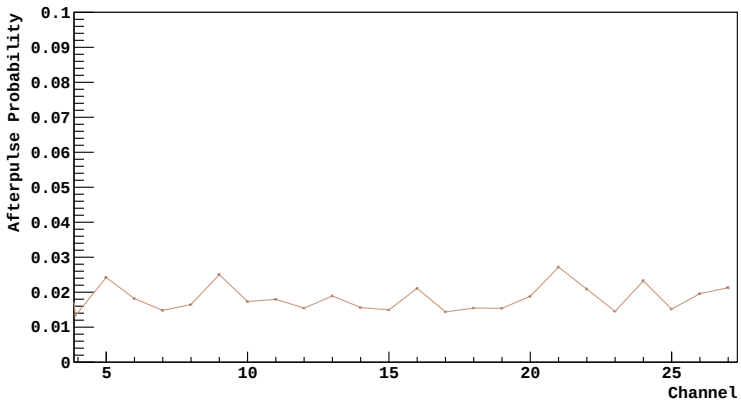

Figure 5.3.2: Distribution of the afterpulse probability in ReD top channels. On average the probability to have an afterpulse given 1 PE in the primary avalanche is $\approx 2\%$.

On average, an afterpulse probability of 1.5 % was found in ReD channels. This is much smaller than the one found in [285], where it is $\approx 13\%$ at $V_{OV} = 6$. This is believed to be due to the peak-finder inefficiency for small time delay.

For the determination of the crosstalk probability, it is fundamental to correct the afterpulse distribution for the peak-finder efficiency in Figure 5.2.10, to know the afterpulse true distribution. The result was then fitted with the sum of two exponentials and a constant.

$$f(x) = A\frac{exp(\tau_1)}{\tau_1} + B\frac{exp(\tau_2)}{\tau_2} + C \tag{5.3.2}$$

For reference, in Figure 5.3.3 the corrected afterpulse distribution is shown in red, together with the uncorrected one, in blue. The correction for the peak finder efficiency shows that the afterpulse probability monotonically decreases with the increase of the time delay, as expected.

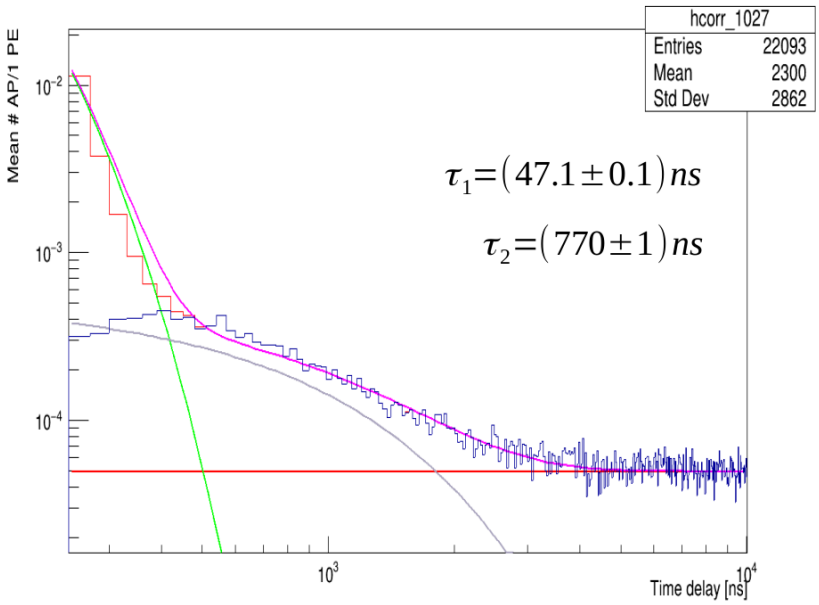

Figure 5.3.3: Time distribution of afterpulses in Channel 27 (blue line), obtained after the subtraction of the peaks found before the primary with the ones found after it. The distribution was then corrected for the peak finder efficiency (red line) and then fitted with the linear combination of two exponential and a constant.

Specifically, before about 500 ns, the SiPM is still recharging back, so the probability to have an afterpulse is much higher than after the average recharge time. In the fit function in Equation 5.3.2 this is related to the two exponentials. In Figure 5.3.4 the characteristic times τ_1 and τ_2 are listed, together with their uncertainty, for all top channels.

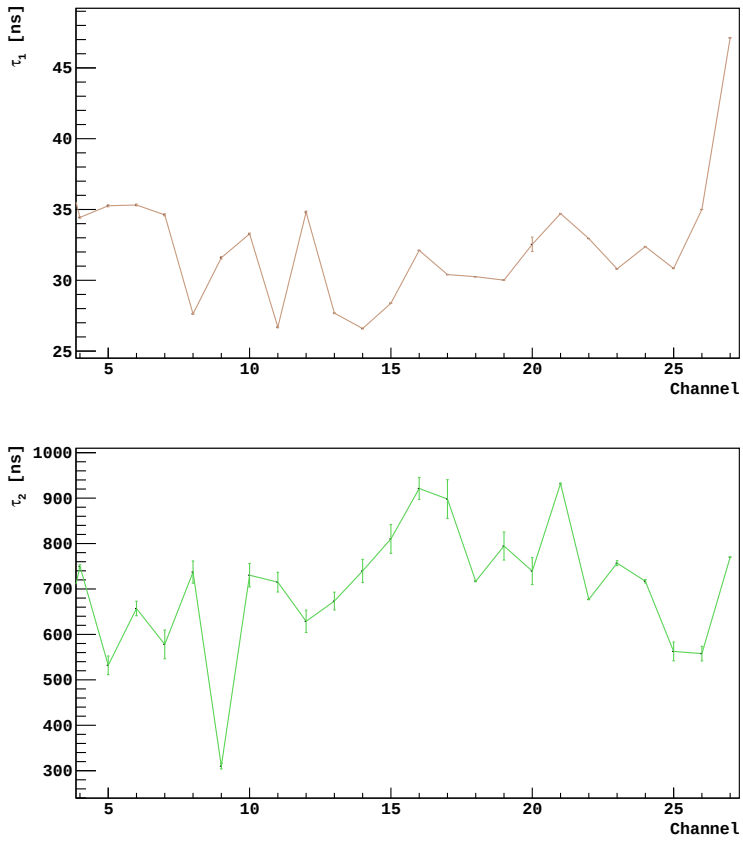

Figure 5.3.4: Characteristic times for the two exponential functions fitting the corrected afterpulse probability, for each ReD top channel.

The final result of the present section is to determine the energy carried by an afterpulse in terms of the time-delay at which it develops. Given the templates of the SiPMs response in all ReD channels due to 1 PE (see Figure 5.2.6), the cumulative of the template starting from a given time delay returns the charge available for an afterpulse avalanche, as can be seen in Figure 5.3.5 for Channel 27. After about 1 μs the whole amount of charge carriers is restored and the afterpulse, if it happens, returns an energy of one entire photoelectron.

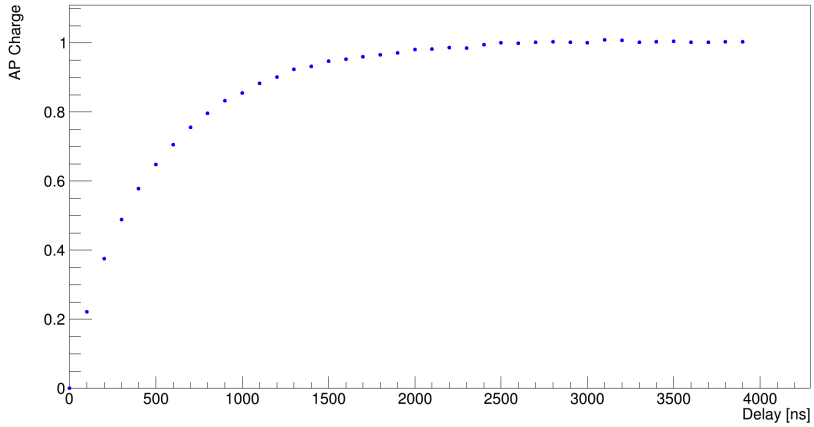

Figure 5.3.5: Afterpulse energy in terms of the time delay for the Channel 27. Avalanches after a small time delay from the primary will also have a small fraction of charge, assuring a negligible impact on the average number of reconstructed photoelectrons.

The afterpulse characterization in ReD channels showed that the smaller the time delay, the higher is the probability to have an afterpulse; on the other hand, the smaller the time delay, the smaller the charge of the afterpulse in itself, due to the long recharge time required by a SPAD.

The signal processing described in Section 5.2 allowed to determine not only the probability to have an afterpulse given 1 PE in the primary, but also their average number and the carried charge for each time delay. All these results will be fundamental for the characterization of Direct Optical Crosstalk, described in the next section.

5.4 Optical Crosstalk characterization

An optical crosstalk can't be identified by the peak finder algorithm, as they are simultaneous to the primary avalanche. So a toy Monte Carlo, simulating laser pulses with afterpulses and crosstalks was performed and compared to the true data: as the afterpulses are already characterized, the only parameter left to constrain is the crosstalk probability.
The starting point is to evaluate the mean occupancy for each ReD channel. Indeed the signal from a laser is tuned at low-intensity, on average equivalent to one single photoelectron. As the number of photoelectron is an integer, the SER amplitude distribution in Figure 5.2.1 would be a Poissonian of the average occupancy μ, without the contribution of correlated noises. For each channel, μ was then evaluated from the fraction N_0 of events in the pedestal

–at 0 PE in Figure 5.2.1– normalized to the number of triggers, as at least 1 PE in the primary event is required to have afterpulses or crosstalk.

$$\mu = -Ln\left(\frac{N_0}{N_{triggers}}\right). \tag{5.4.1}$$

The average value μ is the starting point of the simulation. The "true" signal Q from the laser is simulated according to its Poissonian distribution. Then, any generated photoelectron can give rise to an afterpulse, a crosstalk or to both of them, increasing the number of observed photoelectrons. A flux diagram is shown in Figure 5.4.1 to describe the simulation.

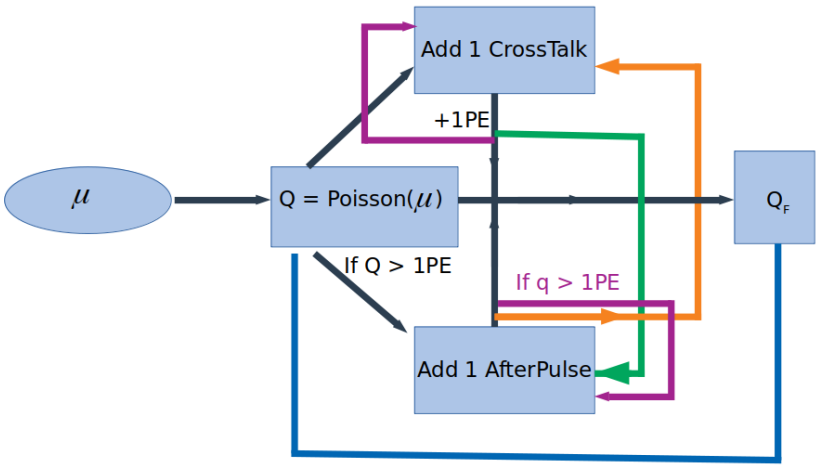

Figure 5.4.1: Diagram of the C++ based Monte Carlo. Once that the primary pulse is generated according to the theoretical poissonian distribution, each photoelectron can give an afterpulse and/or a crosstalk. An afterpulse can give rise to a secondary afterpulse and/or a crosstalk. Same way a crosstalk can give rise to a secondary afterpulse and/or crosstalk; the only condition stands for afterpulses, whose primary pulse must be at least equivalent to one photoelectron. The loop goes on until the number of photoelectrons Q_F stops increasing.

Each pseudoexperiment takes in input the mean occupancy μ, for a given ReD channel. The "true" number of photoelectron Q, without any correlated noise contribution, is the Poissonian of the mean occupancy μ. The resulting charge can give rise to both an afterpulse and a crosstalk. The afterpulse delay time is taken from the time distribution corrected for the peak-finder efficiency (red line in Figure 5.3.3), while the energy corresponding to that delay is taken from Figure 5.3.5. Once that an afterpulse is generated, if its

energy is at least of one photoelectron, it can give rise to both a secondary afterpulse and/or a crosstalk; if it is less than 1 PE, only a crosstalk can be generated.
Crosstalks can themselves generate an other afterpulse, a crosstalk, or both of them. Same way, an afterpulse can give rise to a crosstalk, which do not need one entire photoelectron in the afterpulse. Afterpulses and crosstalks are generated until the number of photoelectrons stops increasing. The loop is infinite in principle, but it converges due to the small probability. The only parameter not known and free to change is the crosstalk probability, which is here the effective probability to have a crosstalk on any of the SPADs surrounding the fired one.

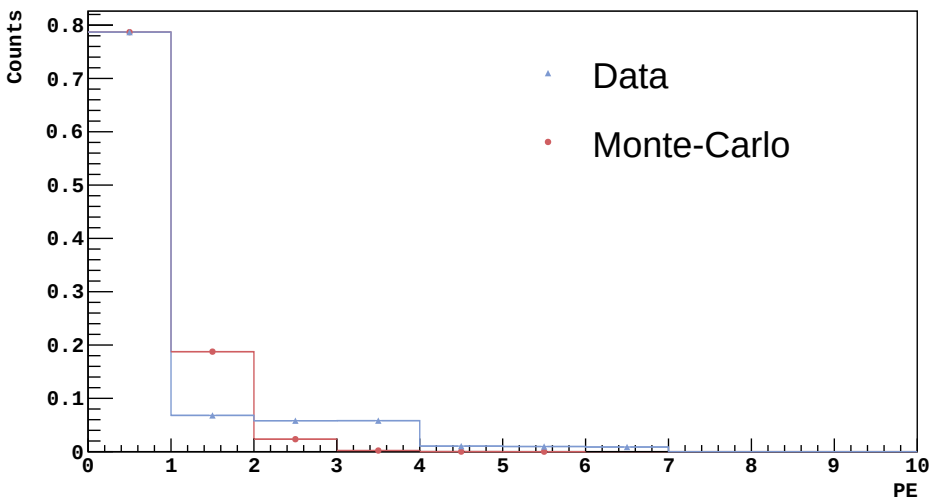

Figure 5.4.2: For Channel 19, the SER amplitude distribution from real data (blue) are compared to the output from the simulation (red), assuming a null Crosstalk Probability, $P_{CT} = 0.0$. Afterpulses in itself increase the number of reconstructed photoelectrons in the laser pulse only of one afterpulse, so that in the simulation the number of events above 2 photoelectrons is negligible. Events in the data at higher PE are due to the contribution of crosstalks.

The height of the gaussians A_i in the SER in Figure 5.2.1 was compared to the same amplitude distribution of the SER got from the simulation. The comparison is shown in Figure 5.4.2 for a null value of the crosstalk probability. The test-statistic chosen is the chi-square. The only parameter to constrain is the effective crosstalk probability. The minimum for the chi-square distribution (Figure 5.4.3) returns the best approximation for the

effective crosstalk probability, as can be seen in Figure 5.4.4 for Channel 27.

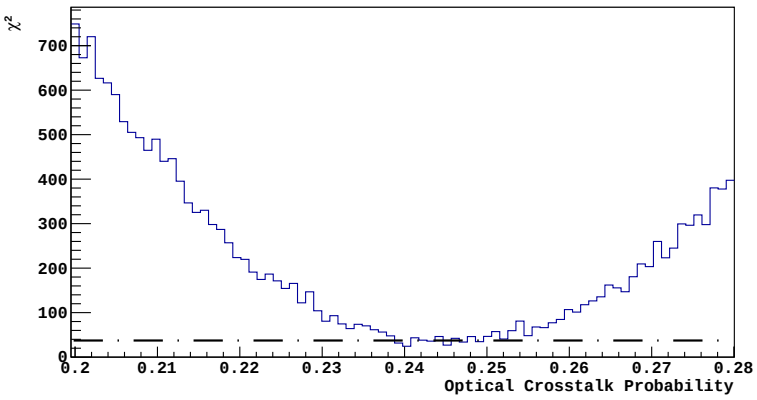

Figure 5.4.3: Chi square distribution vs the Crosstalk Probability for Channel 27. As the only parameter to constrain is the crosstalk probability, the chi-square was chosen as test-statisitc. In this case the probability to observe a crosstalk in Channel 27 is about 24 %, as pointed from the black dotted line.

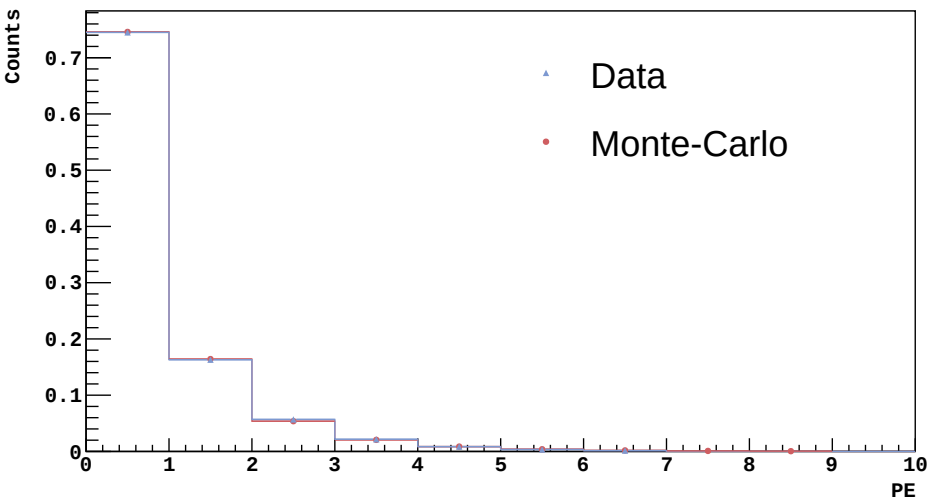

Figure 5.4.4: Comparison with the value of $P_{CT} = 0.24$ which minimizes the chi square between data (blue) and the Toy Monte Carlo (MC) output (red) in Channel 27. As expected, the amplitude distribution matches with the dataset, confirming the result.

The same comparison was performed for each ReD top channel. The distribution of the crosstalk probability is shown in Figure 5.4.5.

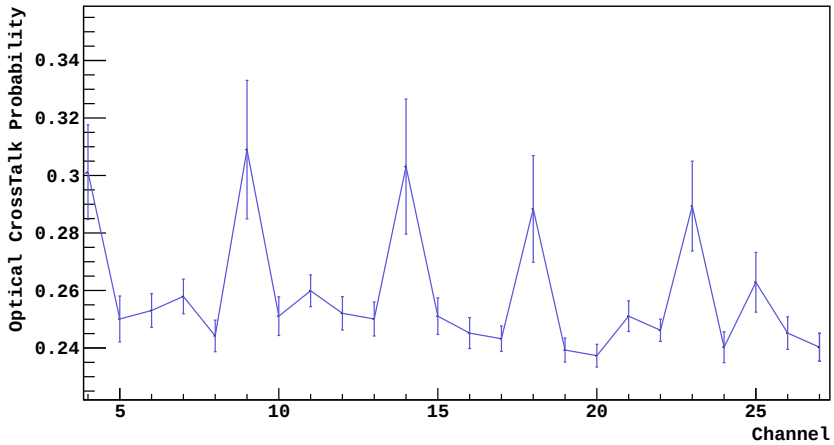

Figure 5.4.5: Distribution of Optical Crosstalks probability through all ReD channels in the top tile.

On average the crosstalk probability is 26 % in ReD; in [285] the crosstalk probability at 87 K and overvoltage $V_{OV} = 6$ V is equal to 20 %. Considering that the crosstalk probability increases with the overvoltage, equal to 7 V in ReD, the two results are in agreement.

5.5 Conclusion

The correlated noise in FBK-NUV-HD LF SiPMs was here characterized through the data from laser runs in ReD experiment. On average the afterpulse probability was found to be $\approx 2\%$ for SiPM, while it is $\approx 27\%$ for the optical crosstalk probability.

These values can be compared to the experimental characterization performed in [285]; here the crosstalk probability at 87 K with $V_{OV} = 6$ V is equal to 20%, which is compatible with our result, considering that the crosstalk probability increases with the overvoltage, which is equal to 7 V in ReD. On the other hand the afterpulse probability found here is much smaller than the one found in [285], where it's $\approx 13\%$ at $V_{OV} = 6$ V. Considering that the crosstalk probabilities were evaluated with the corrected time distribution, the reason of the disagreement for the afterpulse is likely due to the peak finder inefficiency, which extends up to hundreds of nanoseconds.
The values found gives a Total Correlated Noise Probability of about 29 %,

which is smaller than 60 % [282], confirming that FBK-NUV-HD LF SiPMs fulfill all the requirement for the dark matter search in DarkSide-20k. The upgrade from PMT to SiPMs will bring the detector to the highest resolution at low energy ever achieved in LAr, which is one of the keys not only for the dark matter search, but also for the neutrino physics, as for the detection of core-collapse supernova neutrinos.

6 Sensitivity to detection of core-collapse supernova neutrinos in DarkSide-20k and Argo

The present chapter deals with the detection of the neutrino signal from a core-collapse supernova eventually exploding in our galaxy in the next decades, performed by the future tonne-scale liquid argon dark matter detectors from GADMC (Global Argon Dark Matter Collaboration), DarkSide-20k [294] and Argo [295] [296], whose design was given in Section 3.3. Their impressive sensitivity to this signal will be a consequence of the very low background level achievable with the foreseen design and the high energy resolution of the Silicon Photomultipliers.
After a review of the foreseen neutrino detection from an eventual core-collapse supernova (CCSN), in Section 6.2 the process of the core-collapse supernova is reviewed, pointing out where the neutrino emission can answer to open questions. In Section 6.3 the signals of supernova neutrinos in both DarkSide-20k and Argo, the level of backgrounds, and the analysis strategy will be addressed. In Section 6.4, the sensitivity to the neutrino emission from an eventual core-collapse supernova is given for both the detectors. Finally, the observables related to the global supernova neutrino emission, namely, the mean and total energy of supernova neutrinos, are presented.

6.1 Overview

Core-collapse supernovae (CCSNe) are violent explosions of very massive stars at the end of their lives, triggered by the gravitational collapse of the stellar cores [297]. A typical supernova can emit in 10 seconds about 20 times the energy emitted by the Sun in its entire life [298]. About 99% of the supernova's energy is released via neutrinos, mainly emitted by the collapsing core. Then the observation of neutrino signal relies to the processes in the core of the dying star. This is also true for eventual gravitational waves signals, while electromagnetic observations give information only on the outer layers [299] [300].
The interest of this eventual observation comes from the astrophysics as well as from neutrino physics [301] [302]. SN 1987A is the only core-collapse supernova whose neutrino signal has been detected so far. A total of 25 neutrino events were detected [303] [304] [305]. Since then, core-collapse supernova simulations have made several breakthroughs, providing detailed understanding of the neutronization, accretion, and cooling phases [300] [302]; still much uncertainty lies on the details of the explosion mechanism. Moreover, the discovery of neutrino oscillations and neutrino mass raised more

fundamental questions about neutrinos, including their absolute mass and their mass ordering [301], which may be answered by the next detection of galactic supernova neutrinos.
We assume here that both detectors, DarkSide-20k and Argo, will be double-phase time-projection chambers (TPCs), with respectively 50 ton and 370 ton as target mass. These upcoming detectors, mainly thanks to the high energy resolution of the SiPMs, are expected to have an outstanding sensitivity to low energy nuclear recoils, as those induced by supernova neutrinos via coherent elastic neutrino-nucleus scattering (CEνNS) [306] [307].
Two advantages come with the neutrino observation via this specific channel. First, current and upcoming tonne-scale neutrino detectors are and will be sensitive only to electron neutrinos and antineutrinos. Water-Cherenkov detectors like Super-K [308], Hyper-K [309] and IceCube [310] are primarily sensitive to $\bar{\nu}_e$ via inverse beta decay (IBD) [311] [312]. Scintillator detectors like JUNO are sensitive to $\bar{\nu}_e$ via IBD and to all types of neutrinos via neutrino-proton elastic scattering [313]. The DUNE [314] LAr TPC is primarily sensitive to ν_e via the charged current interaction $\nu_e^{40}\mathrm{Ar} \rightarrow^{40} \mathrm{K}^* e^-$. The detection via CEνNS implies instead the same sensitivity to all neutrino flavours, giving an un-oscillated and global supernova neutrino flux.
Moreover, the CEνNS cross-section at low energy is much higher than that from the other detection channels, as shown in Figure 6.1.1, where the main neutrino-liquid argon interactions are compared. Specifically, the coherent elastic scattering cross-section is 50 times greater than charged current one for nuclear recoils in liquid argon due to neutrinos at 10 MeV. This compensates for the relatively small mass target of DarkSide-20k and Argo and will allow for high statistic detection of core-collapse supernova neutrinos.

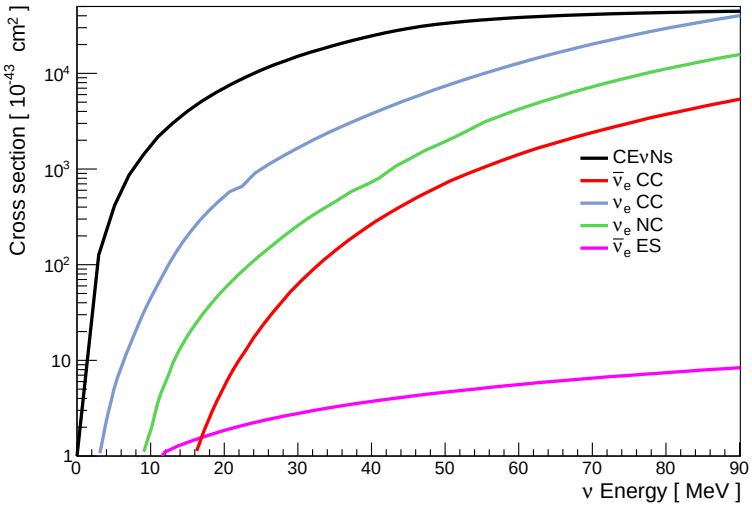

Figure 6.1.1: Comparison of the main detection channels in liquid argon up to 90 MeV. The CEνNS is three order of magnitude greater than elastic scattering and neutral current, and about 50 times greater than charged current. The outstanding cross-section at low energy will compensate for the relatively small mass target of DarkSide-20k and Argo detectors and allow for a sensitivity competitive with large tonne neutrino detectors. Moreover, interactions via CEνNS happen in neutral current, by the exchange of a Z^0 boson, so liquid argon interacts equally to any neutrino flavour, further increasing the statistics, and gives information on the global neutrino emission, without any neutrino oscillation contribution.

The sensitivity of dark matter detectors filled with Xenon to core-collapse supernova neutrinos has already been widely explored, as in XENONnT [315], LZ [316] and DARWIN [317]. A detection in Xenon can count on a larger cross-section compared to Argon; on the other side, the lighter argon nucleus determines a lower energy threshold with a consequent increase of the statistics. The main disadvantage with the liquid argon is the lower density, which results in bigger TPCs and then a greater drift time compared to Xenon-filled TPCs, which decreases the time resolution. On the other side, liquid argon shows to have a higher energy resolution, as lighter nuclei are less quenched; this will allow for a good reconstruction of the main parameters of the CCSN neutrino emission.

6.2 Core Collapse Supernovae

The neutrino emission assumed in this work is from two hydro-dynamical core-collapse supernovae simulations by the Garching group [302], for a progenitor star mass of $11\,M_\odot$ and of $27\,M_\odot$, both 10 kpc far from us. Both the simulations are one-dimensional, so spherical symmetry was assumed, and both follow a Lattimer and Swesty (LS) equation of state [318], where the stellar matter is modeled as a compressible liquid drop and a Skyrme force describes the nucleon interactions. Specifically, the given simulations assumes a compressibility modulus of the liquid drop of K = 220 MeV. In order to understand the neutrino signal from the supernova, in the present section an overview of the core-collapse physics process is given.

The progenitor star of a core-collapse supernova is a very massive star, which can develop into an onion-like structure at the end of its life, with different phases of nuclear fusion occurring in different layers. The silicon burning in the core results in the creation of isotopes like ^{56}Fe, which has the highest nuclear binding energy per nucleon. As no more fusion can occur beyond ^{56}Fe, the stellar core collapse is at first impeded by the electron degeneracy pressure. The sudden reduction of pressure caused by processes like nuclei electron capture and photo-disintegration decreases the core mass down to the Chandrasekhar Mass: the equilibrium is broken and the core collapses under the strong gravity, almost in free-fall [298]. In this "infall" phase mainly electron neutrinos are produced, and leave the core unimpeded. After a few milliseconds, the infall phase is halted by the nucleon degeneracy pressure, reached at nuclear density, at approximately 10^{15} g/cm^3. At this point, the mean free path of neutrinos in the core is comparable with the core radius; thus, they thermalize in the core, with a strong suppression of the neutrino emission [319]; the surface of last scattering defines the neutrinosphere [302]. What happens next is usually divided in three main phases, each characterized by its unique neutrino emission: neutronization, accretion, and cooling phases [320]. The time and average energy profile of the whole neutrino emission is shown in Figure 6.2.1 and Figure 6.2.2.

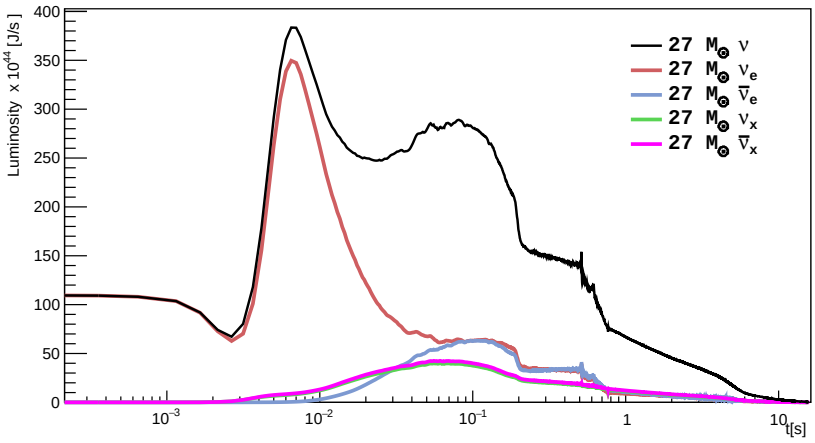

Figure 6.2.1: Neutrino luminosity time evolution $L(t)$ of a core-collapse supernova with $27\,M_\odot$ progenitor star mass and set at 10 kpc for the different neutrino flavours assuming direct neutrino mass ordering, provided by the spherical symmetric simulation of a CCSN with a progenitor star mass of 27 $M_\odot$, LS220K as equation-of-state, set at 10 kpc from the Earth [320], assuming neutrinos Normal Mass Ordering. The ν_x refers to a single species of heavy neutrinos, as any difference in the production rate of muon and tauon (anti)neutrinos is observed to be negligible in the performed CCSN simulations. The rebound time is set at $t = 0$; then, the neutrino trapping follows, lasting about 3 ms. The very characteristic peak of the neutronization burst arises from 4 ms to 30 ms, in which mostly electron neutrinos are released thanks to the propagation of the shock wave in the outer CCSN core; the following accretion phase lasts from 30 ms to 500 ms, envolving also heavy neutrinos from the accreting matter on the collapsing core. Finally the neutron star cooling phase lasts about 10 s, where neutrinos of any flavour are released with mainly the same likelihood.

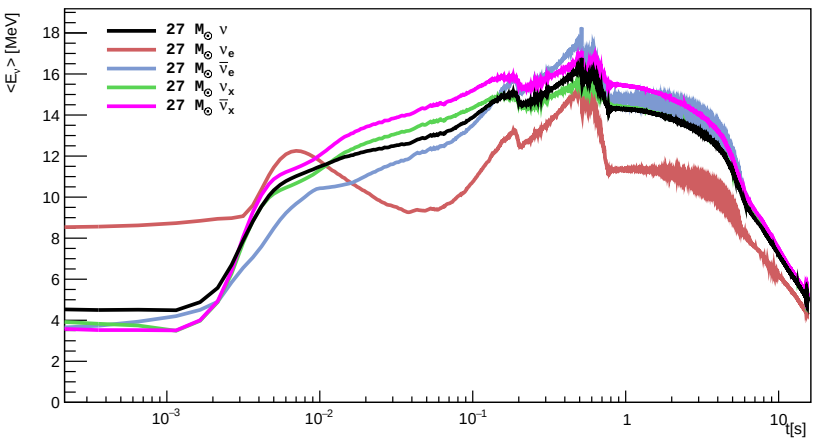

Figure 6.2.2: The time evolution of neutrino mean energy $\langle E_\nu \rangle$ for the different neutrino species as released by the 27 $M_\odot$ core-collapse supernova taken as reference. Neutrinos from the CCSN burst will scatter with an incident energy of about 10 MeV; hence the CEνNS interaction is the most promising one to detect this neutrino signal.

The sudden halt of the core-collapse due to the nuclear degeneracy pressure results into a violent rebound of the matter, which produces a pressure wave propagating outwards and eventually steepening into a shock wave. The shock is so powerful that it dissociates nuclei into free nucleons all along its way to the edge of the core. Free protons quickly interact with the energetic electrons, resulting in neutrons and electron neutrinos (ν_e). This is the neutronization phase, lasting about 30 ms and characterized by a sudden peak of ν_e, called neutronization burst [320] [321].

The observation of the neutronization burst relies to both the astrophysics and the neutrino physics. First, the neutronization burst has not been observed yet. The neutrino events from SN 1987A observed in Kamiokande-2 [303], IMB [304] and Baksan [305] are all electron anti-neutrinos ($\bar{\nu}_e$) from the accretion and cooling phase. Hence, detecting neutrinos from the neutronization burst will test the theory of the first stage of the core-collapse supernova. Moreover, core-collapse supernova simulations show that the energy of the neutronization burst is mainly independent on the progenitor star mass; then, the observation of the neutronization burst allows to measure the distance to the supernova [301].
Furthermore, the neutrino signal in the neutronization burst is related to the neutrino mass ordering. In fact, neutrinos emitted in the neutronization burst are purely electron neutrinos (ν_e). However, due to neutrino oscilla-

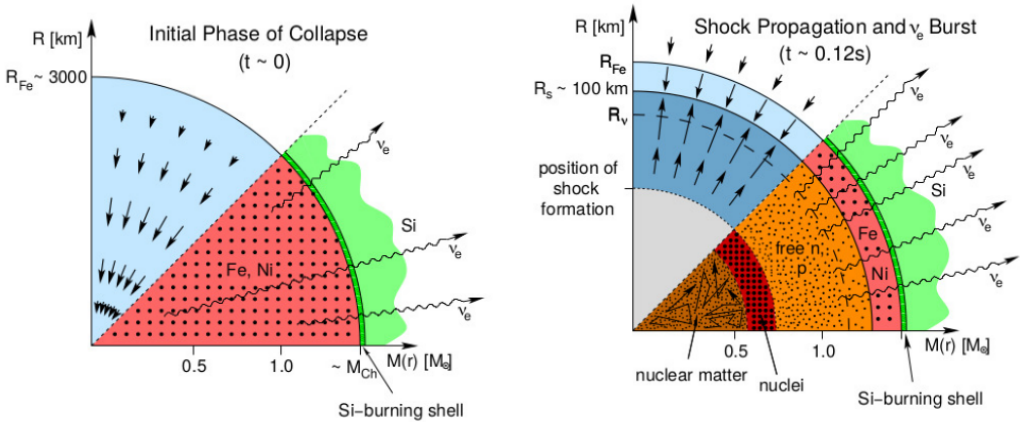

Figure 6.2.3: Representation of the infall phase (left) and the neutronization phase (right) in terms of the mass, in blue, and the local status of the matter. In the infall phase the core collapses due to its own gravity; in the meantime, electron neutrinos produced mainly by nuclei photo-disintegration and electron capture are free to leave the core. When the density in the inner core reaches that of nuclear matter, the nucleon degeneracy pressure suddenly halts the core-collapse, determining the formation of a shock, which propagates back through the outer layers of the core. The shock wave dissociates nuclei along its path, leaving free nucleons and protons and electron neutrinos, who are free to leave the star and determine the neutronization burst. The shock wave never reaches the edge of the core at about 3000 km, but looses its energy at 100-200 km, where it stalls [322].

tion, only a fraction of them remains as ν_e when arriving at the Earth. As the neutrinos travel through the matter from the core to the progenitor's surface, neutrino oscillations with MSW resonance can occur [323]. The survival probability of ν_e is found to depend critically on the neutrino mass ordering. For normal mass ordering, the survival probability is about 0.022 while for inverted mass ordering, the survival probability is about 0.297 [301] [324] [325]. The ratio of a factor 14 between the survival probabilities provides a good opportunity to measure neutrino mass ordering in the neutronization phase [301]. A measurement of the survival probability — and hence of the mass ordering — could be done by comparing the total neutrino flux expected in GADMC LAr TPCs to the ν_e flux measured through charged current interactions, like the one that can be measured e.g. by the DUNE experiment [314].

The shock wave looses its energy in the dissociation of the nuclei and finally get stalled at a radius between 100 and 200 km: the prompt explosion mechanism fails. In the meanwhile, the outern layers of the progenitor star start accreting on the core: the accretion phase begins. The shock wave, however, has to be revived, so that it can reach the core edge, at a radius of about 3000 km, igniting the explosion that was observed for instance from SN1987A. Even if the details of the process are not fully understood, yet, there's agreement among all the performed simulations that neutrinos play the key role in the shock revival mechanism, as they are the only particles that can transport energy and heat from the core to the stalled shock and provide the momentum of the explosion. On the other side, when the spherical symmetry is not assumed in the simulations, it is observed that neutrinos alone can't determine the explosion [326]. Several phenomena in multi-dimensional simulations are believed to contribute to the explosion. Convection can significantly enhance the transportation of energy from the remnants of the core [327] — which is going to develop into a proto-neutron star — to the region beneath the stalled shock. This mechanism is found to be important in most progenitors with relatively small masses. The standing accretion shock instability (SASI) [328] has been observed in many supernova simulations of progenitors with large masses. The shock front oscillates inward and outward, periodically, leading to the oscillation of the neutrino luminosity, which can be detected in presence of high statistics and excellent time resolution. The data used in this study is from a 1D supernova simulation, which shows no signals of SASI. Therefore no sensitivity study for detecting SASI is presented in this paper. Finally, a quasi-stable dipole moment of the luminosity and flux of ν_e and $\bar{\nu}_e$ — called self-sustained lepton number emission asymmetry (LNEA) — came out in recent 3D simulations

[329]. Again, a combined measurement can confirm the role of LNEA in the shock wave revival. DarkSide-20k and Argo can measure the total luminosity of all types of neutrinos through CEνNS; then, the difference between the fraction of electron neutrinos and the fraction of electron anti-neutrinos, will provide sensitivity to the LNEA.
Moreover, the time-lapse itself can give information on the mass and on the equation of state of the progenitor star [330] [331]. Finally, the time duration also may point to an eventual failure of the supernova. In fact, for progenitors with masses larger than approximately $50\,M_{\odot}$, a black hole can be produced by the core collapse [332] [333] [334]. Such supernovae are called "failed supernovae" and their neutrino signals will terminate in the accretion phase: a sudden stop of neutrino signals in the accretion phase will suggest that the collapsed core developed into a black hole, preventing the supernova explosion [335].
The revival of the shock wave leads to the explosion of the supernova, which blows off almost all the matter in the stellar mantle and leaves the hot proto-neutron star. The following cooling phase of the newly-born neutron star by neutrino emission lasts about 10 s [320]. As seen in Figure 6.2.2, the neutrino mean energy $\langle E_{\nu} \rangle$ drops from 15 MeV to 5 MeV in about 10 s, while the neutrino luminosity decreases roughly according to the law of black body radiation, $L \propto T^4 \times R^2$, where T is the surface temperature of the neutron star and R is the radius of the neutrino sphere [336]. High statistics measurement of the time evolution of the neutrino luminosity and mean energy can be performed during the cooling phase. Neutrino signals from the cooling phase can be exploited in indirect dark matter search, usually axion-like particles. In fact, if a component of the supernova energy is eventually released via non-baryonic particles, the cooling time will be shorter than expected [337] [338].

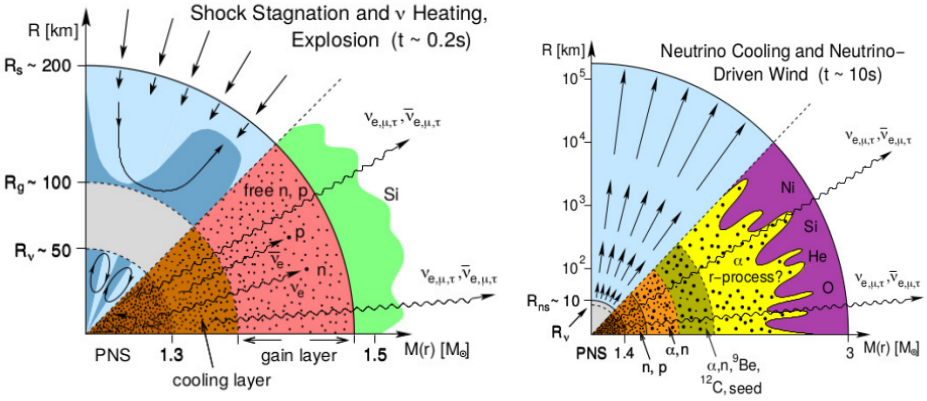

Figure 6.2.4: In the accretion phase (left), the outer layers of the core accretes on the stalled shock wave, while electron antineutrinos are produced by capture of free positrons on nucleons from the inner core; in the meantime, in the outer core, the friction in the accreting matter allows for the production of all neutrino flavours by e+ e- annihilation processes mostly. The cooling phase (right) starts when the shock wave reaches the edge of the core, gravitationally unbinding the star and giving the supernova explosion. The 99 % of the supernova energy is released via neutrinos of all flavours, in about O(10) s. The exact processes occurring in the cooling layers are still under study, while in the center the proto-neutron star is born, with a radius of about 10 km and a mass of 1.4 $M_\odot$ [322].

6.3 Supernova neutrino signal and detector response

For a 27 $M_\odot$ supernova at 10 kpc the neutrino energy spectrum is shown in Figure 6.3.1. The total neutrino energy is $\varepsilon = 2.19 \times 10^{59}$ MeV and the neutrino mean energy is $\langle E_\nu \rangle = 13.03\,\mathrm{MeV}$.

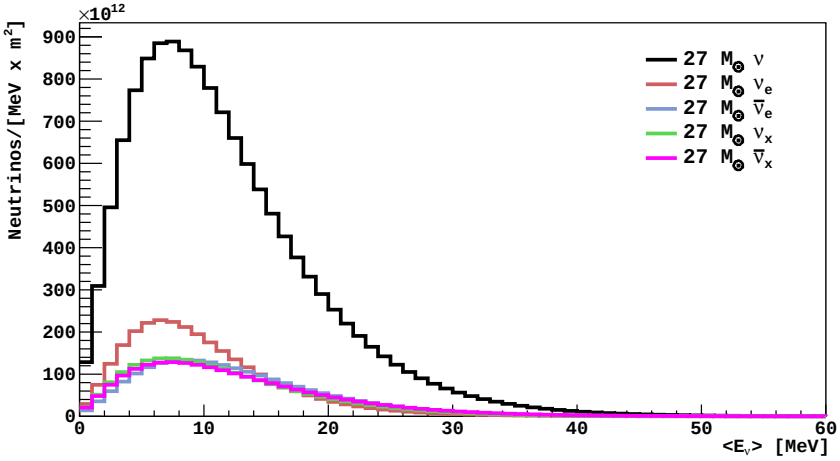

Figure 6.3.1: The energy spectrum of neutrinos emitted from the 27 $M_\odot$ supernova at 10 kpc, assuming direct neutrino mass ordering. Most of the CCSN neutrinos will scatter on the detectors with an incident energy below 30 MeV, where the dominant interaction is CEνNS scattering.

The incident neutrinos will have an average energy of about 10 MeV, as seen in Figure 6.3.1. At such low energies, the dominant cross-section is the coherent elastic neutrino nucleus scattering. The CEνNS differential cross-section as a function of both neutrino energy E_ν and recoil energy E_r is given by

$$\mathrm{d}\sigma(E_\nu, E_r) = \frac{G_F^2}{4\pi} Q_W^2 M_{Ar} \left(1 - \frac{M_{Ar} E_r}{2E_\nu^2}\right) F^2(q) \mathrm{d}E_r \tag{6.3.1}$$

where G_F is the Fermi coupling constant and Q_W is the weak charge of argon nucleus [306] [339],[340] [341] [342]. For the form factor $F(q)$, where $q = \sqrt{2M_{Ar}E_r}$ is the momentum transfer, the Helm model has been assumed, with the Lewin-Smith parametrization [343] [344] [345].

The convolution of the neutrino incident flux with the CEνNS cross-section is the nuclear recoil energy spectrum shown in Figure 6.3.2. The signal is below 100 keV$_{NR}$, with 50 % of the events below 5 keV$_{NR}$. Then, a low energy threshold is fundamental to have a high statistic detection.

The efficiency of a trigger based on the scintillation photons is extremely poor at energy recoils O(1) keV$_{NR}$; on the other hand, a trigger on the S2 ionization signal only allows for a lower energy threshold, down to 0.6 keV$_{NR}$, as the ionization signal is amplified in the gas pocket. This analysis strategy was already applied in [213], allowing to set the world's best exclusion limit on WIMPs in the (2–6) GeV/c^2 mass range; in the same analysis it was shown that the detection efficiency is 100 % for nuclear recoils above 0.46 keV$_{NR}$.

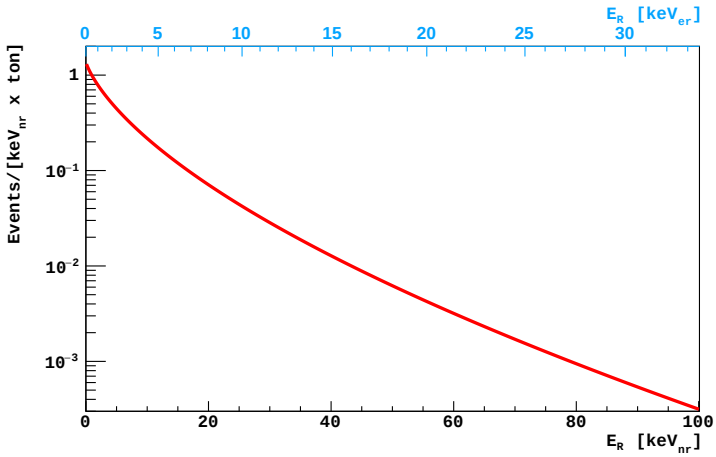

Figure 6.3.2: A simulated spectrum of the nuclear recoil energy E_r in liquid argon from the CEνNS process induced by neutrinos from a core-collapse 27 $M_\odot$ supernova at 10 kpc.

Hence, with the same "S2-only" analysis strategy, the 86 % of the supernova neutrinos events are expected to be detected. The same analysis provides the calibrations for the ionization energy variable N_{e^-}, for both nuclear and electron recoils. The nuclear recoil calibration was determined by the runs in ^{241}Am-^{9}Be and ^{241}Am-^{13}C in DarkSide-50 [213], together with the data from SCENE [346] and ARIS [235] experiments. The calibration for the electron recoils was performed by fitting the Thomas-Imel model [347] with the mean S2 signal measured for the K-shell (2.82 keV) and L-shell (0.27 keV) lines from the electron capture of the cosmogenic ^{37}Ar [348].

6.3.1 Expected Backgrounds

The expected background below 100 keV$_{NR}$ is dominated by the electromagnetic background coming from the liquid argon bulk and the detector materials surrounding the active mass, as the S1 trigger low efficiency prevents any rejection with the pulse shape discrimination technique. The main background above a few keV$_{NR}$ is due to the ^{39}Ar β decays, with a specific activity of 0.7 mBq/kg, as measured in DarkSide-50. While ^{39}Ar is produced by spallation of cosmic rays on ^{40}Ar, ^{85}Kr is released in the atmosphere by fission processes, so the measured activity of 2 mBq/kg was due to an air contamination in UAr happened during its extraction from the underground. The UAr in DarkSide-20k and Argo will be purified by Aria, so the contamination from ^{85}Kr will be entirely suppressed, together with any component of ^{39}Ar due to air contamination, with a reduction of the ^{39}Ar activity. In this

study the ^{85}Kr activity is assumed negligible, while for ^{39}Ar it is assumed the activity measured in DarkSide-50, keeping a very conservative approach. The ^{39}Ar events in DarkSide-20k and Argo is expected to be 0.5 Hz and 4.2 Hz, respectively; only 1.7 % of these actually fall in the energy range $N_{e^-} <$ 100, where the CCSN signal becomes comparable with the ^{39}Ar events.
The external background rate due to radioactive chains and individual isotopes is estimated by material screening campaigns. From G4DS simulations it is confirmed that most of the events perform multi-scattering in the detector, and can be rejected asking single scatter events; after this cut the expected rate is 75 Hz and 320 Hz in DarkSide-20k and Argo, which reduces down to 0.3 Hz and 1.3 Hz in the CCSN neutrinos energy region, below 100 keV$_{NR}$. This left background is finally suppressed by a radial fiducialization of the target volume. In fact, the performed simulations showed that the mean attenuation lenght for this low-energy single scatter electron recoils is about 0.5 cm, so any event withing 5 cm from the detector walls is discarded. The fiducial volume is reduced to 47.1 t in DarkSide-20k and 362.7 t in Argo. The cut on the multi-scattering events won't affect the acceptance of the signal, as the probability that two CCSN neutrino events happen in the same acquisition window, which lasts about 10 μs, is negligible.
A left background is still expected from the top and lower planes. One rejection strategy may be based on the ionization electron diffusion dependence on the interaction vertex height [349] but, as there is no measurement at low energy of the rejection efficiency, this background is conservatively included. This results in a residual rate of 0.2 Hz in DarkSide-20k and 1.1 Hz in Argo.
The sub-keV$_{NR}$ region is dominated by the here called "single electrons", an abundance of events at a few electrons. The origin of this background is still under study, but two populations has been recognized, one not-time correlated and the other one time-correlated with events with a large S2 pulse. The leading hypotesis is that single electrons are due to impurities in the LAr, which trap and then release the drifted electrons. In the present work the whole single-electron spectrum is taken from DarkSide-50 data and rescaled for the two detectors. The measured rate is 380 mHz/ton, which drops down to 1.8 mHz/ton by applying a threshold cut at $N_{e^-} \geq 3$.

6.3.2 Toy Monte Carlo simulation

A C++ based toy Monte Carlo simulation was implemented to simulate the response of DarkSide-20k and Argo detectors to supernova neutrino signals in the presence of the expected backgrounds. The simulation takes into account the LAr intrinsic fluctuations of the ionization and electron-ion recombination processes, assuming a work function in LAr of 19.5 eV [223]. For each

pseudo-experiment and each neutrino flavour, the number of events from CCSN neutrinos was calculated by the integrated rate, assuming a Poisson fluctuation. Then, the arrival time and recoil energy was extracted by the differential event rate. By means of the DarkSide-50 calibrations of ionization signals from nuclear recoils, the recoil energy is converted into the number of ionization electrons, assuming a Binomial fluctuation. The arrival time is added to the drift time along the height of the TPC, equal to 3.5 m and 8 m for DarkSide-20k and Argo respectively. Finally, the signal "recorded" in the pseudo-experiment is stored in terms of the arrival time and the number of electrons N_{e^-}.
Parallelly, the number of expected background events from the listed rates is simulated in each pseudo-experiment, assuming again a Poisson fluctuation. The background is constant in time; once that this is extracted by a uniform distribution, the drift time is added, as performed for the signal events. For both the single-electron background and the ^{39}Ar background, the energy variable $N_{e^-}$is extracted from the spectrum in the N_{e^-}variable, known from DarkSide-50 analysis.
While the energy resolution is a consequence of the fluctuations at each step of the photo-collection in the TPC, the event time resolution is dominated by the electron drift time, which determines a delay respect to the neutrino interaction time, depending on the height of the interaction vertex. The drift velocity in presence of a drift field of 200 V/cm is (0.93 ± 0.01) mm/μs, corresponding to a maximum drift time T_D of 3.8 ms in DarkSide-20k and 5.4 ms in Argo. As the probability of having a scattering is not dependent by the height, the corresponding resolution is $T_D/\sqrt{12}$, so 1.1 ms and 1.6 ms in DarkSide-20k and Argo, respectively.

6.3.3 Event selection

In the present section the selection cuts in both the arrival time and the N_{e^-}variables are set, in order to optimize the signal-to-background ratio and enhance the sensitivity to the CCSN neutrino emission.
Figure 6.3.3 shows the time profile of the CCSN signal compared to background events, for both the 11 $M_\odot$ and 27 $M_\odot$ progenitor star mass. Selection cuts in time and N_{e^-} are applied to maximize the signal to background ratio. As the backgrounds are constant in time, the time selection cuts are determined by the CCSN signal time evolution only. Indeed, after a few seconds, the CCSN neutrino emission strongly decreases, at the end of the cooling phase. So, only events which are detected within 8 s from the start of the burst are selected.
The cuts on the energy variable are instead determined by the energy spec-

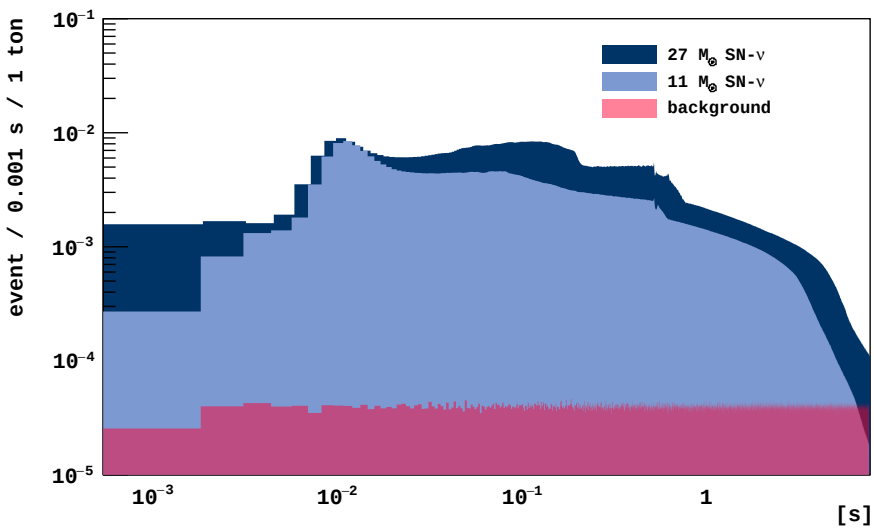

Figure 6.3.3: Time profile of supernova neutrino emission, for both the 11 $M_\odot$ and 27 $M_\odot$ set at 10 kpc of distance, compared with the overall background (purple), considered as a unique population as they are all constant in time. The CCSN signal becomes comparable with the background at 8 s from the start of the burst, so a time selection cut is applied at $t < 8$ s.

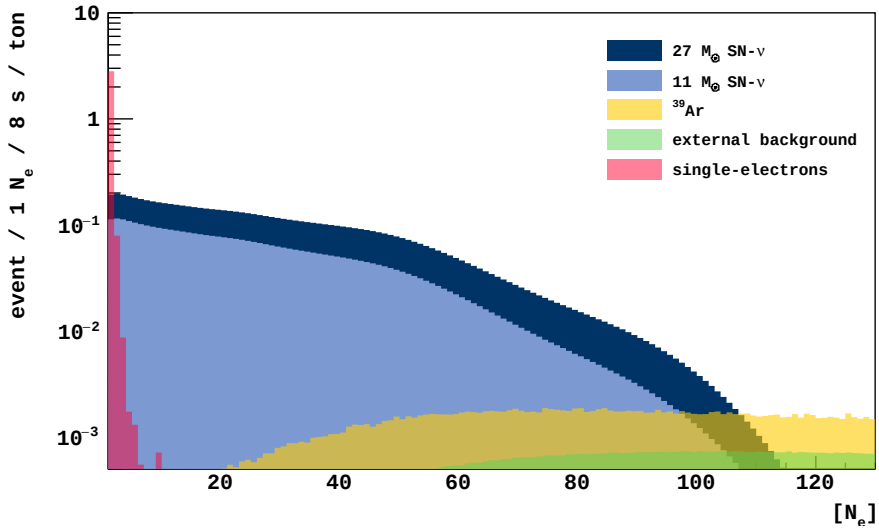

Figure 6.3.4: Energy spectrum in the N_{e^-}-variable of CCSN neutrinos, for both the 11 $M_\odot$ and 27 $M_\odot$ set at 10 kpc of distance, compared with the expected backgrounds, namely "single electron" events (purple), ^{39}Ar decays (yellow) and the external background (green). The selection cut is applied in the energy range $(2 - 100)N_{e^-}$.

trum of the expected background, which is compared in Figure 6.3.4 with the one from CCSN neutrino emission, for both the 11 $M_\odot$ and 27 $M_\odot$ progenitor star mass. At $N_{e^-} \approx 100$, the background from ^{39}Ar and external background is comparable with the signal. Hence, an upper energy cut at $N_{e^-} \leq 100$ is set. At low N_{e^-}, the single-electron background may affect the sensitivity to CCSN neutrinos events. Then, an energy threshold is applied at $N_{e^-} \geq 3$. By taking into account the detection trigger efficiency with this energy threshold shown in Figure 6.3.5, the expected number of signal events from the 11 $M_\odot$ CCSN is 181.4 and 1396.6 in DarkSide-20k and Argo, respectively, while for the 27 $M_\odot$ CCSN it is 336.5 and 2591.6 for the two detectors.

	DarkSide-20k	Argo
11-$M_\odot$ SN-νs	181.4	1396.6
27-$M_\odot$ SN-νs	336.5	2591.6
^{39}Ar	4.3	33.8
external background	1.8	8.8
single-electrons	0.7	5.1

Table 6.1: Event statistics expected in DarkSide-20k and Argo from 11 $M_\odot$ and 27 $M_\odot$ supernovae at 10 kpc of distance, together with the number of expected events from single-electron and ^{39}Ar background components, after applying the selection cuts, so within the [3, 100] N_{e^-} energy window and in 8 s from the beginning of the burst.

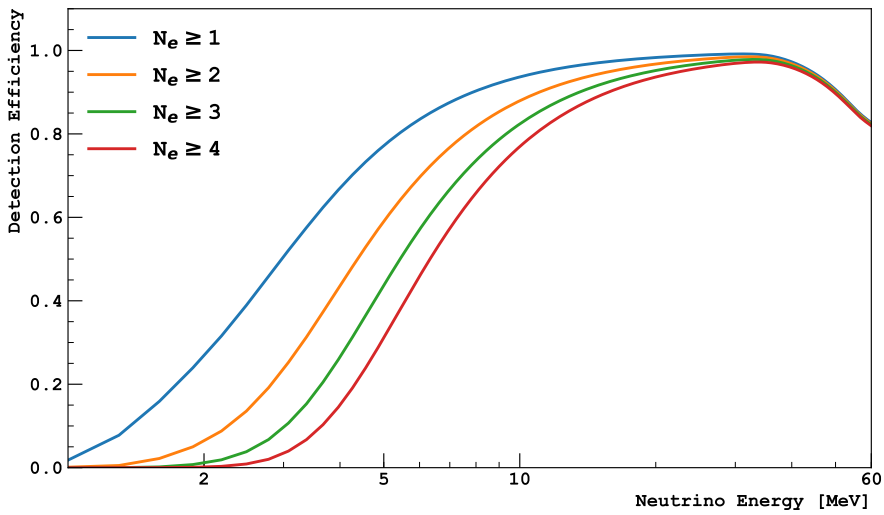

Figure 6.3.5: Detection efficiency to the CCSN signal for different energy threshold. As reference, the neutrino emission from the 27 $M_\odot$ CCSN at 10 kpc of distance was assumed. The threhsold set is at $N_{e^-} \geq 3$, in order to strongly suppress the contribution to the event rate of the single-electron background.

Table 6.1 resumes the expected number of events during the CCSN burst after the listed selection cuts. After their application the overall signal to background ratio is about 27 and 50 for the 11 $M_\odot$ and the 27 $M_\odot$ respectively, promising for a high discovery potential.

CCSN phase	11-$M_\odot$ SN SN-ν [1/t]	S/B DS20k	S/B ARGO	27-$M_\odot$ SN SN-ν [1/t]	S/B DS20k	S/B ARGO
Burst	0.08	212	231	0.09	243	264
Accretion	1.83	105	114	3.30	190	207
Cooling	1.96	16	17	3.76	30	33

Table 6.2: Number of expected events per unit of mass and signal-to-background ratio in DarkSide-20k and Argo from 11 $M_\odot$ and 27 $M_\odot$ CCSNe at 10 kpc, specifically for each phase and after the application of the selection cuts.

Furthermore, the neutronization burst shows by itself a high signal to background ratio in its small time window, about 30 ms. In Table 6.2, the respective neutrino events and background events for each phase is shown. The highest signal to background ratio is reached in the neutronization phase and in the accretion phase, with a factor O(100) for both the supernovae and the detectors; a factor O(10) is foreseen in the cooling phase, which still can count on a higher statistics in the eight seconds of integration time.

6.4 Determination of the Supernovae Neutrino Detection Significance

In this section the sensitivity to the supernova burst and to the main parameters of the emission spectrum is addressed.
The expected background is constant in time; moreover, it will be measured with very high statistics before and after the CCSN burst, so any uncertainty on the background is assumed to be negligible. Thus, the median significance can be extimated using the Asimov approximation for likelihood-based tests [350]. The resulting significance for both the detectors and considered supernovae is shown in Figure 6.4.1, in terms of the supernova distance. The DarkSide-20k discovery potential fully covers the Milky Way, while Argo will have a 5σ detection significance up to the Small Magellanic Cloud. The upper bound of the bands shows the discovery potential assuming a ^{39}Ar contamination level 10 times lower than that in DarkSide-50, as expected after the purging in Aria.
Thanks to the very high signal-to-background ratio, a good discovery potential is also expected on the neutronization phase only, with a 5 σ confidence level at 10 kpc for DarkSide-20k and at 22 kpc for Argo, which is comparable with the farthest edge of the Milky Way. As expected by the slight

dependence of the neutronization phase from the CCSN progenitor mass, the discovery potential of the two considered models in this phase differs very poorly.

Beside working as counting experiments, double phase liquid argon TPCs can also reconstruct the time and energy evolution of the neutrino emission. Again, hundreds of simulations are performed, and on each event the detector response to CEνNS scattering of CCSN neutrinos is applied.
The resulting time profile is shown in Figure 6.4.2 for the 27 $M_\odot$ CCSN set 10 kpc far away, which is taken as reference from now on. The energy selection cut $N_{e^-} \in [3,100]$ is applied, in order to enhance the signal-to-background ratio. The width of the statistical error bands is evaluated according to the sampling of 20 ms and 100 ms for accretion and cooling phase, respectively, where the time resolution is affected by the electron drift time and hence by the height of the TPC. On the other hand, only in Argo the statistics will be high enough to distinguish the temporal structure characterizing the two CCSN phases.

Moreover, a detection in a double phase liquid argon TPC will allow for the reconstruction of the main parameters of the neutrino energy spectrum, namely the average neutrino energy and the total energy of the CCSN neutrinos. An example of the N_{e^-} spectrum from a toy Monte Carlo pseudo-experiment is shown in Figure 6.4.3 for the 27 $M_\odot$ CCSN at 10 kpc of distance. The energy spectrum of CCSN neutrinos is parametrized as [351]

$$f(E_\nu) = \frac{\varepsilon}{4\pi D^2} \frac{(\alpha+1)^{\alpha+1} {E_\nu}^\alpha e^{-\frac{E_\nu(\alpha+1)}{\langle E_\nu \rangle}}}{\Gamma(\alpha+1)\langle E_\nu \rangle^{\alpha+1}} \ . \tag{6.4.1}$$

where Γ is the Euler gamma function, E_ν is the neutrino energy, while $\langle E_\nu \rangle$ and ϵ are the average and total energy of neutrinos released from a supernova at a distance D. The pinching parameter α takes into account how much the emission is close to the Maxwell-Boltzmann distribution, in which case $\alpha = 2.0$. This effective value for the α actually fits well the neutrino emission in the cooling phase; for the accretion phase is $\alpha = 2.3$, where the neutrino emission starts to approach the thermal spectrum. In the neutronization phase it is $\alpha = 3.0$. Seen the difference between the neutronization phase and the other two phases, and also considered the low statistics available in its short time lapse, in the following only the energy spectra in two cases are considered: the accretion phase only, and the cooling plus accretion phase spectrum, assuming a full thermal spectrum in both cases.

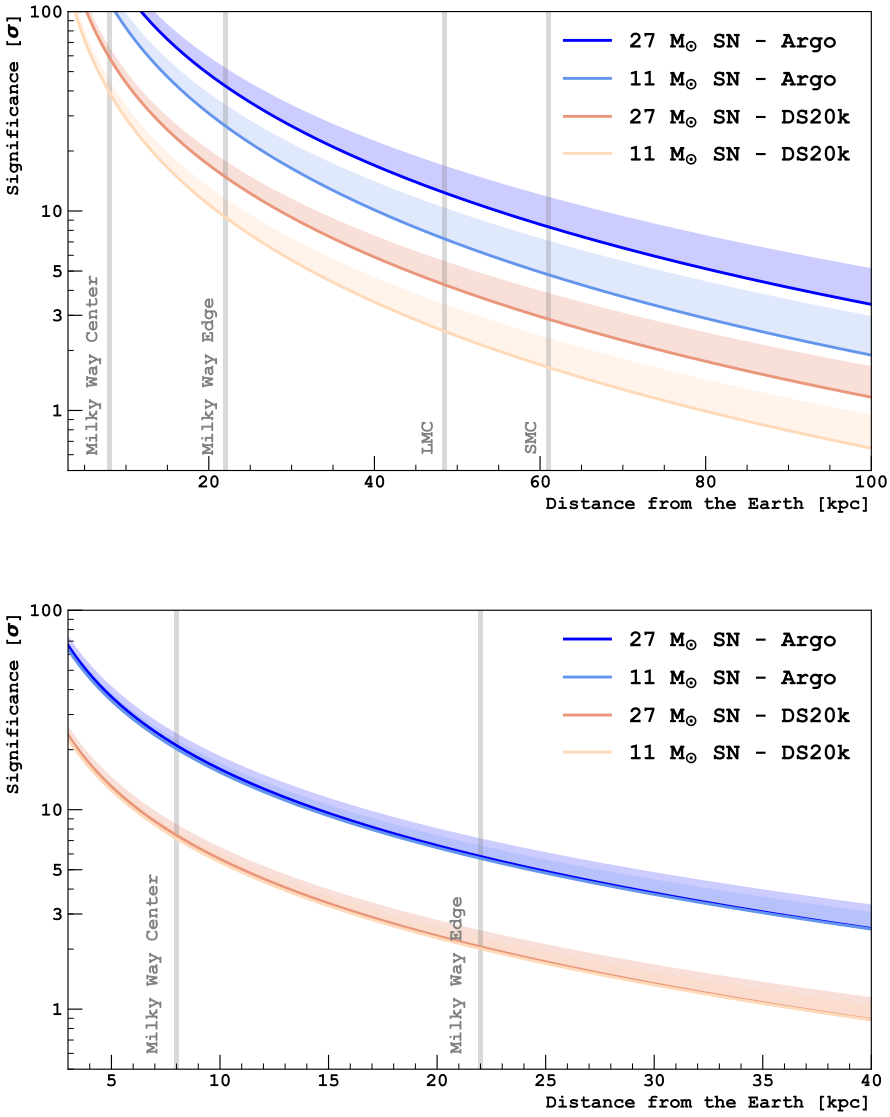

Figure 6.4.1: DarkSide-20k and Argo discovery potential to 11 $M_\odot$ and 27 $M_\odot$ SNe (top) and to its neutronization burst only (bottom) as a function of the distance, assuming the standard background hypothesis (solid line) and by considering a lower contamination of ^{39}Ar, up to a factor of 10 less (band) . Vertical lines represent the distance from the Earth to the Milky Way center, to its farthest edge and to Large (LMC) and Small (SMC) Magellanic Clouds.

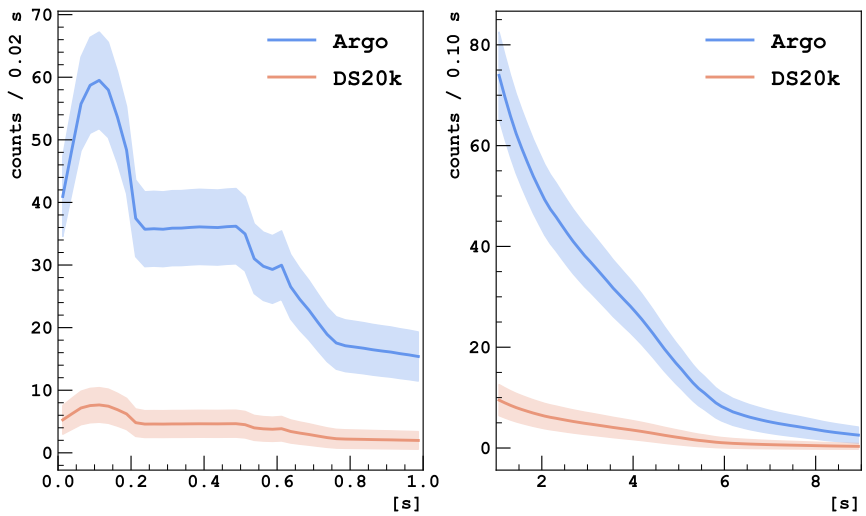

Figure 6.4.2: Time profile of neutrinos from the accretion (left) and cooling (right) phases of a 27 $M_\odot$ CCSN at 10 kpc distance, as detected by DarkSide-20k and Argo. The bands represent the statistical uncertainty, depending on the time binning of 20 ms and 100 ms for DarkSide-20k and Argo.

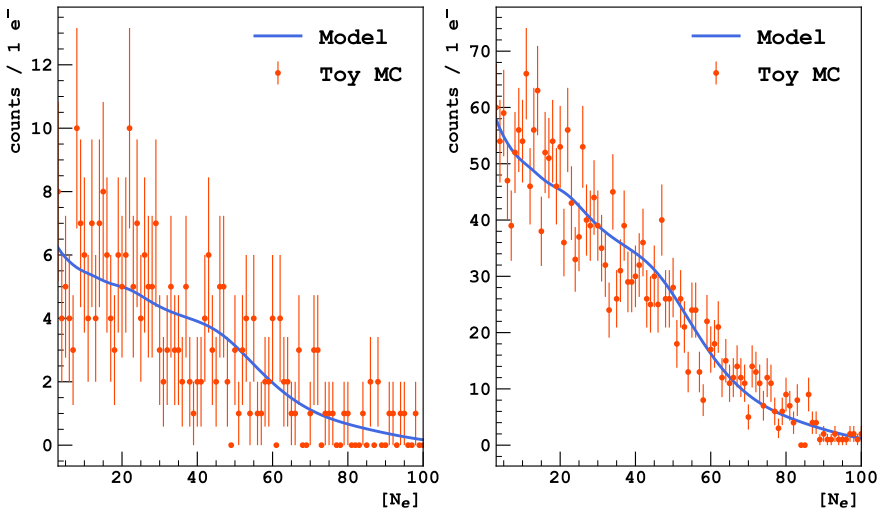

Figure 6.4.3: Examples of fit of the Monte Carlo neutrino interaction samples from the accretion phase plus cooling phase in a 27 $M_\odot$ CCSN burst at 10 kpc of distance, performed in DarkSide-20k (left) and Argo (right) and generated in the [0.02, 8] s time range.

The parametrized flux in Equation 6.4.1 is convoluted with the CEνNS cross-section and the detector response; the result is fit with the Monte Carlo output samples, as shown in Figure 6.4.3. A migration matrix, transforming nuclear recoil energy in N_{e^-} is employed to take into account the non-gaussian fluctuations in the detector response, mainly close to the energy threshold.

The sensitivity to the average neutrino energy and the total CCSN energy released via neutrinos is evaluated for both DarkSide-20k and Argo. A set of 5×10^4 samples are fitted with the convoluted flux, for both the cooling phase and the accretion-plus-cooling phase. The significance bands for 1 σ, 2 σ and 3 σ are computed from the best values of the fit, and finally compared to the theoretical values as expected from the CCSN simulations in input, as shown in Figure 6.4.4. Both the detectors are able to reconstruct the true average neutrino energy and the total neutrino energy within 1 σ, with a systematic shift due to the non-normal response of the detector and eventual approximations on the parametrization performed.
The mean neutrino energy in the accretion phase is reconstructed within 3 σ of confidence level in DarkSide-20k and Argo with an accuracy of 21 % and

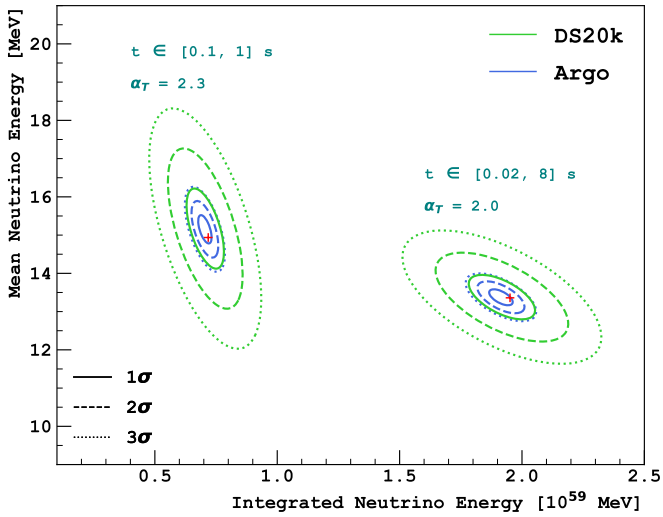

Figure 6.4.4: DarkSide-20k and Argo sensitivities to the average neutrino energy and the integrated neutrino energy from a 27 $M_\odot$ CCSN set at 10 kpc, evaluated for the accretion phase in the [0.1, 1] s time range and the cooling plus the accretion phase, in the [0.02, 8] s time range. The two parameters are obtained by fitting 5×10^4 toy Monte Carlo samples with α equal to 2.3 and 2.0 for the two time range respectively. Red crosses represent the true values from the simulation in input.

7 % respectively, which becomes 13 % and 5 % by including also the cooling phase.
At 3 σ level, the total neutrino energy is reconstructed in DarkSide-20k and Argo with an accuracy of 32 % and 11 % respectively in the accretion phase only and within 21 % and 7 % respectively from the accretion-plus-cooling phases.

6.5 Conclusion

If a core-collapse supernova will explode after their build, the next GADMC detectors DarkSide-20k and Argo, with fiducial target masses of 47.1 t and 362.7 t, respectively, will detect its neutrino signal via CEνNS scattering, with a statistics competitive with multi-tonne neutrino experiments, down to an energy threshold of 0.46 keV$_{nr}$, by triggering on the S2-signal only.

Thanks to the low energy threshold and the resolution in the SiPM single-electron response, a good accuracy in the reconstruction of the average neutrino energy and the total CCSN energy released via neutrinos is expected for both the detectors. Furthermore, the time-profile of the neutrino emission will be reconstructed within a time resolution of 1.1 ms and 1.6 ms for DarkSide-20k and Argo, respectively, mainly determined by the electron drift time.
The discovery potential of a supernova was also evaluated in terms of its distance from the Earth. Thanks to the high signal to noise ratio, DarkSide-20k will be sensitive to 11 $M_\odot$ CCSNe up to the Milky Way edge, while Argo up to the Small Magellanic Cloud. Furthermore, DarkSide-20k will also eventually detect the neutrinos from specifically the neutronization burst, for any CCSN up to beyond the Milky Way center; with Argo this sensitivity is pushed up to the Milky Way edge. These results assumes the most conservative predictions of ^{39}Ar contamination, by just scaling the activity measured in the DarkSide-50 experiment for the detectors active volume; this background level is expected to be suppressed by a factor of 10 in the liquid argon target mass of DarkSide-20k and Argo, with a consequent enhancement of the DarkSide-20k and Argo sensitivities to the CCSN neutrinos.

7 Conclusion

The direct detection in liquid argon is one of the most promising technique in the dark matter search. Indeed, liquid argon shares with the other noble liquid the high ionization and scintillation yield, the transparency to its own scintillation light and the high electron mobility, who enhances the collection efficiency of both the scintillation (S1) signal and, in a double phase TPC, the ionization signal (S2). Furthermore, differently from other noble liquid targets, it can count on the outstandind background rejection power of the pulse shape discrimination technique. During my Ph.D thesis I had the chance to work with both DEAP and DarkSide collaboration, accessing the physics potential of liquid argon detectors in both the dark matter search and the neutrino physics.

As described in Chapter 3, detectors designed for WIMP search are also sensitive to dark matter candidates at much higher cross-section, more similar to a strong interaction, and higher mass, near the Planck Mass; as more theoretical frameworks can give such a candidate, this class is grouped under the name of MIMPs, massive particles performing multiple scattering in the detector. This is in contrast with WIMPs, which are expected to perform at most one scatter in the detector. Hence custom selection cuts have been figured out, to optimize the rejection of the expected background. The most annoying background is found to be that of pile-ups and of muons, whose expectated statistics is evaluated for the lifetime of the available dataset. Three Region of Interests are finally determined, each with its selection cuts and left background level, fully setting up the upcoming unblinding of the dataset.

Liquid argon dark matter detectors show also an interesting potential in the neutrino physics, which increases with the size of the target mass. Indeed with the next detectors from the GADMC, DarkSide-20k and Argo, WIMPs will be found or excluded down to the neutrino floor, fully covering the space-of-parameters available by the counting detection technique. Specifically, the analysis performed with DarkSide-50, the only dark matter running experiment from DarkSide collaboration, showed that the recoil energy threshold can go down to 0.6 keV, enhancing the detectors sensitivity to WIMPs at mass below 10 GeV/c^2 and also to low energy neutrinos, with an incident energy of about 10 MeV, as the ones produced from a core-collapse supernova.

This sensitivity at low energy will be mainly determined by the high energy resolution of the photosensors, the Silicon Photomultipliers (SiPMs). Custom SiPMs have been developed, fulfilling all the requirements for the dark matter search in DarkSide-20k. In ReD experiment, a small TPC set in

Naples strictly connected to DarkSide collaboration, these photosensors have been exploited for the very first time in liquid argon. SiPMs have a higher radiopurity and photo-detection efficiency that the Photomultipliers Tubes employed in DEAP-3600 and in DarkSide-50; neverthless, they show to have correlated noise, namely afterpulses and optical crosstalks, which may affect the pulse shape discrimination and the energy resolution. Hence, Chapter 4 deals with the characterization of the two correlated noise in ReD laser runs. As aforementioned, the SiPM high energy resolution will determine the high sensitivity at low energy of the future GADMC detectors, DarkSide-20k and Argo. This bring also to an outstanding sensitivity to the neutrino emission from a core-collapse supernova (CCSN), a very rare astrophysical event, lasting about 10 s. CCSN neutrinos will perform coherent elastic scattering in liquid argon, allowing for a high statistics and flavour-insensitive detection. In the case of a CCSN exploding in the next decades, it was shown that the two liquid argon detectors will be able to record the signal from any galactic supernova, up to the Large Magellan Cloud. Moreover, an interesting sensitivity is foreseen to the prompt-peak of the neutrino emission, called neutronization burst. This detection, compared to the one from neutrino experiments working in charged current, may allow for setting limits on the neutrno mass ordering. Furthermore, the high energy resolution and the low background level foreseen in such a short time-lapse allow for a good reconstruction of the time profile of the burst, with a resolution of few milliseconds, and the reconstruction of the main parameters of the energy spectrum, namely the neutrino average energy and the total energy released via neutrinos.

References

[1] F. Zwicky, *Die Rotverschiebung von extragalaktischen Nebeln*, *Helv. Phys. Acta* **6** (1933) 110.

[2] S. Smith, *The Mass of the Virgo Cluster*, *Astrophys. J.* **83** (1936) 23.

[3] F. Zwicky, *On the Masses of Nebulae and of Clusters of Nebulae*, *Astrophys. J.* **86** (1937) 217.

[4] H. W. Babcock, *The rotation of the Andromeda Nebula*, *Lick Observatory Bulletin* **498** (1939) 41.

[5] H. C. van de Hulst, E. Raimond and H. van Woerden, *Rotation and density distribution of the Andromeda nebula derived from observations of the 21-cm line*, **14** (1957) 1.

[6] M. S. Roberts, *A High-Resolution 21-CM Hydrogen-Line Survey of the Andromeda Nebula*, **144** (1966) 639.

[7] V. C. Rubin and J. Ford, W. Kent, *Rotation of the Andromeda Nebula from a Spectroscopic Survey of Emission Regions*, **159** (1970) 379.

[8] M. ROBERTS and A. ROTS, *Comparison of rotation curves of different galaxy types*, *Astronomy astrophysics* **26** (1973) 483.

[9] J. Einasto, *Galactic models and stellar orbits*, in *Proceedings of the First European Astronomical Meeting Athens, September 4–9, 1972*, L. N. Mavridis, ed., (Berlin, Heidelberg), pp. 291–325, Springer Berlin Heidelberg, 1974.

[10] Noordermeer, E., van der Hulst, J. M., Sancisi, R., Swaters, R. A. and van Albada, T. S., *The westerbork hi survey of spiral and irregular galaxies - iii. hi observations of early-type disk galaxies*, *A&A* **442** (2005) 137.

[11] P. Kalberla, L. Dedes, J. Kerp and U. Haud, *Dark matter in the Milky Way, II. the HI gas distribution as a tracer of the gravitational potential*, *Astron. Astrophys.* **469** (2007) 511 [0704.3925].

[12] SDSS collaboration, *The Milky Way's Circular Velocity Curve to 60 kpc and an Estimate of the Dark Matter Halo Mass from Kinematics of ~2400 SDSS Blue Horizontal Branch Stars*, *Astrophys. J.* **684** (2008) 1143 [0801.1232].

[13] G. Gilmore, M. I. Wilkinson, R. F. Wyse, J. T. Kleyna, A. Koch, N. Evans et al., *The Observed properties of Dark Matter on small spatial scales*, *Astrophys. J.* **663** (2007) 948 [astro-ph/0703308].

[14] W. G. Mathews, *The enormous mass of the elliptical galaxy M87: a model for the extended X-ray source.*, **219** (1978) 413.

[15] J. N. Bahcall and C. L. Sarazin, *Parameters and predictions for the X-ray emitting gas of Coma, Perseus, and Virgo.*, **213** (1977) L99.

[16] M. S. Roberts and R. N. Whitehurst, *The rotation curve and geometry of M31 at large galactocentric distances.*, **201** (1975) 327.

[17] P. Fischer, G. Bernstein, G. Rhee and J. Tyson, *The mass distribution of the cluster 0957+561 from gravitational lensing*, *Astron. J.* **113** (1997) 521 [astro-ph/9608117].

[18] M. Milgrom and J. Bekenstein, *The modified newtonian dynamics as an alternative to hidden matter*, *Symposium - International Astronomical Union* **117** (1987) 319–333.

[19] D. Clowe et al., *Weak lensing mass reconstructions of the eso distant cluster survey*, *Astron. Astrophys.* **451** (2006) 395 [astro-ph/0511746].

[20] D. Clowe, A. Gonzalez and M. Markevitch, *Weak-Lensing Mass Reconstruction of the Interacting Cluster 1E 0657-558: Direct Evidence for the Existence of Dark Matter*, **604** (2004) 596 [astro-ph/0312273].

[21] M. Markevitch, A. Gonzalez, D. Clowe, A. Vikhlinin, L. David, W. Forman et al., *Direct constraints on the dark matter self-interaction cross-section from the merging galaxy cluster 1E0657-56*, *Astrophys. J.* **606** (2004) 819 [astro-ph/0309303].

[22] D. Clowe, M. Bradac, A. H. Gonzalez, M. Markevitch, S. W. Randall, C. Jones et al., *A direct empirical proof of the existence of dark matter*, *Astrophys. J. Lett.* **648** (2006) L109 [astro-ph/0608407].

[23] G. R. Blumenthal, S. M. Faber, J. R. Primack and M. J. Rees, *Formation of galaxies and large-scale structure with cold dark matter.*, **311** (1984) 517.

[24] Supernova Search Team collaboration, *Observational evidence from supernovae for an accelerating universe and a cosmological constant*, *Astron. J.* **116** (1998) 1009 [astro-ph/9805201].

[25] A. G. Riess et al., *New Hubble Space Telescope Discoveries of Type Ia Supernovae at z¿=1: Narrowing Constraints on the Early Behavior of Dark Energy*, *Astrophys. J.* **659** (2007) 98 [astro-ph/0611572].

[26] Supernova Cosmology Project collaboration, *Measurements of Ω and Λ from 42 high redshift supernovae*, *Astrophys. J.* **517** (1999) 565 [astro-ph/9812133].

[27] N. A. Bahcall, J. P. Ostriker, S. Perlmutter and P. J. Steinhardt, *The Cosmic triangle: Assessing the state of the universe*, *Science* **284** (1999) 1481 [astro-ph/9906463].

[28] J. Frieman, M. Turner and D. Huterer, *Dark Energy and the Accelerating Universe*, *Ann. Rev. Astron. Astrophys.* **46** (2008) 385 [0803.0982].

[29] V. S. Alpher, *Ralph A. Alpher, George Antonovich Gamow, and the Prediction of the Cosmic Microwave Background Radiation*, 1411.0172.

[30] A. A. Penzias and R. W. Wilson, *A Measurement of excess antenna temperature at 4080-Mc/s*, *Astrophys. J.* **142** (1965) 419.

[31] C. L. Bennett, M. Halpern, G. Hinshaw, N. Jarosik, A. Kogut, M. Limon et al., *First-year wilkinson microwave anisotropy probe (wmap) observations: Preliminary maps and basic results*, *The Astrophysical Journal Supplement Series* **148** (2003) 1–27.

[32] Planck collaboration, *Planck 2013 results. I. Overview of products and scientific results*, *Astron. Astrophys.* **571** (2014) A1 [1303.5062].

[33] "Intermediate guide to the acoustic peaks and polarization (2001).."

[34] W. Hu and S. Dodelson, *Cosmic Microwave Background Anisotropies*, *Ann. Rev. Astron. Astrophys.* **40** (2002) 171 [astro-ph/0110414].

[35] V. Springel, S. D. M. White, A. Jenkins, C. S. Frenk, N. Yoshida, L. Gao et al., *Simulations of the formation, evolution and clustering of galaxies and quasars*, **435** (2005) 629 [astro-ph/0504097].

[36] V. Springel, C. S. Frenk and S. D. White, *The large-scale structure of the Universe*, *Nature* **440** (2006) 1137 [astro-ph/0604561].

[37] L. Gao, V. Springel and S. D. White, *The Age dependence of halo clustering*, *Mon. Not. Roy. Astron. Soc.* **363** (2005) L66 [astro-ph/0506510].

[38] L. Gao, S. D. M. White, A. Jenkins, C. S. Frenk and V. Springel, *Early structure in ΛCDM*, **363** (2005) 379 [astro-ph/0503003].

[39] D. J. Croton, V. Springel, S. D. M. White, G. De Lucia, C. S. Frenk, L. Gao et al., *The many lives of active galactic nuclei: cooling flows, black holes and the luminosities and colours of galaxies*, **365** (2006) 11 [astro-ph/0508046].

[40] T. Di Matteo, V. Springel and L. Hernquist, *Energy input from quasars regulates the growth and activity of black holes and their host galaxies*, **433** (2005) 604 [astro-ph/0502199].

[41] J. F. Navarro, A. Ludlow, V. Springel, J. Wang, M. Vogelsberger, S. D. M. White et al., *The diversity and similarity of simulated cold dark matter haloes*, *Monthly Notices of the Royal Astronomical Society* **402** (2010) 21 [https://academic.oup.com/mnras/article-pdf/402/1/21/18573804/mnras0402-0021

[42] MACHO collaboration, *The MACHO project dark matter search*, *ASP Conf. Ser.* **88** (1996) 95 [astro-ph/9510104].

[43] M. Moniez, *Review of results from eros microlensing search for massive compact objects*, 2009.

[44] T. Lin, *Dark matter models and direct detection*, *PoS* **333** (2019) 009 [1904.07915].

[45] E. W. Kolb and M. S. Turner, *The Early Universe*, vol. 69. 1990.

[46] Planck collaboration, *Planck 2018 results. VI. Cosmological parameters*, 1807.06209.

[47] KATRIN collaboration, *First neutrino mass measurement with the KATRIN experiment*, *J. Phys. Conf. Ser.* **1468** (2020) 012180.

[48] J. L. Feng, *Dark Matter Candidates from Particle Physics and Methods of Detection*, *Ann. Rev. Astron. Astrophys.* **48** (2010) 495 [1003.0904].

[49] E. Bulbul, M. Markevitch, A. Foster, R. K. Smith, M. Loewenstein and S. W. Randall, *Detection of An Unidentified Emission Line in the Stacked X-ray spectrum of Galaxy Clusters*, *Astrophys. J.* **789** (2014) 13 [1402.2301].

[50] Y. Ali-Haïmoud and M. Kamionkowski, *Cosmic microwave background limits on accreting primordial black holes*, *Phys. Rev. D* **95** (2017) 043534.

[51] M. Sasaki, T. Suyama, T. Tanaka and S. Yokoyama, *Primordial black holes—perspectives in gravitational wave astronomy*, *Class. Quant. Grav.* **35** (2018) 063001 [1801.05235].

[52] A. M. Green and B. J. Kavanagh, *Primordial Black Holes as a dark matter candidate*, 2007.10722.

[53] E. W. Kolb, D. J. Chung and A. Riotto, *WIMPzillas!*, *AIP Conf. Proc.* **484** (1999) 91 [hep-ph/9810361].

[54] G. Giudice and R. Rattazzi, *Theories with gauge mediated supersymmetry breaking*, *Phys. Rept.* **322** (1999) 419 [hep-ph/9801271].

[55] S. Raby, *Gauge-mediated susy breaking at an intermediate scale*, *Phys. Rev. D* **56** (1997) 2852.

[56] K. Hamaguchi, Y. Nomura and T. Yanagida, *Superheavy dark matter with discrete gauge symmetries*, *Phys. Rev. D* **58** (1998) 103503 [hep-ph/9805346].

[57] K. Benakli, J. R. Ellis and D. V. Nanopoulos, *Natural candidates for superheavy dark matter in string and M theory*, *Phys. Rev. D* **59** (1999) 047301 [hep-ph/9803333].

[58] D. J. Chung, P. Crotty, E. W. Kolb and A. Riotto, *On the Gravitational Production of Superheavy Dark Matter*, *Phys. Rev. D* **64** (2001) 043503 [hep-ph/0104100].

[59] V. Berezinsky, M. Kachelrieß and A. Vilenkin, *Ultrahigh energy cosmic rays without greisen-zatsepin-kuzmin cutoff*, *Phys. Rev. Lett.* **79** (1997) 4302.

[60] Y. Hochberg, E. Kuflik, T. Volansky and J. G. Wacker, *Mechanism for thermal relic dark matter of strongly interacting massive particles*, *Phys. Rev. Lett.* **113** (2014) 171301.

[61] S. Bruggisser, F. Riva and A. Urbano, *Strongly Interacting Light Dark Matter*, *SciPost Phys.* **3** (2017) 017.

[62] J. Schissel, *A New bound on supersymmetric Q-balls*, hep-ph/0608014.

[63] Y. Bai, A. J. Long and S. Lu, *Dark Quark Nuggets*, *Phys. Rev. D* **99** (2019) 055047 [1810.04360].

[64] B. J. Kavanagh, *Earth scattering of superheavy dark matter: Updated constraints from detectors old and new*, *Phys. Rev. D* **97** (2018) 123013.

[65] J. Rich, R. Rocchia and M. Spiro, *A search for strongly interacting dark matter*, *Physics Letters B* **194** (1987) 173 .

[66] E. K. Shirk and P. B. Price, *Charge and energy spectra of cosmic rays with Z 60: the Skylab experiment.*, **220** (1978) 719.

[67] G. D. Mack, J. F. Beacom and G. Bertone, *Towards closing the window on strongly interacting dark matter: Far-reaching constraints from earth's heat flow*, *Phys. Rev. D* **76** (2007) 043523.

[68] XENON Collaboration collaboration, *First dark matter search results from the xenon1t experiment*, *Phys. Rev. Lett.* **119** (2017) 181301.

[69] CRESST collaboration, *First results on low-mass dark matter from the CRESST-III experiment*, *J. Phys. Conf. Ser.* **1342** (2020) 012076 [1711.07692].

[70] CRESST collaboration, *Results on MeV-scale dark matter from a gram-scale cryogenic calorimeter operated above ground*, *Eur. Phys. J. C* **77** (2017) 637 [1707.06749].

[71] J. H. Davis, *Probing sub-gev mass strongly interacting dark matter with a low-threshold surface experiment*, *Phys. Rev. Lett.* **119** (2017) 211302.

[72] I. F. M. Albuquerque and L. Baudis, *Direct detection constraints on superheavy dark matter*, *Phys. Rev. Lett.* **90** (2003) 221301.

[73] CDMS Collaboration collaboration, *Exclusion limits on the wimp-nucleon cross section from the cryogenic dark matter search*, *Phys. Rev. D* **66** (2002) 122003.

[74] G. Steigman, B. Dasgupta and J. F. Beacom, *Precise relic wimp abundance and its impact on searches for dark matter annihilation*, *Phys. Rev. D* **86** (2012) 023506.

[75] K. Griest and M. Kamionkowski, *Unitarity limits on the mass and radius of dark-matter particles*, *Phys. Rev. Lett.* **64** (1990) 615.

[76] M. Cahill-Rowley, S. El Hedri, W. Shepherd and D. G. Walker, *Perturbative Unitarity Constraints on Charged/Colored Portals*, *Phys. Dark Univ.* **22** (2018) 48 [1501.03153].

[77] B. W. Lee and S. Weinberg, *Cosmological lower bound on heavy-neutrino masses*, *Phys. Rev. Lett.* **39** (1977) 165.

[78] S. D. McDermott, H.-B. Yu and K. M. Zurek, *Turning off the lights: How dark is dark matter?*, *Phys. Rev. D* **83** (2011) 063509.

[79] W. L. Xu, C. Dvorkin and A. Chael, *Probing sub-gev dark matter-baryon scattering with cosmological observables*, *Phys. Rev. D* **97** (2018) 103530.

[80] T. R. Slatyer and C.-L. Wu, *Early-universe constraints on dark matter-baryon scattering and their implications for a global 21 cm signal*, *Phys. Rev. D* **98** (2018) 023013.

[81] J.-T. Li and T. Lin, *Dynamics of millicharged dark matter in supernova remnants*, *Phys. Rev. D* **101** (2020) 103034 [2002.04625].

[82] J. Liang, Z. Liu, Y. Ma and Y. Zhang, *Millicharged particles at electron colliders*, *Phys. Rev. D* **102** (2020) 015002 [1909.06847].

[83] S. Gninenko, D. Kirpichnikov and N. Krasnikov, *Probing millicharged particles with NA64 experiment at CERN*, *Phys. Rev. D* **100** (2019) 035003 [1810.06856].

[84] R. Plestid, V. Takhistov, Y.-D. Tsai, T. Bringmann, A. Kusenko and M. Pospelov, *New Constraints on Millicharged Particles from Cosmic-ray Production*, 2002.11732.

[85] DEAP collaboration, *Constraints on dark matter-nucleon effective couplings in the presence of kinematically distinct halo substructures using the DEAP-3600 detector*, 2005.14667.

[86] M. Pospelov, A. Ritz and M. B. Voloshin, *Secluded WIMP Dark Matter*, *Phys. Lett. B* **662** (2008) 53 [0711.4866].

[87] N. Arkani-Hamed, D. P. Finkbeiner, T. R. Slatyer and N. Weiner, *A theory of dark matter*, *Phys. Rev. D* **79** (2009) 015014.

[88] J. Jaeckel, *A force beyond the Standard Model - Status of the quest for hidden photons*, *Frascati Phys. Ser.* **56** (2012) 172 [1303.1821].

[89] S. Knapen, T. Lin and K. M. Zurek, *Light dark matter: Models and constraints*, *Phys. Rev. D* **96** (2017) 115021.

[90] V. Ir˘ sič et al., *New Constraints on the free-streaming of warm dark matter from intermediate and small scale Lyman-α forest data*, *Phys. Rev. D* **96** (2017) 023522 [1702.01764].

[91] R. Murgia, V. Ir˘ sič and M. Viel, *Novel constraints on noncold, nonthermal dark matter from Lyman- α forest data*, *Phys. Rev. D* **98** (2018) 083540 [1806.08371].

[92] W. Hu, R. Barkana and A. Gruzinov, *Fuzzy cold dark matter: The wave properties of ultralight particles*, *Phys. Rev. Lett.* **85** (2000) 1158.

[93] L. Hui, J. P. Ostriker, S. Tremaine and E. Witten, *Ultralight scalars as cosmological dark matter*, *Phys. Rev. D* **95** (2017) 043541.

[94] A. Hook, *TASI Lectures on the Strong CP Problem and Axions*, *PoS* **TASI2018** (2019) 004 [1812.02669].

[95] G. Raffelt and L. Stodolsky, *Mixing of the photon with low-mass particles*, *Phys. Rev. D* **37** (1988) 1237.

[96] A. G. Dias, J. Leite, J. W. Valle and C. A. Vaquera-Araujo, *Reloading the Axion*, 2008.10650.

[97] A. Zhitnitsky, *On Possible Suppression of the Axion Hadron Interactions. (In Russian)*, *Sov. J. Nucl. Phys.* **31** (1980) 260.

[98] J. E. Kim, *Weak-interaction singlet and strong* CP *invariance*, *Phys. Rev. Lett.* **43** (1979) 103.

[99] G.-W. Yuan, Z. Xia, C. Tang, Y. Zhao, Y.-F. Cai, Y. Chen et al., *Testing the ALP-photon coupling with polarization measurements of Sagittarius A**, 2008.13662.

[100] H.-J. Li, J.-G. Guo, X.-J. Bi, S.-J. Lin and P.-F. Yin, *Limits on axion-like particles from Mrk 421 with 4.5-years period observations by ARGO-YBJ and Fermi-LAT*, 2008.09464.

[101] F. Calore, P. Carenza, M. Giannotti, J. Jaeckel and A. Mirizzi, *Bounds on axion-like particles from the diffuse supernova flux*, 2008.11741.

[102] G. Lucente, P. Carenza, T. Fischer, M. Giannotti and A. Mirizzi, *Heavy axion-like particles and core-collapse supernovae: constraints and impact on the explosion mechanism*, 2008.04918.

[103] P. Sikivie, *Experimental tests of the "invisible" axion*, *Phys. Rev. Lett.* **51** (1983) 1415.

[104] R. Bähre et al., *Any light particle search II —Technical Design Report*, *JINST* **8** (2013) T09001 [1302.5647].

[105] J. Hoskins et al., *Modulation sensitive search for nonvirialized dark-matter axions*, *Phys. Rev. D* **94** (2016) 082001 [1804.08770].

[106] D. Cangemi and R. Jackiw, *Gauge invariant formulations of lineal gravity*, *Phys. Rev. Lett.* **69** (1992) 233 [hep-th/9203056].

[107] M. Giannotti, J. Ruz and J. K. Vogel, *IAXO, next-generation of helioscopes*, *PoS* **ICHEP2016** (2016) 195 [1611.04652].

[108] G. Bertone, D. Hooper and J. Silk, *Particle dark matter: evidence, candidates and constraints*, *Physics Reports* **405** (2005) 279 .

[109] A. Ibarra, D. Tran and C. Weniger, *Indirect Searches for Decaying Dark Matter*, *Int. J. Mod. Phys. A* **28** (2013) 1330040 [1307.6434].

[110] L. E. Strigari, *Galactic searches for dark matter*, *Physics Reports* **531** (2013) 1 .

[111] J. Aleksić, S. Ansoldi, L. Antonelli, P. Antoranz, A. Babic, P. Bangale et al., *Optimized dark matter searches in deep observations of segue 1 with MAGIC*, *Journal of Cosmology and Astroparticle Physics* **2014** (2014) 008.

[112] H.E.S.S. Collaboration collaboration, *Search for dark matter annihilation signatures in h.e.s.s. observations of dwarf spheroidal galaxies*, *Phys. Rev. D* **90** (2014) 112012.

[113] T. Arlen, T. Aune, M. Beilicke, W. Benbow, A. Bouvier, J. H. Buckley et al., *Constraints on cosmic rays, magnetic fields, and dark matter from gamma-ray observations of the coma cluster of galaxies with veritas andfermi*, *The Astrophysical Journal* **757** (2012) 123.

[114] A. Albert, B. Anderson, K. Bechtol, A. Drlica-Wagner, M. Meyer, M. Sánchez-Conde et al., *SEARCHING FOR DARK MATTER ANNIHILATION IN RECENTLY DISCOVERED MILKY WAY SATELLITES WITHFERMI-LAT*, *The Astrophysical Journal* **834** (2017) 110.

[115] E. Bulbul, M. Markevitch, A. Foster, R. K. Smith, M. Loewenstein and S. W. Randall, *DETECTION OF AN UNIDENTIFIED EMISSION LINE IN THE STACKED x-RAY SPECTRUM OF GALAXY CLUSTERS*, *The Astrophysical Journal* **789** (2014) 13.

[116] A. Boyarsky, O. Ruchayskiy, D. Iakubovskyi and J. Franse, *Unidentified line in x-ray spectra of the andromeda galaxy and perseus galaxy cluster*, *Phys. Rev. Lett.* **113** (2014) 251301.

[117] IceCube collaboration, *Search for Neutrinos from Dark Matter Self-Annihilations in the center of the Milky Way with 3 years of IceCube/DeepCore*, *Eur. Phys. J. C* **77** (2017) 627 [1705.08103].

[118] ANTARES collaboration, *Limits on Dark Matter Annihilation in the Sun using the ANTARES Neutrino Telescope*, *Phys. Lett. B* **759** (2016) 69 [1603.02228].

[119] Super-Kamiokande Collaboration collaboration, *Search for neutrinos from annihilation of captured low-mass dark matter particles in the sun by super-kamiokande*, *Phys. Rev. Lett.* **114** (2015) 141301.

[120] N. W. Evans, C. A. O'Hare and C. McCabe, *Refinement of the standard halo model for dark matter searches in light of the Gaia Sausage*, *Phys. Rev. D* **99** (2019) 023012 [1810.11468].

[121] M. C. Digman, C. V. Cappiello, J. F. Beacom, C. M. Hirata and A. H. Peter, *Not as big as a barn: Upper bounds on dark matter-nucleus cross sections*, *Phys. Rev. D* **100** (2019) 063013 [1907.10618].

[122] R. H. Helm, *Inelastic and elastic scattering of 187-mev electrons from selected even-even nuclei*, *Phys. Rev.* **104** (1956) 1466.

[123] J. Lewin and P. Smith, *Review of mathematics, numerical factors, and corrections for dark matter experiments based on elastic nuclear recoil*, *Astropart. Phys.* **6** (1996) 87.

[124] SuperCDMS collaboration, *Dark matter effective field theory scattering in direct detection experiments*, *Phys. Rev. D* **91** (2015) 092004 [1503.03379].

[125] DarkSide-50 collaboration, *Effective field theory interactions for liquid argon target in DarkSide-50 experiment*, *Phys. Rev. D* **101** (2020) 062002 [2002.07794].

[126] G. Arcadi, A. Bally, F. Goertz, K. Tame-Narvaez, V. Tenorth and S. Vogl, *EFT Interpretation of XENON1T Electron Recoil Excess: Neutrinos and Dark Matter*, 2007.08500.

[127] A. Gutlein et al., *Solar and Atmospheric Neutrinos: Limitations for Direct Dark Matter Searches*, *Nucl. Phys. Proc. Supl.* **229-232** (2012) 536 [1009.3815].

[128] A. K. Drukier, K. Freese and D. N. Spergel, *Detecting cold dark-matter candidates*, *Phys. Rev. D* **33** (1986) 3495.

[129] D. P. Snowden-Ifft, C. J. Martoff and J. M. Burwell, *Low pressure negative ion time projection chamber for dark matter search*, *Phys. Rev. D* **61** (2000) 101301.

[130] T. Marrodán Undagoitia and L. Rauch, *Dark matter direct-detection experiments*, *J. Phys. G* **43** (2016) 013001 [1509.08767].

[131] D. Mei and A. Hime, *Muon-induced background study for underground laboratories*, *Phys. Rev. D* **73** (2006) 053004 [astro-ph/0512125].

[132] S. Westerdale and P. Meyers, *Radiogenic Neutron Yield Calculations for Low-Background Experiments*, *Nucl. Instrum. Meth. A* **875** (2017) 57 [1702.02465].

[133] M. Bossa, *DarkSide-50, a background free experiment for dark matter searches*, *Journal of Instrumentation* **9** (2014) C01034.

[134] B. Cabrera, L. M. Krauss and F. Wilczek, *Bolometric detection of neutrinos*, *Phys. Rev. Lett.* **55** (1985) 25.

[135] T. K. Gaisser, *Atmospheric neutrinos*, 2019.

[136] S. Anandagoda, D. H. Hartmann, M. Ajello and A. Desai, *The diffuse supernova neutrino background*, *Research Notes of the AAS* **4** (2020) 4.

[137] COHERENT collaboration, *COHERENT Collaboration data release from the first detection of coherent elastic neutrino-nucleus scattering on argon*, 2006.12659.

[138] L. E. Strigari, *Neutrino Coherent Scattering Rates at Direct Dark Matter Detectors*, *New J. Phys.* **11** (2009) 105011 [0903.3630].

[139] A. Gütlein, C. Ciemniak, F. von Feilitzsch, N. Haag, M. Hofmann, C. Isaila et al., *Solar and atmospheric neutrinos: Background sources for the direct dark matter searches*, *Astroparticle Physics* **34** (2010) 90 .

[140] F. Ruppin, J. Billard, E. Figueroa-Feliciano and L. Strigari, *Complementarity of dark matter detectors in light of the neutrino background*, *Phys. Rev. D* **90** (2014) 083510.

[141] A. Münster, M. v Sivers, G. Angloher, A. Bento, C. Bucci, L. Canonica et al., *Radiopurity of CaWO4 crystals for direct dark matter search with CRESST and EURECA*, *Journal of Cosmology and Astroparticle Physics* **2014** (2014) 018.

[142] R. Bernabei, *Crystal scintillators for low background measurements*, in *European Physical Journal Web of Conferences*, vol. 65 of *European Physical Journal Web of Conferences*, p. 01001, Jan., 2014, DOI.

[143] DarkSide collaboration, *Results From the First Use of Low Radioactivity Argon in a Dark Matter Search*, *Phys. Rev. D* **93** (2016) 081101 [1510.00702].

[144] EXO Collaboration collaboration, *Improved measurement of the $2\nu\beta\beta$ half-life of ^{136}xe with the exo-200 detector*, *Phys. Rev. C* **89** (2014) 015502.

[145] K. Abe, J. Hosaka, T. Iida, M. Ikeda, K. Kobayashi, Y. Koshio et al., *Distillation of liquid xenon to remove krypton*, *Astroparticle Physics* **31** (2009) 290–296.

[146] D. Akerib, X. Bai, S. Bedikian, E. Bernard, A. Bernstein, A. Bolozdynya et al., *The large underground xenon (lux) experiment*, *Nuclear Instruments and Methods in Physics Research Section A: Accelerators, Spectrometers, Detectors and Associated Equipment* **704** (2013) 111 .

[147] S. Lindemann and H. Simgen, *Krypton assay in xenon at the ppq level using a gas chromatographic system and mass spectrometer*, *Eur. Phys. J. C* **74** (2014) 2746 [1308.4806].

[148] DAMA collaboration, *The DAMA/LIBRA apparatus*, *Nucl. Instrum. Meth. A* **592** (2008) 297 [0804.2738].

[149] R. Bernabei et al., *Final model independent result of DAMA/LIBRA-phase1*, *Eur. Phys. J. C* **73** (2013) 2648 [1308.5109].

[150] C. Savage, G. Gelmini, P. Gondolo and K. Freese, *Compatibility of DAMA/LIBRA dark matter detection with other searches*, *JCAP* **04** (2009) 010 [0808.3607].

[151] R. Bernabei et al., *Investigating the DAMA annual modulation data in a mixed coupling framework*, *Phys. Lett. B* **509** (2001) 197.

[152] R. Bernabei et al., *Investigating the DAMA annual modulation data in the framework of inelastic dark matter*, *Eur. Phys. J. C* **23** (2002) 61.

[153] R. Bernabei et al., *Investigating pseudoscalar and scalar dark matter*, *Int. J. Mod. Phys. A* **21** (2006) 1445 [astro-ph/0511262].

[154] J. H. Davis, *The Past and Future of Light Dark Matter Direct Detection*, *Int. J. Mod. Phys. A* **30** (2015) 1530038 [1506.03924].

[155] J. Amaré et al., *From ANAIS-25 towards ANAIS-250*, *Phys. Procedia* **61** (2015) 157 [1404.3564].

[156] J. Amaré et al., *First Results on Dark Matter Annual Modulation from the ANAIS-112 Experiment*, *Phys. Rev. Lett.* **123** (2019) 031301 [1903.03973].

[157] DM-Ice collaboration, *First search for a dark matter annual modulation signal with NaI(Tl) in the Southern Hemisphere by DM-Ice17*, *Phys. Rev. D* **95** (2017) 032006 [1602.05939].

[158] E. Shields, J. Xu and F. Calaprice, *SABRE: A New NaI(T1) Dark Matter Direct Detection Experiment*, *Phys. Procedia* **61** (2015) 169.

[159] SABRE collaboration, *Dark matter search with the SABRE experiment*, *J. Phys. Conf. Ser.* **1342** (2020) 012060 [1807.00584].

[160] SABRE collaboration, *The SABRE Proof of Principle*, *J. Phys. Conf. Ser.* **1468** (2020) 012029.

[161] PICO-LON collaboration, *Dark matter search project PICO-LON*, *J. Phys. Conf. Ser.* **718** (2016) 042022 [1512.04645].

[162] KIMS collaboration, *KIMS: Dark matter search experiment in Korea*, *AIP Conf. Proc.* **805** (2005) 75.

[163] KIMS collaboration, *Limits on Interactions between Weakly Interacting Massive Particles and Nucleons Obtained with NaI(Tl) crystal Detectors*, *JHEP* **03** (2019) 194 [1806.06499].

[164] CoGeNT collaboration, *Search for An Annual Modulation in Three Years of CoGeNT Dark Matter Detector Data*, 1401.3295.

[165] C. Aalseth et al., *Maximum Likelihood Signal Extraction Method Applied to 3.4 years of CoGeNT Data*, 1401.6234.

[166] TEXONO Collaboration collaboration, *New limits on spin-independent and spin-dependent couplings of low-mass wimp dark matter with a germanium detector at a threshold of 220 ev*, *Phys. Rev. D* **79** (2009) 061101.

[167] CDEX collaboration, *Improved limits on solar axions and bosonic dark matter from the CDEX-1B experiment using the profile likelihood ratio method*, *Phys. Rev. D* **101** (2020) 052003 [1911.03085].

[168] CDMS collaboration, *Search for Weakly Interacting Massive Particles with the First Five-Tower Data from the Cryogenic Dark Matter Search at the Soudan Underground Laboratory*, *Phys. Rev. Lett.* **102** (2009) 011301 [0802.3530].

[169] *Dark matter search results from the cdms ii experiment*, *Science* **327** (2010) 1619 [https://science.sciencemag.org/content/327/5973/1619.full.pdf].

[170] CDMS-II collaboration, *Search for annual modulation in low-energy CDMS-II data*, 1203.1309.

[171] SuperCDMS Collaboration collaboration, *Search for low-mass weakly interacting massive particles with supercdms*, *Phys. Rev. Lett.* **112** (2014) 241302.

[172] SuperCDMS collaboration, *Low-mass dark matter search with CDMSlite*, *Phys. Rev. D* **97** (2018) 022002 [1707.01632].

[173] SuperCDMS Collaboration collaboration, *Results from the super cryogenic dark matter search experiment at soudan*, *Phys. Rev. Lett.* **120** (2018) 061802.

[174] SuperCDMS collaboration, *New Results from the Search for Low-Mass Weakly Interacting Massive Particles with the CDMS Low Ionization Threshold Experiment*, *Phys. Rev. Lett.* **116** (2016) 071301 [1509.02448].

[175] A. Broniatowski, X. Defay, E. Armengaud, L. Bergé, A. Benoit, O. Besida et al., *A new high-background-rejection dark matter ge cryogenic detector*, *Physics Letters B* **681** (2009) 305 .

[176] EDELWEISS collaboration, *EDELWEISS-III experiment: Status and first low WIMP mass results*, *J. Phys. Conf. Ser.* **718** (2016) 042053.

[177] EDELWEISS collaboration, *First germanium-based constraints on sub-MeV Dark Matter with the EDELWEISS experiment*, 2003.01046.

[178] EDELWEISS collaboration, *Recent results from EDELWEISS Dark Matter searches*, *J. Phys. Conf. Ser.* **1468** (2020) 012018.

[179] G. Angloher et al., *Limits on WIMP dark matter using scintillating $CaWO_4$ cryogenic detectors with active background suppression*, *Astropart. Phys.* **23** (2005) 325 [astro-ph/0408006].

[180] CRESST collaboration, *First results from the CRESST-III low-mass dark matter program*, *Phys. Rev. D* **100** (2019) 102002 [1904.00498].

[181] EURECA collaboration, *EURECA Conceptual Design Report*, *Phys. Dark Univ.* **3** (2014) 41.

[182] N. Coron et al., *2010 update on the ROSEBUD project*, *PoS* **IDM2010** (2011) 054.

[183] COUPP collaboration, *First Dark Matter Search Results from a 4-kg CF_3I Bubble Chamber Operated in a Deep Underground Site*, *Phys. Rev. D* **86** (2012) 052001 [1204.3094].

[184] PICO collaboration, *Dark Matter Search Results from the Complete Exposure of the PICO-60 C_3F_8 Bubble Chamber*, *Phys. Rev. D* **100** (2019) 022001 [1902.04031].

[185] PICASSO collaboration, *Constraints on Low-Mass WIMP Interactions on ^{19}F from PICASSO*, *Phys. Lett. B* **711** (2012) 153 [1202.1240].

[186] M. Felizardo et al., *Final Analysis and Results of the Phase II SIMPLE Dark Matter Search*, *Phys. Rev. Lett.* **108** (2012) 201302 [1106.3014].

[187] F. Seitz, *On the theory of the bubble chamber*, *The Physics of Fluids* **1** (1958) 2 [https://aip.scitation.org/doi/pdf/10.1063/1.1724333].

[188] PICO collaboration, *Dark Matter Search Results from the PICO-60 C_3F_8 Bubble Chamber*, *Phys. Rev. Lett.* **118** (2017) 251301 [1702.07666].

[189] PICO collaboration, *PICO-60 Results and PICO-40L Status*, *J. Phys. Conf. Ser.* **1468** (2020) 012043.

[190] DRIFT collaboration, *First background-free limit from a directional dark matter experiment: results from a fully fiducialised DRIFT detector*, *Phys. Dark Univ.* **9-10** (2015) 1 [1410.7821].

[191] DRIFT collaboration, *Low Threshold Results and Limits from the DRIFT Directional Dark Matter Detector*, *Astropart. Phys.* **91** (2017) 65 [1701.00171].

[192] D. Santos, *Dark Matter Directional Detection with MIMAC*, *J. Phys. Conf. Ser.* **1029** (2018) 012005.

[193] Y. Tao et al., *Dark Matter Directionality Detection performance of the Micromegas-based μTPC-MIMAC detector*, 2003.11812.

[194] S. Vahsen, H. Feng, M. Garcia-Sciveres, I. Jaegle, J. Kadyk, Y. Nguyen et al., *The directional dark matter detector (d3)*, *EAS Publications Series* **53** (2012) 43–50.

[195] DMTPC collaboration, *Directional dark matter detection with the DMTPC m^3 experiment*, *J. Phys. Conf. Ser.* **718** (2016) 042035.

[196] DEAP-3600 collaboration, *Design and Construction of the DEAP-3600 Dark Matter Detector*, *Astropart. Phys.* **108** (2019) 1 [1712.01982].

[197] XMASS collaboration, *A direct dark matter search in XMASS-I*, *Phys. Lett. B* **789** (2019) 45 [1804.02180].

[198] DEAP collaboration, *Measurement of the scintillation time spectra and pulse-shape discrimination of low-energy β and nuclear recoils in liquid argon with DEAP-1*, *Astropart. Phys.* **85** (2016) 1 [0904.2930].

[199] A. Hitachi, T. Takahashi, N. Funayama, K. Masuda, J. Kikuchi and T. Doke, *Effect of ionization density on the time dependence of luminescence from liquid argon and xenon*, *Phys. Rev. B* **27** (1983) 5279.

[200] DEAP-3600 collaboration, *Analysis and Dark Matter Search Results from DEAP-3600 with 231 Live Days at SNOLAB*, *J. Phys. Conf. Ser.* **1468** (2020) 012031.

[201] A. Lansiart, A. Seigneur, J.-L. Moretti and J.-P. Morucci, *Development research on a highly luminous condensed xenon scintillator*, *Nuclear Instruments and Methods* **135** (1976) 47 .

[202] LUX Collaboration collaboration, *Results from a search for dark matter in the complete lux exposure*, *Phys. Rev. Lett.* **118** (2017) 021303.

[203] D. Akimov, G. Alner, H. Araújo, A. Bewick, C. Bungau, A. Burenkov et al., *The zeplin-iii dark matter detector: Instrument design, manufacture and commissioning*, *Astroparticle Physics* **27** (2007) 46 .

[204] LZ collaboration, *The LUX-ZEPLIN (LZ) Experiment*, *Nucl. Instrum. Meth. A* **953** (2020) 163047 [1910.09124].

[205] PandaX-II collaboration, *Results of Dark Matter Search using the Full PandaX-II Exposure*, 2007.15469.

[206] PandaX collaboration, *Dark matter direct search sensitivity of the PandaX-4T experiment*, *Sci. China Phys. Mech. Astron.* **62** (2019) 31011 [1806.02229].

[207] XENON collaboration, *Dark Matter Search Results from a One Ton-Year Exposure of XENON1T*, *Phys. Rev. Lett.* **121** (2018) 111302 [1805.12562].

[208] XENON collaboration, *Projected WIMP Sensitivity of the XENONnT Dark Matter Experiment*, 2007.08796.

[209] M. Ibe, W. Nakano, Y. Shoji and K. Suzuki, *Migdal effect in dark matter direct detection experiments*, *Journal of High Energy Physics* **2018** (2018) .

[210] U. K. Dey, T. N. Maity and T. S. Ray, *Prospects of migdal effect in the explanation of xenon1t electron recoil excess*, *Physics Letters B* **811** (2020) 135900.

[211] XENON collaboration, *Observation of Excess Electronic Recoil Events in XENON1T*, 2006.09721.

[212] DarkSide collaboration, *DarkSide-50 532-day Dark Matter Search with Low-Radioactivity Argon*, *Phys. Rev. D* **98** (2018) 102006 [1802.07198].

[213] DarkSide collaboration, *Low-Mass Dark Matter Search with the DarkSide-50 Experiment*, *Phys. Rev. Lett.* **121** (2018) 081307 [1802.06994].

[214] P. Benetti, F. Calaprice, E. Calligarich, M. Cambiaghi, F. Carbonara, F. Cavanna et al., *Measurement of the specific activity of 39ar in natural argon*, *Nuclear Instruments and Methods in Physics Research Section A: Accelerators, Spectrometers, Detectors and Associated Equipment* **574** (2007) 83–88.

[215] J. Bigeleisen, *Statistical mechanics of isotope effects on the thermodynamic properties of condensed systems*, *The Journal of Chemical Physics* **34** (1961) 1485.

[216] J. N. Canongia Lopes, A. A. H. Pádua, L. P. N. Rebelo and J. Bigeleisen, *Calculation of vapor pressure isotope effects in the rare gases and their mixtures using an integral equation theory*, *The Journal of Chemical Physics* **118** (2003) 5028 [https://doi.org/10.1063/1.1545445].

[217] DarkSide collaboration, *DArT, a detector for measuring the ^{39}Ar depletion factor*, *JINST* **15** (2020) C02044 [2001.08077].

[218] DarkSide-20k collaboration, *Design and Construction of a New Detector to Measure Ultra-Low Radioactive-Isotope Contamination of Argon*, *JINST* **15** (2020) P02024 [2001.08106].

[219] D.-M. Mei, Z.-B. Yin, L. Stonehill and A. Hime, *A model of nuclear recoil scintillation efficiency in noble liquids*, *Astroparticle Physics* **30** (2008) 12 .

[220] T. Doke, A. Hitachi, J. Kikuchi, K. Masuda, H. Okada and E. Shibamura, *Absolute scintillation yields in liquid argon and xenon for various particles*, *Japanese Journal of Applied Physics* **41** (2002) 1538.

[221] SCENE Collaboration collaboration, *Measurement of scintillation and ionization yield and scintillation pulse shape from nuclear recoils in liquid argon*, *Phys. Rev. D* **91** (2015) 092007.

[222] P. Agnes, *Simulation of the argon response and light detection in a dual-phase TPC*, *JINST* **15** (2020) C01044.

[223] P. Agnes, I. Albuquerque, T. Alexander, A. Alton, D. Asner, H. Back et al., *Simulation of argon response and light detection in the darkside-50 dual phase tpc*, *Journal of Instrumentation* **12** (2017) P10015.

[224] P. A. et al., *First results from the darkside-50 dark matter experiment at laboratori nazionali del gran sasso*, *Physics Letters B* **743** (2015) 456 .

[225] J. Lindhard, V. Nielsen, M. Scharff and P. V. Thomsen, *Integral equations governing radiation effects. (notes on atomic collisions, iii)*, *Kgl. Danske Videnskab., Selskab. Mat. Fys. Medd.* .

[226] J. Birks, *Scintillations from Organic Crystals: Specific Fluorescence and Relative Response to Different Radiations*, *Proc. Phys. Soc. A* **64** (1951) 874.

[227] J. LaVerne and A. Hitachi, *Scintillation and ionization in allene-doped liquid argon irradiated with and ions of 30 mev/u*, *Physical Review B - Condensed Matter and Materials Physics* **54** (1996) 15724.

[228] E. Aprile, K. L. Giboni, P. Majewski, K. Ni, M. Yamashita, R. Hasty et al., *Scintillation response of liquid xenon to low energy nuclear recoils*, *Phys. Rev. D* **72** (2005) 072006.

[229] D. Akimov, A. Bewick, D. Davidge, J. Dawson, A. Howard, I. Ivaniouchenkov et al., *Measurements of scintillation efficiency and pulse shape for low energy recoils in liquid xenon*, *Physics Letters B* **524** (2002) 245 .

[230] A. et al., *Scintillation efficiency of nuclear recoil in liquid xenon*, *Nuclear Instruments and Methods in Physics Research, Section A: Accelerators, Spectrometers, Detectors and Associated Equipment* **449** (2000) 147.

[231] SCENE Collaboration collaboration, *Observation of the dependence on drift field of scintillation from nuclear recoils in liquid argon*, *Phys. Rev. D* **88** (2013) 092006.

[232] D. Gastler, E. Kearns, A. Hime, L. C. Stonehill, S. Seibert, J. Klein et al., *Measurement of scintillation efficiency for nuclear recoils in liquid argon*, *Phys. Rev. C* **85** (2012) 065811.

[233] W. Creus, Y. Allkofer, C. Amsler, A. Ferella, J. Rochet, L. Scotto-Lavina et al., *Scintillation efficiency of liquid argon in low energy neutron-argon scattering*, *Journal of Instrumentation* **10** (2015) P08002.

[234] R. Brunetti, E. Calligarich, M. Cambiaghi, F. Carbonara, A. Cocco, C. D. Vecchi et al., *Warp liquid argon detector for dark matter survey*, *New Astronomy Reviews* **49** (2005) 265 .

[235] P. Agnes et al., *Measurement of the liquid argon energy response to nuclear and electronic recoils*, *Phys. Rev. D* **97** (2018) 112005 [1801.06653].

[236] P.-A. Amaudruz, M. Batygov, B. Beltran, J. Bonatt, K. Boudjemline, M. Boulay et al., *Measurement of the scintillation time spectra and pulse-shape discrimination of low-energy and nuclear recoils in liquid argon with deap-1*, *Astroparticle Physics* **85** (2016) 1–23.

[237] M. G. B. and, *DEAP-3600 dark matter search at SNOLAB*, *Journal of Physics: Conference Series* **375** (2012) 012027.

[238] DarkSide collaboration, *Electroluminescence pulse shape and electron diffusion in liquid argon measured in a dual-phase TPC*, *Nucl. Instrum. Meth. A* **904** (2018) 23 [1802.01427].

[239] B. Broerman, M. Boulay, B. Cai, D. Cranshaw, K. Dering, S. Florian et al., *Application of the TPB wavelength shifter to the DEAP-3600 spherical acrylic vessel inner surface*, *Journal of Instrumentation* **12** (2017) P04017.

[240] F. Duncan, A. Noble and D. Sinclair, *The construction and anticipated science of snolab*, *Annual Review of Nuclear and Particle Science* **60** (2010) 163 [https://doi.org/10.1146/annurev.nucl.012809.104513].

[241] K. Rielage, M. Akashi-Ronquest, M. Bodmer, R. Bourque, B. Buck, A. Butcher et al., *Update on the miniclean dark matter experiment*, *Physics Procedia* **61** (2015) 144 .

[242] S. Agostinelli, J. Allison, K. Amako, J. Apostolakis, H. Araujo, P. Arce et al., *Geant4—a simulation toolkit*, *Nuclear Instruments and Methods in Physics Research Section A: Accelerators, Spectrometers, Detectors and Associated Equipment* **506** (2003) 250 .

[243] R. Brun and F. Rademakers, *Root — an object oriented data analysis framework*, *Nuclear Instruments and Methods in Physics Research Section A: Accelerators, Spectrometers, Detectors and Associated Equipment* **389** (1997) 81 .

[244] DEAP collaboration, *Search for Dark Matter with Liquid Argon and Pulse Shape Discrimination: Results from DEAP-1 and Status of DEAP-3600*, in *49th Rencontres de Moriond on Electroweak Interactions and Unified Theories*, pp. 487–490, 2014, 1406.0462.

[245] P.-A. Amaudruz, M. Batygov, B. Beltran, K. Boudjemline, M. Boulay, B. Cai et al., *Radon backgrounds in the deap-1 liquid-argon-based dark matter detector*, *Astroparticle Physics* **62** (2015) 178 .

[246] M. Bodmer, N. Phan, M. Gold, D. Loomba, J. A. J. Matthews and K. Rielage, *Measurement of optical attenuation in acrylic light guides for a dark matter detector*, *Journal of Instrumentation* **9** (2014) P02002.

[247] T. Pollmann, M. Boulay and M. Kuźniak, *Scintillation of thin tetraphenyl butadiene films under alpha particle excitation*, *Nuclear Instruments and Methods in Physics Research Section A: Accelerators, Spectrometers, Detectors and Associated Equipment* **635** (2011) 127 .

[248] L. Veloce, M. Kuźniak, P. D. Stefano, A. Noble, M. Boulay, P. Nadeau et al., *Temperature dependence of alpha-induced scintillation in the 1,1,4,4-tetraphenyl-1,3-butadiene wavelength shifter*, *Journal of Instrumentation* **11** (2016) P06003.

[249] M. Kuźniak, M. Boulay and T. Pollmann, *Surface roughness interpretation of 730kgdays cresst-ii results*, *Astroparticle Physics* **36** (2012) 77 .

[250] W. Wilson, R. Perry, W. Charlton and T. Parish, *Sources: A code for calculating (alpha, n), spontaneous fission, and delayed neutron sources and spectra*, *Progress in Nuclear Energy* **51** (2009) 608 .

[251] S. Westerdale and P. Meyers, *Radiogenic neutron yield calculations for low-background experiments*, *Nuclear Instruments and Methods in Physics Research Section A: Accelerators, Spectrometers, Detectors and Associated Equipment* **875** (2017) 57 .

[252] J. Xu, F. Calaprice, C. Galbiati, A. Goretti, G. Guray, T. Hohman et al., *A study of the trace 39ar content in argon from deep underground sources*, *Astroparticle Physics* **66** (2015) 53 .

[253] DUNE collaboration, *The Single-Phase ProtoDUNE Technical Design Report*, 1706.07081.

[254] DUNE collaboration, *Long-Baseline Neutrino Facility (LBNF) and Deep Underground Neutrino Experiment (DUNE): Conceptual Design Report, Volume 1: The LBNF and DUNE Projects*, 1601.05471.

[255] I. Ostrovskiy, F. Retiere, D. Auty, J. Dalmasson, T. Didberidze, R. DeVoe et al., *Characterization of silicon photomultipliers for nexo*, *IEEE Transactions on Nuclear Science* **62** (2015) 1825.

[256] M. D'Incecco, C. Galbiati, G. K. Giovanetti, G. Korga, X. Li, A. Mandarano et al., *Development of a very low-noise cryogenic preamplifier for large-area sipm devices*, *IEEE Transactions on Nuclear Science* **65** (2018) 1005.

[257] M. D'Incecco, C. Galbiati, G. K. Giovanetti, G. Korga, X. Li, A. Mandarano et al., *Development of a novel single-channel, 24 cm2, sipm-based, cryogenic photodetector*, *IEEE Transactions on Nuclear Science* **65** (2018) 591.

[258] M. Kuźniak, B. Broerman, T. Pollmann and G. Araujo, *Polyethylene naphthalate film as a wavelength shifter in liquid argon detectors*, *Eur. Phys. J. C* **79** (2019) 291 [1806.04020].

[259] M. Cadeddu et al., *Directional dark matter detection sensitivity of a two-phase liquid argon detector*, *JCAP* **01** (2019) 014 [1704.03741].

[260] DarkSide collaboration, *SiPM-matrix readout of two-phase argon detectors using electroluminescence in the visible and near infrared range*, 2004.02024.

[261] C. Jacoby and S. Nussinov, *The Relic Abundance of Massive Colored Particles after a Late Hadronic Annihilation Stage*, 0712.2681.

[262] J. Kang, M. A. Luty and S. Nasri, *The Relic abundance of long-lived heavy colored particles*, *JHEP* **09** (2008) 086 [hep-ph/0611322].

[263] D. Hooper, G. Krnjaic and S. D. McDermott, *Dark radiation and superheavy dark matter from black hole domination*, *Journal of High Energy Physics* **2019** (2019) .

[264] Y. Bai, M. Korwar and N. Orlofsky, *Electroweak-symmetric dark monopoles from preheating*, 2020.

[265] D. J. H. Chung, E. W. Kolb and A. Riotto, *Superheavy dark matter*, *Physical Review D* **59** (1998) .

[266] E. W. Kolb, D. J. H. Chung and A. Riotto, *Wimpzillas!*, 1998.

[267] H. Davoudiasl and G. Mohlabeng, *GeV-Scale Messengers of Planck-Scale Dark Matter*, *Phys. Rev.* **D98** (2018) 115035 [1809.07768].

[268] A. Coskuner, D. M. Grabowska, S. Knapen and K. M. Zurek, *Direct Detection of Bound States of Asymmetric Dark Matter*, *Phys. Rev.* **D100** (2019) 035025 [1812.07573].

[269] E. Ponton, Y. Bai and B. Jain, *Electroweak Symmetric Dark Matter Balls*, 1906.10739.

[270] B. V. Lehmann, C. Johnson, S. Profumo and T. Schwemberger, *Direct detection of primordial black hole dark matter*, 1906.06348.

[271] R. Bernabei, P. Belli, R. Cerulli, F. Montecchia, M. Amato, G. Ignesti et al., *Extended limits on neutral strongly interacting massive particles and nuclearites from nai(tl) scintillators*, *Phys. Rev. Lett.* **83** (1999) 4918.

[272] M. C. Digman, C. V. Cappiello, J. F. Beacom, C. M. Hirata and A. H. Peter, *Not as big as a barn: Upper bounds on dark matter-nucleus cross sections*, *Physical Review D* **100** (2019) .

[273] L. E. Strigari, *Neutrino coherent scattering rates at direct dark matter detectors*, *New Journal of Physics* **11** (2009) 105011.

[274] J. Engel, *Nuclear form-factors for the scattering of weakly interacting massive particles*, *Phys. Lett. B* **264** (1991) 114.

[275] J. Engel, S. Pittel and P. Vogel, *Nuclear physics of dark matter detection*, *Int. J. Mod. Phys. E* **1** (1992) 1.

[276] "U.s. standard atmosphere, https://strives-uploads-prod.s3.us-gov-west-1.amazonaws.com/19770009539/19770009539.pdf?awsaccesskeyid=akiasevskc45zttm42xz&expires=1599745122&signature=lrrqtgclzz2wgbtvaprt77oodbo%3d,."

[277] "Earth reference model, u.s. standard atmosphere, https://www.cfa.harvard.edu/~lzeng/papers/prem.pdf,."

[278] B. J. Kavanagh, *Earth scattering of superheavy dark matter: Updated constraints from detectors old and new*, *Phys. Rev. D* **97** (2018) 123013 [1712.04901].

[279] J. Lundberg and J. Edsjo, *WIMP diffusion in the solar system including solar depletion and its effect on earth capture rates*, *Phys. Rev. D* **69** (2004) 123505 [astro-ph/0401113].

[280] DEAP collaboration, *Search for dark matter with a 231-day exposure of liquid argon using DEAP-3600 at SNOLAB*, *Phys. Rev. D* **100** (2019) 022004 [1902.04048].

[281] DEAP collaboration, *Electromagnetic backgrounds and potassium-42 activity in the DEAP-3600 dark matter detector*, *Phys. Rev. D* **100** (2019) 072009 [1905.05811].

[282] DarkSide collaboration, *Cryogenic Characterization of FBK RGB-HD SiPMs*, *JINST* **12** (2017) P09030 [1705.07028].

[283] M. D'Incecco, C. Galbiati, G. K. Giovanetti, G. Korga, X. Li, A. Mandarano et al., *Development of a Novel Single-Channel, 24 cm^2, SiPM-Based, Cryogenic Photodetector*, *IEEE Trans. Nucl. Sci.* **65** (2017) 591 [1706.04220].

[284] C. Aalseth et al., *DarkSide-20k: A 20 tonne two-phase LAr TPC for direct dark matter detection at LNGS*, *Eur. Phys. J. Plus* **133** (2018) 131 [1707.08145].

[285] F. Acerbi et al., *Cryogenic Characterization of FBK HD Near-UV Sensitive SiPMs*, *IEEE Trans. Electron. Dev.* **64** (2016) 521 [1610.01915].

[286] XENON Collaboration collaboration, S. D'Amato, "Characterization of siliconphotomultiplier arrays in liquidxenon and development of dedicatedread-out electronics."

[287] J. Becker, E. Fretwurst and R. Klanner, *Measurements of charge carrier mobilities and drift velocity saturation in bulk silicon of <111> and <100> crystal orientation at high electric fields*, *Solid State Electron.* **56** (2011) 104 [1007.4432].

[288] B. Aull, A. H. Loomis, D. J. Young, R. M. Heinrichs, B. J. Felton, P. J. L. Daniels et al., *Geiger-mode avalanche photodiodes for three-dimensional imaging*, 2002.

[289] A. Vil, A. Arbat, E. Vilella and A. Dieguez, *Geiger-Mode Avalanche Photodiodes in Standard CMOS Technologies*. 03, 2012. 10.5772/37162.

[290] J. Rosado, V. Aranda, F. Blanco and F. Arqueros, *Modeling crosstalk and afterpulsing in silicon photomultipliers*, *Nuclear Instruments and Methods in Physics Research Section A: Accelerators, Spectrometers, Detectors and Associated Equipment* **787** (2015) 153 .

[291] G. Turin, *An introduction to matched filters*, *IRE Transactions on Information Theory* **6** (1960) 311.

[292] J. ROTHSTEIN, *Probability and information theory, with applications to radar. p. m. woodward. mcgraw-hill, new york; pergamon press, london, 1953. 128 pp.*, *Science* **119** (1954) 874 [https://science.sciencemag.org/content/119/3103/874.1.full.pdf].

[293] B. F. Schutz, *Gravitational wave astronomy*, *Classical and Quantum Gravity* **16** (1999) A131–A156.

[294] C. Aalseth, F. Acerbi, P. Agnes, I. Albuquerque, T. Alexander, A. Alici et al., *Darkside-20k: A 20 tonne two-phase lar tpc for direct dark matter detection at lngs*, *The European Physical Journal Plus* **133** (2018) 131.

[295] M. Boulay and U. C. Visions, *Argon dark matter searches: Darkside-20k and beyond*, *New Ideas DM* (2017) .

[296] Y. Wang, *A global liquid argon dark matter search program*, *Bulletin of the American Physical Society* **64** (2019) .

[297] A. Burrows, J. Hayes and B. A. Fryxell, *On the nature of core collapse supernova explosions*, *Astrophys. J.* **450** (1995) 830 [astro-ph/9506061].

[298] S. Woosley and T. Janka, *The physics of core-collapse supernovae*, *Nature Physics* **1** (2005) 147.

[299] B. Abbott, R. Abbott, T. Abbott, M. Abernathy, F. Acernese, K. Ackley et al., *First targeted search for gravitational-wave bursts from core-collapse supernovae in data of first-generation laser interferometer detectors*, *Physical Review D* **94** (2016) .

[300] H.-T. Janka, K. Langanke, A. Marek, G. Martínez-Pinedo and B. Müller, *Theory of core-collapse supernovae*, *Physics Reports* **442** (2007) 38.

[301] S. Horiuchi and J. P. Kneller, *What can be learned from a future supernova neutrino detection?*, *Journal of Physics G: Nuclear and Particle Physics* **45** (2018) 043002.

[302] A. Mirizzi, I. Tamborra, H.-T. Janka, N. Saviano, K. Scholberg, R. Bollig et al., *Supernova neutrinos: production, oscillations and detection*, *String Theory* **39** (2016) 1.

[303] K. Hirata, T. Kajita, M. Koshiba, M. Nakahata, Y. Oyama, N. Sato et al., *Observation in the kamiokande-ii detector of the neutrino burst from supernova sn1987a*, *Physical Review D* **38** (1988) 448.

[304] T. Haines, C. Bratton, D. Casper, A. Ciocio, R. Claus, M. Crouch et al., *Neutrinos from sn1987a in the imb detector*, *Nuclear Instruments and Methods in Physics Research Section A: Accelerators, Spectrometers, Detectors and Associated Equipment* **264** (1988) 28.

[305] E. Alexeyev, L. Alexeyeva, I. Krivosheina and V. Volchenko, *Detection of the neutrino signal from sn 1987a in the lmc using the inr baksan underground scintillation telescope*, *Physics Letters B* **205** (1988) 209.

[306] D. Z. Freedman, *Coherent effects of a weak neutral current*, *Physical Review D* **9** (1974) 1389.

[307] D. Akimov, J. Albert, P. An, C. Awe, P. Barbeau, B. Becker et al., *Observation of coherent elastic neutrino-nucleus scattering*, *Science* **357** (2017) 1123.

[308] S. Fukuda, Y. Fukuda, T. Hayakawa, E. Ichihara, M. Ishitsuka, Y. Itow et al., *The super-kamiokande detector*, *Nuclear Instruments and Methods in Physics Research Section A: Accelerators, Spectrometers, Detectors and Associated Equipment* **501** (2003) 418.

[309] K. Nakamura, *Hyper-kamiokande—a next generation water cherenkov detector*, *International Journal of Modern Physics A* **18** (2003) 4053.

[310] R. Abbasi, Y. Abdou, T. Abu-Zayyad, M. Ackermann, J. Adams, J. Aguilar et al., *The design and performance of icecube deepcore*, *Astroparticle physics* **35** (2012) 615.

[311] M. Ikeda, A. Takeda, Y. Fukuda, M. Vagins, K. Abe, T. Iida et al., *Search for supernova neutrino bursts at super-kamiokande*, *The Astrophysical Journal* **669** (2007) 519.

[312] R. Abbasi, Y. Abdou, T. Abu-Zayyad, M. Ackermann, J. Adams, J. Aguilar et al., *Icecube sensitivity for low-energy neutrinos from nearby supernovae*, *Astronomy and Astrophysics* **535** (2011) A109.

[313] F. An, G. An, Q. An, V. Antonelli, E. Baussan, J. Beacom et al., *Neutrino physics with juno*, *Journal of Physics G: Nuclear and Particle Physics* **43** (2016) 030401.

[314] B. Abi, R. Acciarri, M. Acero, M. Adamowski, C. Adams, D. Adams et al., *The dune far detector interim design report volume 1: Physics, technology and strategies*, *arXiv preprint arXiv:1807.10334* (2018) .

[315] R. F. Lang, C. McCabe, S. Reichard, M. Selvi and I. Tamborra, *Supernova neutrino physics with xenon dark matter detectors: A timely perspective*, *Phys. Rev. D* **94** (2016) 103009.

[316] S. Chakraborty, P. Bhattacharjee and K. Kar, *Observing supernova neutrino light curve in future dark matter detectors*, *Phys. Rev. D* **89** (2014) 013011.

[317] C. J. Horowitz, K. J. Coakley and D. N. McKinsey, *Supernova observation via neutrino-nucleus elastic scattering in the clean detector*, *Phys. Rev. D* **68** (2003) 023005.

[318] J. M. Lattimer and D. F. Swesty, *A generalized equation of state for hot, dense matter*, **535** (1991) 331.

[319] H.-T. Janka, *Conditions for shock revival by neutrino heating in core-collapse supernovae*, *Astronomy & Astrophysics* **368** (2001) 527.

[320] S. W. Bruenn, A. Mezzacappa, W. R. Hix, E. J. Lentz, O. B. Messer, E. J. Lingerfelt et al., *Axisymmetric ab initio core-collapse supernova simulations of 12-25 m stars*, *The Astrophysical Journal Letters* **767** (2013) L6.

[321] S. Bruenn, A. Mezzacappa, W. Hix, J. Blondin, P. Marronetti, O. Messer et al., *Mechanisms of core-collapse supernovae & simulation results from the chimera code*, in *AIP Conference Proceedings*, vol. 1111, pp. 593–601, AIP, 2009.

[322] H.-T. Janka, K. Langanke, A. Marek, G. Martínez-Pinedo and B. Müller, *Theory of core-collapse supernovae*, *Physics Reports* **442** (2007) 38 .

[323] S. Mikheyev and A. Y. Smirnov, *Resonant amplification of ν oscillations in matter and solar-neutrino spectroscopy*, *Il Nuovo Cimento C* **9** (1986) 17.

[324] H. Duan, G. M. Fuller, J. Carlson and Y.-Z. Qian, *Neutrino mass hierarchy and stepwise spectral swapping of supernova neutrino flavors*, *Physical review letters* **99** (2007) 241802.

[325] C. Lunardini and A. Y. Smirnov, *Probing the neutrino mass hierarchy and the 13-mixing with supernovae*, *Journal of Cosmology and Astroparticle Physics* **2003** (2003) 009.

[326] C. Y. Cardall, *Core-collapse supernova explosion simulations*, *Nuclear Physics - Section B - Proceeding Supplements* **217** (2011) 275.

[327] C. L. Fryer and M. S. Warren, *Modeling core-collapse supernovae in three dimensions*, *The Astrophysical Journal Letters* **574** (2002) L65.

[328] I. Tamborra, F. Hanke, B. Müller, H.-T. Janka and G. Raffelt, *Neutrino signature of supernova hydrodynamical instabilities in three dimensions*, *Physical Review Letters* **111** (2013) 121104.

[329] I. Tamborra, F. Hanke, H.-T. Janka, B. Müller, G. G. Raffelt and A. Marek, *Self-sustained asymmetry of lepton-number emission: A new phenomenon during the supernova shock-accretion phase in three dimensions*, *The Astrophysical Journal* **792** (2014) 96.

[330] J. M. Blondin, A. Mezzacappa and C. DeMarino, *Stability of standing accretion shocks, with an eye toward core-collapse supernovae*, *The Astrophysical Journal* **584** (2003) 971.

[331] W. Iwakami, K. Kotake, N. Ohnishi, S. Yamada and K. Sawada, *Three-dimensional simulations of standing accretion shock instability in core-collapse supernovae*, *The Astrophysical Journal* **678** (2008) 1207.

[332] C. L. Fryer, *Mass limits for black hole formation*, *The Astrophysical Journal* **522** (1999) 413.

[333] E. O'Connor and C. D. Ott, *Black hole formation in failing core-collapse supernovae*, *The Astrophysical Journal* **730** (2011) 70.

[334] J. F. Beacom, R. Boyd and A. Mezzacappa, *Black hole formation in core-collapse supernovae and time-of-flight measurements of the neutrino masses*, *Physical Review D* **63** (2001) 073011.

[335] I. Sagert, T. Fischer, M. Hempel, G. Pagliara, J. Schaffner-Bielich, A. Mezzacappa et al., *Signals of the qcd phase transition in core-collapse supernovae*, *Physical Review Letters* **102** (2009) 081101.

[336] H.-Y. Chiu and P. Morrison, *Neutrino emission from black-body radiation at high stellar temperatures*, *Physical Review Letters* **5** (1960) 573.

[337] M. S. Turner, *Axions from sn1987a*, *Physical Review Letters* **60** (1988) 1797.

[338] A. B. Balantekin, J. Gava and C. Volpe, *Possible cp-violation effects in core-collapse supernovae*, *Physics Letters B* **662** (2008) 396.

[339] K. Scholberg, *Prospects for measuring coherent neutrino-nucleus elastic scattering at a stopped-pion neutrino source*, *Physical Review D* **73** (2006) 033005.

[340] J. Barranco, O. G. Miranda and T. I. Rashba, *Probing new physics with coherent neutrino scattering off nuclei*, *Journal of High Energy Physics* **2005** (2005) 021.

[341] R. P. Feynman and M. Gell-Mann, *Theory of the fermi interaction*, *Physical Review* **109** (1958) 193.

[342] T. van Ritbergen and R. G. Stuart, *On the precise determination of the fermi coupling constant from the muon lifetime*, *Nuclear Physics B* **564** (2000) 343.

[343] L. E. Strigari, *Neutrino coherent scattering rates at direct dark matter detectors*, *New Journal of Physics* **11** (2009) 105011.

[344] J. Engel, *Nuclear form factors for the scattering of weakly interacting massive particles*, *Physics Letters B* **264** (1991) 114.

[345] J. Engel, S. Pittel and P. Vogel, *Nuclear physics of dark matter detection*, *International Journal of Modern Physics E* **1** (1992) 1.

[346] H. Cao, T. Alexander, A. Aprahamian, R. Avetisyan, H. Back, A. Cocco et al., *Measurement of scintillation and ionization yield and scintillation pulse shape from nuclear recoils in liquid argon*, *Physical Review D* **91** (2015) 092007.

[347] J. Thomas and D. A. Imel, *Recombination of electron-ion pairs in liquid argon and liquid xenon*, *Phys. Rev. A* **36** (1987) 614.

[348] The DarkSide Collaboration collaboration, *Constraints on sub-gev dark-matter–electron scattering from the darkside-50 experiment*, *Phys. Rev. Lett.* **121** (2018) 111303.

[349] P. Agnes, I. M. Albuquerque, T. Alexander, A. Alton, D. Asner, M. Ave et al., *Electroluminescence pulse shape and electron diffusion in liquid argon measured in a dual-phase tpc*, *Nuclear Instruments and Methods in Physics Research Section A: Accelerators, Spectrometers, Detectors and Associated Equipment* **904** (2018) 23 .

[350] G. Cowan, K. Cranmer, E. Gross and O. Vitells, *Asymptotic formulae for likelihood-based tests of new physics*, *The European Physical Journal C* **71** (2011) 1554.

[351] M. T. Keil, G. G. Raffelt and H.-T. Janka, *Monte carlo study of supernova neutrino spectra formation*, *The Astrophysical Journal* **590** (2003) 971.

8 List of Figures

List of Figures

2.1.1 Rotational curve for M31, the Andromeda Galaxy, from optical and 21-cm line observations compared to the expectation from the surface density [16]. 14

2.1.2 Merging 'bullet' cluster 1E0657-558, both in optical (left) and X-ray (right). In both panels, green contours are the equipotential gravitational curves of the cluster, found using weak lensing of distant galaxies. The contours of the gravitational potential coincide with visible galaxies but are far from the location of the X-ray gas (the dominant baryonic component of clusters). This is straightforward to explain with the assumption of a non-baryonic matter component, which would mainly not interact during the merging, besides the gravitational force. The disagreement was also observed in other clusters, with a quantitatively spread of the distance between the gravitational and the luminous mass centers of gravity. This non-universal disagreement is then easier to explain with a different mass distribution/abundance instead of a universal modification of general relativity [22]. 15

2.1.3 Cosmic Microwave Background from Planck(2013) [32]. The signal is mainly isotropic but shows slight temperature variations, of the scale of 10^{-5}. This is due to the local fluctuations of the cold photons-matter plasma which preceded the recombination process. 17

2.1.4 Multipole expansion for the Cosmic Microwave Background. l is the acoustic peaks' wavenumber: low l corresponds to high wavelength and then wider angles. The first peak is related to the universe curvature, which is almost null. The relative height of the second peak compared to the first one relies on the baryonic contribution. The third and following odd peaks are second-order contribution, so from the dark matter, which does not interact with photons [33]. 18

2.2.1 Constrains on the sterile neutrino as dark matter candidate, mainly coming from observations on small-scale galactic structures. Red curves show theoretical predictions for sterile neutrinos constituting all the dark matter with lepton numbers L=0, 0.003, 0.01 [49]. 24

2.2.2 Dark matter main models, according to the mass of the dark matter particle [44]. 25
2.2.3 Constraints on the fraction of dark matter to which PBHs may account for, according to their mass, expressed both in grams and Solar Mass units [52]. 26
2.2.4 Constraints on strongly interacting dark matter from direct detection experiments, based on the nuclear scattering of dark matter particles on baryonic nuclei [64]. The orange regions were excluded by high-altitude experiments, such as RSS [65] and SKYLAB [66], fully reviewed in [67]. The grey shaded is bounded from below by constraints from Xenon1T [68] and from the left by CRESST-III [69] and the CRESST 2017 surface run [70] [71]. The black line denotes the previous cross-section reach from [72]. The shaded blue area shows the additional region of parameter space excluded by the reanalysis in [64] of the CDMS-I limits [73]. 27
2.2.5 Updated axion and ALPs exclusion plot. The yellow band refers to the space of parameters in which Axions are expected. By relaxing any constraint on the mass-coupling ratio, the Axion-Like-Particle candidate follows [107]. 33
2.3.1 Scheme of the dark matter detection strategies. The direct detection (horizontal lines) looks for the scattering of dark matter particles on baryon atoms, so the input and output is a particle from the Standard Model. At colliders the annihilation between baryons can produce dark matter particles. Finally, indirect detection looks for the signal from the decay of the annihilation of dark matter particles. 34
2.3.2 Squared Helm form factor for different nuclei, assuming Lewin-Smith parametrization. 37
2.3.3 Recoil energy spectra for WIMP $m_\chi = 60$ GeV$/^2$ and $\sigma_0 = 10^{-44}$ cm^2, for Argon, Xenon, Neon, Germanium and Tungsten, contained in $CaWO_4$ crystals [127]. 39

2.3.4 Muon flux as a function of depth in km water equivalent (km w.e.), for underground laboratories in which dark matter search is performed: the Waste Isolation Pilot Plant (WIPP) in the USA, the Laboratoire Souterrain à Bras Bruit (LSBB) in France, the Kamioka Observatory in Japan, the Soudan Underground Laboratory in the USA, the Yand Yand Underground Lab (Y2L) in Corea, the Boulby Underground Laboratory in the U.K., the Laboratori Nazionali del Gran Sasso (LNGS) in Italy, the Laboratoire Souterrain de Modane (LSM) in France, the Sanford Underground Research Facility (SURF) in the USA, the SNOLAB in Canada and finally the Jin-Ping laboratory in China [130]. 41
2.3.5 Representation of the main detectors for each detection strategy: the ionization charge, the scintillation light, the heat (phonons). 44
2.3.6 Representation of the inner vessel of a single-phase noble liquid detector. The shape is usually spherical and is usually completely filled with the noble liquid, which is observed by a dense array of photosensors. Only the scintillation photons are collected in these detectors. 49
2.3.7 Representation of the inner vessel of a double phase noble liquid detector. The shape is usually cylindrical: when an incident particle scatters on the noble liquid, the scintillation signal is observed: the "S1" signal. Then, a vertical potential drifts the ionization electrons up to an extraction grid, by which they are injected into the noble gas pocket. Here they are accelerated, giving a second amplified signal, called S2. . . 50
2.3.8 Updated exclusion plot in the WIMP mass- Spin-independent cross-section, only shown for the leading experiments [200]. . . 53
3.1.1 Recombination probability in liquid argon, for a drift field of 200 V/cm [223]. 58
3.1.2 Mean light yield (in red) from DarkSide-50 data. On average the light yield was measured to be 6 PE/keV with a drift potential of 200 V/cm, with a peak below 30 keV up to 7.5 PE/keV [222] 59

3.1.3 Scheme of the origins of the signals due to a particle scattering on liquid argon. The fraction f_L of the recoil energy goes in thermal motion. The left energy may excite or ionize argon atoms. In the first case, it will bound in a quite unstable excimer, which may be either in a triplet or a singlet state, according to the spin configuration. Whatever the case, a photon peaked at 128 nm is released. The ions also can recombine with electrons, bringing to a very excited argon dimer, which first decays vibrationally and only then radially, again either from a triplet or a singlet configuration. Both processes - exciton self-trapping and recombination- contribute to the S1 signal, both in a single and in a double phase liquid argon detector. Finally ions which do not recombine also correspond to electrons which are not captured. In a double phase chamber a drift field is applied to collect them and produce the S2 signal in the gas pocket. 60
3.1.4 Comparison between the Lindhard model, the Mei model, the modified-Mei model developed from DarkSide collaboration with the experimental data from SCENE [231], MicroCLEAN [232], W.Creus et al. [233] and WARP [234]. Beside MicroCLEAN and W.Creus at al. at low energy, the modified-Mei model shows agreement with the measurements available in the literature and is now the favourite effective quenching model in liquid argon. 64
3.1.5 Distribution of the f90 parameter versus S1, in 532 days of data taking in DarkSide-50 [212]. Events at $f_{90} = 0.3$ are electron recoils, hence scattering events from γs or βs. The main contribution comes from ^{39}Ar β decays. At $f_{90} = 0.7$ nuclear recoils are expected, as they have a higher singlet state likelihood and then a faster scintillation signal. Nuclear recoils are neutrons and eventually WIMPs, which are specifically expected in the blue area. The three dotted lines show the f90 cuts at which 1 %, 50 % and 99% of the WIMPs would "survive", i.e. of WIMP acceptance, obtained thanks to calibrations with the neutron AmBe source. 66
3.2.1 DEAP-3600 detector design showing the inner vessel, the LGs, the PMTs and the filler blocks, out to the stainless steel outer vessel, together with its neck. The representation does not shown the TPB coating and the ultra-pure water veto, in which the outer vessel is immersed [196]. 69

3.2.2 Cross-section of the inner detector, from the acrylic vessel to the stainless steel shell. The light from the LAr is brought by the acrylic light guide to the PMT, which is thermally isolated. Filler blocks help with thermal gradient between the photosensors and the inner vessel, together with the passive neutron suppression [196]. 70
3.2.3 Assemblying of the inner detector. In (A) the acrylic vessel was connected to the light guides, to which in (B) reflectors and magnetic shielding was applied. In (C) the view from the inside of the inner vessel is given, to show the Tyvek (white) and the PMT installing. The installation of the filler blocks is shown in its preliminary stage in (D) and completed in (E) [196]. 71
3.2.4 Flow diagram of the cryogenic system in DEAP-3600. The argon gas is first injected in the loop via a flow control valve and a double diaphragm process pump. Then the argon is chemically purged in the SAES getter and then radon-purified in the radon trap. The condenser liquefies the argon from the radon trap to the inner vessel, while the gas argon is delivered to the boiler. Finally, the liquid argon from the vessel is also delivered to the boiler, where it is recirculated in the cryogenic loop [196]. 73
3.2.5 Flow diagram of the DAQ system. The SCBs takes in input the signal from the three photodetection systems: the neck, the inner vessel and the Veto PMTs. The DTM checks if those signals fall in the ^{39}Ar region and hence whether to trigger or not. The triggered signals are sent to the digitizers, which finally send the waveform to the reconstruction and filter software and then store the digitized waveform in the disk [196]. 76
3.2.6 The space of parameters E_{prompt} and F_{prompt} for a typical physics run, evaluated by the DTM. Events in region X are discarded, while specific trigger conditions are applied in region A, B, C and D. Usually 99 % of the events in region C are "pre-scaled", which means that only DTM information are kept. The lowest energy bound of E is the ^{39}Ar endpoint [196]. 78

3.3.1 Rendering of the main component of DS-20k detector. In grey the PMMA acrylic vessel is shown, with the SiPM top array installed. In green, the Gd-loaded acrylic Shell (GdAS) will separate two AAr active layers, called Inner and Outer Active Buffer (IAB and OAB respectively). All of this is contained in the ProtoDUNE-like cryostat, in red, and stands on a support on the floor of the cryostat during the installation, but will then suspended by ropes when the construction will be completed. 82
3.3.2 Snapshot of a Photodetection Module developed for DarkSide-20k, composed by a 50 x 50 mm^2 tile, together with its amplifier board and the mechanical structure. 83
3.3.3 Square MotherBoard (SQB) made by 25 PDMs assembled at LNGS. SQBs will be the very photodetection unit in DarkSide-20k. 85
3.3.4 SQB array in DarkSide-20k. Two arrays will be installed at the top and at the bottom of the inner vessel, each consisting of 4140 PDMs. Motherboards in the corners of the octagonal plant will be modified to have only 15 over 25 supplied PDMs . 86
3.3.5 Representation of the inner vessel, made in PMMA acrylic, internally covered with the ESR reflectors. The top and bottom SiPM arrays, placed just outside the vessel, follow the octagonal plant of the TPC. 87
3.3.6 Rapresentation of the cryogenic system. 91
3.3.7 View of the DS-20k veto detector. Two layers of Atmospheric Argon are separated by the Gd-loaded PMMA foils composing the GdAS, in blue. The veto is contained in the Faraday cage, shown in brown. The height subdivision panels dividing the AAR inner and outer buffers are shown in green. 93
3.3.8 Design of the test front end board (FEB) coupled with the tile. In the veto a peculiar geometry for the coupling of the SiPMs tile to the FEB is foreseen, with two parallel devices for the veto detector. 94
3.4.1 The Time Projection Chamber of ReD. The TPC is surrounded by a field cage of nine copper rings and is contained by a PTFE structure. It is also possible to see the two FEBs, with each cable connected to its channel. 99

3.4.2 Scheme of the cryogenic system developed by Criotec company for ReD experiment. During the filling, commercial gas argon is purified and then condensed by means of the cryocooler. From there it drops into the dewar, which contains the active volume, until it reaches a level of 30 cm. Then the flowing of the commercial gas is stopped, and the system enters into the recirculation mode: from the TPC evaporated argon is circulated into the purifier and hence to the cryocooler, restarting the circle. 100
3.4.3 Mapping for the laser runs which entered the present analysis (top view of the TPC). On the top, the four bottom channel, each composed by the input of six SiPMs. On the bottom, the top tile, with its 24 read-out channels. Two CAEN ADC boards, each with 16 channels, amplify and digitize all the 28 channels. 101
3.4.4 Top view of the FEB for the top tile, custom developed from INFN Naples together with DarkSide Bologna and LNGS. It is possibile to see the 24 read-out channels, four for side, which assured to ReD the best x-y reconstruction available. 101
4.2.1 Scaling between the per nuclear and the elastic per nucleon cross-section for a elementary dark matter particle interacting with liquid argon through a repulsive top-hat potential. . . . 107
4.3.1 Sensitivity of DEAP-3600 to MIMPs with three years of data taking, assuming no background. Thanks to its wide exposure, it would be the only running experiment with a mass reach greater than Planck Mass. The lowest cross section at which DEAP-3600 is sensitive is $\sigma_{\chi-T} = 5.6\ 10^{-25}$ cm^2, assuming no background. Lower mass ranges has already been excluded [272]. 111
4.4.1 Average MIMP incoming direction at SNOLAB, where the angle α is defined between the MIMP average incoming direction and the detector position vector from the Earth center. For reference, the flux modulation is shown along the whole year, starting from the 11th July. 112
4.4.2 Propagation of the MIMPs along different paths, depending on the incoming direction in the detector frame. The overburden is divided into: atmosphere (blue), crust/mantle (green), core (red). θ is defined as the angle between the incoming MIMP direction and the detector zenith. 113

4.4.3 List of the elements composing the mantle and the core. The core is assumed to be uniform, while the mantle also includes the crust [279]. 114
4.4.4 Attenuation of a MIMP particle coming from different directions (the zenith is set at $\theta = 0$) in DEAP-3600 with mass $M_\chi = 10^{16}$ GeV and cross-section $\sigma_{\chi-T} = 2.6 \times 10^{-18}$ cm^2 after passing through the atmosphere (blue) and the mantle (green). 116
4.5.1 Waveform for a simulated MIMP event in DEAP-3600, with $\sigma_{\chi-T} = 2.6\ 10^{-22}$ cm^2 and $M_\chi = 10^{18}$ GeV. The MIMP passes through the inner vessel in 6 μs; then a tail of afterpulses follows. 118
4.5.2 Distribution in the qPE vs Fprompt plane of MIMPs at the same MIMP-nucleus cross-section $\sigma_{\chi-T} = 2.6 \times 10^{-22}$ cm^2 and different mass, $M_\chi = 10^{16}$ GeV and $M_\chi = 10^{19}$ GeV. 121
4.5.3 Comparison of MIMPs in terms of qPE and FPrompt variables. The cross-sections shown go from $\sigma_{\chi-T} = 10^{-24}$ cm^2 to $\sigma_{\chi-T} = 10^{-22}$ cm^2, while the mass is $M_\chi = 10^{18}$ GeV. For each cross-section, qPE agrees with the number of expected scatterings, assuming average recoil energy of 8-12 keV$_{ee}$ for each scattering, and hence increases with the cross-section. FPrompt, on the other hand, decreases with the increase of the cross-section, as the number of scatterings which fall out of the prompt window increases. 122
4.5.4 FmaxPE distribution for MIMPs at different cross-sections. FmaxPE shows a behaviour analog to Fprompt: a monotone but non-linear increase with the cross-section decrease, with a spread at FmaxPE higher than 0.1 only at low cross-sections, below 4000 qPE. 123
4.5.5 Distribution of Top Charge Ratio, the fraction of charge in the first and second top PMT rings normalized to qPE, for MIMPs at different cross-sections. At high energy, above the LAr endpoint, Top Charge Ratio is below 0.05, while at lower energies, it spreads up to 0.1. 124
4.5.6 Waveform for a simulated MIMP event in DEAP-3600, with $\sigma_{\chi-T} = 2.6 \times 10^{-23}$ cm^2 at $M_\chi = 10^{18}$ GeV. SubeventN returns the number of highest peaks along with the acquisition gate, recognized by the waveform derivative's significance. Only if the peak has a derivative above 5ADC/sample, it is stored as Subevent. For O(10) scatterings, the value of SubeventN does not match with the number of scatterings, but is proportional to it. 125

4.5.7 Waveform for a simulated MIMP event in DEAP-3600, with $\sigma_{\chi-T} = 2.6 \times 10^{-24}$ cm^2 and $M_\chi = 10^{18}$ GeV. At such low cross-section SubeventN mainly matches with the number of scatterings. 126
4.5.8 Distribution of SubeventN for a wide range of cross-sections and hence of deposited energy. The variable SubeventN shows not-monotone behaviour. Going from about $\sigma_{\chi-T} = 10^{-24}$ cm^2 up to about $\sigma_{\chi-T} = 10^{-23}$ cm^2, it increases with the cross-section and the number of scatterings. Then it starts decreasing with the increase of the cross-section. This is a consequence of the MultiEvent processor tuning, which looks at the peaks along the waveform and saves peaks as "subevent" only if their derivative is significant. 127
4.6.1 Waveform from a simulated pile-up from two ^{39}Ar recoils. . . . 128
4.6.2 Pile-up events from Physics Run 022677. The performed cut are $Fprompt < 0.4$ and $SubeventN > 1$. As expected from statistics, the main pile-up source is ^{39}Ar due to high activity. 130
4.6.3 Pile-up events in the qPE-SubeventN plane from Physics Run 022677, lasting about three hours. A major cut at SubeventN > 1 and Fprompt < 0.4 is applied, to show the pile-up events which overlap on the MIMP signal in Fprompt variable. The maximum qPE reached in three hours is below 25000; in three years of data taking pile-ups are expected up to about 10 MeV, as it will be better explained in Section 4.6.2 131
4.6.4 Electromagnetic background in DEAP-3600, for a lifetime of 247 days [281]. The more the trigger rate of an event, the higher the maximum pile-up order. Thanks to the Monte Carlo validation, an upper bound on the expected number of pile-ups in three years of data taking is set. Pile-ups due to ^{39}Ar and γs from inner vessel are expected up to SubeventN = 6 below 2.8 MeV and up to SubeventN = 4 below 4 MeV. Then up to 10 MeV, the highest order of pile-up is at SubeventN = 3. 132
4.7.1 Electromagnetic single scatter events from Physics Run 022677. The electron recoil bands is centered at Fprompt ≈ 0.3, dominated by the ^{39}Ar β decays up to about 4000 qPE and then by the natural radioactivity of the materials composing the inner detector, mainly from the PMTs. 135

4.7.2 Comparison in the SubeventN variable between the dataset and the MC simulation. The Dataset is Run 022677 with Fprompt < 0.4 and SubeventN > 1, as only electromagnetic pile-ups are here reconstructed; the MC simulation sums all the events expected to be triggered listed in Table 4.3. 137
4.7.3 Single scatter events from Run 020412, in which the neutron ^{241}AmBe source is set at the calibration tube CalE, in the equator. Neutrons are captured by the materials surrounding the TPC, giving high energy γs. In the present dataset, events at qPE < 8000 were cut, as there the EM background is dominated by the ^{39}Ar. 139
4.7.4 Single scatter spectrum at $Fprompt < 0.4$ from Run 020412. The lowest energy neutron capture γs come from H capture, which is abundant in the acrylic vessel. Then it follows the γs at 4.4 MeV released by the ^{241}AmBe source, set at CalE tube, in the equator. Finally at about 7 MeV the contribution of heavier elements as Iron, Nickel or Chromium, mainly from the vessel and the PMTs, becomes significant. 140
4.7.5 Distribution of EM pile-up events in Run 020412 compared to the MC simulations of the expected triggered events. 142
4.8.1 Average qPE expected in terms of the dark matter-nucleus cross-section. This relation will allow determining the MIMP-nucleus cross-section corresponding to each energy range. . . . 143
4.8.2 Selection cut on the Fprompt variable. Below 4000 qPE, Fprompt is asked to be < 0.3; then, at higher energies and cross-sections, the cut is tightened at Fprompt < 0.1. 144
4.8.3 Selection cut on FmaxPE. As well as Fprompt the cut is stronger above the ^{39}Ar endpoint, where is FmaxPE < 0.02, while above it the condition is relaxed to FmaxPE < 0.03. . . 145
4.8.4 Selection cut on Top Charge Ratio, the sum of the charge in the first and the second top PMT rings normalized to qPE. At high energies, which means also high cross-section, the number of scatterings is higher, giving a widely uniform distribution of the scintillation light, so the MIMPs are asked to have Top Charge Ratio < 0.05 (black line); at lower energies, only a bunch of scatterings are expected, so MIMPs are asked to have Top Charge Ratio < 0.06 (green line). 146
4.8.5 Cut in the qPE vs. SubeventN plane, tuned on the expected pile-up distribution in three years of lifetime. 147

4.8.6 Acceptance for the ROI # 1 and ROI # 2 in Table 4.6. The non-monotone behaviour of the acceptance is a consequence of the selection cuts in SubeventN, necessary to reject the pile-up background from MIMP events. 148
4.8.7 Distribution in the qPE-Fprompt plane of the events in the muon sideband, asking the coincidence within 100 us from the MC trigger. 662 events are found, apparently distributed in two populations. The overabundance of the events compared to the ones expected from muons -about 600- is very likely due to the lack of low-level cut and to the contribution of pathological events, due to the PMT saturation. 152
5.1.1 Illustration of an Avalanche Photodiode set in Geiger mode. The production of an electron-hole pair by photoelectric effect determines an avalanche of electrons and holes, drifted by the reverse bias respectively in the n+ and p+ doped regions [286]. 157
5.1.2 Equivalent circuit for a SPAD coupled with its quenching resistor R_Q. When the circuit is closed, the capacitance -at first charged to V_{bias}- discharges through the whole circuit. R_Q quenches the flowing current below the breakdown voltage: the switch opens. Then the capacitance recharges back to V_{bias}. As usually $R_Q >> R_S$, the recharge is expected to be much slower than the discharge process [286] [289]. 159
5.1.3 Equivalent circuit for a SiPM. SPADs -or pixels- are set in parallel, all charged to the same V_{bias}. When one of the SPAD's circuit closes, its quenching resistor R_Q decreases not only its SPAD's potential, but consequently the potential through all the pixels, whose capacitance then recharges back to V_{bias} [286] [289]. 160
5.1.4 Illustration from a side view of correlated noises from a SPAD. Once that one pixel is fired, giving the "primary avalanche", the acceleration of charge carriers releases near-infrared photons according to a isotropic spatial distribution. The emitted photons eventually reach one close pixel, giving an Optical Crosstalk, which is Direct or Delayed depending on whether the photon is directly absorbed in the active region after passing through the isolation trench or it is first reflected by the Silicon substrate, with a resulting delay of O(10) ns. The same primary avalanche can also -but not necessarily- determine an afterpulse in the primary pixel, if one or more charge carriers has been trapped and then released by defects in the Silicon lattice [290]. 161

5.1.5 Breakdown Voltage for FBK-NUV-HD Low Field and High Field SiPMs measured at cryogenic temperatures [285]. 162
5.1.6 The amplitude of the average signal from a SPAD increases with the overvoltage. For any overvoltage a slight increase with the temperature is observed [285]. 163
5.1.7 The characteristic recharge time is determined by the quenching resistor, equal to 10 MΩ in FBK-NUV-HD LF SiPMs [285]. 163
5.1.8 The gain is the number of charge carriers accelerated in an avalanche. It strongly depends on the overvoltage and the temperature [285]. 164
5.1.9 Distribution of correlated and uncorrelated noise in terms of the delay time, in absence of light at 77 K. After the primary pulse, the small population of Delayed Crosstalks is focused at a few nanoseconds. Then the afterpulses, together with the optical crosstalks induced are scattered at a few microseconds, with an amplitude that goes up to a maximum of one entire photoelectron. Finally the dark count rate is recognized between a few milliseconds up to O(100)s, together with their induced optical crosstalks, whose amplitude is proportional to the number of fired SPADs [285]. 165
5.2.1 SER for ReD Channel 27, in the top tile. Each peak corresponds to the events with 0,1,2.. photoelectrons in input to the SiPM, and is fitted with a gaussian whose average is a multiple of the "gain", as can be seen in Equation 5.2.2 . . . 167
5.2.2 Calibration of the Integration Charge for ReD Channel 27 in the top tile. Each photoelectron gives a waveform with an integral of $(2.4 \pm 1) \times 10^3$ ADC x TDC. 168
5.2.3 Gain for the integration charge for each ReD channels in the top tile, on average equal to 2400 ADC x TDC. 168
5.2.4 Percentage SER energy resolution for all ReD channels, calculated as the ratio between the smearing of the peak at one photoelectron in the SER and the gain. On average the SER resolution in ReD top channel is 24 %. 169
5.2.5 Laser pulse from Channel 15 due to one photoelectron. The fit function is the sum of a fast component -which determines the rise of the signal and is described by an exponential- and a slow component, which is characterized by the recharge time of the SPAD and it is fitted with the convolution of a gaussian and an exponential. The digitizer has a sampling rate of 500 MHz, so each TDC sample corresponds to 2 ns. 170

5.2.6 Fit parameters for the first twelve channels in the top tile. On average $\sigma \approx 4.5$ ns, $\tau \approx 400$ ns and $p_s \approx 0.94$. 171
5.2.7 Simulated waveform in ReD from 2 simultaneous photoelectrons before (top) and after (bottom) the application of the matched filter. Notice how the electronic noise is strongly suppressed, while the information on the relative amplitudes of the pulses are kept, together with their arrival time. The peak-finder algorithm provides for each peak the time and the "prominence", which is shown in red and is defined as the height of the filtered peak after subtraction of the local baseline and close dominant peaks. 173
5.2.8 Simulated waveform in ReD from 5 photoelectrons followed by one afterpulse before (top) and after (bottom) the application of the matched filter. Notice how the electronic noise is strongly suppressed, while the informations on the relative amplitudes of the pulses are kept, together with their position. 174
5.2.9 The peak found by the peak finder algorithm are drawn in red, along a simulated and filtered waveform from eight photoelectrons. The second peak was not found as it was below the prominence threshold at 3. Also any peak with a filtered amplitude less than 4 would not be seen, as it would be below the height threshold. Finally all the ripples left after the filtering are also suppressed by asking a minimum distance of 1 sample between two peaks. 175
5.2.10 Peak finder efficiency in terms of the afterpulse time delay in Channel 15. Any peak with a time delay of at least 500 ns will be "seen" by the peak finder. Below 150 ns the algorithm is completely inefficient. For this reason this technique was applied to find afterpulses, but not delayed optical crosstalk, whose time delay is O(10 ns). 176
5.2.11 SER for the prominence charge in Channel 14, in the top tile. Events at zero photoelectron are not counted, as the height and/or the prominence would be below threshold. Each photoelectron returns a peak prominence of about 5.1. The energy resolution is $\sigma_1/gain = 7\%$. 177
5.2.12 Calibration for the Prominence variable. The errors are the standard deviations of the gaussian in the SER figure. 177
5.2.13 Gain for the prominence charge, for all ReD top channels. On average a peak of 5 as prominence corresponds to 1 PE. . . . 178

5.2.14 Resolution for the prominence charge in top tile. The charge defined from the prominence shows to have a resolution of about 6.5 %. 178
5.3.1 Peaks found before and after the primary avalanche in 5043 events from Channel 27, where the primary pulse carries 1 PE in the expected trigger time, at 5920 ± 40 ns. For each events, the primary peak is not stored. The primary peak time is taken as zero; then all the found peaks in that event are stored according to their arrival time respect to the primary pulse. Dark (uncorrelated) noise is distrubuted with the same probability before and after the primary peak, while afterpulses can lay only after the primary avalanche. The drop below about 50 ns is due to the prominence of the peaks nearby the primary pulse, which results to be below the peak-finder prominence threshold. 180
5.3.2 Distribution of the afterpulse probability in ReD top channels. On average the probability to have an afterpulse given 1 PE in the primary avalanche is ≈ 2% 181
5.3.3 Time distribution of afterpulses in Channel 27 (blue line), obtained after the subtraction of the peaks found before the primary with the ones found after it. The distribution was then corrected for the peak finder efficiency (red line) and then fitted with the linear combination of two exponential and a constant. 182
5.3.4 Characteristic times for the two exponential functions fitting the corrected afterpulse probability, for each ReD top channel. 183
5.3.5 Afterpulse energy in terms of the time delay for the Channel 27. Avalanches after a small time delay from the primary will also have a small fraction of charge, assuring a negligible impact on the average number of reconstructed photoelectrons. 184
5.4.1 Diagram of the C++ based Monte Carlo. Once that the primary pulse is generated according to the theoretical poissonian distribution, each photoelectron can give an afterpulse and/or a crosstalk. An afterpulse can give rise to a secondary afterpulse and/or a crosstalk. Same way a crosstalk can give rise to a secondary afterpulse and/or crosstalk; the only condition stands for afterpulses, whose primary pulse must be at least equivalent to one photoelectron. The loop goes on until the number of photoelectrons Q_F stops increasing. 185

5.4.2 For Channel 19, the SER amplitude distribution from real data (blue) are compared to the output from the simulation (red), assuming a null Crosstalk Probability, $P_{CT} = 0.0$. Afterpulses in itself increase the number of reconstructed photoelectrons in the laser pulse only of one afterpulse, so that in the simulation the number of events above 2 photoelectrons is negligible. Events in the data at higher PE are due to the contribution of crosstalks. 186
5.4.3 Chi square distribution vs the Crosstalk Probability for Channel 27. As the only parameter to constrain is the crosstalk probability, the chi-square was chosen as test-statisitc. In this case the probability to observe a crosstalk in Channel 27 is about 24 %, as pointed from the black dotted line. 187
5.4.4 Comparison with the value of $P_{CT} = 0.24$ which minimizes the chi square between data (blue) and the Toy Monte Carlo (MC) output (red) in Channel 27. As expected, the amplitude distribution matches with the dataset, confirming the result. . 187
5.4.5 Distribution of Optical Crosstalks probability through all ReD channels in the top tile. 188
6.1.1 Comparison of the main detection channels in liquid argon up to 90 MeV. The CEνNS is three order of magnitude greater than elastic scattering and neutral current, and about 50 times greater than charged current. The outstanding cross-section at low energy will compensate for the relatively small mass target of DarkSide-20k and Argo detectors and allow for a sensitivity competitive with large tonne neutrino detectors. Moreover, interactions via CEνNS happen in neutral current, by the exchange of a Z^0 boson, so liquid argon interacts equally to any neutrino flavour, further increasing the statistics, and gives information on the global neutrino emission, without any neutrino oscillation contribution. 193

6.2.1 Neutrino luminosity time evolution $L(t)$ of a core-collapse supernova with 27 $M_\odot$ progenitor star mass and set at 10 kpc for the different neutrino flavours assuming direct neutrino mass ordering, provided by the spherical symmetric simulation of a CCSN with a progenitor star mass of 27 $M_\odot$, LS220K as equation-of-state, set at 10 kpc from the Earth [320], assuming neutrinos Normal Mass Ordering. The ν_x refers to a single species of heavy neutrinos, as any difference in the production rate of muon and tauon (anti)neutrinos is observed to be negligible in the performed CCSN simulations. The rebound time is set at $t = 0$; then, the neutrino trapping follows, lasting about 3 ms. The very characteristic peak of the neutronization burst arises from 4 ms to 30 ms, in which mostly electron neutrinos are released thanks to the propagation of the shock wave in the outer CCSN core; the following accretion phase lasts from 30 ms to 500 ms, envolving also heavy neutrinos from the accreting matter on the collapsing core. Finally the neutron star cooling phase lasts about 10 s, where neutrinos of any flavour are released with mainly the same likelihood. 195
6.2.2 The time evolution of neutrino mean energy $\langle E_\nu \rangle$ for the different neutrino species as released by the 27 $M_\odot$ core-collapse supernova taken as reference. Neutrinos from the CCSN burst will scatter with an incident energy of about 10 MeV; hence the CEνNS interaction is the most promising one to detect this neutrino signal. 196
6.2.3 Representation of the infall phase (left) and the neutronization phase (right) in terms of the mass, in blue, and the local status of the matter. In the infall phase the core collapses due to its own gravity; in the meantime, electron neutrinos produced mainly by nuclei photo-disintegration and electron capture are free to leave the core. When the density in the inner core reaches that of nuclear matter, the nucleon degeneracy pressure suddenly halts the core-collapse, determining the formation of a shock, which propagates back through the outer layers of the core. The shock wave dissociates nuclei along its path, leaving free nucleons and protons and electron neutrinos, who are free to leave the star and determine the neutronization burst. The shock wave never reaches the edge of the core at about 3000 km, but looses its energy at 100-200 km, where it stalls [322]. 197

6.2.4 In the accretion phase (left), the outer layers of the core accretes on the stalled shock wave, while electron antineutrinos are produced by capture of free positrons on nucleons from the inner core; in the meantime, in the outer core, the friction in the accreting matter allows for the production of all neutrino flavours by e+ e- annihilation processes mostly. The cooling phase (right) starts when the shock wave reaches the edge of the core, gravitationally unbinding the star and giving the supernova explosion. The 99 % of the supernova energy is released via neutrinos of all flavours, in about O(10) s. The exact processes occurring in the cooling layers are still under study, while in the center the proto-neutron star is born, with a radius of about 10 km and a mass of 1.4 $M_\odot$ [322]. 200
6.3.1 The energy spectrum of neutrinos emitted from the 27 $M_\odot$ supernova at 10 kpc, assuming direct neutrino mass ordering. Most of the CCSN neutrinos will scatter on the detectors with an incident energy below 30 MeV, where the dominant interaction is CEνNS scattering. 201
6.3.2 A simulated spectrum of the nuclear recoil energy E_r in liquid argon from the CEνNS process induced by neutrinos from a core-collapse 27 $M_\odot$ supernova at 10 kpc. 202
6.3.3 Time profile of supernova neutrino emission, for both the 11 $M_\odot$ and 27 $M_\odot$ set at 10 kpc of distance, compared with the overall background (purple), considered as a unique population as they are all constant in time. The CCSN signal becomes comparable with the background at 8 s from the start of the burst, so a time selection cut is applied at t $<$ 8 s. . . 205
6.3.4 Energy spectrum in the N_{e^-}-variable of CCSN neutrinos, for both the 11 $M_\odot$ and 27 $M_\odot$ set at 10 kpc of distance, compared with the expected backgrounds, namely "single electron" events (purple), ^{39}Ar decays (yellow) and the external background (green). The selection cut is applied in the energy range $(2-100)N_{e^-}$. 206
6.3.5 Detection efficiency to the CCSN signal for different energy threshold. As reference, the neutrino emission from the 27 $M_\odot$ CCSN at 10 kpc of distance was assumed. The threhsold set is at $N_{e^-} \geq 3$, in order to strongly suppress the contribution to the event rate of the single-electron background. 207

6.4.1 DarkSide-20k and Argo discovery potential to 11 $M_\odot$ and 27 $M_\odot$ SNe (top) and to its neutronization burst only (bottom) as a function of the distance, assuming the standard background hypothesis (solid line) and by considering a lower contamination of ^{39}Ar, up to a factor of 10 less (band) . Vertical lines represent the distance from the Earth to the Milky Way center, to its farthest edge and to Large (LMC) and Small (SMC) Magellanic Clouds. 210
6.4.2 Time profile of neutrinos from the accretion (left) and cooling (right) phases of a 27 $M_\odot$ CCSN at 10 kpc distance, as detected by DarkSide-20k and Argo. The bands represent the statistical uncertainty, depending on the time binning of 20 ms and 100 ms for DarkSide-20k and Argo. 211
6.4.3 Examples of fit of the Monte Carlo neutrino interaction samples from the accretion phase plus cooling phase in a 27 $M_\odot$ CCSN burst at 10 kpc of distance, performed in DarkSide-20k (left) and Argo (right) and generated in the [0.02, 8] s time range. 212
6.4.4 DarkSide-20k and Argo sensitivities to the average neutrino energy and the integrated neutrino energy from a 27 $M_\odot$ CCSN set at 10 kpc, evaluated for the accretion phase in the [0.1, 1] s time range and the cooling plus the accretion phase, in the [0.02, 8] s time range. The two parameters are obtained by fitting 5×10^4 toy Monte Carlo samples with α equal to 2.3 and 2.0 for the two time range respectively. Red crosses represent the true values from the simulation in input. 213

9 List of Tables

List of Tables

4.1 List of assumed rates for the main EM background sources in DEAP-3600 [281]. The main contribution comes from the LAr bulk with ^{39}Ar βs and the ^{232}Th and ^{235}U chains in the PMTs. 129

4.2 Three energy regions are set, according to the pile-up distribution in three years of data taking. For each energy range, the expected maximum pile-up order, and hence the maximum value for SubeventN, is given for the foreseen lifetime. The left pile-up background after applying the selection cut SubeventN > SubeventN$_{MAX}$ is given. An overall 10 % of uncertainty is assumed for the residual pile-up background, according to the validation of the Monte Carlo simulation performed in Section 4.7. 133

4.3 Expected pile-up events in Run 022677. The statistics determines the number of pile-ups happening in the detector; the validation follows by looking for the number of events that are actually triggered; this means taking into account the percentage which is prescaled by the DTM and the efficiency in distinguishing all the pulses and correctly tag a pile-up of n recoils at SubeventN = n. 136

4.4 List of assumed rates for the dominant neutron capture γ sources in DEAP-3600. 140

4.5 Expected pile-up events in Run 020412. As already performed with the low-energy calibration, the number of pile-up events expected to be triggered takes into account the percentage which "survive" to the DTM prescaling and the fraction that is correctly recognized at Subevent N = n, if n is the number of recoils in the acquisition window. Furthermore GEANT4 simulations returned the fraction of events falling below 8000 qPE, where the dataset was cut. 141

4.6 List of the identified ROIs for MIMPs in DEAP-3600, with both the qPE and MIMP-nucleus cross-section range. The maximum background is the number of events expected to survive the SubeventN cut, which removes pile-up events, according to the expectations given in Section 4.6, confirmed by the Monte Carlo validation performed in Section 4.7; an overall uncertainty of 10 % was assumed for the background level, one order of magnitude greater than the actual uncertainty on the background retrieved in Section 4.7. The ROI #0, at low cross-section and energy, is not accessible by the present analysis, due to the DTM prescaling, which rejects 99 % of the events below the ^{39}Ar endpoint; still, the left background and the selection cuts to reject MIMPs in this energy range is here shown, for reference. Finally, in ROI #3 the Monte Carlo simulations of MIMPs were not available due to the wide number of scatterings; also, the simulations at millions of qPE are not trustworthy. The expected background here comes from muons, which will be mainly rejected by the muon veto cut, leaving maximum 18.5 not-tagged muons. The opening of the muon sideband in the data will allow evaluating the impact of a tight cut in Fprompt on the muon rejection. In the next section this table will be updated, after the optimization of the Fprompt cut in ROI # 3. 149
4.7 List of the selection cuts that will be applied in each ROI and energy range. An overall Muon-Veto cut will be applied, removing all the events within [-1, 100] μs from the water tank trigger. As the analysis threshold is set at 4000 qPE, the ROI#0 is here not listed. 153
4.8 List of the identified ROIs for MIMPs in DEAP-3600, with both the qPE and MIMP-nucleus cross-section range. The Muon Veto cut, rejecting any events within 100 us from the muon veto trigger is applied in any ROI. The analysis threshold is set at 4000 qPE. The maximum expected background is finally given after the selection cuts in SubeventN, Fprompt, FmaxPE and Charge Top Ratio in the ROI#1 and ROI#2; in the ROI#3 only the Fprompt cut at 0.05 will be applied, thanks to the optimization performed with the unblinding of the muon sideband. 154

6.1 Event statistics expected in DarkSide-20k and Argo from 11 $M_\odot$ and 27 $M_\odot$ supernovae at 10 kpc of distance, together with the number of expected events from single-electron and ^{39}Ar background components, after applying the selection cuts, so within the [3, 100] N_{e^-} energy window and in 8 s from the beginning of the burst. 207
6.2 Number of expected events per unit of mass and signal-to-background ratio in DarkSide-20k and Argo from 11 $M_\odot$ and 27 $M_\odot$ CCSNe at 10 kpc, specifically for each phase and after the application of the selection cuts. 208